Fundamental Studies of the Electrode Regions in Arcjet Thrusters

FINAL AFOSR REPORT

Prepared by:

Mark A. Cappelli
Stanford University
Thermosciences Division
Department of Mechanical Engineering
Stanford University, Stanford, CA 94305-3032

Phone: (650) 725-2020
FAX: (650) 723-1748
e-mail: cap@leland.stanford.edu

Mechanical Engineering Department
Stanford University
Stanford, California 94305

REPORT DOCUMENTATION PAGE		Form Approved OMB No. 0704-0188

1. AGENCY USE ONLY *(Leave blank)*	2. REPORT DATE MARCH 1998	3. REPORT TYPE AND DATES COVERED FINAL REPORT 1 AUG 95 - 30 NOV 97

4. TITLE AND SUBTITLE
FUNDAMENTAL STUDIES OF THE ELECTRODE REGIONS IN ARCJET THRUSTERS

5. FUNDING NUMBERS
F49620-95-1-0317

2308/AS

61102F

6. AUTHOR(S)
MARK A. CAPPELLI

7. PERFORMING ORGANIZATION NAME(S) AND ADDRESS(ES)
STANFORD UNIVERSITY
THERMOSCIENCES DIVISION
DEPARTMENT OF MECHANICAL ENGINEERING
STANFORD, CA 94305-3032

8. PERFORMING ORGANIZATION REPORT NUMBER

9. SPONSORING/MONITORING AGENCY NAME(S) AND ADDRESS(ES)
AIR FORCE OFFICE OF SCIENTIFIC RESEARCH (AFOSR)
110 DUNCAN AVENUE SUITE B115
BOLLING AFB DC 20332-8050

10. SPONSORING/MONITORING AGENCY REPORT NUMBER

11. SUPPLEMENTARY NOTES

12a. DISTRIBUTION AVAILABILITY STATEMENT
APPROVED FOR PUBLIC RELEASE, DISTRIBUTION IS UNLIMITED

12b. DISTRIBUTION CODE

13. ABSTRACT *(Maximum 200 words)*
This research focuses on the understanding of the plasma dynamics in the near-node and near-cathode region of arcjets with an emphasis on the development of an extensive database for the validation of arcjet models. During the first year of this research period, the arc-cathode interaction was investigated by in-situ spectroscopic imaging and by axial emission spectroscopy, providing measurements of cathode current dinsity, cathode temperature, and near-cathode plasma properties. In addition, during this grant period, we have extended the use of laser-induced fluorescence (LIF) to make measuremtns of plasma propertie within the expanding region of the nozzle and have accumlated an extended data base that includes, in addition to the use of pure hydrogen propullant, mixtures of hydrogen and nitrogen to simulate hydrazine decomposition products. In the final year, a new laser-based diastic, Doppler-Free Absorption Spectrosocpy (DFAS) was developed and applied to measure the exit plane electron number density in a hydrogen arcjet, one of the last properties needed to provide closure to the vast data set that we have generated for low power hydrogen arcjet. As a spin-off to this grant, the LIF diagnostics that was developed for arcjet through this program was extended to the study xenon plasmas, and implemented to measure both neutral and ionized on velocities at the exit of a Hall thruster. This contributed to a comprehensive study of the near-exit region of our Hall discharge device. To compliment the LIF diagnostics on our Hall thrusters, we have made etensive measurements of the transient and time-average plasma properties using conventional electrostatic probes.

14. SUBJECT TERMS

15. NUMBER OF PAGES

16. PRICE CODE

17. SECURITY CLASSIFICATION OF REPORT UNCLASSIFIED	18. SECURITY CLASSIFICATION OF THIS PAGE UNCLASSIFIED	19. SECURITY CLASSIFICATION OF ABSTRACT UNCLASSIFIED	20. LIMITATION OF ABSTRACT

1997 FINAL REPORT
(From 1 August 1995 to 30 Nov. 1997)

Fundamental Studies of the Electrode Regions in Arcjet Thrusters

Mark A. Cappelli
Stanford University

High Temperature Gasdynamics Laboratory
Department of mechanical Engineering
Stanford University, Stanford, CA 94305-3032

Phone: (650) 725-2020
FAX: (650) 723-1748
e-mail: cap@leland.stanford.edu

Executive Summary

This research focuses on the understanding of the plasma dynamics in the near-node and near-cathode region of arcjets with an emphasis on the development of an extensive database for the validation of arcjet models. During the fist year of this research period, the arc-cathode interaction was investigated by in-situ spectroscopic imaging and by axial emission spectroscopy, providing measurements of cathode current density, cathode temperature, and near-cathode plasma properties. In addition, during this grant period, we have extended the use of laser-induced fluorescence (LIF) to make measurements of plasma properties within the expanding region of the nozzle and have accumulated an extended data base that includes, in addition to the use of pure hydrogen propellant, mixtures of hydrogen and nitrogen to simulate hydrazine decomposition products. In the final year, a new laser-based diagnostic, Doppler-Free Absorption Spectroscopy (DFAS) was developed and applied to measure the exit plane electron number density in a hydrogen arcjet, one of the last properties needed to provide closure to the vast data set that we have generated for low power hydrogen arcjet. As a spin-off to this grant, the LIF diagnostics that was developed for arcjet through this program was extended to the study xenon plasmas, and implemented to measure both neutral and ionized xenon velocities at the exit of a Hall thruster. This contributed to a comprehensive study of the near-exit region of our Hall discharge device. To compliment the LIF diagnostics on our Hall thrusters, we have made extensive measurements of the transient and time-average plasma properties using conventional electrostatic probes.

SUMMARY OF ACCOMPLISHMENTS/NEW FINDINGS

Our accomplishments during this grant period include: (i) the direct measurement of electrode temperatures in low and high power arcjet thrusters; (ii) the development and application of impact pressure and mass flux probes to the study of the structure of the anode region and plume of low power arcjets (iii) a laser-induced fluorescence and emission studies of the near-electrode flowfield region of arcjet thrusters, including the collection of data on mixtures of hydrogen and nitrogen to simulate hydrazine decomposition products; (iv) the application of a relatively new laser-based diagnostic, Doppler-Free Absorption Spectroscopy (DFAS) to measure the exit plane electron number density; (v) a thermodynamic analysis of arcjet flowfields, (vi) extensive laser-induced fluorescence and electrostatic probe studies of a Hall thruster, in particular, the measurements of both neutral and ionized xenon velocities, and (vii) the measurements of the transient and time-average Hall plasma properties, including a characterization of the turbulent plasma behavior within the acceleration channel.

The following paragraphs briefly summarize the findings in these individual areas. They reference Ph.D. dissertations and publications (some included as Appendices), which provide a detailed description of the findings of these studies.

(i) Electrode Temperature Measurements

During this grant period, we have made the first reported measurements of operating cathode temperatures and cathode current distribution in arcjet thrusters. These measurements were motivated by the need to better understand arc-electrode interactions, which, in many cases, is the main determinate of arcjet lifetime. Measurements such as these may also provide the needed boundary conditions on current density for use in numerical arcjet simulations. A non-intrusive in-situ measurement technique based on the spectral imaging of the cathode during arcjet operation is described in Ref. 12 and Appendix A. The measured peak cathode temperatures in a high power (~20kW) hydrogen arcjet range from 3900-4000K, and are at or near the melting point of tungsten. A model based on field-enhanced thermionic emission is used to determine the current density distribution and electric field strength at the cathode surface. The peak values at nominal operating conditions are 5×10^8 A/m^2 and 5×10^8 V/m respectively. For space-charge limited electron conduction near the cathode, these values indicate that the plasma conductivity is approximately two orders of magnitude (factor of 100) times that determined from a local thermodynamic calculation at the cathode temperature. This indicates that the plasma near the cathode is overdense with respect to Saha equilibrium. In accordance with previous models of arc contraction, these measured results indicate that the arc attachment at the cathode is strongly two-dimensional, and any detailed analysis of the arc contraction in the cathode region must include two-dimensional heat conduction.

(ii) Impact pressure and Mass Flux Measurements

We have investigated the structure of the near exit plane (anode region) of low power hydrogen arcjet thrusters through spatially-resolved probe-based measurements of impact pressure and mass flux. These measurements were motivated by the need to add closure to wide database that has been established on these types of arcjets at the low (1-1.5 kW) operating conditions with

hydrogen as a propellant. Details of these measurements can be found in Refs. 9 and 14, and also in a preprint included here as Appendix B.

Comparisons of the measured mass flux and impact pressures are made to direct simulation Monte Carlo models for the non-ignited flow, and continuum magnetohydrodynamic models for the arc-ignited flow conditions. The cold-flow impact probes were found to be able to resolve major flow features and were in general agreement with the model predictions. Arc-heated flow impact pressures were also found to be in agreement with model predictions, and it is also noteworthy that thrust densities, derived directly from the impact pressure studies, were in excellent agreement with the more involved measurements of thrust taken from an inverted pendulum thrust stand. Using velocity and temperature data obtained from laser-induced fluorescence measurements, the local density, pressure, and thrust profiles were derived from the measured mass flux profiles across the exit plane. This indirect measure of thrust was also found to be in agreement with that determined by thrust-stand deflection and by the impact pressure studies.

(iii) Emission and LIF Diagnostics of the Internal Arcjet Flowfield

An extensive study has been performed of the axial and radial emission from a low and moderate power hydrogen arcjet. The axial emission measurements were motivated by the desire to have a second, independent measurement of the near-cathode electron density for comparison to that estimated from the cathode current density distribution. The exit-plane radial emission measurements were motivated by the need for electron temperature and electron number densities, which, at the time of these experiments, were only available from Langmuir probe studies performed on similar arcjets operating with mixtures of hydrogen and nitrogen. Details of the emission measurements (axial and radial) can be found in Refs. 3,5, and 6, and in copies of papers included here as Appendixes C and D.

In the axial studies, a numerical simulation of the one-dimensional radiation transport is used to predict the axial spectral emission. The complete visible spectrum is modeled, taking into account the thermal emission from the cathode, and plasma emission through bound-bound, free-free, and free-bound electronic transitions involving atomic hydrogen. A collisional-radiative model prediction of the excited electronic state densities in atomic hydrogen is used to generate the needed state conditions for the radiation transport simulation. The simulation indicates that the shape of the distant wings of the Stark-broadened Balmer-α transition is a suitable diagnostic for electron number density in the near cathode (within 1 mm) region of the high-density plasma within the constrictor. Electron densities extracted from experimental measurements of the axial emission are found to be in the range of 10^{23} and 10^{24} m^{-3}, are only moderately sensitive to specific power, and are in favorable agreement with magnetohydrodynamic simulations of the arcjet flow.

In the radial emission studies, high-resolution spectral lineshapes associated with the Balmer-α transition are recorded along a line-of-sight chord passing through the exit plane. An Abel transformation (assuming axis-symmetry) is used to determine the spectral emission lineshapes at varying radial positions. The profiles are approximated to be Voigt in shape, with the collision-broadened Lorentzian component deconvolved from the Doppler-broadened Gaussian component. The former allows a measure of the radial variation in the exit plane electron number density while the later provides a measure of the translational temperature. The

4

translational temperature is found to be in good agreement with Stark-corrected laser-induced fluorescence measurements of temperature. The electron number densities are in the 10^{12}-10^{13} cm^{-3} range, consistent (within experimental uncertainty) with model predictions. The absolute emission from excited states is also recorded, providing a measure of the absolute excited (electronic) state concentrations. A comparison is made to the excited state populations predicted using the collisional-radiative model developed, with the electron temperature taken as a fitting parameter. This exercise permitted a direct non-intrusive but indirect estimate of the exit plane electron temperature, which was found to be typically 1eV. This temperature is much higher than the translational temperature (peaking at approximately 0.25 eV), indicating a departure from thermal equilibrium. This is not surprising, as it is believed that a significant fraction of the Ohmic dissipation is taking place in the low density expanding region of the nozzle, where the collisional energy transfer between the electrons and hydrogen atoms and molecules is less efficient.

These emission-based measurements of electron density prompted a re-analysis of previous LIF based measurements of translational temperature. A detailed description of this reanalysis is provided in Ref.2 and a copy of the publication is attached as Appendix E. The re-analysis better accounts for electron Stark broadening made possible by the recent publication of improved Stark width theories. The electron Stark contributions to the total laser-induced spectral linewidth is now understood to be greater than originally anticipated, and the translational temperatures at the exit plane are in good agreement with those based on emission, and also now in agreement with MHD model predictions.

We have extended the use of laser-induced fluorescence of the Balmer-α transition in hydrogen to study the internal nozzle flow characteristics of a 1 kW arcjet thruster operating on either hydrogen and simulated hydrazine propellants. Unlike that of a pure hydrogen flow, the complex gas mixture associated with a simulated hydrazine propellant better resembles the actual propellants employed in practice, and poses a greater challenge to simulations which must capture the viscous behavior of the flow at extreme temperatures. These studies are described in detail in Refs. 1,3,7,13, and 20. Reprints of two published papers are included as Appendices F and G.

In these complex high temperature chemically-reacting flows, it is a challenge in itself to adequately calculate the transport coefficients such as the thermal conductivity and viscosity. The focus of this study has been to make measurements of axial velocities, translational temperature, and electron number densities along the centerline of the arcjet nozzle. As with the previous exit-plane studies, axial velocities are measured using the detected Doppler-shift in the Hα fluorescence excitation. Detailed line-shape analysis including both Doppler and Stark broadening allowed us to extract both the translational temperature and electron number densities.

A major finding is that the axial velocity distribution along centerline within the nozzle is quite different for the pure hydrogen flow in comparison to that of the simulated hydrazine flow. Furthermore, an interesting finding is that the fluid along the nozzle centerline is undergoing a rapid deceleration in both cases (hydrogen and simulated hydrazine), however, the deceleration seems to be more pronounced with hydrogen. This is explained in part by the vastly different viscosities of hydrogen and simulated hydrazine mixtures. Simulated hydrazine, with a much higher mixture viscosity, is expected to greatly delay the development of the sonic point in the

vicinity of the throat. It is found that the location of the sonic point is some 2-4 mm further downstream in comparison to the pure hydrogen case. Furthermore, the increased viscosity in the nozzle is likely to more rapidly transport axial momentum to larger radial locations, consistent with the more rapid deceleration of the flow between z = -8 and z = -4 mm. It is noteworthy that our measurements made in pure hydrogen are in excellent agreement with MHD arcjet model predictions. As of yet, no comparison has been made between our measurements in simulated hydrazine flows and the model. Such a comparison will be a stringent test of the simulation's capability to confidently model the transport properties of the flow.

(iv) Sub-Doppler Laser Absorption Measurements of Electron Density

The measured electron number densities from our LIF and emission studies were obtained from a deconvolution of the Hα lineshapes, which are often dominated by Doppler broadening. This masking of the Stark broadening component, in particular near the line core, sets an upper limit to the accuracy of the measured electron densities (of about an order of magnitude). While previous emission measurements attempted to overcome these limitations by studying the shape of the distant linewings, those measurements suffered from an inadequate theory for the shape of these distant linewings, especially at the relatively low plasma densities expected near the exit plane. In order to overcome some of these limitations, we have applied a laser-based Doppler-free Absorption Spectroscopy (DFAS) method, which, like LIF, provides a measurement of the Hα lineshape, however, without the dominating affect associated with Doppler broadening. Details of these studies can be obtained from Ref. 19, included here as Appendix H.

In DFAS an intense laser is used to saturate an electronic transition of a particular species of interest, in this case, the Hα transition in atomic hydrogen. If the laser is incident onto a purely heterogeneously-broadened (Doppler-broadened) class of absorbers, then the laser photons, of frequency are only absorbed by that velocity class of absorbers that have a velocity such that in their moving reference frame, the photon energy equals the energy associated with the electronic transition. If the laser is tuned to the unshifted line-center of the transition, then only absorbers having a laboratory frame velocity of v = 0 will interact with this laser beam. As a result, a saturating laser beam creates a "hole" in the otherwise Maxwellian population of v = 0 absorbers, greatly depleting the electronic ground state density of these v=0 absorbers, and increasing the excited electronic state density to levels that are above their undisturbed values. This "hole" in the velocity distribution of absorbers is known as the "Bennett" hole. The saturating laser modifies the absorption coefficient of the medium by the creation of this Bennett hole. A second "probe" laser can be used to study the extent of the creation of a Bennett hole. If a second counter-propagating laser of equal wavelength is directed into the medium, then only absorbers with v = 0 can potentially interact with both laser photons. As a result, the probe beam will experience a reduced attenuation due to the Bennett hole in the v = 0 population produced by the saturating laser. On the other hand, for an absorber moving with v ≠ 0, neither the saturating or probe beam interact with the absorber, and both pass through the medium unattenuated. In practice, the absorbers in a Doppler broadened medium experience homogeneous broadening mechanisms such as natural broadening and both impact and quasi-steady collision broadening, and the spectral absorption characteristics of the probe beam will reflect these additional broadening mechanisms. The intense (now non-saturating) beam produces a Bennett hole that gives rise to a spectral absorption coefficient that has a Voigt profile. In the homogeneously-

broadened case, the counter-propagating probe beam of equal wavelength to the weak pump beam can interact with non-zero velocity absorbers, however, the wavelength dependence of the interaction will always follow the homogeneously broadened lineshape. As a result, the spectral absorption of the probe beam in the weak pump limit is expected to track the homogeneous broadened component in the spectral absorption lineshape, which for the H_a transition in atomic hydrogen at conditions near the arcjet exit plane, is primarily a result of collisional interactions with the electrons and ions, i.e., Stark broadening.

Using the calculated Stark broadening rates of Stehle and Feautrier (*J. Phys. B* **17**, 1477 (1984)) the DFAS linewidths can be reduced to electron number density. The measured electron number densities are found to be in remarkable agreement with those predicted by the model simulations. The measurements are also in agreement with the previous electron number densities measured using LIF and emission, although the DFAS based methods are more accurate. The direct consequence of this agreement is that there is further confidence in the Doppler widths that were extracted from the LIF deconvolution spectra. These Doppler widths provided the measurements of the translation temperature in the arcjet flowfield.

(v) Thermodynamic Analysis of Arcjet Flowfield

The accumulated database of flow properties associated with these low power hydrogen arcjets have permitted us to examine the thermodynamic limitations of such devices, when viewed as a simple thermodynamic system comprising of a gas undergoing an irreversible expansion. This analysis is described in detail in Ref. 11, and reproduced in this report as Appendix I. In this analysis, we have identified performance limitations based on a second-law perspective, and have used the overall balances to show that in certain limiting cases, the arcjet can be viewed as a simple Carnot engine, the efficiency of which scales as the ratio of the anode temperature to peak arc temperature.

(vi) LIF Diagnostics of Hall Thrusters

As a new development in this AFOSR sponsored research, we have diverted our attention to the study of closed-drift plasma accelerators, or so-called Hall thrusters. These devices are gaining popularity as sources that provide higher specific impulses (1500s range) at remarkably high thrust efficiencies (50%). During the past two years, we have designed, fabricated, and tested a series of Hall thrusters (see for example, Ref. 16). More recently, we have developed and applied a laser-induced fluorescence diagnostic for velocities (both neutral and ionized xenon) and temperature. These efforts are described in detail in Refs. 4,8,10, and 15. Copies of two archived publications are included here as Appendices J and K.

In our Hall thruster studies, we have measured the neutral xenon species temperature and velocity using LIF excitation of the $6s[3/2]_2^o$-$6p[3/2]_2$ electronic transition. Over the past two years, we have developed an understanding of the $6s[3/2]_2^o$-$6p[3/2]_2$ LIF transition lineshape, which is centered at approximately 823 nm, and have only recently demonstrated this to be a powerful diagnostic approach for Hall thrusters. Recently, we have extended this LIF diagnostic to measure the velocities of singly-ionized xenon by exciting the $5d^4D_{7/2}$ - $6p^4P^o_{5/2}$ transition centered at 605 nm. Measurements of both neutral xenon and ionized xenon velocities within the acceleration zone of the Hall thruster are of specific interest in the understanding of the charge-

exchange phenomenon, a performance-limiting characteristic. This past year, we have mapped out the neutral and ionized xenon axial velocity component at several axial and radial locations near the exit of our Hall thruster. To compliment these measurements, we have used electrostatic probes (emissive, floating potential) to measure the spatial distribution in the space potential.

An important finding from these studies is that both the neutral and singly-ionized xenon accelerate to their full velocities over a spatial region located *outside* of the discharge channel. It is found that the neutral xenon velocity also increases dramatically outside the thruster, between the exit plane and cathode plane. This increase is attributed to charge exchange collisions between neutral and ionized xenon. The apparent fall in neutral xenon velocities beyond the cathode plane (20 mm from exit plane) is attributed to the large amount of slow-moving neutral xenon injected into the flow from the cathode discharge.

Consistent with these findings is that the plasma potential drop ("acceleration zone") also lies outside of the thruster, as measured using hot emissive probes. At a discharge voltage of about 90 V, we find that only approximately 10% of the voltage drop lies inside of the thruster channel. In this thruster, we also find that the ionization zone (location of the peak in electron temperature) lies within the discharge channel and is therefore separated from the acceleration region, more typical of a "thruster with anode layer" - TAL type Hall discharge.

While these measurements offer a first glimpse at the structure of the plasma in the near-electrode region, future measurements will focus on extending the operating envelop of our Stanford-built thrusters to more closely resemble that of typical Stationary Plasma Thrusters (SPT).

(vii) Transient Characteristics of Hall Thrusters

In recent work, we have also studied the turbulent structure in these devices, which is believed to play an important role in the cross-field electron transport. Low-impedance, negatively biased (relative to the plasma potential) probes are used to collect the ion-saturation current, and to provide a temporal map of the local fluctuations in the plasma density. Details of these studies are presented in Refs. 17 and 18. A copy of Ref. 18 is included as Appendix L.

The measurements confirm the existence of low-frequency coherent azimuthal disturbances near the exit plane of our hall thrusters, as well as more stochastic disturbances within the acceleration channel. The properties of these waves depend on the precise location within the thruster, and on the discharge operating conditions, i.e., where in the current-voltage operating window. The average azimuthal wave speed at the exit plane is measured and compared to the E x B drift velocity, and found to be 20-40% that of the E x B drift speed, consistent with the findings of others in similar devices. In the studies reported so far, measurements of the local field fluctuations were not made to a sufficient accuracy to allow for an accurate determination of the effective Hall parameter (or Bohm diffusion coefficient). However, preliminary findings suggest that the anomalous transport associated with this low frequency azimuthal disturbance cannot for the overall conductivity of the plasma. This result warrants further studies of this anomalous transport effect in this family of co-axial plasma thrusters.

PERSONNEL SUPPORTED ON THIS GRANT (Directly, or Partially)

Professor M. A. Cappelli (P.I.)
Graduate Students P.V. Storm, W. Hargus, R. Cedolin
Undergraduate Student N. Meezan

Publications in Peer Reviewed Journals (August 1, 1995 - November 30, 1997)

1. "Fluorescence Measurements of Atomic Hydrogen Velocity in the Interior of an Arcjet Nozzle," P.V. Storm and M.A. Cappelli, AIAA Journal 34, 853, 1996.

2. "Stark Broadening Corrections to Laser Induced Fluorescence Temperature Measurements in a Hydrogen Arcjet Plume", P.V. Storm and M.A. Cappelli, Applied Optics 35, 4913-4918, 1996.

3. "Interior Plasma Diagnostics of Arcjet Thrusters," M.A. Cappelli and P.V. Storm, Journal of Propulsion and Power, **12**, 1070-1076, 1996.

4. "Laser-induced Fluorescence Measurements of Resonance Broadening in Xenon," R. J. Cedolin, R. K. Hanson, and M. A. Cappelli, Phys. Rev. A **54**, 335-342, 1996.

5. "Radiative Emission Analysis of an Expanding Hydrogen Arc Plasma I: Arc Region Diagnostics Through Axial Emission," P.V. Storm and M.A. Cappelli, *JQSRT* **56**, 901-918, 1996.

6. "Radiative Emission Analysis of an Expanding Hydrogen Arc Plasma II: Plume Region Diagnostics Through Radial Emission," P.V. Storm and M.A. Cappelli, *JQSRT* **56** 919-932, 1996.

7. "Arcjet Nozzle Flowfield Characterization by Laser-Induced Fluorescence," P.V. Storm and M.A. Cappelli, to appear in *Applied Optics*, 1997.

8. "Laser-Induced Fluorescence Study of a Xenon Hall Thruster," R.J. Cedolin, W.A Hargus, Jr., P.V. Storm, R.K. Hanson, and M.A. Cappelli, to appear in *Applied Physics B*, 1997.

9. "The Structure of an Expanding Hydrogen Arcjet Plasma," W.A. Hargus and M.A. Cappelli, to appear in *Physics of Fluids*, 1998.

Publications/Presentations at Conferences (August 1, 1995 - November 30, 1997)

10. "Laser-Induced Fluorescence Diagnostics for Xenon Hall Thrusters,R.J. Cedolin, W.A. Hargus, R. K.Hanson, and M.A. Cappelli," AIAA 96-2986, 32nd Joint Propulsion Conference, Lake Buena Vista, FL, July 1996.

11. "Thermodynamic Analysis Based on Measurements of Flowfield Properties in Low Power Hydrogen Arcjet Thrusters," M. Cappelli, D. Berns, W. Hargus, and P.V. Storm, AIAA 96-3293, 32nd Joint Propulsion Conference, Lake Buena Vista, FL, July 1996.

12. "Plasma and Cathode Emission from a High Power Hydrogen Arcjet," M. Cappelli, P.V. Storm, D. Berns, W. Hargus, R. Spores, and K. McFall, AIAA 96-2703, 32nd Joint Propulsion Conference, Lake Buena Vista, FL, July 1996.

13. "LIF Characterization of Arcjet Nozzle Flows," P.V. Storm and M.A. Cappelli, AIAA 96-2987, 32nd Joint Propulsion Conference, Lake Buena Vista, FL, July 1996.

14. "Mass Flux Measurements in the Plume of a Low Power Arcjet Nozzle, W. Hargus and M. Cappelli, AIAA 96-3190, 32nd Joint Propulsion Conference, Lake Buena Vista, FL, July 1996.

15. "Laser-Induced Fluorescence Study of a Xenon Hall Thruster," R.J. Cedolin, W.A. Hargus, Jr., R.K. Hanson, and M.A. Cappelli, AIAA-97-3053, 33rd Joint Propulsion Conference, Seattle, WA, July, 1997.

16. "A Performance Study of a Low Power Hall Thruster," W.A. Hargus, Jr., R.J. Cedolin, N.B. Meezan, and M.A. Cappelli, AIAA-97-3081, 33rd Joint Propulsion Conference, Seattle, WA, July, 1997.

17. "Transient Behavior of a Low Power Hall Thruster," W.A. Hargus, Jr., N.B. Meezan, and M.A. Cappelli, AIAA-97-3050, 33rd Joint Propulsion Conference, Seattle, WA, July, 1997.

18. "A Study of a Low Power Hall Thruster Transient Behavior," W.A. Hargus, Jr., N.B. Meezan, and M.A. Cappelli, IEPC 97-058, 25th International Electric Propulsion Conference, Cleveland, OH, August 1997.

19. "Doppler-Free Laser-Absorption Measurements of Electron Density in a 1-kW Hydrogen Arcjet," P.V. Storm, Q. Walker, and M.A. Cappelli, IEPC 97-195, 25th International Electric Propulsion Conference, Cleveland, OH, August 1997.

Archived Graduate Dissertations (August 1, 1995 - November 30, 1997)

20. "Optical Investigations of Plasma Properties in the Interior of Arcjet Thrusters", Ph.D. Dissertation, Mechanical Engineering Department, Stanford University, March, 1997.

21. "Laser-Induced Fluorescence Diagnostics of Xenon Plasmas", Ph.D. Dissertation, Mechanical Engineering Department, Stanford University, June, 1997.

Plasma and Cathode Emission from a High Power Hydrogen Arcjet

D.H. Berns[t], P.V. Storm[t], W.A. Hargus, Jr.[t], M.A. Cappelli[∞]
Department of Mechanical Engineering
Stanford University
Stanford, California

K.A. McFall[**], R.A. Spores[**]
Propulsion Directorate
OL-AC Phillips Laboratory
Edwards Air Force Base, California

Abstract

An experimental study of the measurement of cathode temperature, current distribution, and near-cathode electron number density in a high power hydrogen arcjet is presented. This study is motivated by the desire to better understand arc-electrode interactions in arcjet thrusters, which in many cases, is the main determinate of arcjet lifetime. Measurements such as these may also provide the needed boundary conditions for numerical arcjet simulations, presently under development. We describe in this paper the application of a non-intrusive in-situ measurement technique for on-axis, spectral imaging of the electrode region of arcjets, and the application of this technique to the measurement of the cathode and anode temperatures, cathode spot size, and current distribution in a 30kW hydrogen arcjet thruster. A relatively large field of view (twice the throat diameter) and high spatial resolution (9 μm) are achieved. We find that the maximum cathode temperatures are at or near the melting point of tungsten. We also find that field-enhancement of the thermionic emission process is necessary in order to account for the overall current balance at the cathode. The electric fields extracted are reasonable, given the relatively low plasma conductivity that is estimated on the basis of an LTE and space-charge limited current flow. The current density profiles are sensitive to mass flow rate and arcjet power. In addition to the cathode imaging studies, we have employed axial plasma emission spectroscopy to measure the near-cathode electron number density. The properties estimated from these measurements are used as limits in a model for the cathode current contraction zone.

I. Introduction

The performance of arc discharges as arcjet thrusters for satellite propulsion depends on several key factors, of which electrode erosion and arc-electrode interaction are important. The present use of arcjets for satellite propulsion has expanded the operating realm of these devices and has increased the desire for further understanding of the electrode erosion processes and plasma-electrode interaction. In arcjet thrusters, the measurement of electrode temperatures and the study of arc attachment is often difficult due to the fact that these electrode surfaces are seemingly inaccessible, and that the plasma arc itself is a likely source of optical interference.

Previous studies of arc attachment in prototype arcjets designed for space propulsion have focused primarily on the anode region [1-4]. In these studies, it was learned that the arc anode-attachment can either be diffuse (when the attachment is downstream of the nozzle throat in a low pressure region), or constricted (when the attachment is upstream of the nozzle throat in the high pressure region). Imaging of an exposed cathode in a flowing low pressure plasma has been reported [5]. Although these measurements were not performed on an arcjet, they provided valuable information on arcjet erosion mechanisms, when combined with a model of the near-cathode plasma and conduction within the electrode.

Recently Hoskins et al. applied an optical imaging strategy to measure the anode temperature distribution in regeneratively-cooled arcjets [6]. Although quantitative temperature data is difficult to extract because of the re-radiation of cathode and plasma emission from the observed

---

[t] Research Assistant, Member AIAA
[∞] Associate Professor, Member AIAA
[**] Member AIAA

anode surfaces, the results were qualitatively useful in understanding the performance improvements that can be gained by regenerative-cooling. We have previously reported measurements of cathode temperature and current density distribution in low power hydrogen arcjet thrusters [7]. We showed that field-enhanced thermionic emission was necessary to account for the discharge currents used. Field strengths in excess of 10^8 V/m were inferred from these past measurements. Cathode properties have been measured in high current discharges [8], however, as far as we know, no previous direct measurements of cathode properties in high power arcjets have been reported.

Axial and radial spectroscopic plasma emission measurements have been presented previously for both low and medium power arcjets [9-12]. It was shown that the Stark broadened emission in the distant spectral linewings of the H_α transition originates from the hottest, near-cathode regions of these arcjets. From these measurements various parameters were calculated including cathode temperature and electron number densities within the arcjet.

In this paper, we present the results of spectroscopic emission studies implemented to image cathode temperatures and to measure the near-cathode plasma densities. The purpose of the work presented herein was to better understand the near-electrode regions of arcjets, and the differences that may exist between the arc-physics in low and high power arcjets. In addition, these measurements can provide the cathode current density and cathode temperature boundary conditions often imposed in detailed arcjet models. The imaging strategy described here is flexible and can be used with any size of arcjet or arcjet-type of device. This method allows the measurement of the anode throat temperature which has not been done with axial emission measurements. The anode throat size can also be inferred from the images. This allows a monitoring technique for throat closure, which can be an operating limitation in the smaller geometry, higher specific power arcjets of the present.

II. Experimental Setup

Arcjet and Vacuum Facility

An overview of the experimental setups for the axial cathode imaging and the axial plasma emission studies are shown in Fig. 1 and a

schematic of the high power arcjet thruster investigated is shown in Fig. 2. The arcjet was operated in a 2.5 m diameter steel vacuum chamber maintained at a typical background pressure of 80 mtorr during thruster operation by mechanical roughing pumps backing 11,000 l/s blowers. The arcjet was designed and built at Phillips lab and was previously tested using ammonia as a propellant [13]. The arcjet nozzle had a designed throat diameter of 2.54 mm with an 19 degree half angle divergence section leading to an exit diameter of 25.4 mm (100 area ratio). The arcjet cathode was machined from a 3/8" diameter thoriated tungsten rod with a conical tip at a 30 degree half angle. The cathode was set back approximately 4.5 mm from contact with the anode/nozzle constrictor.

Cathode and Anode Imaging

In order to directly study the cathode and anode throat region of the arcjet, a high-resolution (12 μm per pixel - 384 x 578 pixel area) CCD camera coupled to a long distance microscope was used to view the internal surfaces of the arcjet during operation (see Fig. 1a). Optical access to the arcjet was acquired through a 1.5" diameter window downstream of the exit plane in the vacuum facility side flange. The end-on view of the arcjet provided optical access to the cathode tip and a portion of the diverging side of the anode/nozzle. The CCD camera and the long distance microscope were the major components of this cathode/anode imaging system. The long distance microscope is a Questar Corporation, Model DR1 magnifying device. The device has a focal range of 36" to 96" with magnification of 17x (at 36") and 7x (at 96"). The advantage of this device for this application was its large field width, 10mm (at 36") and 23mm (at 96"). With other lenses and attachments the magnification could be increased. The CCD camera used is a Model # TE/CCD-576/UV, temperature controlled device manufactured by Princeton Instruments Inc. The camera has 14 bit A/D conversion, exposure times of 5ms-23 hours, a readout rate with 100kHz capability, and a shutter time of 5-6ms. Based on our previous studies of cathode emission in low power arcjets [7], we found that for wavelengths greater than 700 nm, the intensity of axial emission is dominated by thermal emission from the cathode, and there is little or no interference from the luminous plasma. Therefore, a 700nm, 10 nm bandwidth, and an 810nm, 10 nm bandwidth interference filter were chosen such that the cathode emission could be

2

isolated from the hydrogen lines and the continuum emission due to free electrons in the plasma.

Light emitted from the arcjet was collected by the long distance microscope through a series of redirecting mirrors. The long distance microscope was adjusted such that the focal plane was at the cathode surface of the arcjet. The light exiting the long distance microscope was then focused onto the photo-sensitive array in the CCD camera. For a given arcjet operating level, the appropriate exposure time (controlled by the camera shutter speed) was chosen such that the array was not saturated but a significant signal was obtained. The image was converted to a set of digital signals (one value for each pixel of the array) within the detector/controller and the signals were then stored on a P.C. for post-processing. Images were acquired for several specific power levels (input power/propellant flow rate). Intensity calibration was performed with a tungsten filament lamp, placed at the position of the arcjet, the temperature of which was determined by a single color Minolta Cyclops 152 optical pyrometer, accounting for the temperature-dependent spectral emissivity [14].

Separate images were taken of the cathode region with both filters for several different arcjet operating conditions. This data was used to calculate all of the cathode properties presented in this paper. At each operating level, the cathode shutter speed was adjusted so that the radiation emitting from the cathode tip could be captured without saturating the CCD array. The images capture the cathode tip, the anode throat, and between radii of 0.3 mm to 2.3 mm of the diverging section of the anode, depending on the orientation of the camera.

Axial Plasma Emission Studies

The axial plasma emission was measured and analyzed in a manner similar to previous studies performed on 1-kW and 5-kW arcjets [9,10]. The experimental setup is shown in Fig. 1b. A 400 mm focal length achromat lens was used to collect light axially from the arcjet throat and bring it to a focus on a 50 μm diameter spatial filter. The image at the spatial filter was then focused, using an 100 mm focal length achromat lens, onto the entrance slit of an Acton Research Corp. (model SpectraPro 500) 0.5 m monochromator containing a 2400 gr/mm grating. The entrance and exit slits of the monochromator were each set to 5 μm, yielding a

spectral resolution of 0.004 nm. A Hamamatsu R928 photomultiplier tube was used as the photodetector. Phase-sensitive detection was performed for background noise rejection using a Stanford Research Systems SR850 digital lock-in amplifier. The reference signal was provided by a mechanical beam chopper placed near the intermediate focus at the spatial filter and set at a chopping rate of 1 kHz. The digitized output of the lock-in amplifier was transferred to a personal computer for spectral analysis. To minimize the light collection volume from the arcjet plume and hence reduce the possibility of collecting molecular hydrogen emission, an aperture stop of 11 mm diameter was placed in front of the collection lens, providing a collection optics f/# of approximately 150. The image magnification at the spatial filter was approximately 0.3 which provided a resulting spatial resolution at the arcjet constrictor of approximately 160 μm. As with the cathode imaging experiments, intensity calibration was performed using an 18 A tungsten filament lamp placed at the location of the arcjet, and the temperature of the lamp was determined by optical pyrometry.

Axial emission scans of the hydrogen Balmer-alpha (Hα) line were taken at four different operating conditions and several radial positions across the constrictor diameter. Three of the operating conditions were at a mass flow rate of 123.5 mg/s, the same flow rate used in part of the cathode imaging study, while the fourth condition was at a lower flow rate (82.0 mg/s). The scans were performed in a period of 2 minutes and data was sampled at 8 Hz, resulting in 960 data points per scan. The recorded lineshapes were analyzed to determine electron number density in the arc region near the cathode as explained in the results section below. In addition to the Hα scans, the axial emission over the complete visible spectrum (400-700 nm) was collected, in 5 minute scans, on the arcjet centerline at three different operating conditions in an attempt to determine the cathode temperature from the spectral distribution of the cathode emission.

III. Results

Spectral axial plasma emission scans of the arcjet are shown in Fig. 3 for the wavelength range between 400 nm and 700 nm. Previous axial plasma emission measurements performed on a medium-power hydrogen arcjet [10] revealed that the hydrogen Balmer-series line emission dominates

most of the visible spectrum. However, unlike these prior studies, we find here that the continuum emission between the Hα and Hβ spectral lines was greater than that which can be accounted for by cathode emission and free-free or free-bound transitions alone, and speculate that the source of this emission may be electronically excited molecular hydrogen. It is evident from Fig. 3 that in the spectral region beyond the Hα line, the continuum emission intensity falls dramatically. Beyond approximately 700nm, the cathode thermal emission is assumed to dominate in the emission. As a result, we selected 700 nm and 810 nm as candidate wavelengths for electrode imaging. Although longer wavelengths may further reduce the contributions from interfering emission, wavelengths beyond 810 nm were not selected due to the loss of sensitivity in the CCD camera. Also, at 3900 K the peak of the back-body emission is located at 743 nm, therefore, going farther into the infrared would reduce the signal from the cathode emission.

In addition to direct observation of the cathode, the field of view of the long distance microscope also provided for imaging of a large fraction of the anode in the region of the nozzle throat. Thermal emission from the anode surface very near the throat is expected to be only weakly affected by re-radiation of plasma and cathode emission from other regions of the anode.

The cathode images were obtained during arc operation by acquiring the continuous radiation emitted from the high temperature cathode tip and the throat region of the anode. From these images, the cathode radial temperature distribution could be measured. The cathode temperature was calculated from comparison of the cathode tip local radiation, again for various arcjet operation levels, with calibrated data obtained from a tungsten arc lamp. Given the temperature distribution, other properties were determined such as the current density distribution along the cathode, the cathode spot size, and the electric field in front of the cathode. The cathode spot diameters were inferred from the current density profiles. Due to the Gaussian shape of the current density profile, measurement of the halfwidth of the profile (position of greatest slope) provides a good estimate for the cathode spot diameter. The spot diameters calculated with this method range from 0.5 to 0.75 mm.

From the calibration procedure, the CCD signal was converted to graybody intensity (W/m^3/Sr):

$$I_\lambda(\lambda,T) = \varepsilon_\lambda I_{\lambda,b}(\lambda,T) = \frac{2hc_o{}^2\varepsilon_\lambda}{\lambda^5\left[exp\left(\dfrac{hc_o}{\lambda kT}-1\right)\right]} \quad (1)$$

Here, $I_{\lambda,b}$ is the Planck distribution, relating the wavelength (λ) dependent intensity of an ideal blackbody to the object temperature, T. The constants h, k, and c_o refer to Planck's constant, Boltzmann's constant, and the speed of light in vacuum, respectively. We believe the largest source of error to be in the selection of the spectral emissivity, ε_λ, at the wavelength of interest. The spectral emissivity of tungsten at or above the melting point has not been previously measured. For the calculations described here, we have used a value of 0.4 [14].

Fig. 4 is a typical intensity image acquired by viewing the arcjet electrode region during operation. The left and right figures are the same image but with different intensity threshold settings to illustrate all of the features of the electrode region. The figures show the entire throat of the arcjet, the portion of the cathode visible through the throat, and a portion of the diverging section of the anode. The left figure shows the varying levels of intensity across the cathode, with a label tagged to the center of the cathode. The right figure identifies the throat region. The two sides of the throat along the cross-section are labeled "A" and "B" for reference. It is clear from these images that the cathode was misaligned in this arcjet. This misalignment causes asymmetric temperature and current density profiles. The bright spots on the diverging section of the anode are believed to be previously melted droplets of tungsten (the origin of which is unclear) that have resolidified. The most remarkable finding from this study is that the identification of the cathode and throat are quite clear, along with features such as these droplets, despite the fact that we are observing these internal surfaces through an intense arc that is probably heated to temperatures above 15,000K. The cathode temperature profile is taken along a vertical cross-section through the image, denoted by the dashed line. All of the profiles presented in this paper are taken from this same orientation. The top of the figure is referenced as the negative position side in the temperature and current density profiles.

Fig. 5 shows the measured temperature profiles obtained from images of the electrode region of the arcjet for three different operating conditions. The profiles are cross-sections through the nozzle. The centerline (r=0) is a local center, determined by choosing the location of the peak temperature, and does not necessarily correspond to the exact geometric center of the cathode tip or the constrictor. This choice of r=0 is the method used for all figures. The uncertainties in temperature have been estimated to be approximately ± 220 K near the cathode (from centerline out to a radius of about 0.3 mm) and ± 180 K in the anode regions (beyond radius of 0.3 mm). These uncertainties are based on an expected error in the calibration constant of 10%, an error in emissivity of ±0.05, and an error in the signal due to dark noise in the camera.

For operation on hydrogen at a current of 154 A and a flow rate of 123.5 mg/s the cathode peak temperature is 3911 K, the anode temperature ranges from 2700 K on one side of the throat to about 2450 K 3.2 mm away from the throat (axial distance). It can be seen that there is no discernible temperature step at the cathode throat. This implies that the cathode and anode temperatures at this radial point are nearly the same. The temperature decreases as you go out from the throat for a short distance, then increases several hundred degrees, and finally decreases again. The increase coincides with the hot spot on the images, which as previously discussed, appears to be a resolidified droplet of tungsten. The temperature of this droplet appears to be higher than its surroundings. These anode temperature values are probable upper limits to the temperatures since reflections from the interior surface of the nozzle are not taken into account in the calculation of relative intensity at a given radial location. This correction requires knowledge of the angular and temperature dependence of the spectral emissivity.

For the same flowrate, 123.5 mg/s, increasing the current to 210 A causes the temperature profile to widen and increases the temperature values along both the cathode and the anode. The cathode peak temperature is nearly the same at 3965 K. As will be shown by the current density profiles, increasing the current at the same flowrate causes the cathode spot to widen (from 0.64 mm to 0.73 mm) and therefore broadens the temperature profiles. All of the temperature values increase due to the increased energy density at the cathode surface caused by the increased current.

For nearly the same current, 146 A, increasing the mass flow rate causes the temperature profile to narrow and decreases the temperature values along both the cathode and the anode. The cathode peak temperature is again nearly the same at 3954 K. As will be shown by the current density profiles, increasing the flowrate for a fixed current causes the cathode spot to narrow (from 0.64 mm to 0.58 mm) and thereby narrows the temperature profile. All of the temperature values decrease because the energy density in the flow, or the specific power, decreases. An interesting but perhaps not significant finding is that at nearly comparable currents (154A and 146A), increasing the mass flow rate from 123.5 mg/s to 179 mg/s increased the center cathode temperature slightly (while decreasing the spot size). Increasing the mass flow rate appears to constrict the arc, requiring a higher centerline arc temperature to provide the higher electron emission necessary to conduct the same amount of total current through less of an area.

Fig. 6 shows the calculated current density profiles for the temperature profiles shown in Fig. 5. In Fig. 7, we display three current density profiles for the same arcjet operating conditions: (i) the current density for a purely thermionic emitting cathode and a work function equal to that of pure tungsten; (ii) the current density for a field-enhanced (Schottky-enhanced) thermionic cathode using the work function of pure tungsten and a finite (and relatively high value) for the electric field at the surface, and (iii) a curve illustrating that the profile generated in the field-enhanced case could also be obtained using pure thermionic emission if the work function were lowered.

The results of previous studies [15] have suggested that the cathodes in these types of devices emit electrons based on the principle of field-enhanced thermionic emission, where the electric field at the cathode surface acts to reduce the potential barrier at the surface for electron emission. The field-enhanced thermionic emission current density is derived from the equation [16,17]:

$$J_{th} = AT_c^2 \exp\left[\frac{-e}{kT_c}\left(\phi_w - \left(\frac{eE_s}{4\pi\varepsilon_0}\right)^{1/2}\right)\right] \qquad (2)$$

where T_c is the local cathode temperature, ϕ_w is the work function of the cathode (4.5 V for pure tungsten [18]), E_s is the electric field strength at the surface of the cathode, and A is a constant

equal to 1.202×10^6 A/m^2/K^2. Purely thermionic emission is governed by the same equation with $E_S=0$. Previous experiments showed that the thorium in the cathode migrates out of the cathode tip and after short operation times the cathode tip is left with virtually no detectable thorium [15]. This cathode had been run extensively, therefore, it was expected that the cathode tip was pure tungsten.

Based on the measured temperature distributions it is possible to calculate the current density at each radial location where there is a temperature value. The integral of current density times the differential area gives the total enclosed current. In this calculation, the electric field is changed iteratively until the total enclosed current matches the measured current of the arcjet.

For the arcjet operating conditions of 123.5 mg/s and 154 A, it was necessary to use an electric field of 5.45×10^8 V/m in order to reproduce the total enclosed current (see Fig. 7). In the absence of field-enhanced emission, a pure tungsten cathode with the measured temperature distribution would emit a total current of 8.85 A, far below the actual measured current. Note that the measured total current density of 154 A could be obtained with pure thermionic emission if the work function were lowered to 3.61 V.

A comparison of the current density profiles in Fig. 6 illustrates the dependence of cathode arc attachment on current and flowrate. For arcjet operating conditions of 123.5 mg/s of hydrogen and 154 A, the peak current density is 4×10^8 A/m^2. The uncertainty in current density at the centerline is estimated to be approximately 1×10^8 A/m^2. This uncertainty is based on an expected error in the work function of $\pm$ 0.1 V and the expected error in temperature of $\pm$ 220 K. For the same flow rate, increasing the current to 210 A, causes the current density profile to widen and the values at all radial positions to increase, with a peak of 5.1×10^8 A/m^2. The calculated electric field of 5.77×10^8 V/m is nearly the same as for the 154 A case. As discussed within the context of the measured temperature, the cathode spot diameter increases. It is expected that this coincides with a broadening of the arc column diameter with increased current.

For nearly the same current (146A), increasing the mass flow rate causes the current density profile to become more narrow, while increasing the peak value to 5×10^8 A/m^2. This is consistent with the interpretation of the temperature profiles, i.e., for a narrower profile the peak must increase in order to have the same total current

(area under the profile). The narrower profile corresponds to a smaller diameter cathode spot. This is attributed to a narrower arc column. For the same current, when the flowrate is increased there is an increase in the convective heat transfer from the arc causing the arc to constrict to smaller diameters and causing a corresponding increase in the arc temperature, a necessary response so that there is an increase in the electrical conductivity.

Previous studies of the axial emission from 1-kW and 5-kW arcjets have demonstrated that the arc electron number densities in the near-cathode region can be determined from an analysis of the atomic hydrogen Hα line [9,10]. This is accomplished by fitting a Lorentzian line to the linewings only, since the line center is strongly affected by radiative transfer in the nozzle expansion region and in the plasma plume [9]. The FWHM of the best fit Lorentzian is a direct measure of the electron number density in the arc by the Stark broadening mechanism. The conditions within the arc, as determined by models of low power arcjets [19], indicate that Stark broadening is the only significant broadening mechanism in the arc region.

Typical scans of the Hα line as a function of radial position at one operating condition (123.5 mg/s and 20 kW) are given in Fig. 8. The dip near the linecenter is due to reabsorption by the cooler, less dense plasma in the nozzle expansion region and in the plasma plume. This dip was predicted by a radiation model for a 1-kW arcjet and was previously seen in the axial emission of 1-kW and 5-kW arcjets [9,10]. The far wings of the lineshape are determined by charged-particle collisional broadening of the line emission in the hot arc region near the cathode. By fitting a Lorentzian lineshape to the far wings of the line, the electron number density was determined from the linewidth, using dynamic-ion Monte-Carlo simulations of the Stark broadening of Hα [20]. The calculated electron number densities are shown as a function of arcjet power and radial position in Figs. 9 and 10. These results indicate that the arc electron number density increases slightly with arcjet power at a constant propellant flow rate. This result was previously observed in a 5-kW arcjet [10] and is consistent with the increase in the arc current with increasing arcjet power. The higher current must be supported by greater current densities in the arc, which requires a greater plasma conductivity, hence, a greater electron number density.

The large uncertainties displayed in Fig. 9 are primarily a result of the sensitivity of the best fit Lorentzian linewidth to the amount of the linewings used in the fitting procedure. This uncertainty constitutes the limiting factor in accurately determining the arc electron number density from the linewings. On the one hand, to ensure that the fit is performed only to the part of the line originating near the cathode, it would be desirable to fit only the very far wings. This will reduce the systematic error associated with the radiation transfer near line center. On the other hand, since the noise is larger in the wings of the line, performing a line fit to only the far wings results in a very large statistical error in the determination of the linewidth. As a consequence the measured near-cathode electron number density has considerable uncertainty. The error bars were intentionally omitted from Fig. 10 to avoid cluttering the figure; however, the uncertainties were similar to those given in Fig. 9.

The complete visible spectrum of the axial emission is shown in Fig. 3 for three operating conditions. The region of the spectrum away from the Balmer series lines constitutes background graybody emission from the cathode surface and plasma emission from sources other than atomic hydrogen, which includes continuum radiation from the electrons and molecular hydrogen emission. An attempt was made to determined the peak cathode temperature from the region of the spectrum between the H_α and H_β lines; however the measured intensities were much greater than that which would be produced by thermal emission from the cathode at a reasonable temperature. This indicates that the background emission in this region of the spectrum is dominated by either continuum electron emission (bremsstrahlung radiation) or molecular hydrogen emission.

IV. Discussion

The measured peak cathode temperatures range from 3900-4000K (±220K). These temperatures are above the melting point of tungsten, suggesting that there may be a highly non-equilibrium process associated with evaporation of tungsten from the surface. The electric fields calculated for the operating conditions in the above cases are on the order of 5.0×10^8 V/m ($\pm 1.0 \times 10^8$ V/m). These electric fields are on the same order of magnitude as values previously reported [7,10,15,21]. It should be noted

that fields in excess of approximately 10^7 V/m start to distort the potential barrier for electron emission at the electrode to the extent that electron tunneling through the barrier becomes significant [22]. This tunneling phenomenon, commonly referred to as field emission, becomes important when the thickness of the barrier approaches the wavelength of the free electrons in the tungsten electrode. In essence, the mechanism for current transfer from cathodes in these arcjets may be more complicated then previously thought [15,21], and a mechanism based simply on field-enhanced thermionic emission may be a simplification of the actual case.

In order to understand the physical significance of such high field strengths inferred from the analysis, we have undertaken a simple analysis based on the assumption of space-charge limited electron current flow. Very near the cathode, we would expect that the plasma conducts the thermionically emitted electron current according to the space-charge limited value:

$$J_e \approx \sigma_{es} E_s \qquad (3)$$

where σ_{es} represents the electrical conductivity of the plasma adjacent to the cathode surface. If we assume a value of $\sigma_{es} = 0.01$ mho/m, which is very near that of an atmospheric pressure plasma in local thermodynamic equilibrium at a temperature of 4000 K [23] (typical of the peak temperatures measured), then the required field needed to conduct an emitted electron current of 150 A near the central cathode region is greater than 5×10^{10} V/m. The measured fields of 10^8 V/m suggest that the plasma conductivity is approximately 100 times that of the equilibrium conductivity. Therefore, the plasma in front of the cathode is expected to be overdense with electrons and ions as compared to Saha equilibrium.

The measured electron density distributions in Fig. 10. indicate that the arc column in the vicinity of the most luminous (highest temperature) region is nearly the diameter of the throat, i.e. 2.5 mm, as inferred from the FWHM of the electron number density profiles. This suggests that the arc contracts at the cathode surface since the diameter of the arc root attachment at the cathode surface, as previously discussed, is approximately 1 mm. This contraction is necessary since the plasma conductivity near the cathode is expected to drop dramatically (the cathode is maintained at a temperature that is considerably lower than the arc). The contraction of an arc at a cathode surface has been modeled previously by Felderman and

McDermott [24] within the framework of a quasi-one-dimensional model for heat conduction from the arc plasma to the cathode. In that study, they introduce the so-called concentration layer thickness, L_c, which defines the distance near the cathode over which the arc contracts. If we assume that the thermal conductivity of the plasma is unchanging over this distance, then an expression for the concentration layer thickness is given in Ref. 24 as:

$$L_c = \frac{\xi}{J_c} \left\{ \frac{(T_{arc} - T_c)\sigma_{arc}k_{arc}}{\ln\xi - 1} \right\}^{1/2} \qquad (4)$$

where ξ is the current contraction parameter [24]:

$$\xi = \frac{J_c}{J_{arc}} \left\{ \frac{\sigma_{arc}}{\sigma_c} \right\}^{1/2} - 1 \qquad (5)$$

Here, J_c and J_{arc} are the average current densities at the cathode surface and in the distant arc respectively; σ_c and σ_{arc} are the plasma electrical conductivities at the cathode surface and in the distant arc, k_{arc} is the thermal conductivity of the arc, and T_{arc} is the average arc temperature. Using a value of $T_{arc} \approx 12,000K$ (which is consistent with what is calculated using the measured electron number densities and a pressure which is close to the pressure upstream of the cathode, assuming full ionization), $J_c = 3.0\times10^8$ A/m^2 (approximately the average of the measured current density in Fig. 6), $J_{arc} = 4.8\times10^7$ A/m^2 (calculated from the typical operating current of 150 A and the arc diameter estimated from Fig. 10 of 2 mm), $\sigma_{arc} = 4 \times 10^3$ mho/m at the arc temperature [23], $\sigma_c = 2$ mho/m (from the measured current density and electric field at the cathode), and an arc conductivity k_{arc} =5.5 W/m/K [23], we arrive at: ξ=280 and L_c=5.7 mm.

It appears therefore that within the framework of the quasi-1D model, the arc in the constrictor contracts to the diameter of the cathode spot over a distance greater than the sum of the setback distance of the cathode from the constrictor and the constrictor length. The result of this simple analysis and the expectation of a strong radial conduction loss near or within the constrictor indicates that in an arcjet thruster the arc attachment and contraction at the cathode is a strongly two-dimensional phenomenon, and any analysis of the cathode region must be based on a two-dimensional analysis of heat conduction.

V. Summary

We have presented an experimental study of the measurement of cathode temperature, current distribution, and near-cathode electron number density in a high power hydrogen arcjet. The cathode temperature and current distribution measurements are based on a non-intrusive, in-situ technique for on-axis spectral imaging of the electrode region. A relatively large field of view (twice the throat diameter) and high spatial resolution (9 μm) are achieved. We find that the maximum cathode temperatures are in the range of 3800-4000K. We also find that field-enhancement of the thermionic emission process is necessary in order to account for the overall current balance at the cathode. The electric fields extracted are typically 5x10^8 V/m, a reasonable magnitude given the relatively low plasma conductivity that is estimated on the basis of LTE and space-charge limited current flow. The maximum current densities are typically 4x10^8 A/m^2 to 5x10^8 A/m^2 and the profiles are found to be sensitive to mass flow rate and arcjet power. As expected, the current density profiles constrict in size when the mass flow rate is increased for a constant current and expand in size as the current is increased for a constant mass flowrate. In addition to the cathode imaging studies we have employed axial plasma emission spectroscopy to measure the near-cathode electron number density and its variation with radial position. The properties estimated from these measurements are used as limits in a quasi 1-D model for the cathode current contraction zone. It is deduced that the contraction of the arc at the cathode is a strongly two-dimensional phenomenon and models describing cathode attachment in arcjets must account for two-dimensional effects.

Acknowledgments

References

1.   Curran, F.M., et al., "Performance Characterization of a Segmented Anode Arcjet Thruster," AIAA 90-2582, (also NASA TM 103227), July 1990.

2.   Curran, F.M. and Manzella, D.H., "The effect of Electrode Configuration on Arcjet Performance," NASA TM 102346, 1989.

3.   Sankovic, J.M. and Berns, D.H., "Performance of a Low-Power Subsonic-Arc-Attachment Arcjet Thruster," AIAA 93-1898, June 1993.

4.   Berns, D.H. and Sankovic, J.M., "Investigation of a Subsonic-Arc-Attachment Thruster Using Segmented Anodes," AIAA 93-1899, June 1993.

5.   Zhou, X., Berns, D.H., and Heberlein, J., "Investigation of Arc-Cathode Interaction," AIAA 94-3129, June 1994.

6.   Hoskins, W.A., Butler, G.W., and Kull, A.E., "A Comparison of Regenerative and Conventional Arcjet Performance," AIAA 94-3124, June 1994.

7.   Berns, D.H., Storm, P.V., and Cappelli, M.A., "Spectral Imaging of the Arcjet Electrode Region," AIAA 95-1957, June 1995.

8.   Goodfellow, K.D. and Polk, J.E., "Experimental Verfication of a High-Current Cathode Thermal Model," AIAA 95-3062, July 1995.

9.   Storm, P.V. and Cappelli, M.A., "Axial Emission Diagnostics of a Low Power Hydrogen Arcjet Thruster," IEPC-93-219, September 1993.

10.   Storm, P.V. and Cappelli, M.A., "Axial Emission Measurements on a Medium-Power Hydrogen Arcjet Thruster," AIAA 94-2743, June 1994.

11.   Cappelli, M.A and Storm, P.V.., "Interior Plasma Diagnostics of Arcjet Thrusters," AIAA-94-2654, June 1994.

12.   Ishii, M. and Kuriki, K., "Optical and Analytical Studies of Arc Column in DC Arcjet," AIAA-87-1086, May 1987.

13.   Hargus, W.A., Micci, M., and Spores, R., "Interior Spectroscopic Investigation of the Propellant Energy Modes in an Arcjet Nozzle," AIAA-94-3302, 30th Joint Propulsion Conference, June, 1994.

14.   Larrabee, R.D., J. Optical Society of America, **49,** 619, 1959.

15.   Curran, F.M. and Haag, T.W., "Arcjet Cathode Phenomena," JANNAF Propulsion Meeting, 1989, (also NASA TM 102009).

16.   Koester, J.K., "Analytical and Experimental Studies of Thermionically Emitting Electrodes in Contact with Dense Seeded Plasmas", Ph.D. Thesis, C.I.T., 1970.

17.   Cobine, J.D., Gaseous Conductors, Dover Publications, New York, 1958.

18.   CRC Handbook of Chemistry and Physics, 73rd Ed., CRC Press Inc., Boca Raton, FL, 1992.

19.   Butler, G.W., Kull, A.E., and King, D.Q., " Numerical Simulations of Hydrogen Arcjet Performance," IEPC-93-249, September 1993.

20.   Kelleher, D.E., Wiese, W.L., Helbig, V., Greene, R.L, and Oza, D.H., "Advances in Plasma Broadening of Atomic Hydrogen," *Phys. Scripta,* **T47,** pp. 75-79, 1993.

21.   Bade, W.L. and Yos, J.M., "Theoretical and Experimental Investigation of Arc Plasma Generation Technology," AVCO Corp., 1962.

22.   Bardeen, J., "Flow of Electrons and Holes in Semiconductors," Handbook of Physics, sect. 8, ch.6, pg. 79, McGraw Hill, 1967.

23.   Boulos, M.I., Fauchais, P., and Pfender, E., Thermal Plasmas, Volume 1, Plenum Press, New York, 1994.

24.   Felderman, E.J. and MacDermott, W.N., "Near-electrode Model with Nonequilibrium Ionization (at 100atm)," AIAA-95-1993, 1995.
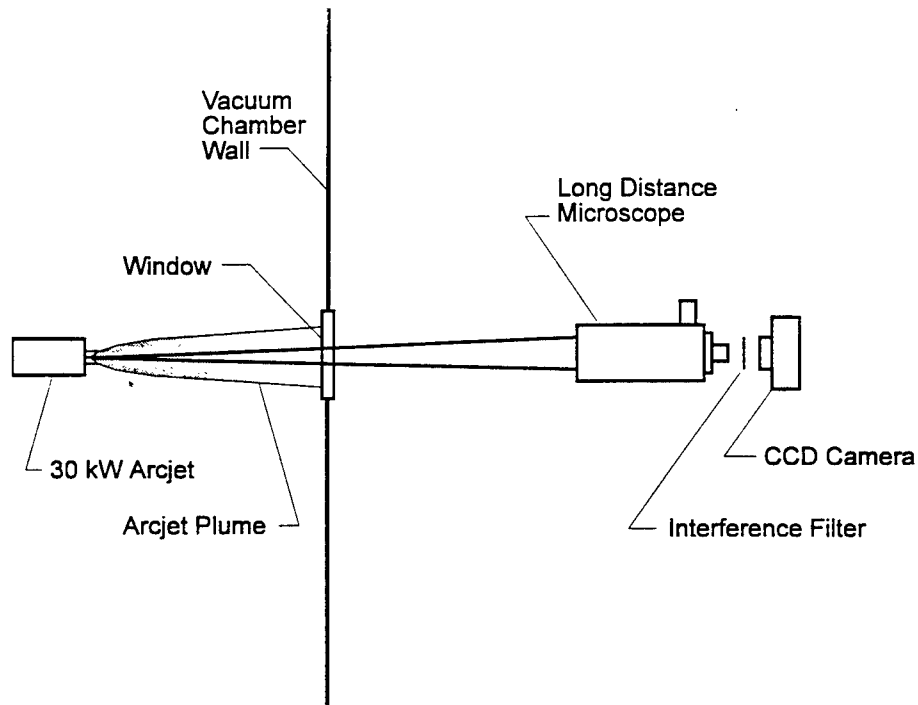
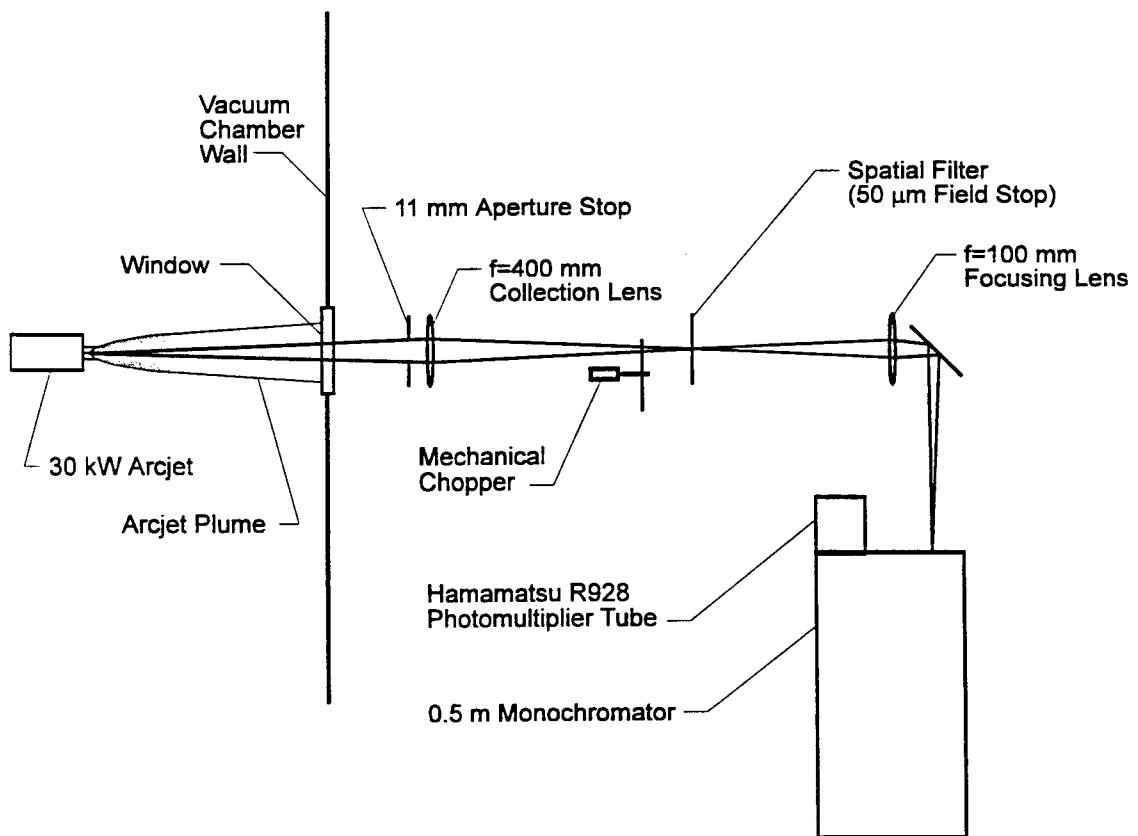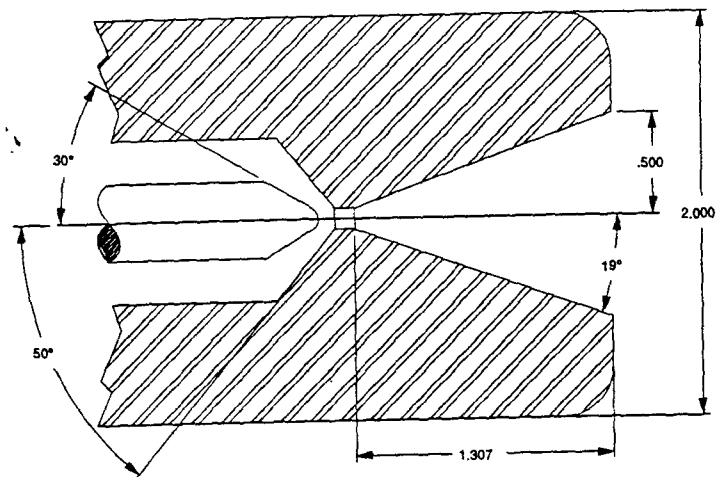Figure 1a. Experimental setup for the cathode imaging study.

Figure 1b. Experimental setup for the axial emission study.

all dimensions in inches
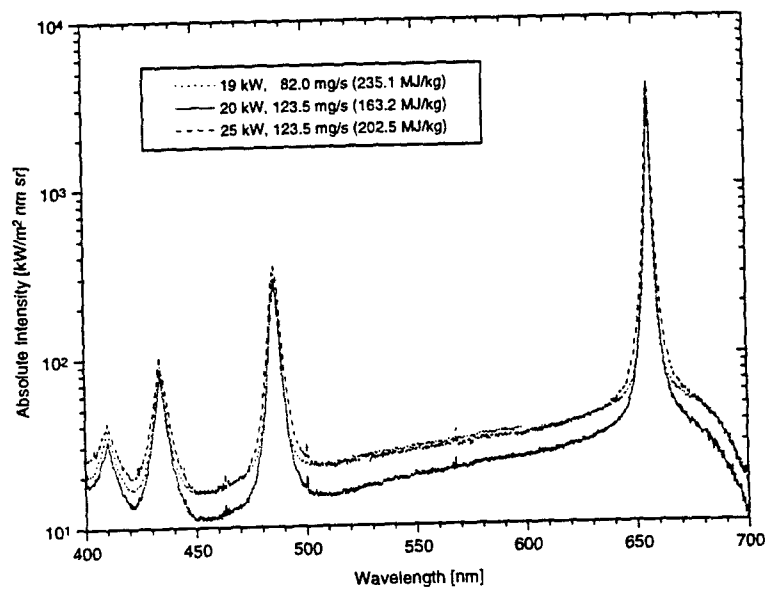
Figure 2. High Power Arcjet Electrode Region

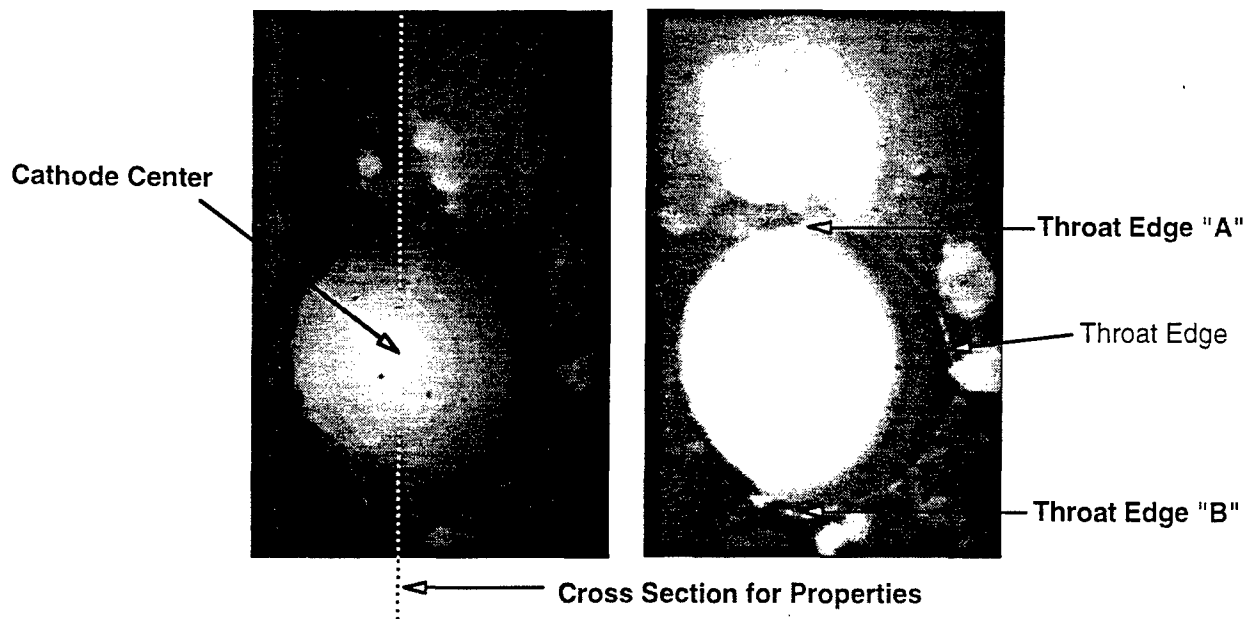Figure 3. Calibrated axial emission intensity over the complete visible spectrum.

Figure 4. Typical electrode image taken during arcjet operation. Left and right are the same image with different intensity threshold
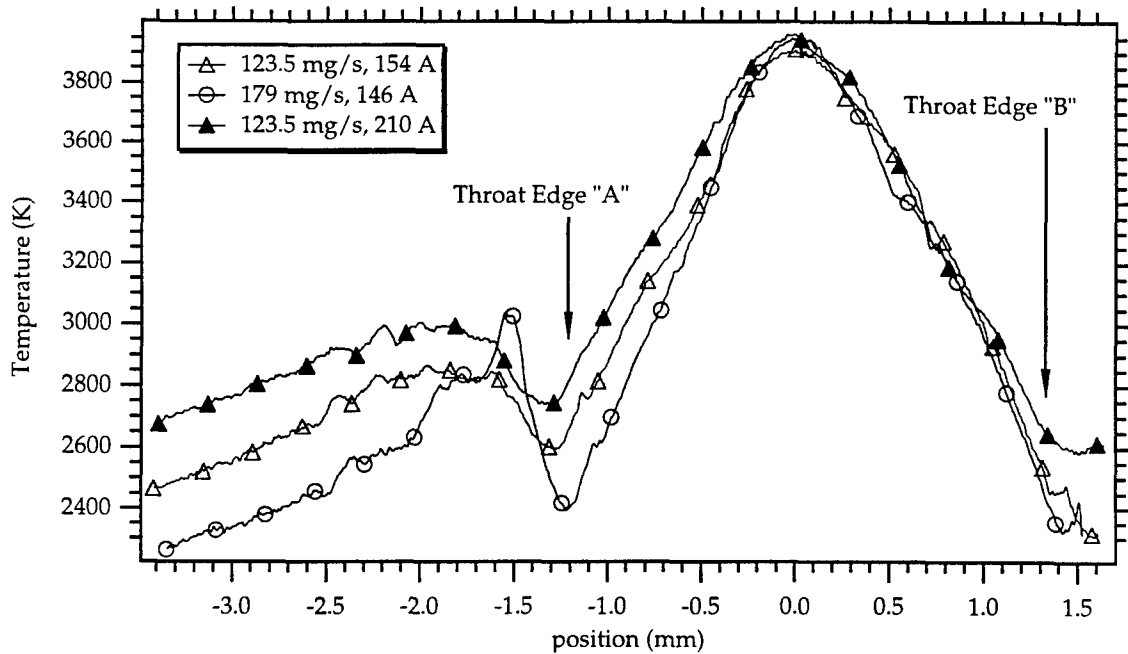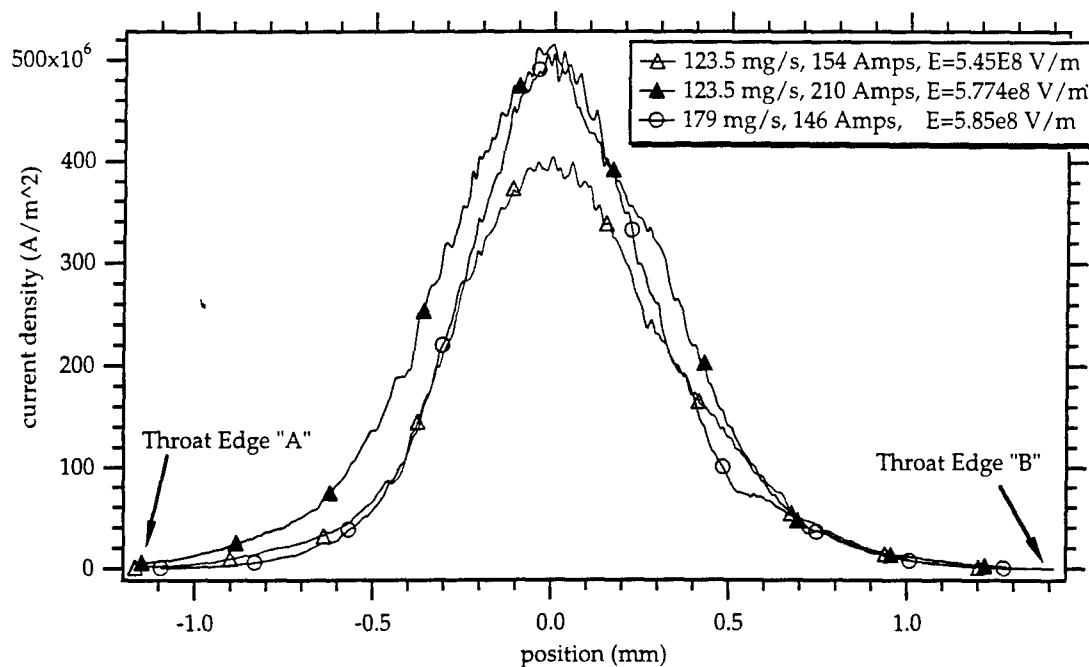

Figure 5. Arcjet electrode temperature as a function of radial location

Figure 6. Current density as a function of radial location
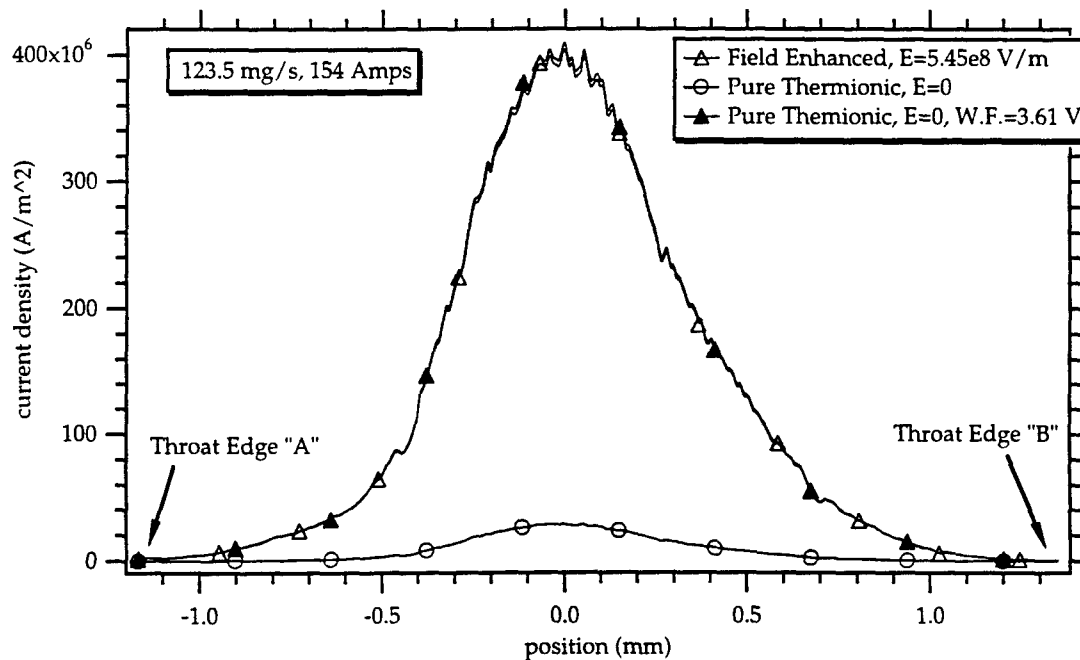
Figure 7. Pure thermionic emission verses field-enhanced thermionic emission as a function of radial location
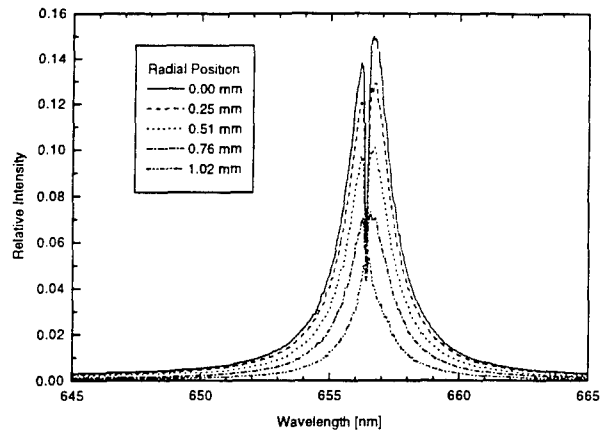
Figure 8. Uncalibrated H_α lineshapes at various radial positions for the operating condition: 20 kW, 123.5 mg/s (163.2 MJ/kg).
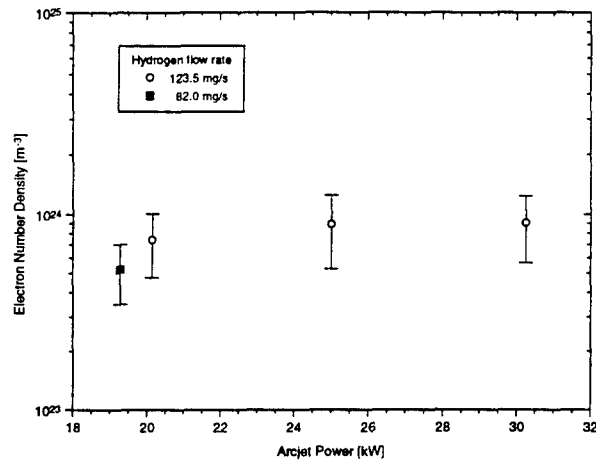
Figure 9. Centerline arc electron number density as a function of arcjet power.
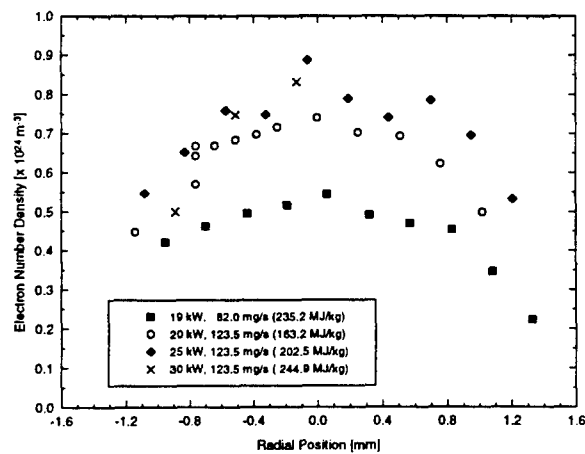
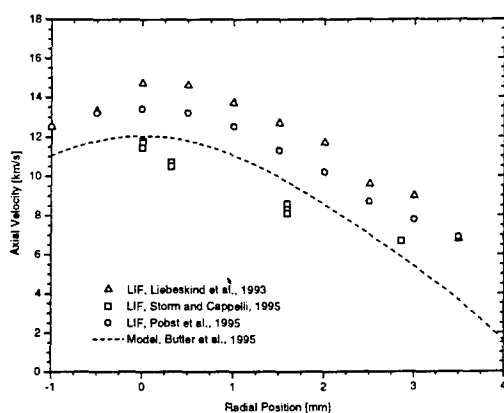Figure 10. Arc electron number density as a function of radial position.

14

Figure 1. Radial variation in the axial component of the velocity at the exit plane of a low power hydrogen arcjet.
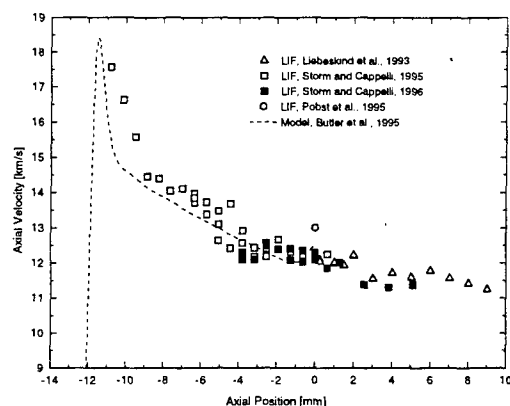

Figure 2. Axial variation in the axial component of velocity along the flow centerline of a low power hydrogen arcjet.
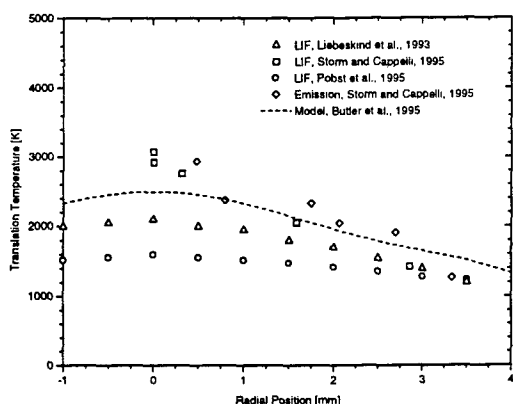

Figure 3. Radial variation in the translation temperature at the exit plane of a low power hydrogen arcjet.
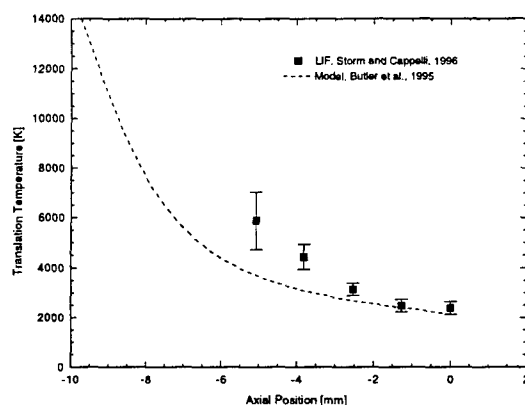

Figure 4. Axial variation in the translational temperature along the flow centerline of a low power hydrogen arcjet.
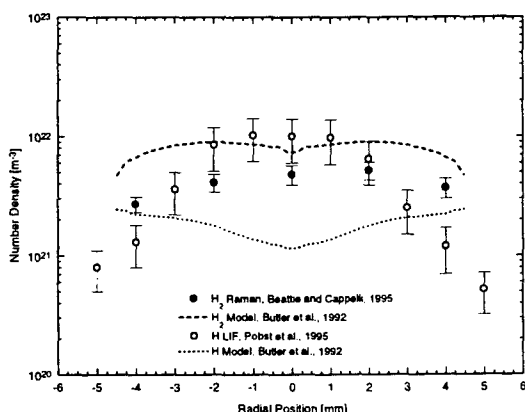

Figure 5. Radial variation in the molecular and atomic hydrogen number densities at the exit plane of a low power hydrogen arcjet.
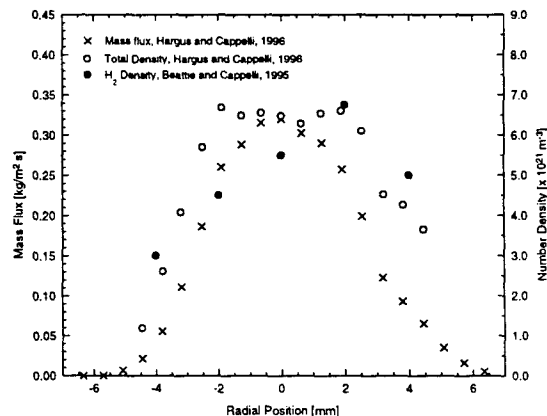

Figure 6. Radial variation in the measured mass flux, inferred total density (using the measured velocity profile), and hydrogen number densities at the exit plane of a low power hydrogen arcjet.
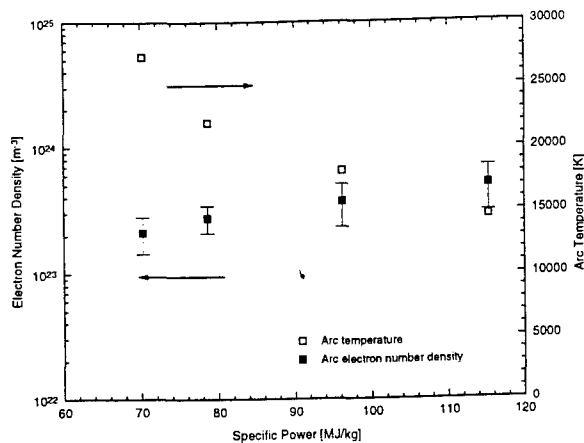
Figure 7. Variation in the measured arc electron number densities and inferred plasma temperature (assuming full ionization).
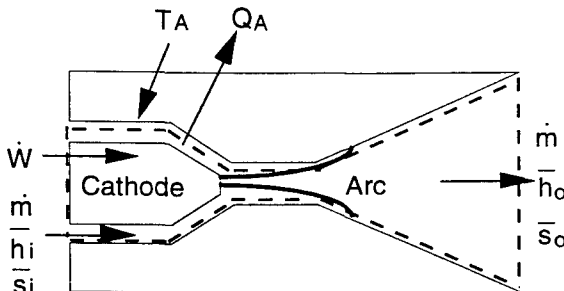

Figure 8. Measured cathode and anode temperature distribution.

Figure 9. Schematic illustration of the arcjet system, depicting the inflow and outflow of mass, enthalpy, entropy, and heat.
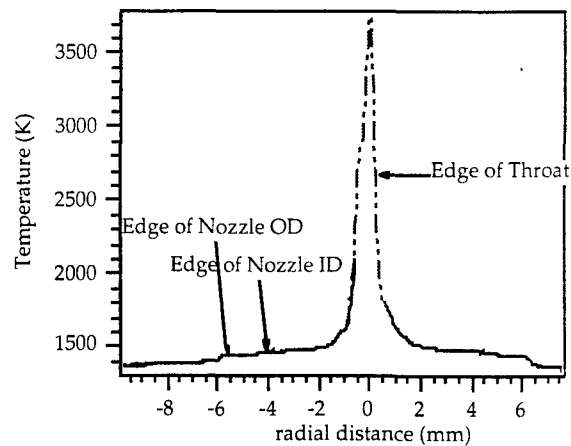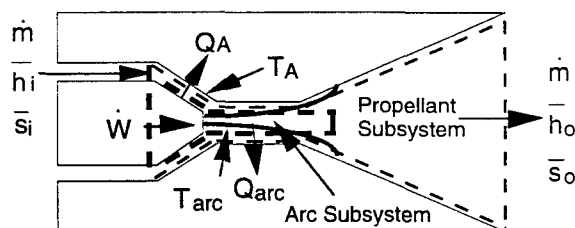

Figure 10. Schematic illustration of the arcjet subsystems including the system boundary for the arc, and system boundary for the flowing propellant.

Figure 11. Variation in the adiabatic thrust efficiency with exit plane fractional dissociation, for an exit pressure of 2 Torr, inlet pressure of 2 atm, inlet propellant temperature of 300K, and nominal operating conditions of 1.4 kW and 13mg/s.

Figure 12. Variation in the adiabatic thrust efficiency with peak exit plane temperature for $\theta_D = 0.15$.

10

The structure of an expanding hydrogen arcjet plasma

William A. Hargus, Jr. and Mark A. Cappelli*

Thermosciences Division

Mechanical Engineering Department

Stanford University

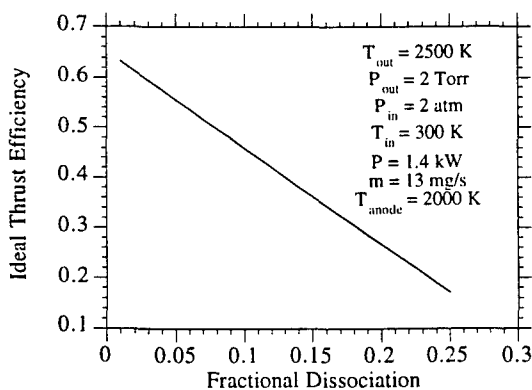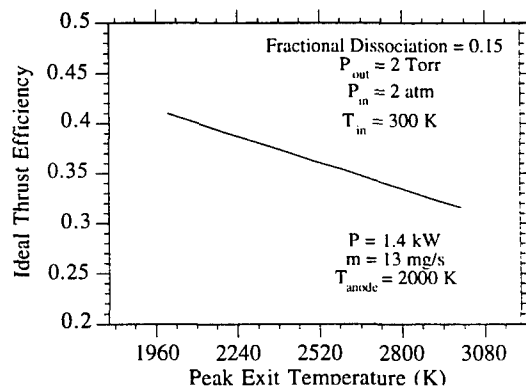Stanford, CA 94305

Abstract

The structure of an expanding low-power hydrogen arcjet plasma is investigated through probe-based measurements of impact pressure and mass flux. Comparisons are made to direct simulation Monte Carlo models (DSMC) of the non-ignited flow (cold flow) and continuum magnetohydrodynamic (MHD) models of the arc-heated flow. While general agreement with previous spectroscopic data and DSMC calculations are obtained, the cold flow impact pressures are shown to exhibit features that may be due to probe-flow interactions and rarefied gas effects. The ability to identify shocks in the plume, predicted by the DSMC model and previously observed by Raman spectroscopy, shows that the cold flow probes were capable of resolving major flow features. The impact pressure measurements of arc-heated flow also agree quite well with the results calculated from the MHD model, and it is demonstrated that integrated thrust densities derived from impact pressure measurements are in agreement with direct measurements of thrust using an inverted pendulum thrust stand. Cold flow mass flux measurements appear to agree well with the DSMC model in the core portion of the flow. Using velocity and temperature data obtained from previous laser induced fluorescence measurements; density, pressure, and thrust profiles were derived from the measured mass flux profiles. The density profile indicates that the dissociation fraction at the exit plane was within the uncertainty of the only direct spectroscopic molecular hydrogen density measurements available in the literature.

I. INTRODUCTION

The rapid expansion of an arc-heated plasma is the principle mechanism which generates thrust in an arcjet propulsion device. Due to their high specific impulse and moderate thrust levels, arcjet thrusters are playing an increasingly important role in satellite propulsion. Existing and planned applications of arcjet thrusters include stationkeeping and on-orbit maneuvering. Low power hydrazine arcjets are now in use on the TelStar IV class of communications satellites and the first space test of a high power arcjet will be launched in 1998 under the Air Force ESEX program [1,2]. Arcjet technology is steadily maturing as an understanding of the physics governing their operation increases. Efforts that combine both experimental and theoretical studies are necessary to build reliable models of arcjet performance which can serve as design tools for the next generation thrusters. The research presented here is motivated by the need to measure arcjet flow properties that can be used to verify the predictions of simulations based on both continuum-magnetohydrodynamic (MHD)[3] and Direct Simulation Monte Carlo (DSMC)[4] models of the non-equilibrium arcjet flow. In this paper, we discuss the results of impact pressure and mass flux measurements in the plume of a low power hydrogen arcjet thruster as well as direct measurements of thrust for both cold and arc-heated flow conditions. These results complement the many non-intrusive spectroscopic studies that have been performed on low power hydrogen arcjet plumes[5-11], including measurements of velocity[5-7], translational temperature[6-9], rotational temperature[10,11], molecular[10,11] and atomic hydrogen number density[9], and electron temperature[8]. With some of the results of these previous studies, it is possible to calculate density and static pressure distributions using the measured mass flux distributions presented here.

There have been only a few reported studies that have used pressure and mass flux probes to understand the properties of these electrothermal thruster plumes. Van Camp et al.[12] reported on impact pressure and mass flux measurements taken in the plume of several 30 kW class hydrogen arcjets. A more recent study by Penko et al.[13], examined the plume of a nitrogen resistojet with an impact pressure probe for verification of direct simulation Monte Carlo (DSMC) and Navier Stokes continuum models. To our knowledge, no mass flux measurements have been published on low power arcjets. In this study, we add to the large body of measurements taken on these low-power arcjets operating with hydrogen as a propellant and make direct comparisons to both particle and continuum simulations.

II. EXPERIMENTS

A. Thruster and Test Facility

The thruster and Stanford arcjet facility have been discussed in detail elsewhere in the literature[5-8,10] and therefore are only briefly described here. The arcjet thrust used here is a 1 kW class thruster designed and constructed by the NASA Lewis Research Center[14]. Thrusters of this particular design have been used as testbeds for investigating the performance of arcjets on a variety of propellants, and thus offer an excellent opportunity for a detailed comparison to model predictions. In our studies reported on here the thruster is operated at a nominal power of 1.42 kW (154V, 9.22 A) and a mass flow of 13.7 mg/s of hydrogen. This operating condition is within experimental uncertainty of the laser and emission studies reported previously[5-7,9-10]. The nozzle has a 0.64 mm throat diameter with a 20° expansion half angle and an area ratio of 225. The arcjet is mounted on a two-axis translational system within a 0.6 meter diameter, 1.1 meter long vacuum tank. The vacuum facility was evacuated by two Roots blowers backed by mechanical roughing pumps for a combined pumping speed of 2,500 l/s. In order to align the probe to the conical flow during flow angle and mass flux measurements, the probe was mounted on an rotational translation stage. This configuration allowed the probe to be placed fully perpendicular to the flow during measurements. The arcjet mass flow rate for all tests was controlled by a Unit Instruments hydrogen calibrated mass flow controller with a full scale flow rate of 10 standard liters per minute. Thrust measurements were performed in a larger vacuum chamber consisting of a non-magnetic stainless steel tank approximately 1 m in diameter and 1.5 m in length. This facility is pumped by a 425 l/s mechanical pump. Typical background pressures within the facility during thrust measurements were approximately 70 Pa.

B. Experimental Set Up

Fig. 1 schematically illustrates the mounting of the arcjet and mass flux or impact pressure probe within the vacuum chamber. A series of impact pressure measurements were performed by mounting the probe on an additional linear stage with motion orthogonal to the X-Y axes. Impact pressures were then measured using a 0-13,000 Pa capacitance manometer. For flow angle and mass flux measurements, angular motion of the probe was provided by placing the probe on a rotational translation stage. For mass flux measurements, the time rate of pressure rise within an initially evacuated 185 liter dump tank was measured with the use of a 0 - 1300 Pa capacitance manometer. All three translation stages and the pressure sensor were computer controlled and monitored. The result was a near automation of the data acquisition process and a uniformity in test procedure.

Fig. 2 provides a detailed schematic of the probe tips used for impact pressure measurements. The cold flow probe (top probe in Fig.2) was approximately 22 mm in length and 6.4 mm in diameter with a half angle of 9.5°. The probe tip was machined from brass and soldered onto a stainless steel body. The probe tip used for arc heated impact pressure measurements was constructed from copper and was

approximately 29 mm long and 16 mm in diameter with a half angle of 18.5°. The larger size of this probe is necessary to accommodate a water jacket that surrounds the 3.18 mm diameter inner copper tubing (not shown) that connected the probe to the capacitance manometer. Water cooling is necessary for the probe to survive in the plume environment during arc heated flow. This probe tip was attached to a copper collar-body assembly with the necessary coolant connections. For all impact pressure probes, the opening at the tip was 0.51 mm in diameter.

Mass flux measurements were made with the probe tip shown in Fig. 3. This probe design is similar to that used by Witte[15] to make mass flux and impact pressure studies in the plume of an argon magnetohydrodynamic thruster. A design consisting of a sharp leading edge and expanding entrance region enabled the probe to swallow the bow shock. The probe tip was approximately 25 mm in length and 13 mm in diameter. The probe had an outer half angle of 20° and an inner expansion angle of 14°. In order to be machined with the sharpest possible and most uniform opening of 0.80 mm, it was necessary to have a lip of 0.40 mm. The probe tip used for cold flow measurements was machined from brass and soldered onto a 6.4 mm diameter stainless steel tubing that formed the body of the probe. The probe tip used for arc heated measurements was machined from high conductivity, oxygen free copper and was identical to the one used for the cold flow measurements. However in this case, the probe body included a water jacket between copper tubes with diameters of 6.4 and 12.7 mm.

The thrust stand used in this study has been discussed extensively in the literature[16-17]. It is an inverted pendulum type thrust stand built by the Jet Propulsion Laboratory according to the design of Haag[16]. Thrust is determined from the pendulum displacement measured by a linear voltage differential transducer. Calibration is provided in-situ by loading the stand with four 5 g weights between arcjet tests. Thermal drift during arcjet operation is minimized by water cooling surfaces exposed to the thruster plume and the portion of the stand that supports the thruster. For each thrust measurement presented, the thruster was operated for a period of 10-15 minutes to stabilize the thruster operation and to allow the thrust stand to reach thermal equilibrium. After equilibrium is reached, five measurements of the thrust stand displacement were made, interspersed with induced oscillations to minimize stiction of the thrust stand components. After a number of measurements, power to the thruster was terminated and the zero drift and linearity changes due to thermal effects were characterized by a final calibration. All error estimates given for the thrust measurements include uncertainties associated with zero drifts and departures from linearity in the response of the thrust stand.

III. CALCULATIONS

A. Impact Pressure Measurements

A bow shock will form in front of the impact pressure probe. The pressure measured by the impact pressure probe is the stagnation pressure downstream of the normal shock. In comparing the

measured impact pressure (the stagnation pressure after the normal shock) to model predictions, the predicted flow properties are used to calculate the shock strength, or expected pressure rise across the normal shock. For continuum flow, the normal shock strength is given by[18]:

$$\frac{P_{oy}}{P_{ox}} = \frac{\left(\dfrac{2\gamma M^2 - (\gamma-1)}{(\gamma+1)}\right)^{-1/(\gamma-1)}}{\left(\left[\dfrac{(\gamma+1)M^2}{2+(\gamma-1)M^2}\right]\right)^{\gamma/(\gamma-1)}} \tag{1}$$

where M is the freestream Mach number, γ is the ratio of specific heat, P_{oy} is the stagnation pressure after the shock, and P_{ox} is the stagnation pressure before the normal shock. This relation is only valid for normal shocks.

B. Mass Flux Measurements

In order to correctly interpret the measure the mass flux data near the arcjet exit plane, a number of conditions must be satisfied[15,18]. First, the probe must be able to swallow the shock. This constrains the probe tip geometry. It must be sufficiently sharp and requires a diverging interior so that the shock is captured in the probe interior. It is further necessary to carefully align the probe to the flow direction to capture the normal component of the mass flux. For this test, a series of mass flux measurements were taken at angles varying between ±35° in 5° increments. Mass flux measurements were found to be much more sensitive to probe orientation than were similar impact pressure measurements. The dump tank volume must be sufficiently large so that during the sampling period the tank pressure remains below the static pressure of the flow. Finally, the temperature of the gas in the dump tank must be known. By retaining approximately 120 cm of line between the dump tank and the probe tip during cold flow measurements and water cooling during arc heated measurements, it was assumed that the gas with in the dump tank was at, or near, room temperature.

The local mass flux was calculated by determining the mass flow into the dump tank by use of the ideal gas law, differentiated in time:

$$\Lambda = \frac{\dot{m}_p}{A_p} = \frac{V}{A_p RT}\,dP/dt \tag{2}$$

where $\dot{m}_p$ is the mass flow rate collected by the probe, A_p is the probe area, dP/dt is the rate of pressure rise within the dump tank, V is the volume of the dump tank, T is the temperature of the hydrogen within the dump tank, and R is the gas constant for molecular hydrogen.

C. Thrust Measurements

From the measured thrust and mass flow, mean propellant exit velocity, specific impulse, and thrust efficiency were computed using[19]:

$$v = \frac{T_h}{\dot{m}} \tag{3}$$

$$I_{sp} = \frac{T_h}{\dot{m}g} \tag{4}$$

$$\eta = \frac{2P_e}{T_h v} \tag{5}$$

Here, v is the mean exit velocity, $\dot{m}$ is the mass flow rate, T_h is the measured thrust, I_{sp} is the specific impulse, g is the earth's gravitational constant, η is the thrust eficiency, and P_e is the electrical power dissipated by the arcjet thruster.

IV. RESULTS AND ANALYSIS

A. Cold Flow

The first measurement of impact pressure consisted of a survey of a vertical plane located 0.5 mm from the thruster exit plane. All cold flow tests were performed at a mass flow rate of 13.7 mg/s and background pressure of 40 Pa. Fig.4 shows the impact pressure contour for this condition. The contour is a somewhat symmetric peak with an annular wing structure. It is believed that the annular structure is the result of a barrel shock in the over expanded nozzle flow. The lack of overall symmetry may be due to a number of small irregularities visible in the lower left quadrant of the nozzle.

Fig.5 shows the impact pressure profile detemined from the DSMC calculations of Boyd et al.[11] using Eq.1 for this nozzle with similar flow conditions. Also shown are measurements taken from a horizontal sweep of the probe through the geometric center of the nozzle. In comparison to the measured impact pressures, continuum shock results computed from the DSMC data exhibit a slightly wider impact pressure profile. The numerical model profile is also much flatter than the experimental result in the core of the flow. The DSMC result exhibits some of the features seen in the experimental profile including the higher pressure annular region, however, it does not seem to capture the distinctive peak in the impact pressure seen very near the flow centerline. A portion of the difference between the curves in Fig.5 may be due to the fact that measured impact pressures in rarefied flows are higher than the stagnation pressures behind a normal shock. Corrections for rarefied gas effects are known to be available in the literature, but were not used in this study [11].

A direct thrust measurement of 28.5 mN was obtained for the conditions of the data shown in Fig.5. This value compares quite well with a thrust of 29.1 mN derived from the integrated impact pressure profile shown in Fig.5. Boyd's DSMC calculations give a value approximately 5% higher than the directly measured thrust, but agreement between all three thrust measurements is exceptional. In previous impact pressure studies of high power arcjet thruster, Van Camp et al[12]. also found excellent agreement between the integrated impact pressure and the directly measured thrust for nearly all arc heated conditions examined. Direct thrust measurements for other cold flow conditions as well as arc heated conditions (discussed below) are summarized in Table I while thrusts calculated from integrated impact pressure profiles are summarized in Table II.

Fig.6 shows the cold flow plume impact pressure field for distances of approximately 15 mm downstream of the exit plane. The high pressure annulus extends into the plume with the central core impact pressure dropping until a strong feature is encountered at a location 12 to 14 mm downstream of the exit plane. This location agrees exceptionally well with the shock location predicted by DSMC and qualitatively with the Raman scattering-based measurements of the J = 1 rotational state density of molecular hydrogen, as shown in Fig.7[11]. It is noteworthy that the shock location derived from the impact probe location remains somewhat ambiguous due to probe perturbation of the flow. Also, the number densities measured by Raman scattering represent an average over a probe volume that extends 4 mm in length along the axial direction[11].

Fig.8 compares the measured near exit plane (within 0.5 mm) cold-flow mass flux to that calculated from the results of Boyd's DSMC[11]. We see good agreement between the measurements and the model in the central core region of the flow. However, in the wings of the mass flux profile, the measured values of the mass flux are significantly lower than the model predictions. While some of this discrepancy can be attributed to the lack of complete capture of the flow in the subsonic layer adjacent to the nozzle wall, it is likely that the remaining discrepancy is associated with shock interactions causing a departure from ideal mass capture conditions near the high pressure annulus. Numerical integration of the measurements indicates that in the cold flow case the integrated mass collected by the probe accounts for only 50% of the total mass flow through the nozzle. Despite the inability to rely on the use of the mass flux probe to characterize the entire flowfield, it is seen that it captures the inner core flow structure quite well, and is used below to characterize the centerline flow properties up to a few diameters down stream of the exit plane. Fig. 9 compares the measured cold flow angle to the exit flow angle calculated using DSMC[11]. Again, there is fair agreement in the central core region of the flow, but the flow angles become larger than the nozzle half angle (20°) beyond approximately 1.5 mm from the center of the flow. Another interesting property of the cold flow condition is seen in Fig.9. At a radius of approximately 0.7 mm, the flow direction exhibit a small, but discernible and symmetric flow structure. This structure, at a location corresponding to the annular high impact pressure feature and to the annular maximum of the predicted and measured mass

flux, appears to be an expansion fan[18], however, the poor spatial resolution and low signal in this region of the flow prevents an assignment of this feature with any great degree of certainty.

Fig.10 compares the measured mass flux variation along the flow centerline downstream of the exit plane to the population of the first vibrational level of molecular hydrogen as calculated by DSMC and measured using Raman scattering[11]. We see that there is good agreement between the DSMC calculations and the mass flux measurements on the shock location, whereas there is an apparent disagreement between the spectroscopic measurements and the DSMC calculations. This result leads us to attribute the discrepancy to experimental uncertainty in the Raman scattering data. The general shape of the axial mass flux profile departs from the shape of the first vibrational state population distribution predicted by DSMC beyond about 15 mm, at about the position where the impact pressure field (see Fig.6) indicates the presence of complex shock features.

B. Arc Heated Flow

The second portion of this study concentrated on impact pressure and mass flux measurements in arc heated flows. A number of powers varying from 1.5 kW to 900 W were examined, although a complete data set of mass flux measurements was only generated at a power level of 1.4 kW. In all cases, the mass flow rate was 13.7 mg/s and the chamber background pressure was 40-50 Pa.

Fig.11 shows the impact pressure contour at an axial distance of 0.5 mm from the exit plane for an arcjet power of 1.45 kW. Unlike the cold flow exit plane data, the impact pressure field is smooth and is generally symmetric. This is further illustrated in the cross-section of the impact pressure profile, shown for various arcjet powers of Fig.12. It is seen that the highest impact pressure is recorded for the highest operating arcjet power, with a monatonic variation in measured impact pressure with arcjet power.

A comparison is made between the directly measured thrust and that derived from the integrated impact pressure profiles at the nozzle exit for a range of arcjet powers in Fig.13. The thrust derived from the impact pressure measurements are generally within 5% of those directly measured with a thrust stand and agree to within the experimental uncertainty over the range of powers studied. The uncertainty in the thrust stand measurements is approximately 2% and is due primarily to a small non-linearity in the thrust stand response curve. The uncertainty of the integrated impact pressure measurements stems primarily from the incomplete symmetry of the profiles and uncertainties in the probe position. The greatest source of error in determining the probe position is the movement in the arcjet nozzle position relative to the placement of the probe following arc ignition as the nozzle insert thermally expands. The combined uncertainty brought about by these two factors is estimated to be 10%.

8

The plume impact pressure field taken at an arcjet power of 1.45 kW is shown in Fig.14. Unlike the cold flow plume, the arc-heated case lacks the complex structure and instead smoothly decays in all directions. It is very symmetric and there is no evidence of a shock in the first 25 mm downstream of the exit plane. Assuming that the plume core flow is isentropic and that the stagnation pressure is constant, the impact pressure along the center line may be used to determine the centerline variation in the Mach number. Together with the measured axial velocities from our previous laser induced fluorescence studies (LIF)[7], we can determine, indirectly, the centerline variation in the plume temperature. For this exercise, we assume a stagnation pressure equal to the maximum calculated at the exit plane by the MHD simulation for a power of 1.4 kW. It is noteworthy that the calculated static pressure is greater than the background pressure, indicating that this plume is under-expanded. The normal shock relation[18] given as Eq.1 (assuming a weakly dissociated flow and full vibrational excitation) is used to determine the local Mach number.

The centerline temperature extracted from the calculated Mach number and measured velocity and impact pressure is shown in Fig.15. For comparison, we include temperatures determined previously for similar operating conditions by Doppler-broadened LIF[7]. The LIF temperatures were later reanalyzed by Storm and Cappelli[19] to account for Stark broadening. As seen in Fig.15, the original LIF-based temperature measurements are higher than those determined from the impact pressure measurements. Correcting for Stark broadening, which is significant only very near the exit plane (where the electron and ion densities are the highest), lowers the LIF temperatures at the exit plane to values that are in closer agreement with the temperatures inferred from the measured impact pressure. Further downstream from the exit plane, the agreement between all temperature measurements is apparent. However, in contrast with the previous LIF measurements[7], there appears to be little or no evidence of a shock at a downstream position of about 20 mm in the impact pressure data. We attribute this discrepancy to a possible perturbation of the flow by the impact pressure probe.

Fig.16 compares the measured mass flux profile to that predicted by the MHD model for an arcjet power of 1.4 kW. It is noted that the model predictions are taken at the exit plane while the experimental data is from a position of approximately 1 mm downstream of the exit plane. Numerical integration of the mass flux measured to a radius if 5.75 mm indicates that only 75% of the total mass flux has been captured. Examination of the LIF velocity and temperature data[6] indicates that the flow transitions to subsonic flow at a radius of between 5.0 and 5.5 mm. Therefore, it is unlikely that this or any similar probe would be able to capture 100% of the flow. It is interesting to note the MHD model predicts a dip in the mass flux near the flow centerline - a feature arising from a drop in the flow density - that is not seen in the measured mass flux profile. It is possible that the finite size of the probe tip (about 1.5 mm) precludes the detection of such a flow structure.

Although subtle, it is apparent from Fig.16 that the measured mass flux profile is not completely symmetrical. This flow asymmetry is further illustrated in Fig.17 which plots the measured flow angle

as determined from the impact pressure measurements. The measured flow angles are, at best, in qualitative agreement with the MHD predictions which are shown as a solid line in the figure. The flow angle is found to be less than 35° throughout much of the flow. The asymmetry in flow angle detected by the impact pressure probe is in agreement with the flow angle asymmetry seen in the previous LIF data[7] and the asymmetry in the density as measured by Raman scattering[10]. This asymmetry has been previously attributed to the effect of the placement of the pumping port in the chamber on the structure of the plume[7]. It is important to note that the background pressure is 40-50 Pa which indicates that the vacuum chamber is still very much in the transitional flow regime.

Using the previous LIF-based velocity measurements[7] taken at similar arcjet operating conditions, it is possible to independently determine the near exit plane distribution in the mass density from the measured mass flux. The resulting density distribution is shown in Fig.18 together with that predicted by the MHD simulations. We see that there is a significant disagreement between the measured and predicted densities. The difference can be attributed in part to the fact that the measurements are taken at a position 1 mm downstream of the exit plane, which is where the MHD simulation ends[3]. Again, the MHD simulation predicts a significant drop in the center of the profile which is not seen in the measurements. The measured mass density has a relatively flat level central core of approximately 4 mm in diameter.

If it is assumed that the dissociation fraction is small, then the molecular hydrogen number density can be estimated by dividing the mass density (experimental data in Fig.18) by the molecular weight of hydrogen. The result is presented in Fig.19 along with the experimental molecular hydrogen densities measured using Raman scattering by Beattie and Cappelli[10]. The agreement between the two data sets is very good. The asymmetry in the plume is more pronounced in the Raman measurements due to the fact that the sample volume of these measurements extended 4 mm in the axial direction. The Raman scattering results are also slightly lower in value, most likely because of this spatial averaging. This result suggests that the dissociation fraction is likely to fall within the combined uncertainty in the two data sets, which we estimate to be approximately 25 - 30%.

The exit plane static pressure distribution can be determined from the LIF-based temperature measurements determined in the previous LIF studies[7,19] and the experimental mass density profile shown in Fig.18. These results are shown in Fig.20, along with the static pressure calculated from the MHD simulations. As in Fig.19, it is assumed that the exit plane dissociation fraction is small (this assumption is supported somewhat by the correspondence of the data in Fig.19). Like the density distribution in Fig.18, the pressure distribution is approximately a factor of two lower than that predicted by the simulations. Although part of this difference can be attributed to the fact that the probe samples from a position that is approximately 1 mm downstream of the exit plane, it is unlikely that the pressure will drop by a factor of two within this distance (discussed further below). No correction to this data is made for the assumption of a weakly dissociated flow, but it is noted that if

10

the flow is 35% dissociated, then the difference between the predicted and experimental static pressures would be within experimental error.

Using the same procedure for deriving the mass density shown in Fig.18, the centerline variation in the plume density was computed to a distance of approximately 40 mm downstream of the exit plane. As shown in Fig.21, the mass density is seen to decay in a near exponential fashion. Unlike the cold flow conditions, there is no direct evidence of a shock, in contrast with the slight rise in temperature observed by Liebeskind et al.[7], from the LIF studies. It is possible that the interaction between the mass flux probe and flowfield partially obscures this feature.

The exit plane thrust density profile obtained from the product of the mass density (Fig.18) and the LIF velocity data[7] is shown in Fig.22. Surprisingly, the experimental thrust density profile is remarkably similar to that predicted by the MHD simulations. General agreement was expected since the MHD simulations did predict a thrust and specific impulse that was within approximately 10% of that measured[3]. However, considering the large discrepancy between the predicted and measured mass flux (Fig.16), the agreement displayed in Fig.22 is misleading. A previous comparison of the predicted and measured velocities showed that while good agreement was observed in the core flow, the predicted velocities were significantly lower than those measured at larger radii[3]. This under-prediction in velocities is nearly exactly compensated by the over-prediction in mass flux in the outer radii while the spatial integration gives less weight to the flowfield near the core. Despite these differences in flow details, an integration of the thrust profile gives 114 mN of thrust for this operating condition in comparison to a value of 106 mN calculated from the MHD simulations. Direct thrust measurements at the same condition resulted in 109 mN while the integrated impact pressure profile resulted in a thrust of 107 mN.

V. DISCUSSION AND CONCLUSIONS

Cold flow impact pressure measurements suggest that the flow has a nearly isentropic core that is not quite as wide as that predicted by DSMC simulations. Although the higher impact pressure annular regions were captured in the simulations there are additional features such as a high pressure core that is not apparent in the DSMC calculation. The ability to detect the presence of a shock at a location of about 20 mm downstream of the exit plane in agreement with both the DSMC calculations and Raman spectroscopy measurements of density shows that impact pressure probes are capable of resolving major flow features.

A water-cooled impact pressure probe was able to survive near the exit plane and plume indefinitely under arc heated conditions and provided measurements of impact pressure for a wide range of arcjet powers. Integrated impact pressure profiles were found to give total thrust values that were in very good agreement with direct thrust measurements. Impact pressure measurements were used to indirectly determine the plume temperature. These temperatures were in general agreement

11

with previous spectroscopic measurements, however, there was no evidence of any shock structure from either the impact or mass flux probes over the region of the plume studied, in contrast with previous LIF measurements.

Analysis of the results the cold flow mass flux measurements indicate that the central core flow behaves as modeled. However, the flow in the wings of the mass flux profile is not being captured. The ability to capture only 50% of the total flow suggests that there are probe-flow interactions at large radial positions or that there are additional flowfield properties not accounted for in the interpretation of the probe data. An improvement was seen in the arc heated flow, where approximately 75% of the flow was captured. In this case, the measured mass flux profile was broader than that predicted at the exit plane by the continuum MHD simulations. A portion of this effect can be attributed to the probe being located approximately 1 mm downstream of the thruster exit plane.

These measurements of impact pressure and mass flux made use of prior LIF and Raman scattering measurements of velocity and temperature to determine other flow properties such as static pressure, mass density, and thrust density. Although the thrust determined by the integrated thrust density is in agreement with that of the MHD model prediction, this agreement is fortuitous in that it is derived from the product of the mass flux profiles and velocity profiles, with which the model predictions have significant shortcomings. The integrated thrust density give thrust values that are within experimental error of those measured directly using an inverted pendulum thrust stand, and indirectly from the impact pressure profiles.

While the measurements of mass density and its comparison to past measurements of hydrogen number density suggest that the dissociation fraction is small (no greater than 25-30%), the uncertainty associated with the later makes a quantitative estimate difficult. A refinement in the Raman scattering-based measurements of absolute molecular hydrogen concentration would be needed before a more accurate assessment of the spatial variation in the dissociation fraction can be obtained.

This study has demonstrated that the use of relatively simple impact pressure and mass flux probes can provide valuable information on the complex flow structure in an arcjet thruster. We have used the information to make direct comparisons to both particle and continuum model predictions. In addition, we have used the impact pressure and mass flux data in conjunction with past laser-based measurements to determine flow Mach number, temperature, static pressure, mass density, and thrust density.

ACKNOWLEDGMENTS

REFERENCES

1. W.W. Smith, "Low power hydrazine arcjet qualification," IEPC 91-148, Proceedings of the 22nd International Electric Propulsion Conference, Viareggio. Italy, Oct. 1991.

2. A. Sutton, "Overview of the Air Force ESEX flight experiment," IEPC 93-057, Proceedings of the 23rd International Electric Propulsion Conference, Seattle, WA, Sept. 1993.

3. G.W. Butler, I.D. Boyd, and M.A. Cappelli, "Nonequilibrium flow phenomenon in low power hydrogen arcjets" AIAA Paper 95-2819, July 1995.

4. I.D. Boyd, "Monte Carlo simulation of nonequilibrium flow in a low-power hydrogen arcjet," Phys. Fluids **9**, 3086, 1997.

5. J.G. Liebeskind, R.K. Hanson, and M.A. Cappelli, "Laser-induced fluorescence diagnostic for temperature and velocity measurements in a hydrogen arcjet plume," Applied Optics, **32.** 6117, 1993.

6. J.G. Liebeskind, R.K. Hanson, and M.A. Cappelli, "Flow diagnostics of an arcjet using laser-induced fluorescence," AIAA Paper 92-3243, July 1992.

7. J.G. Liebeskind, R.K. Hanson. and M.A. Cappelli, "Plume characteristics of an arcjet thruster," AIAA Paper 93-2530, June 1993.

8. P.V. Storm and M.A. Cappelli, "High spectral resolution emission study of a low power hydrogen arcjet plume," AIAA Paper 95-1960, June 1995.

9. J.A. Pobst, I.J. Wysong, and R.A. Spores, "Laser induced fluorescence of ground state hydrogen atoms in an arcjet plume", AIAA Paper 95-1973, June 1995.

10. D.R. Beattie and M.A. Cappelli, "Raman scattering measurements of molecular hydrogen in an arcjet thruster plume," AIAA Paper 95-1956, June 1995.

11. I.D. Boyd, D.R. Beattie, and M.A. Cappelli, "Numerical and experimental investigations of low density supersonic jets of hydrogen", Journal of Fluid Mechanics **280**, 41, 1994.

12. W.M Van Camp, D.W. Esker, R.J. Checkly, W.G. Duke, J.C. Crouton. S.E. Merrifield, and R.A. Williamson, "Study of arcjet propulsion devices: Final report," NASA CR-54691, McDonnell Report E368, Mar. 1966.

13. P.F. Penko, I.D. Boyd, D.L. Meissner. and K.J. DeWitt, "Pressure measurements in a low density nozzle plume for code verification," AIAA Paper 91-2110, June. 1991

14. F.M. Curran and T.W. Haag, "Extended life and performance test of a low power arcjet". AIAA Paper 88-3106, New York, 1988.

15. A.B. Witte, Part I. Experimental Investigation of an Arc-Heated Super Sonic Free Jet and Part II. Analysis of One Dimensional Isentropic Flow for Partly Ionized Argon, Thesis. California Institute of Technology, University Microfilms, Inc., Ann Arbor. MI, 1967.

16. T.W. Haag and F.W. Curran, "Arcjet starting reliability: a multistart test on hydrogen / nitrogen mixtures," AIAA Paper 87-1061, Colorado Springs 1987.

17. K.A. McFall, D.L. Tilley, and F.S. Glulczinski, "Low power arcjet performance evaluation," Paper IEPC-95-18, Proceedings of the 24th International Electric Propulsion Conference, Sept. 19-23, Moscow, Russia.

18. M.A. Saad, Compressible Fluid Flow, Prentice-Hall Inc.. Englewood Cliffs, NJ, 1985.

19. P.G. Hill and C.R. Peterson, Mechanics and Thermodynamics of Propulsion, Addison-Wesley Publishing Co., Menlo Park California, 1965.

20. P.V. Storm, P.V. and M.A. Cappelli, "Stark broadening corrections to laser-induced fluorescence temperature measurements in a hydrogen arcjet plume," Applied Optics, 34, 4913, 1996.

Figure Captions

Figure 1. Test facility and experimental setup. The arcjet is mounted on a two-axis linear translation system with the probe mounted on a third rotational stage. For several tests, an additional linear stage provided motion orthogonal to the X-Z axes.

Figure 2. Probes used for impact pressure measurements of cold(top) and arc heated flows (bottom).

Figure 3. Probe tip design used for cold and hot flow measurements. Note that the dimensions are in millimeters.

Figure 4. Impact pressure (Pa) contour 0.5 mm from exit plane.

Figure 5. Impact pressure profile from experiment and calculated from Boyd.

Figure 6. Centerline impact pressure (Pa)contour into the plume.

Figure 7. Experimental impact pressure compared to measured and calculated (Boyd) first hydrogen vibrational level number densities.

Figure 8. Measured and Boyd's DSMC model calculated cold flow exit plane mass flux distribution.

Figure 9. Measured and Boyd's DSMC model calculated flow angles for cold flow.

Figure 10. Cold flow plume mass flux compared to Beattie's measured and Boyd's calculated first hydrogen vibrational level number densities.

Figure 11. Arc heated exit plane impact pressure contour for a power of 1.45 kW. Impact pressures are labeled in Pa.

Figure 12. Impact pressure profiles at a variety of powers.

Figure 13. Thrust stand measurements compared to integrated impact pressure profiles.

Figure 14. Arc heated plume impact pressure field at a power of 1.45 kW. Impact pressures are in Pa.

Figure 15. Temperature calculations in the plume compared to measured LIF temperatures from Liebeskind, et al. Note that calculated temperatures do not show evidence of a shock.

Figure 16. Arc heated mass flux measurements and results of Butler's MHD model.

Figure 17. Measured and predicted by Butler arc heated flow angles.

Figure 18. Independently determined mass densities compared to Butler's MHD model results.

Figure 19. Arc heated molecular hydrogen number densities calculated from mass flux measurements and as measured by Beattie using Raman scattering.

Figure 20. Static pressure profile computed from mass flux measurements compared to the static pressure profile predicted by Butler.

Figure 21. Plume centerline mass density profile computed from mass flux measurements.

Figure 22. Thrust density profile calculated from mass flux measurements compared to Butler's predicted thrust densities.

Mass Flow (mg/s)	Power (kW)	Thrust (mN)	Specific Impulse (m/s)	(s)	Efficiency
13.7	0.00	28.5	2080	212	X
6.8	0.00	12.4	1820	185	X
13.7	1.50	114.7	8370	853	0.32
13.7	1.41	111.4	8130	829	0.32
13.7	1.40	109.2	7970	812	0.31
13.7	1.30	108.0	7880	804	0.33
13.7	1.19	103.7	7570	771	0.33
13.7	1.09	99.3	7250	739	0.33
13.7	1.00	95.5	6970	710	0.33
13.7	0.90	88.0	6420	655	0.32
13.7	0.79	84.0	6130	625	0.33
13.7	0.71	78.0	5700	581	0.31
14.6	1.41	116.1	7950	811	0.33
11.6	1.41	98.7	8510	867	0.30

Table I. Results of Direct Thrust Measurements

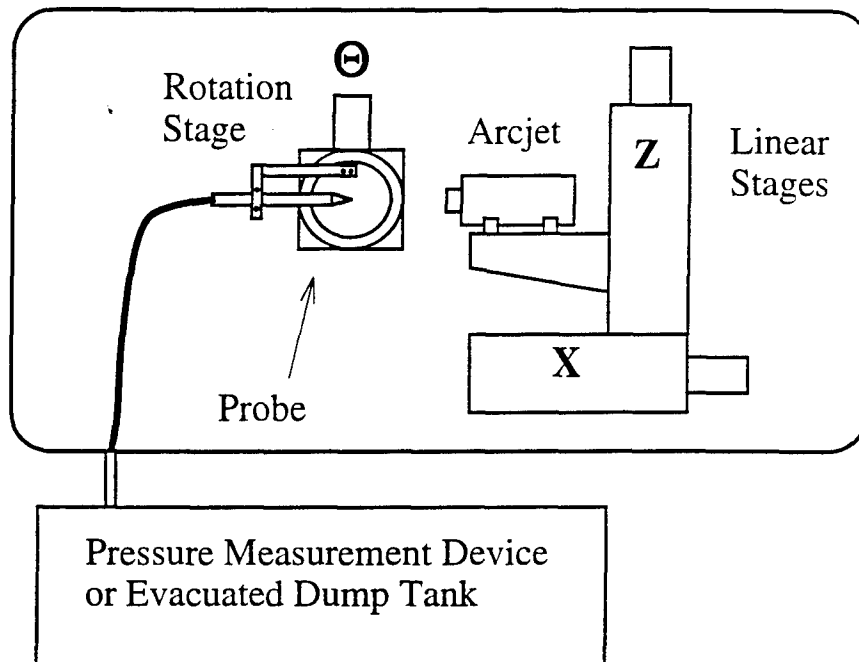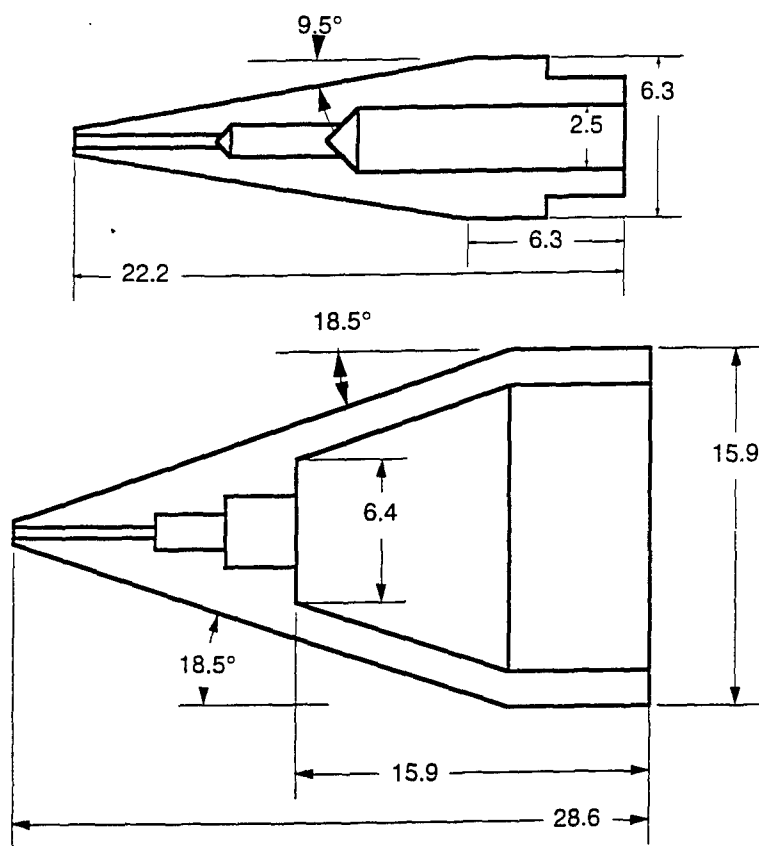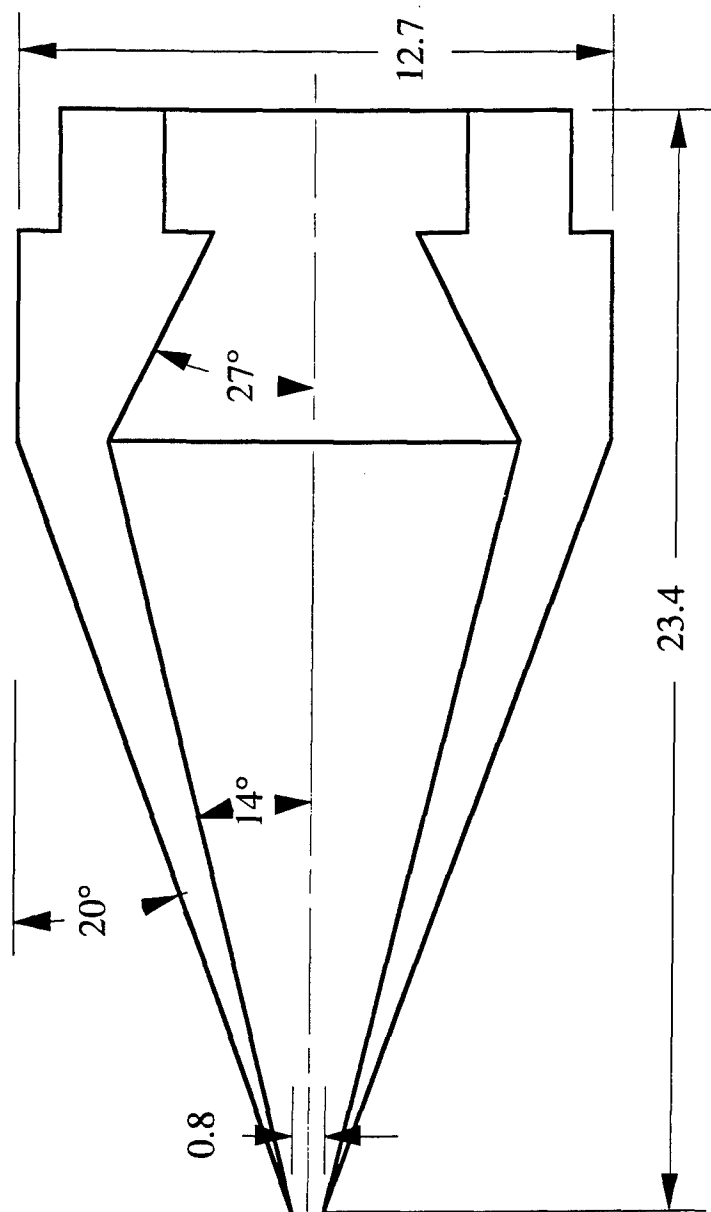| Mass Flow (mg/s)	Power (kW)	Thrust (mN)
13.7	0.00	29.1
13.7	1.45	104.8
13.7	1.39	106.9
13.7	1.29	102.5
13.7	1.22	99.1
13.7	1.09	98.1
13.7	1.00	92.0
13.7	0.90	87.1

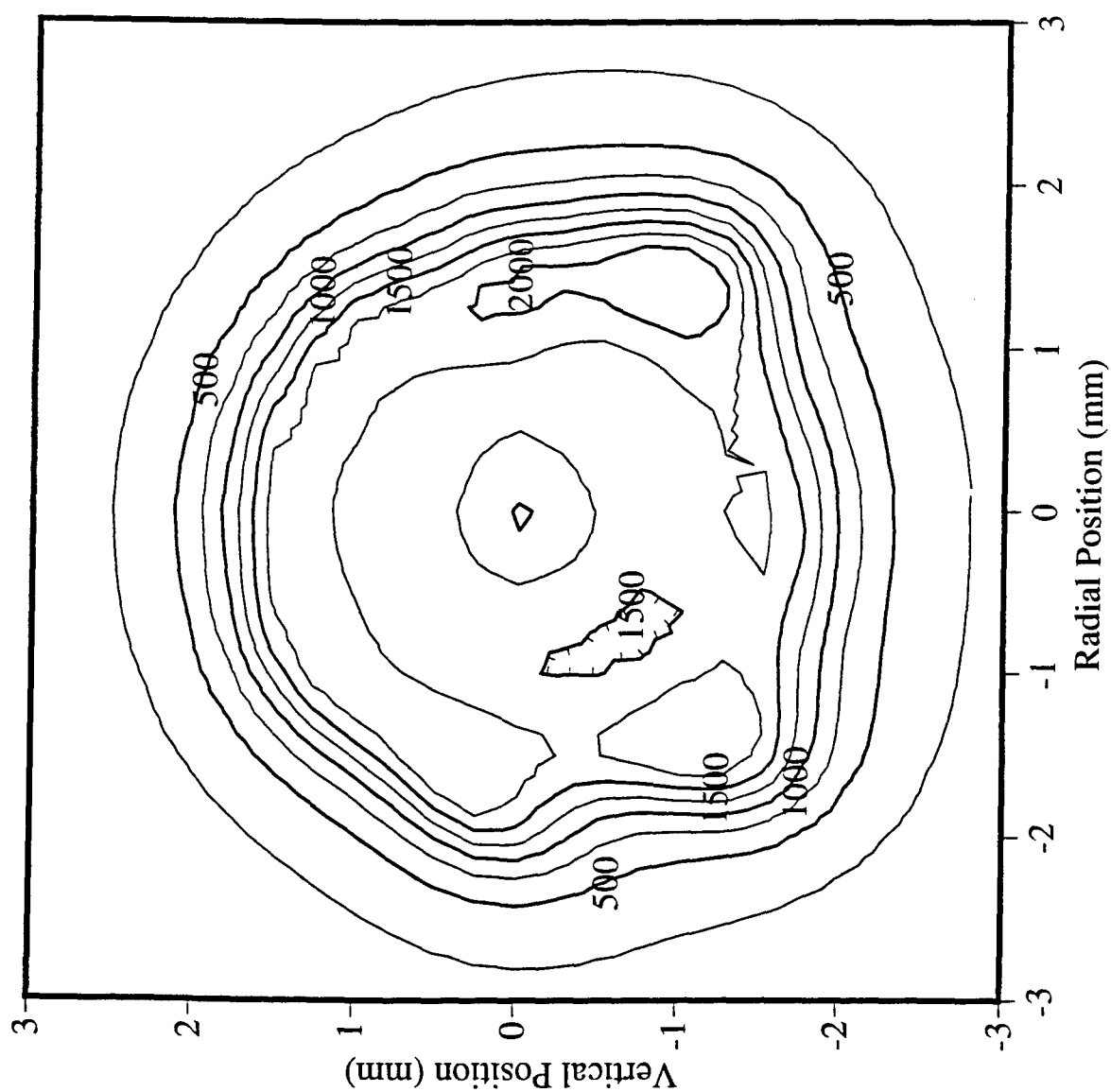Table II. Results of Integrated Impact Pressure Measurements
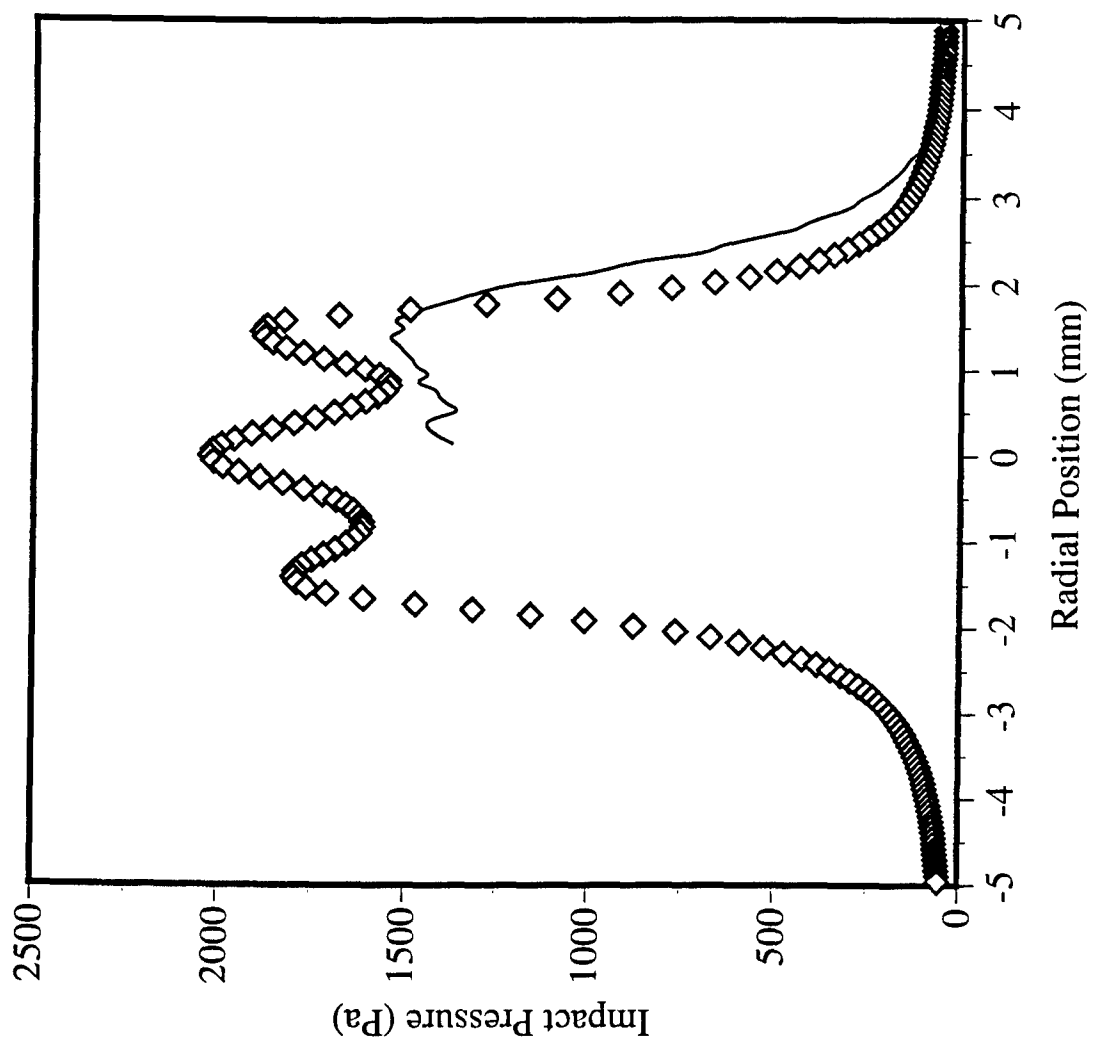
Figure 1.

Figure 2.

Figure 3.

Figure 4

Figure 5

Figure 6

Figure 7

Figure 8

Radial Position (mm)

Mass Flux (kg/m²/s)
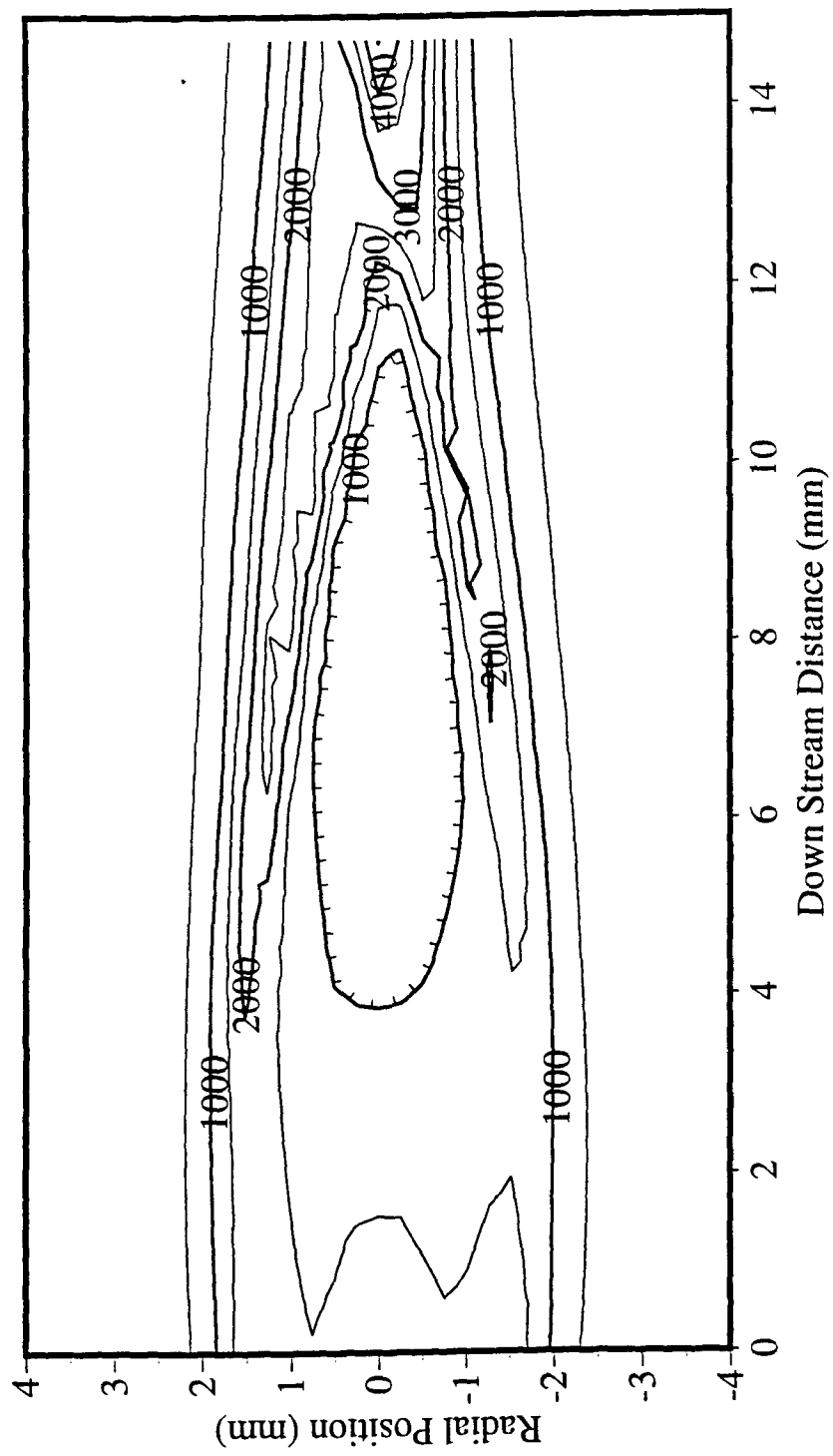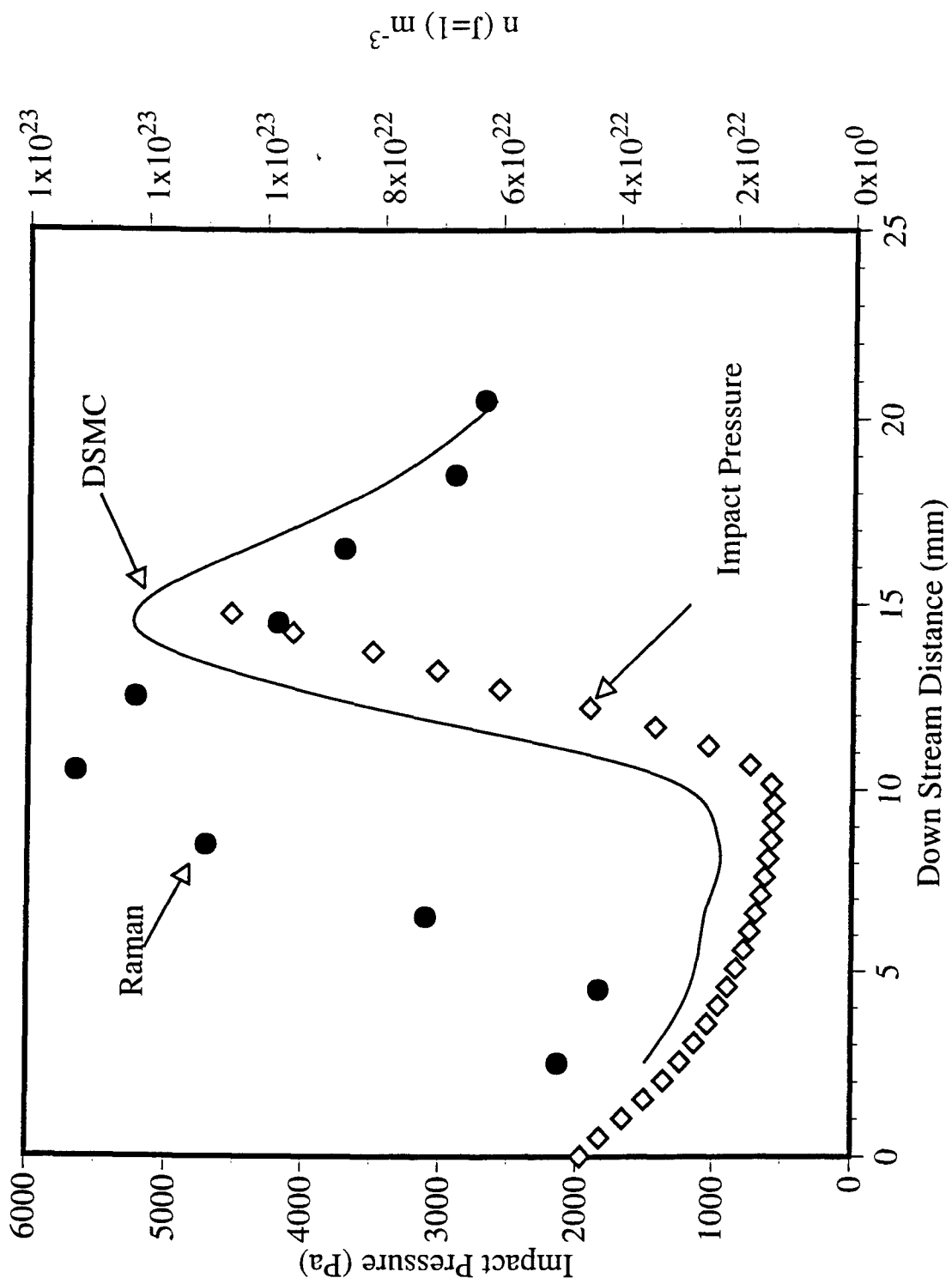
Figure 9

Figure 10

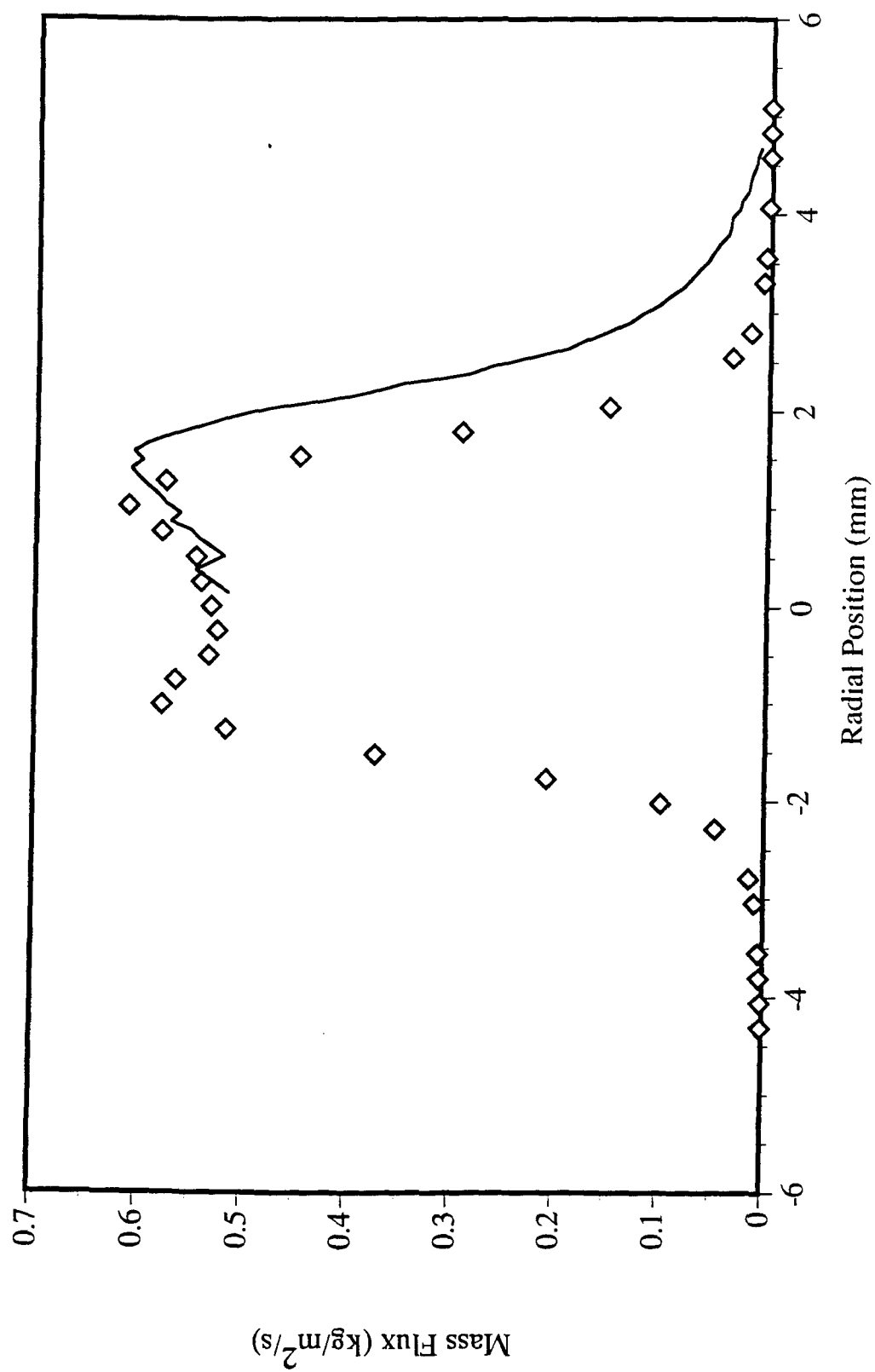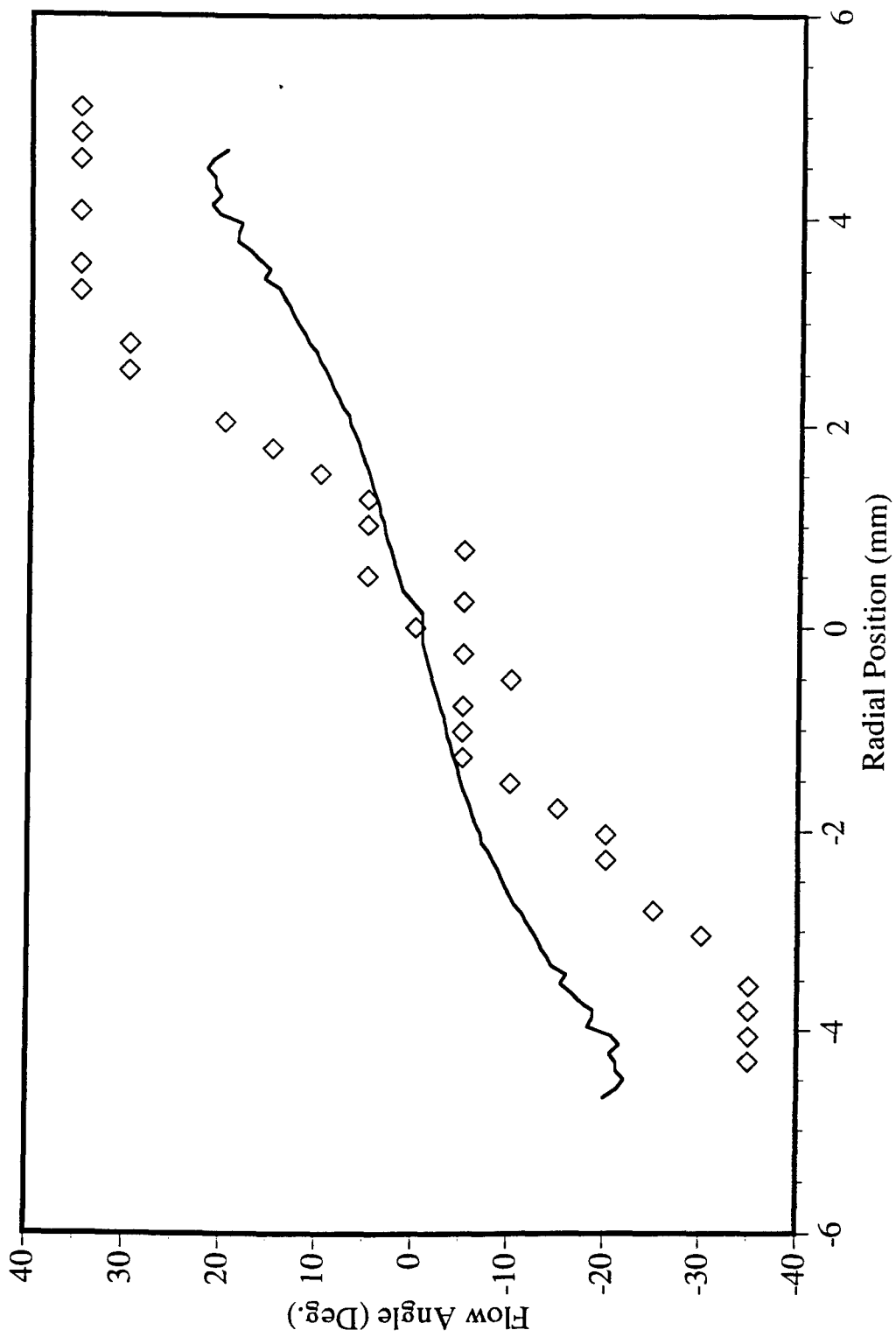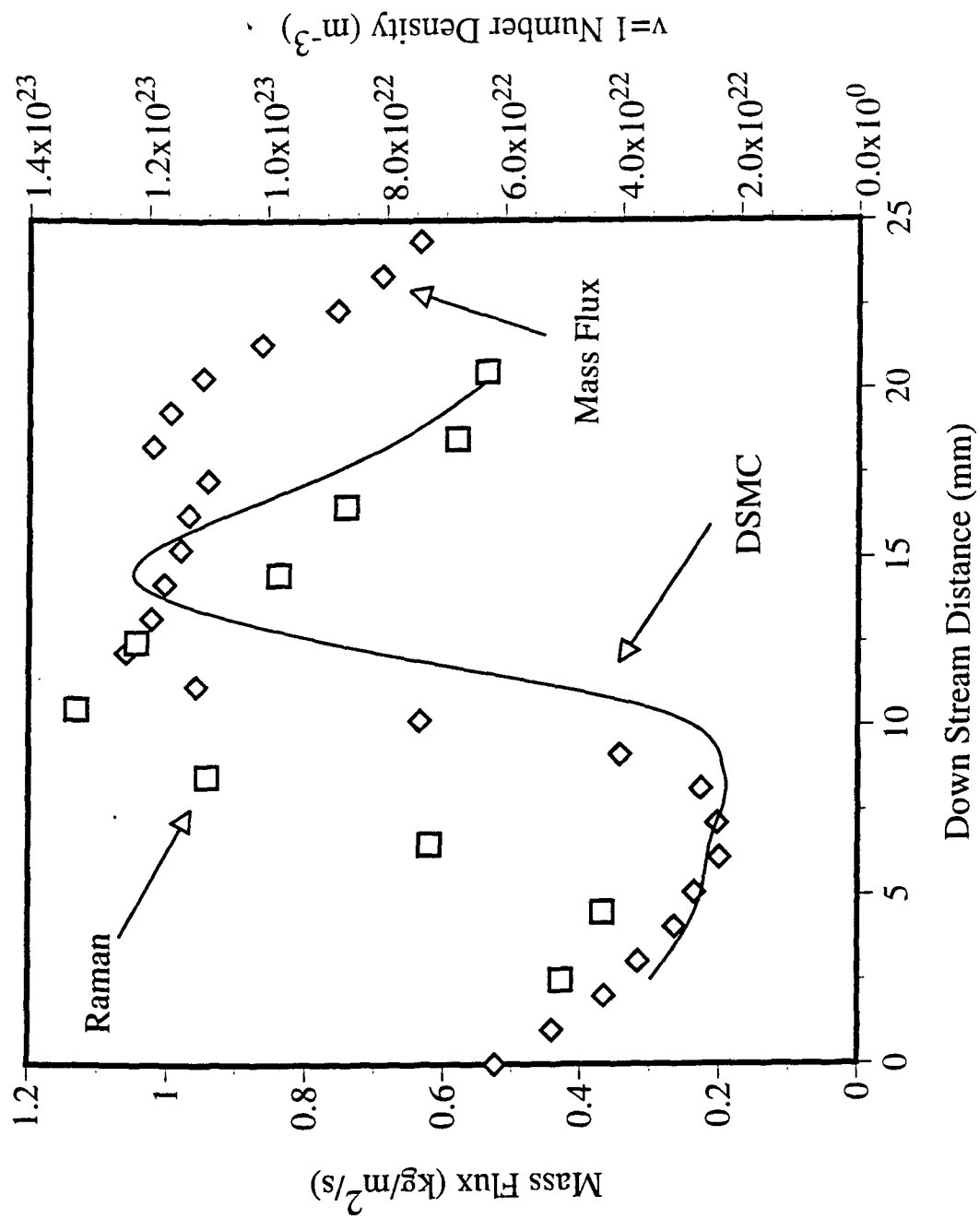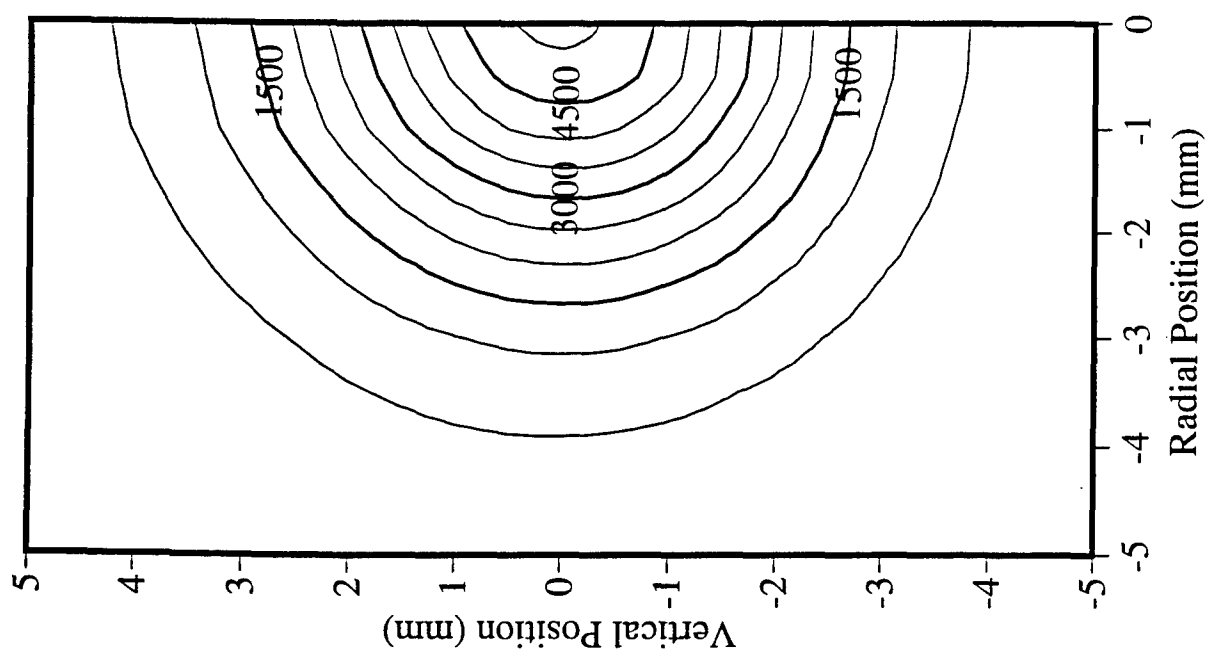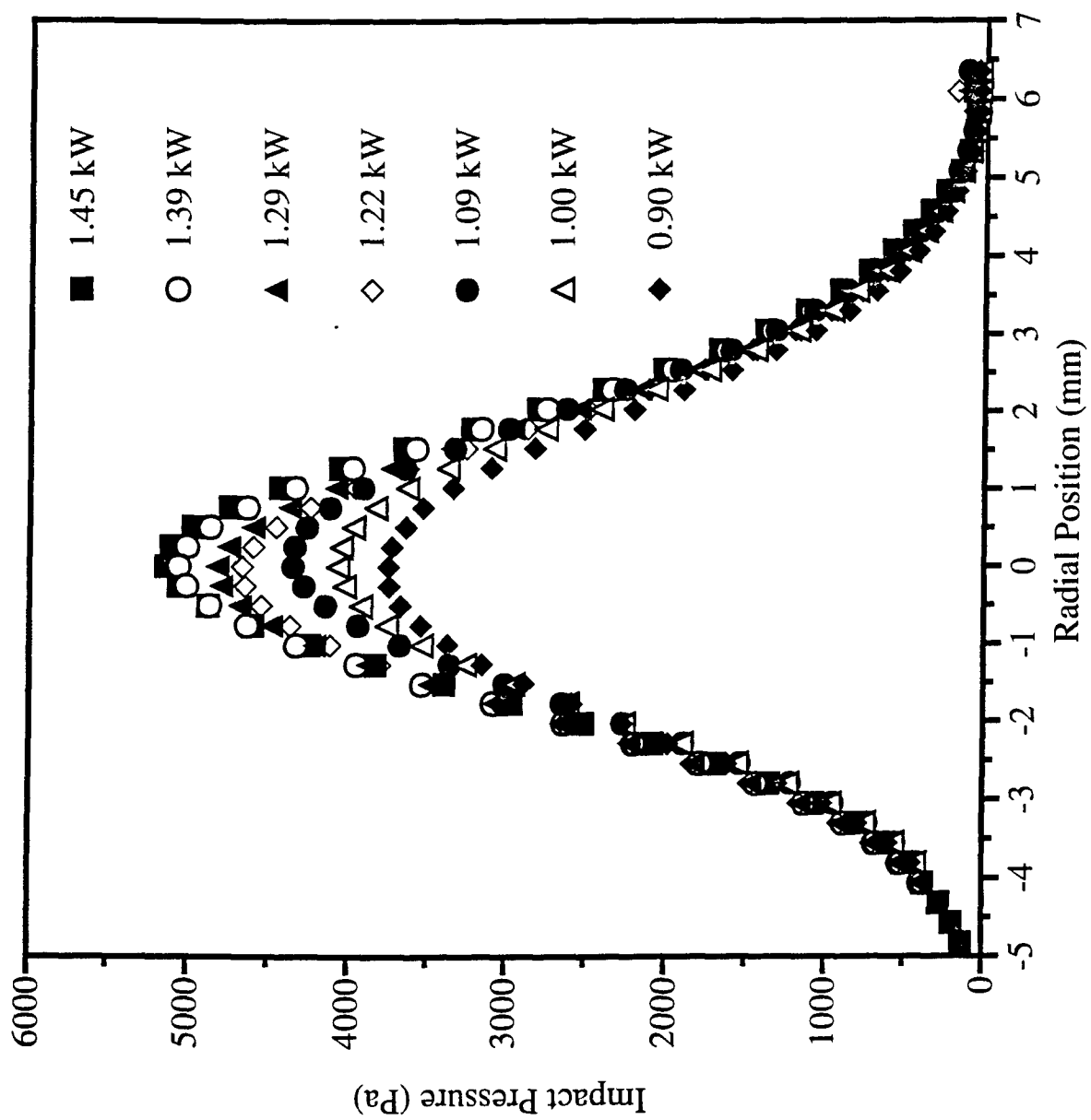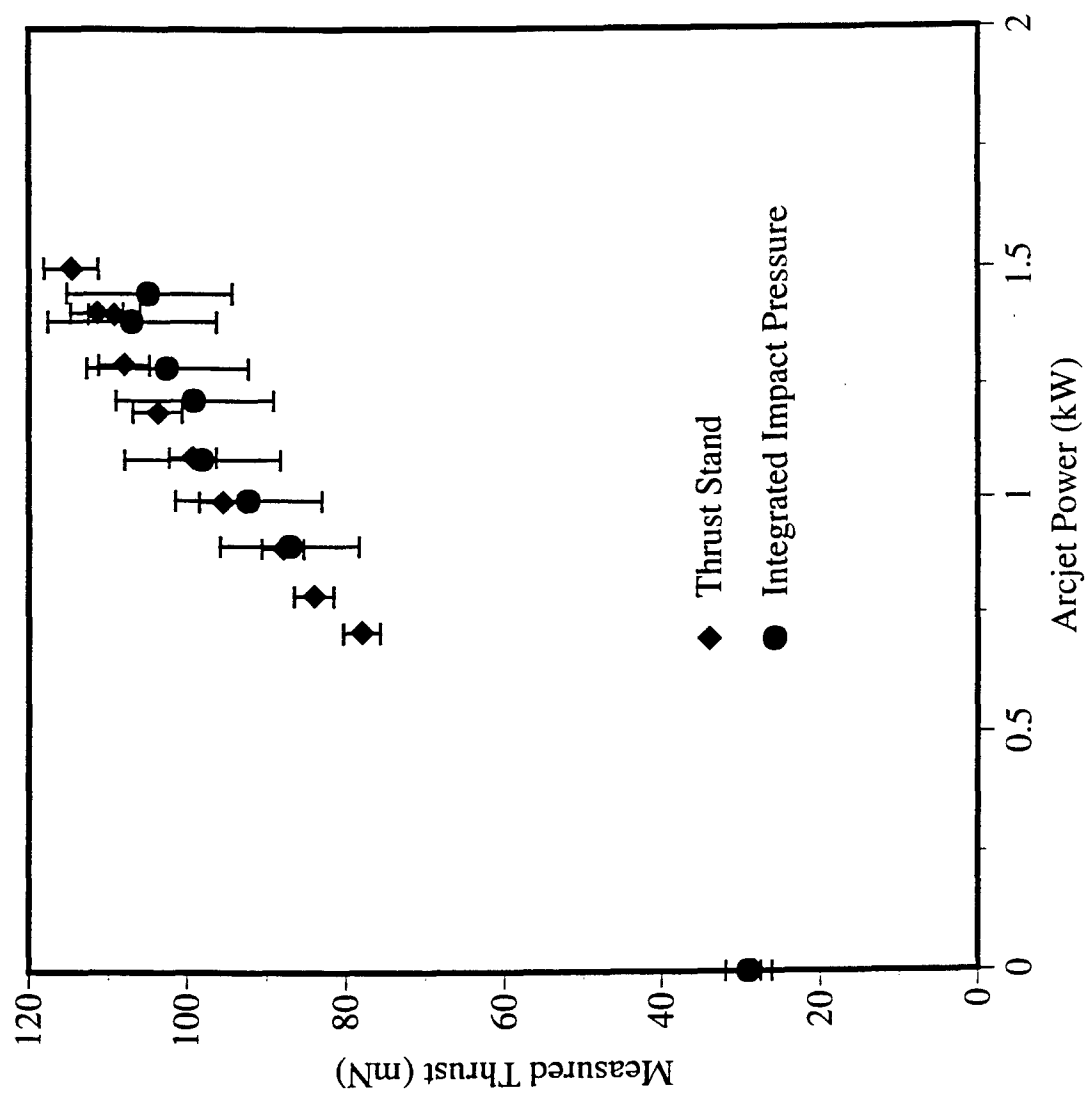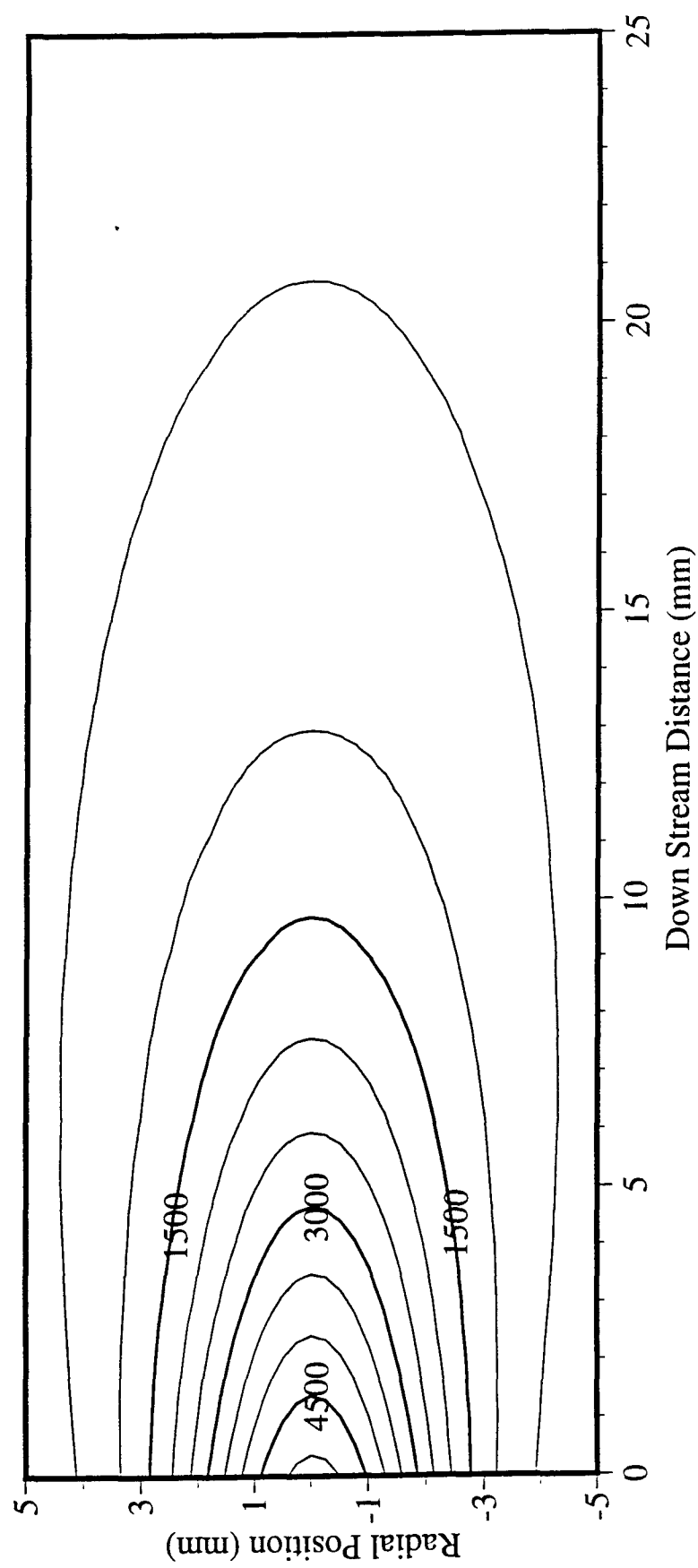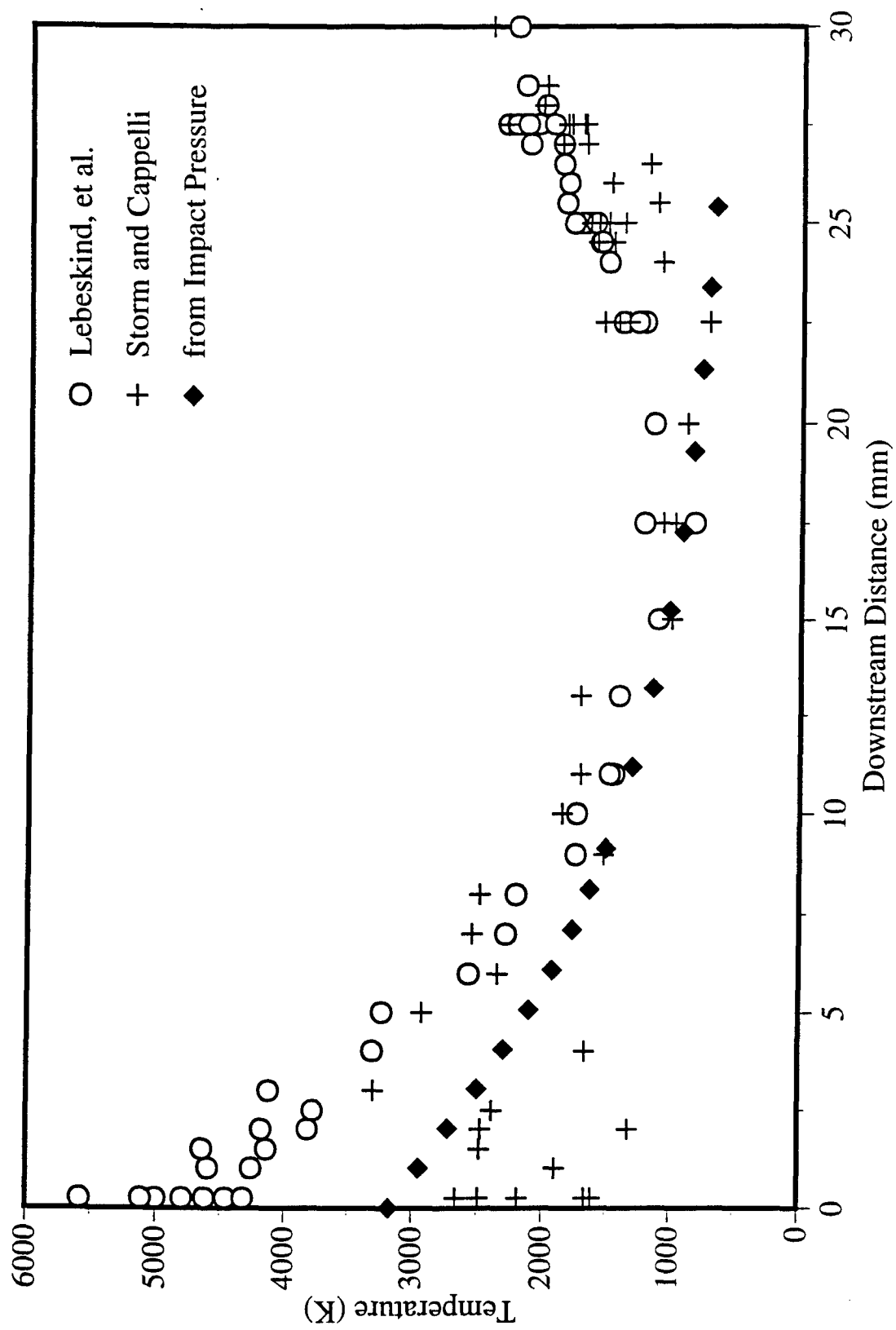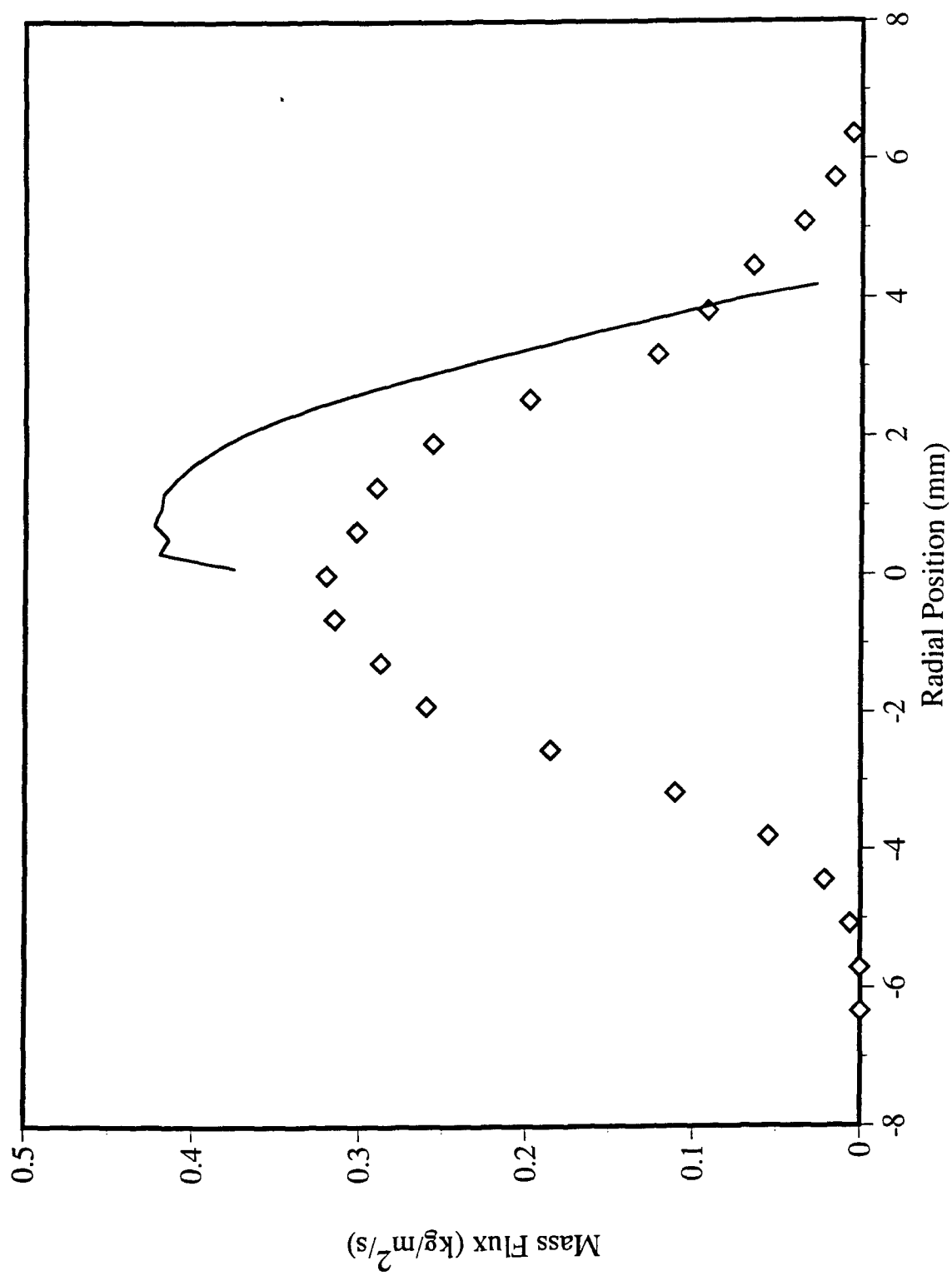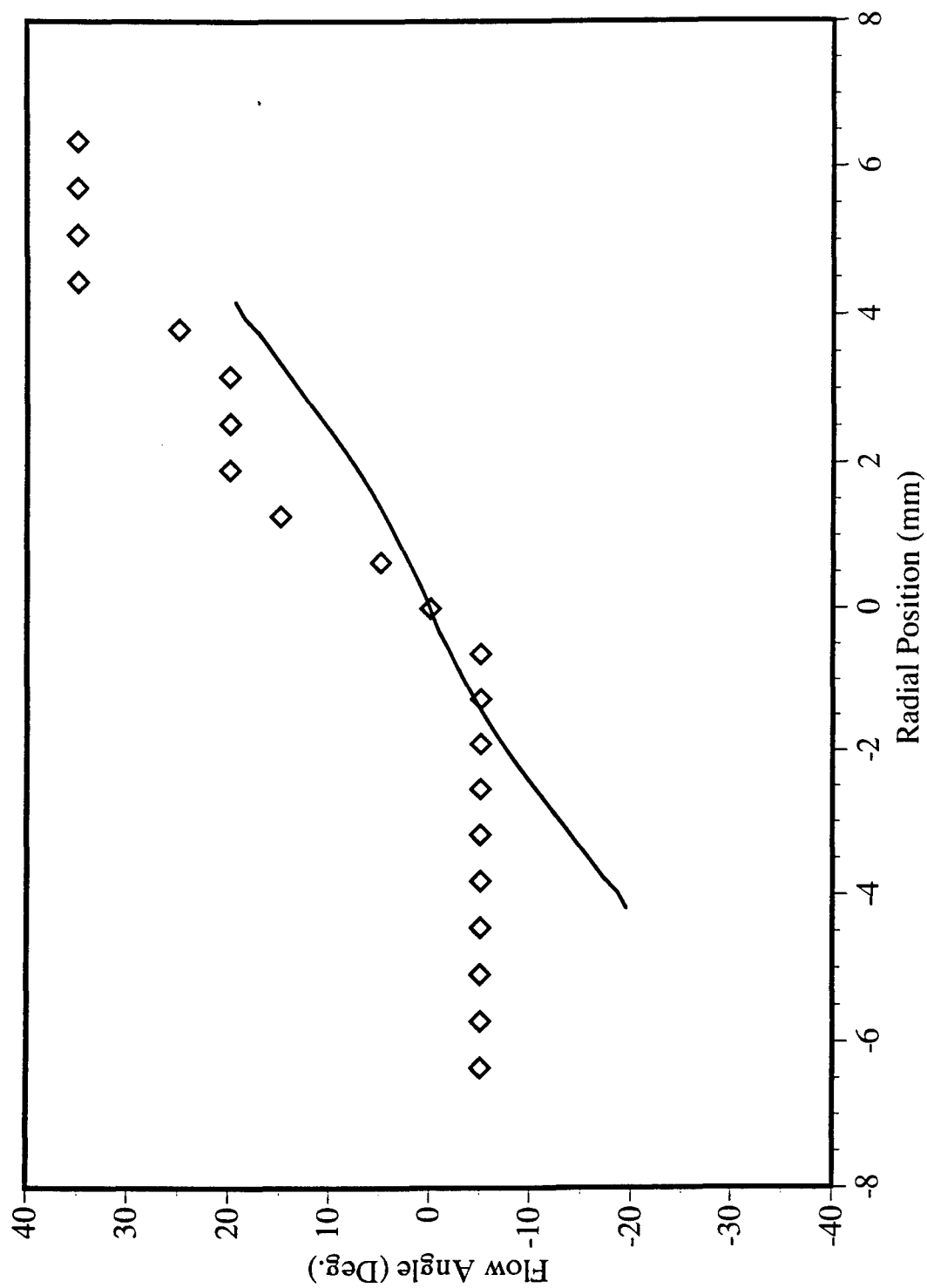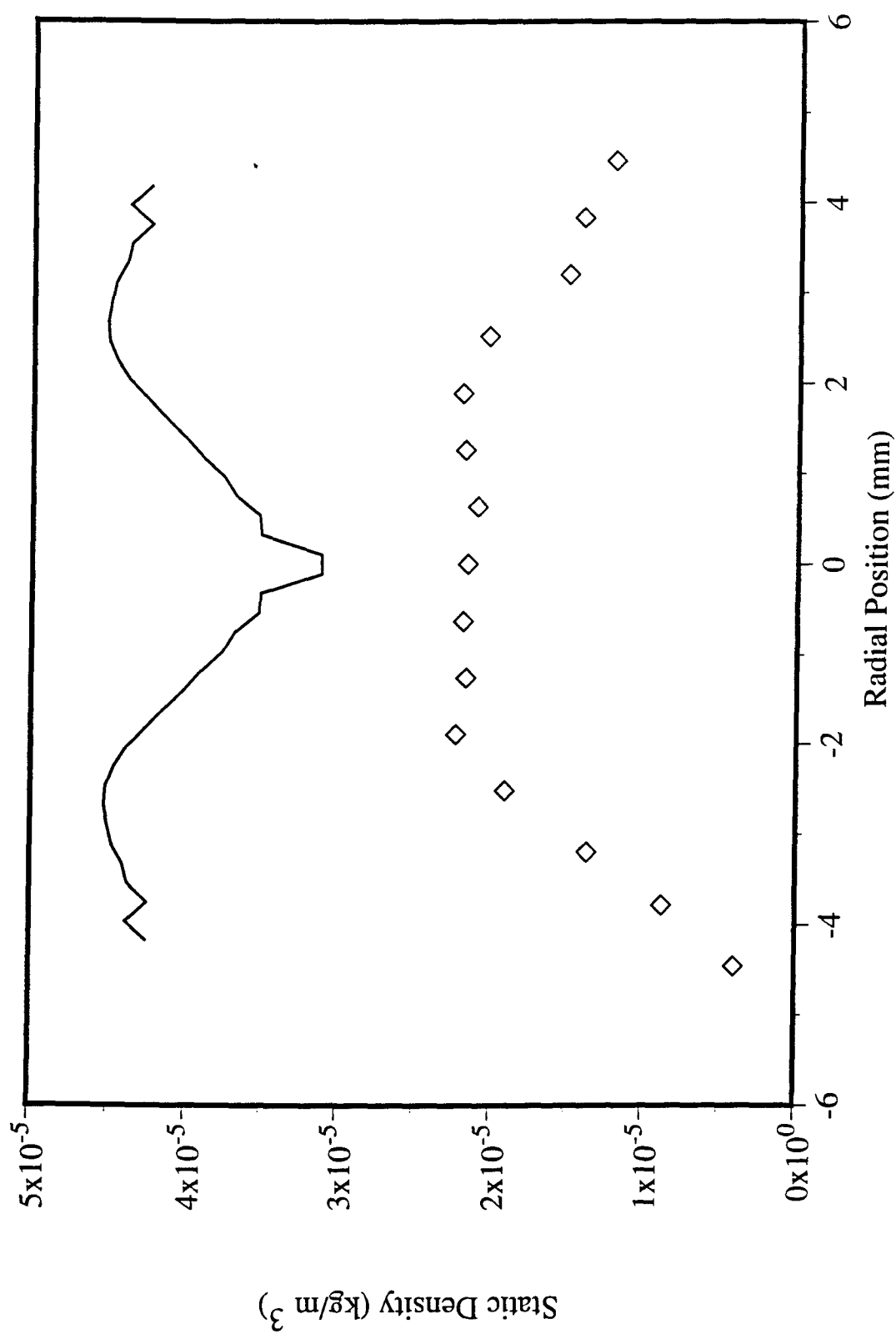Figure 11

Figure 12

Figure 13

Figure 14

Figure 15

Figure 16

Figure 17

Figure 18
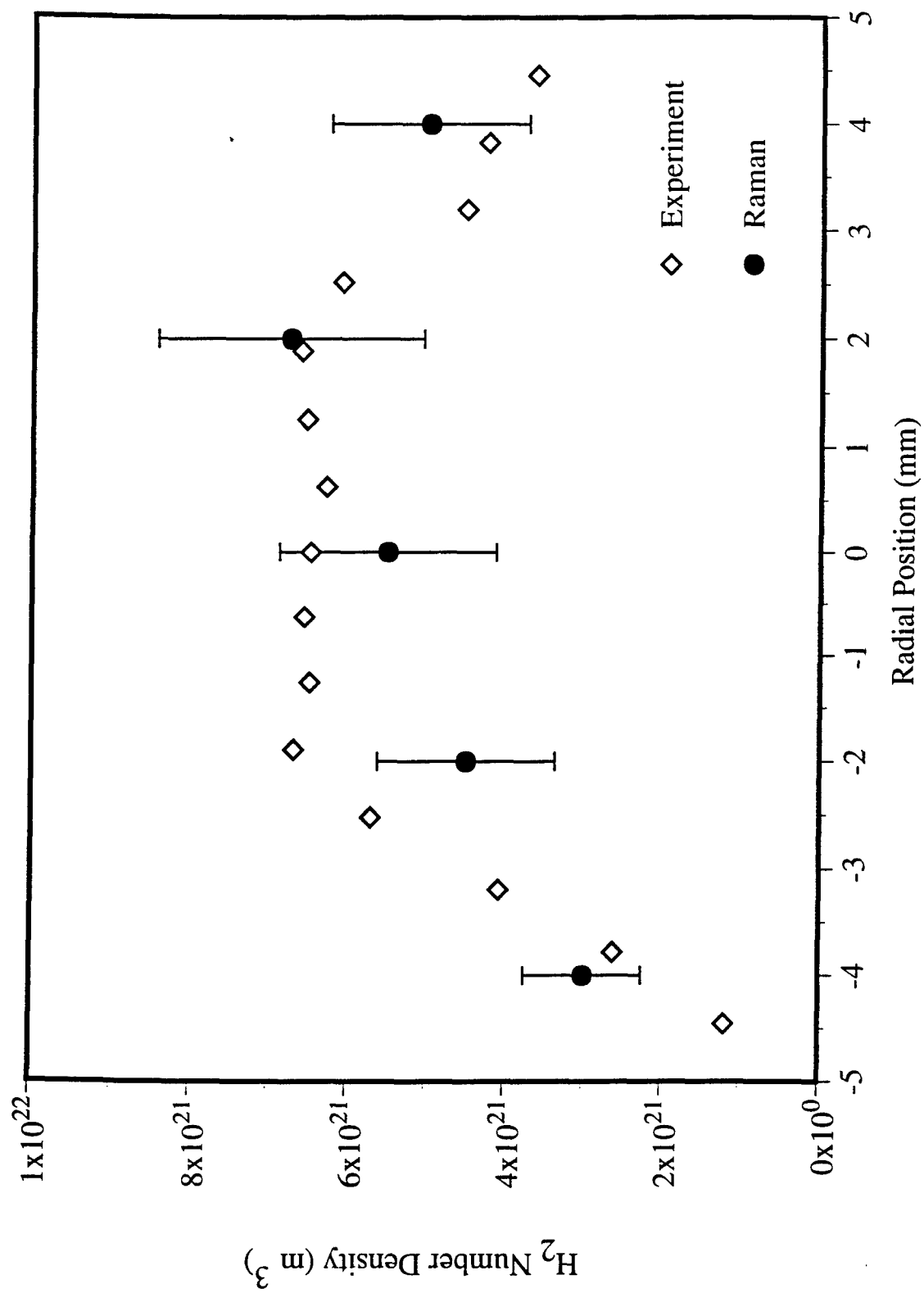
Figure 19
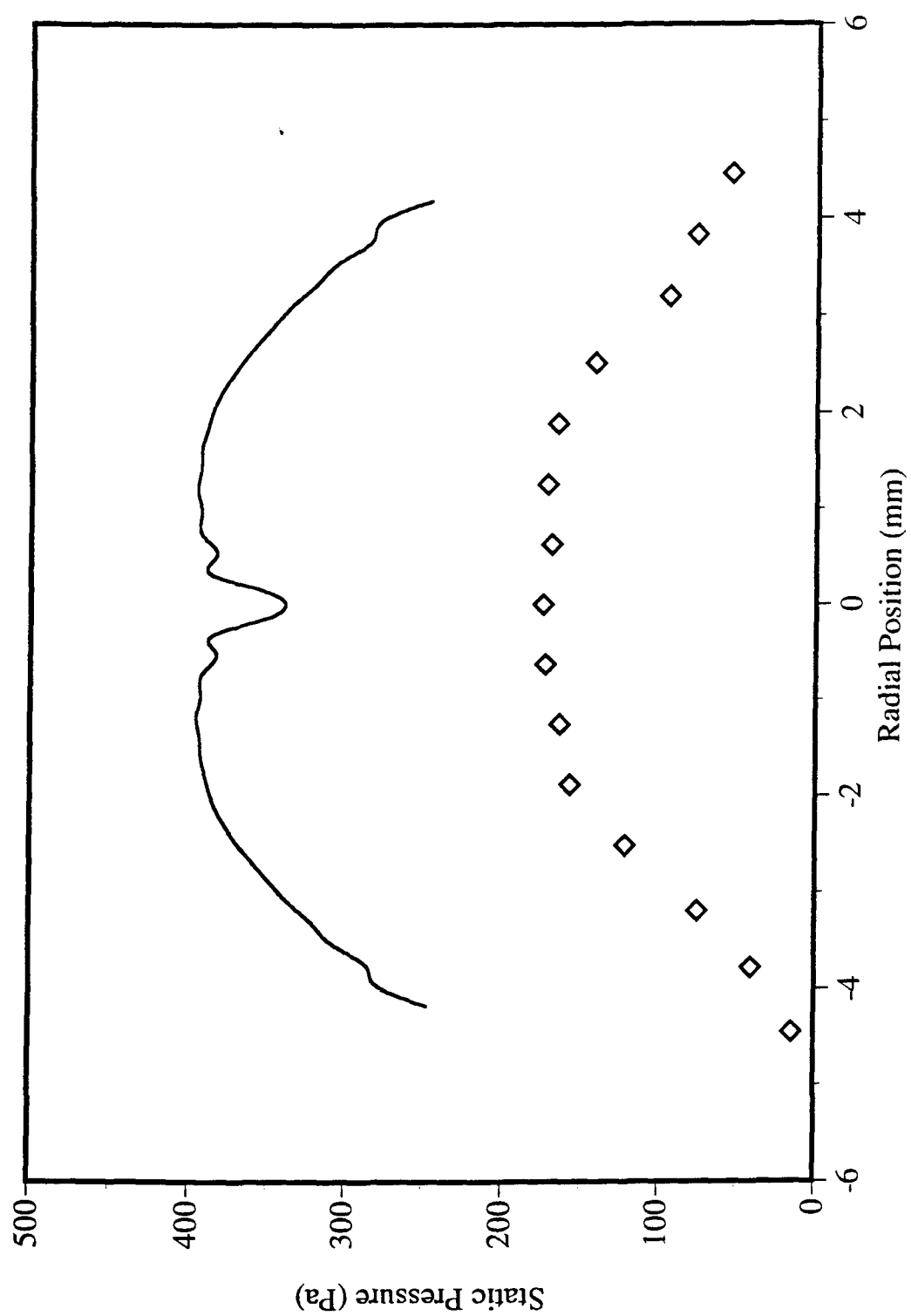
Figure 20
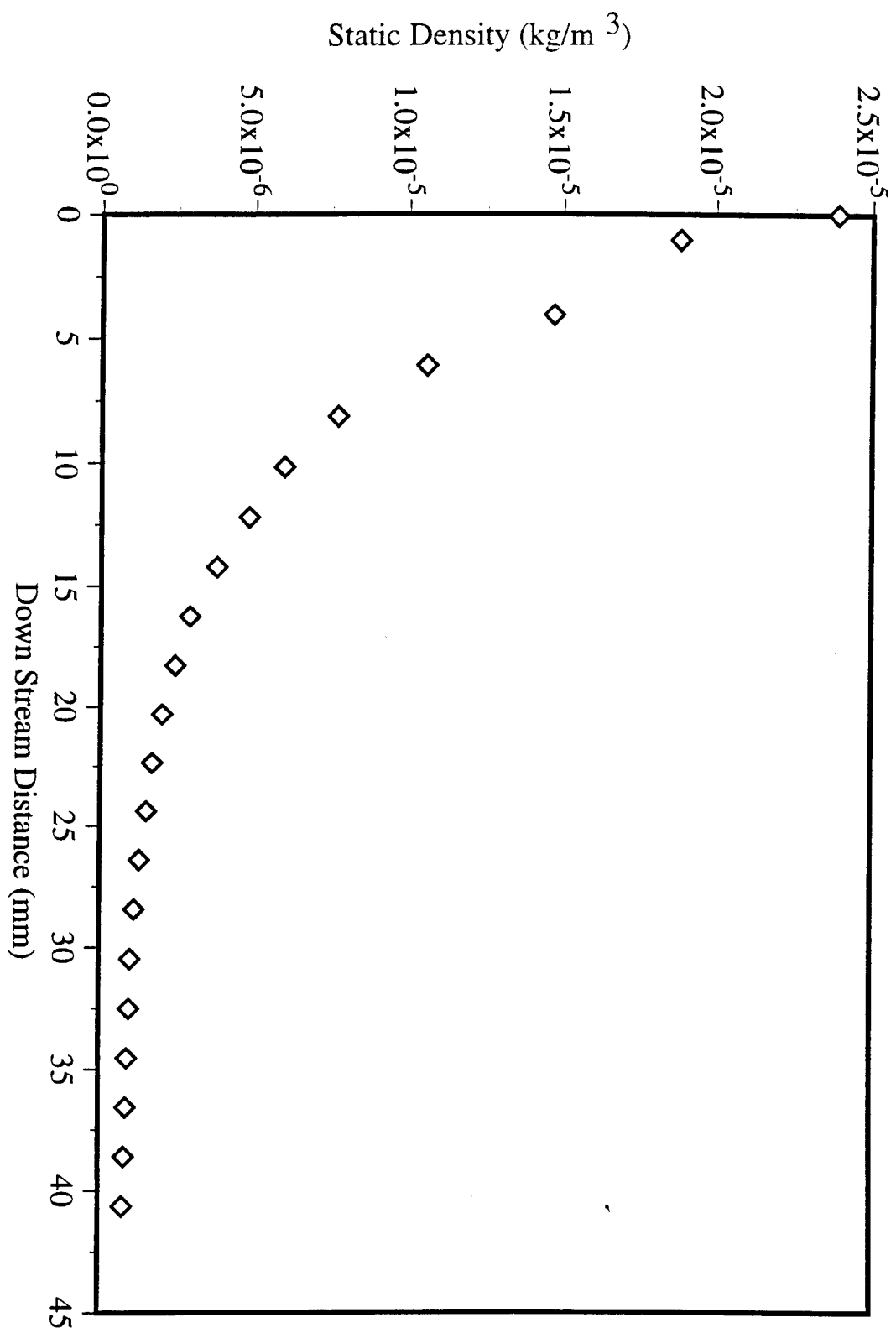
Figure 21
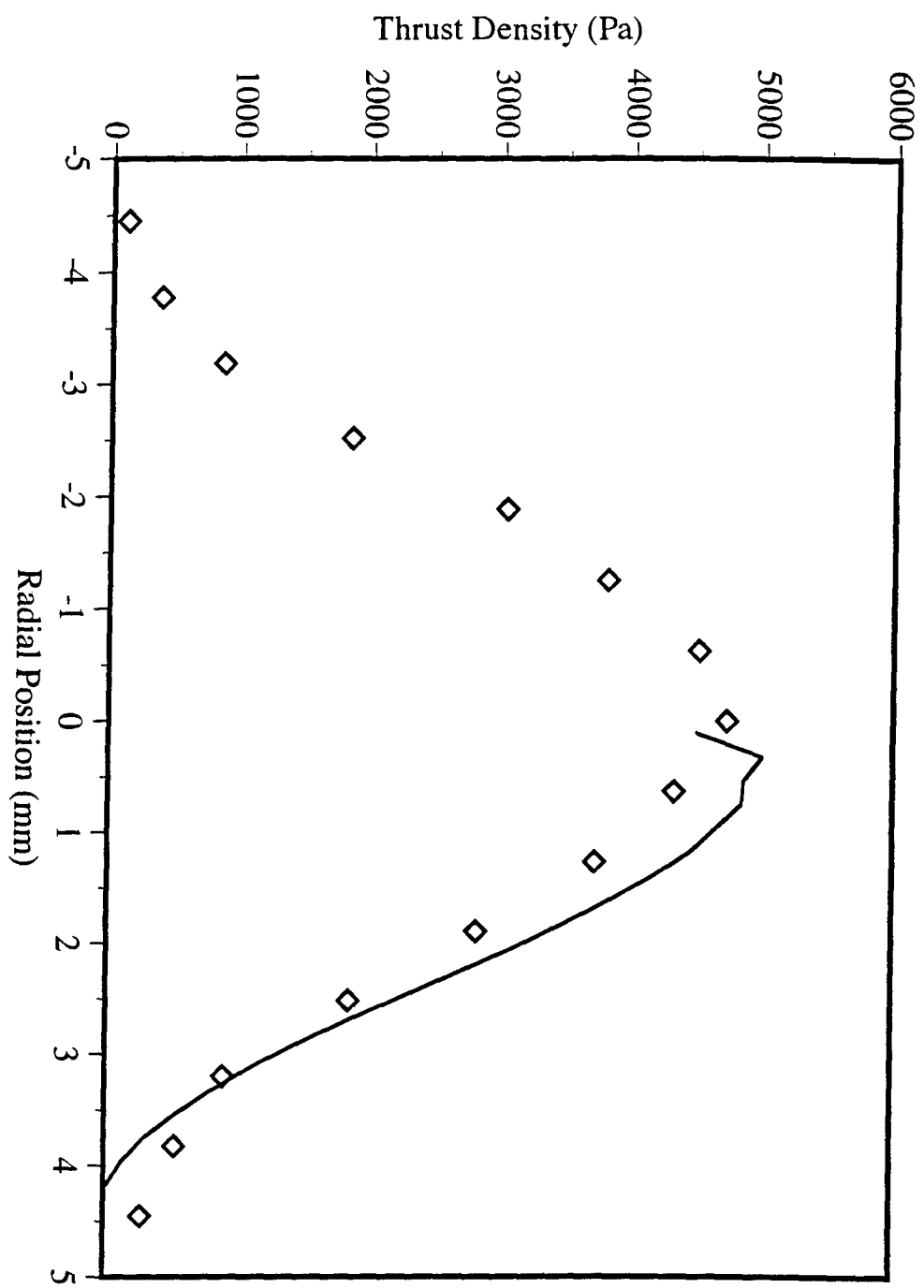
Figure 22

Pergamon

PII: S0022-4073(96)00063-5

RADIATIVE EMISSION ANALYSIS OF AN EXPANDING HYDROGEN ARC PLASMA—I. ARC REGION DIAGNOSTICS THROUGH AXIAL EMISSION

P. VICTOR STORM and MARK A. CAPPELLI†

High Temperature Gasdynamics Laboratory, Department of Mechanical Engineering,
Stanford University, Stanford, CA 94305-3032, U.S.A.

Abstract—A numerical and experimental investigation of the axial emission of 1 and 5 kW radiatively-cooled hydrogen arcjet thrusters is presented. The numerical study consists of an integration of the 1-D radiative transfer equation along the arcjet centerline to predict the axial emission spectral intensity. The complete visible spectrum is modeled, taking into account graybody thermal emission from the cathode and plasma radiation from hydrogen atoms and free electrons. A collisional–radiative model is used to determine the atomic hydrogen line emission. The modeling results suggest the feasibility of determining the cathode temperature and the arc region electron number density from the measured axial emission spectrum. Experimental measurements of the axial emission spectra were performed at several operating conditions. The cathode temperature is found to be in the neighborhood of the tungsten cathode melting point and increases with arcjet power at a constant mass flow rate, suggesting an increase in the current density at the arc attachment point. The measured arc region electron number density is also found to increase with power, confirming an increasing arc current density with arcjet power. Relatively flat radial profiles of electron number density measured in the arc indicate the importance of diffusional transport processes. Copyright © 1996 Elsevier Science Ltd

INTRODUCTION

With the successful deployment of the Telstar IV satellite in 1993, arcjet thrusters have joined the ranks of other electric propulsion thrusters presently in use on geosynchronous satellites. Having a relatively large specific impulse compared to chemical thrusters but low thrust levels, the arcjet satisfies a niche in satellite station keeping operations. The potential employment of arcjets for satellite repositioning and orbit transfer maneuvers has sparked an interest in improving arcjet performance characteristics, including specific impulse, thrust, and most importantly, thermal and thrust efficiencies. Improvements in performance of the thruster can be best achieved through numerical modeling;[1] however, benchmark experimental measurements are necessary for model verification. To date, substantial experimental work has been conducted to measure properties in the arcjet plume using electrical, optical and mass sampling techniques, and several comparisons have been made to the arcjet models.[1-3] Considerably fewer experimental investigations have been undertaken to measure plasma properties within the nozzle of the arcjet,[4] yet it is here where the plasma behavior controls the arcjet performance to a large extent.

In this study the near-cathode region of the arcjet is investigated by the spectral emission in the axial direction.[5,6] The cathode temperature and near-cathode electron number density are determined from the continuum and hydrogen Balmer-alpha line, respectively, of the measured spectrum. Although arcjet thrusters are presently designed for use with hydrazine or ammonia as the propellant, in this study hydrogen was the chosen propellant for two reasons. First, being the lightest molecule, hydrogen offers the greatest specific impulse for a given specific energy, making it a very attractive propellant for future use once storage problems have been solved. Secondly,

---

†To whom all correspondence should be addressed.

having a simple chemistry, hydrogen is considerably easier to model than polyatomic propellants, and is therefore commonly used in arcjet modeling work.

Two different arcjets, namely 1 and 5 kW radiation-cooled arcjets, are investigated. Both arcjets were designed and built at NASA Lewis Research Center as experimental prototypes. The 5 kW arcjet is shown schematically in Fig. 1. Although the 1 kW arcjet is smaller and of slightly different geometry, the arcjets are fundamentally identical. The arcjet generates thrust by acelerating the propellant through a converging–diverging nozzle. Thermal energy is supplied to the propellant by an electric discharge between the cathode and the nozzle wall downstream of the arcjet throat. The arcjet throat is also referred to as the constrictor since the electric discharge in this region is in the form of a constricted arc. A precise description of the arcjets is given below in the experimental section.

AXIAL EMISSION MODELING

The emission spectrum of a hydrogen arcjet consists of atomic and molecular hydrogen line emission, continuum plasma emission from the free electrons, thermal emission from surfaces, and atomic and ionic line emission from tungsten and thorium vaporized from the cathode. In this study, the emission spectrum emanating from the arcjet along its centerline is investigated. To simplify the modeling of the emission spectrum, the molecular hydrogen and metal vapor concentration is assumed low enough that its emission can be neglected relative to that of the atomic hydrogen and free electrons. Furthermore, the only surface which can radiate directly along the axis of the arcjet is the cathode surface. Thus emission from the plasma will be superimposed upon a background of graybody emission from the cathode.

At this point a note concerning the notation is in order. All spectral quantities are identified by the subscript λ which indicates a per unit wavelength basis. The functional dependence of non-constant quantities is given in parentheses, and where the quantity is a function of the plasma properties, such as p_H, n_e, T, T_e and so on, this is indicated by a dependence on the axial position z.

The axial emission spectrum is calculated by integrating the 1-D radiative transfer equation along the centerline of the arcjet, beginning from the tip of the cathode. In steady-state, the 1-D radiative transfer equation is[7]

$$\frac{d}{dz} I_\lambda(\lambda, z) = \epsilon_\lambda(\lambda, z) - k_\lambda(\lambda, z) I_\lambda(\lambda, z) \tag{1}$$

where I_λ is the directional spectral intensity, and ϵ_λ and k_λ are the plasma spectral volume emission and absorption coefficients respectively, which include contributions from both the atomic
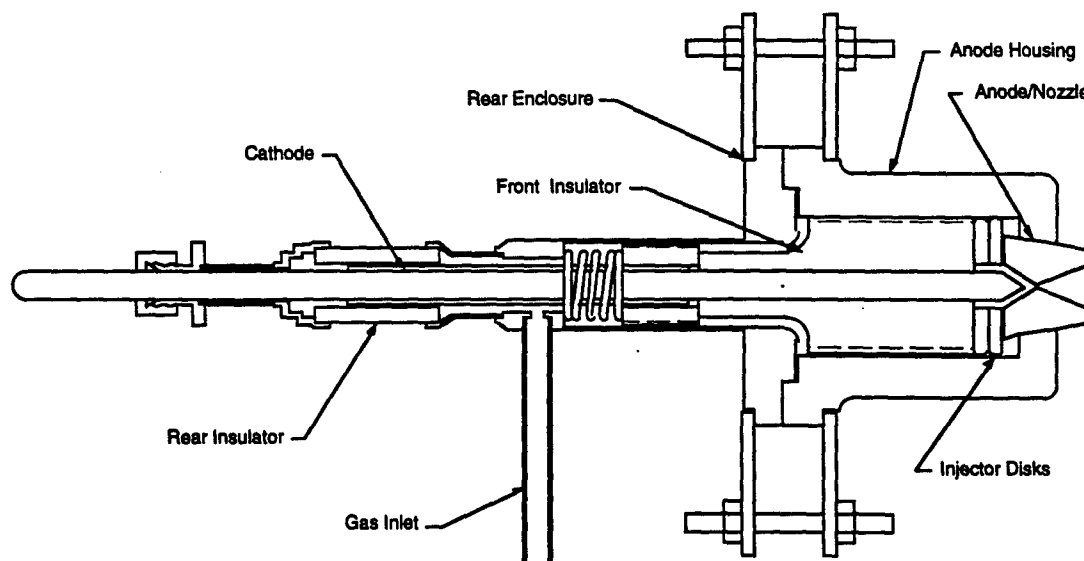
Fig. 1. Schematic drawing of the NASA Lewis Research Center (LeRC) 5 kW arcjet.

hydrogen and the free electrons, as follows

$$\epsilon_\lambda(\lambda, z) = \sum_{i,j} \epsilon_\lambda^{ji}(\lambda, z) + \epsilon_\lambda^{e}(\lambda, z)$$

$$k_\lambda(\lambda, z) = \sum_{i,j} k_\lambda^{ji}(\lambda, z) + k_\lambda^{e}(\lambda, z). \tag{2}$$

The contribution to the plasma spectral emission and absorption coefficients from the free electrons include continuum radiation from free–bound electron–ion interactions, and bremsstrahlung radiation from free–free electron–ion and electron–atom interactions. The total volume emission coefficient for these three processes is given by[8]

$$\epsilon_\lambda^{e}(\lambda, z) = \epsilon_\lambda^{fb,ei}(\lambda, z) + \epsilon_\lambda^{ff,ei}(\lambda, z) + \epsilon_\lambda^{ff,ea}(\lambda, z) \tag{3}$$

where

$$\epsilon_\lambda^{fb,ei} = C_1 \frac{n_e^2}{\lambda^2 \sqrt{T_e}} \frac{g_1^+}{Q^+} \zeta^{fb}(\lambda, T_e)[1 - \exp(-hc/\lambda k T_e)] \tag{4a}$$

$$\epsilon_\lambda^{ff,ei} = C_1 \frac{n_e^2}{\lambda^2 \sqrt{T_e}} \zeta^{ff}(\lambda, T_e) \exp(-hc/\lambda k T_e) \tag{4b}$$

and

$$\epsilon_\lambda^{ff,ea} = C_2 \frac{n_e n_a}{\lambda^2} T_e^{3/2} [(1 + hc/\lambda k T_e)^2 + 1]Q^{el}(T_e) \exp(-hc/\lambda k T_e). \tag{4c}$$

In these expressions g_1^+ and Q^+ are the ion ground state degeneracy and partition function respectively, Q^{el} is the elastic collision cross section, and ζ^{fb} and ζ^{ff} are the Biberman factors, which are unity for atomic hydrogen. The constants in SI units are $C_1 = 1.63 \times 10^{-43}$ W m^4 K$^{1/2}$/sr and $C_2 = 1.026 \times 10^{-34}$ W m^2 K$^{-3/2}$/sr. The corresponding spectral absorption coefficients for these processes are determined from the principle of detailed balance.[9]

The atomic hydrogen contribution involves line radiation from transitions between upper state j and lower state i, for which[8]

$$\epsilon_\lambda^{ji}(\lambda, z) = \frac{hc}{4\pi\lambda} n_j(z)A_{ji}\Phi_\lambda^{ji}(\lambda, z)$$

$$k_\lambda^{ji}(\lambda, z) = \frac{hc}{\lambda} [n_i(z)B_\lambda^{ij} - n_j(z)B_\lambda^{ji}]\Phi_\lambda^{ji}(\lambda, z) \tag{5}$$

where A_{ji}, B_λ^{ij} and B_λ^{ji} are the Einstein coefficients and Φ_λ^{ji} is the spectral lineshape function, subject to the normalization condition

$$\int_\lambda \Phi_\lambda^{ji}(\lambda, z)\, d\lambda = 1. \tag{6}$$

For an equilibrium plasma, the number densities n_i and n_j are determined from a Boltzmann distribution of the atomic state populations. However, since the plasma within the arcjet is not in equilibrium, the number densities of the atomic states are found by solving a set of coupled rate equations in a collisional–radiative model.[10] These equations consist of the steady-state continuity equation for the excited states,

$$\nabla \cdot n_m u_m = \left[\frac{dn_m}{dt}\right]_{CR} \tag{7}$$
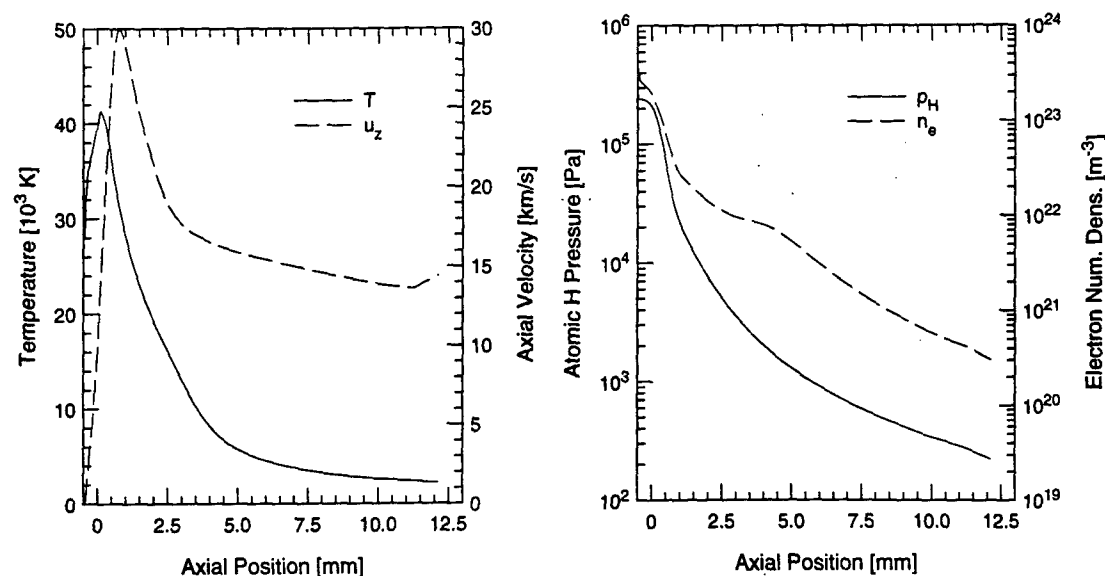
Fig. 2. Axial properties T, u_z, p_H and n_e on the NASA LeRC 1 kW arcjet centerline from a one-fluid MHD code (Butler et al, Ref. 14) at a specific energy of 115 MJ/kg.

for $m = 2 .. l$, where l is the number of levels, and the equation of state,

$$p_H = \sum_m n_m kT \qquad (8)$$

where p_H is the partial pressure of atomic hydrogen. (Aside: in this paper the symbol m is used to indicate principal quantum number, while the symbol n is reserved for number density.) The production term on the right-hand side of Eq. (7) is the net generation of excited state species by inelastic collisional and radiative processes. These processes include electron collisional excitation, de-excitation, ionization and three-body recombination, radiative recombination and spontaneous emission. Photoionization and stimulated emission and absorption have been neglected. In the stationary-state approximation, only the ground atomic state and ion have non-negligible convection terms; hence, the convective flux term for each excited state is zero, and assuming quasi-neutrality, Eq. (7) can be written in full as

$$0 = n_e \sum_{j \neq m} n_j K_{jm} - n_e n_m \sum_{j \neq m} K_{mj} - n_e n_m K_{mc} + n_e^3 \beta_{cm}^{(3)} + n_e^2 \beta_{cm}^{(r)} + \sum_{j > m} n_j \gamma_{jm} A_{jm} - n_m \sum_{j < m} \gamma_{mj} A_{mj} \qquad (9)$$

where K_{mj} and K_{mc} are the electron collisional excitation and ionization rate coefficients, $\beta_{cm}^{(3)}$ and $\beta_{cm}^{(r)}$ are the electron collisional three-body and radiative recombination rate coefficients, and γ_{jm} is an escape factor for radiation between states j and m.[11] The escape factors are taken to be unity except for those corresponding to transitions terminating on the ground state, γ_{j1}, which accounts for the possibility of resonance radiation trapping. The present model uses the semi-empirical approximations for K_{mj} K_{mc}, and $\beta_{cm}^{(r)}$ from Johnson,[12] while $\beta_{cm}^{(3)}$ is determined from K_{mc} by detailed balance.[9] The spontaneous emission coefficients, A_{mj}, are obtained from the literature.[13] The coupled set of equations are solved for the atomic state populations given the kinetic temperatures, the total atomic hydrogen pressure and electron number density. These properties, shown in Fig. 2 as a function of axial position for the 1 kW arcjet, were obtained from a single-fluid MHD arcjet model developed by Butler et al.[14] This arcjet model is described in detail in Ref. 1. As a single fluid model, a unique kinetic temperature was used for both the electrons and heavy particles.

The appropriate number of levels to be used in the collisional–radiative model is determined from Debye shielding of the atoms.[7] Ideally, the number of levels is calculated by assuming that a "bound" electron at 1 Debye length from the nucleus is essentially free. Thus, only the levels within a Debye length of the nucleus should be considered bound levels and accounted for in the model.

Furthermore, the ionization energy should be reduced to the energy of the first "unbound" state beyond the Debye length. However, incorporating the Debye cutoff and ionization energy reduction complicates the model significantly since the Debye length is a function of axial position in the plasma. The high electron density in the arc region results in only a few bound levels, whereas several dozen levels would be required near the exit plane. To avoid this extra complexity in the calculations, we have included in the collisional–radiative model only the ion state and the lowest nine atomic states of hydrogen, and no ionization energy reduction. This was assumed to be sufficiently accurate since the model is being used to calculate hydrogen line intensities for only the first four Balmer series lines, which requires up to the $m = 6$ excited state number density. To test the accuracy of this assumption the excited state number densities were determined by incorporating the Debye cutoff and the ionization energy reduction into the collisional–radiative model and compared to the fixed-level model. Using the plasma properties at several different axial positions, differences in the excited state number densities of only a few percent were observed. The discrepancy was larger for the higher energy levels than the lower ones, and also larger at the exit plane of the arcjet than in the arc region. Since most of the plasma emission originates in the arc region and since the primary interest is in the H_α line, this assumption was justified and the simpler model was used.

To test the validity of the stationary-state approximation, the convective flux terms in Eq. (7) were included but simplified to axial gradients only based on a 1-D approximation. With this simplification and no species diffusion velocity, the continuity equation for the excited states becomes

$$n_m \frac{du_z}{dz} + u_z \frac{dn_m}{dz} \approx \left[\frac{dn_m}{dt} \right]_{CR}. \tag{10}$$

The axial velocities were taken from the model of Butler et al.[14] and are shown in Fig. 2. The excited state number densities were determined at several axial positions with and without this simplified convective flux included in the collisional–radiative model and no difference was observed, indicating that convection does not play a significant role in determining the distribution of the excited state atoms.

The spectral lineshape function, Φ_λ^{ij}, is determined by the plasma broadening mechanisms, of which Stark broadening is dominant in the arc region of the plasma. Although the Stark lineshape is strictly non-Lorentzian in shape, a Lorentzian lineshape is nevertheless assumed in Eq. (5) for simplicity. This assumption is quite inaccurate for most Balmer series lines of hydrogen, but is reasonably well suited for H_α.[15] Doppler and other line broadening mechanisms are neglected in the model. This assumption may lead to a small inaccuracy in the lineshape since Doppler broadening dominates near the exit plane of the arcjet; however, it is certainly justified in the arc region where Stark broadening is significantly larger than Doppler broadening, and it is this region that is of particular interest in this study. Typical values of Stark and Doppler FWHM in the arc region are 1.0 and 0.1 nm respectively. Other broadening mechanisms are significantly smaller. By comparison, the lifetime broadening of H_α is 1.3×10^{-4} nm and pressure broadening of H_α has a maximum value of approximately 2×10^{-3} nm near the cathode. For the higher Balmer lines, the dominance of the Stark broadening mechanism is even more marked.[15]

Having obtained the total volume emission and absorption coefficients as a function of wavelength and axial position, Eq. (1) is numerically integrated along the centerline of the arcjet. The graybody emission intensity from the cathode is used as the initial intensity condition. The cathode emissivity is taken to be 0.4 and the cathode temperature is assumed to be near the melting point of tungsten, 3700 K, but varied as an input parameter to the model. As the radiation field is integrated along the arcjet axis, the Doppler shift is taken into account since the radiation is being emitted and absorbed by the plasma with a varying axially velocity.

Finally, since a rate equation is not written for the ground state number density, no provision is made for photoionization from the ground state. However, this process may be important particularly in the expansion region of the nozzle where collisional processes are less predominant than in the hot arc region. To evaluate the relative significance of photoionization, a photoionization rate from the ground state was determined as a function of axial position based

on the number densities calculated using the collisional–radiative model without photoionization. To estimate an upper limit of the photoionization rate, the radiation field was taken to be a blackbody field from the high temperature arc region. In other words, the plasma was assumed to be optically thick in the arc region giving rise to the most intense equilibrium radiation field possible for the given plasma temperature in the arc, but optically thin between the arc and the region where the photoionization is taking place so that no loss in the radiant intensity occurs due to absorption by the plasma. The calculated photoionization rate is compared to the electron collisional ionization rate and the three-body and radiative recombination rates between the ground state and the continuum in Fig. 3 for the 1 kW arcjet. While the electron collisional ionization rate falls off dramatically in the expansion region of the arcjet, the photoionization rate remains quite large and, in fact, is greater than the recombination rates at the exit plane. However, this upper limit estimation is probably considerably larger than the true photoionization rate. In the other extreme, an estimate of the lower limit can be made by assuming the plasma to be optically thick everywhere and calculating the photoionization rate using a blackbody intensity at the local plasma temperature. This limit yields rates which are as much as 12 orders of magnitude smaller at the exit plane than the upper limit. The true photoionization rate will lie somewhere between these limits; therefore, it is difficult to judge the importance of this process in the collisional–radiative model.

MODELING RESULTS AND DISCUSSION

Before examining the axial emission spectrum predicted by the model, it is first necessary to determine the effect of resonance radiation trapping. Figure 4 shows the number densities of the ground state and the first three excited states of atomic hydrogen calculated from the model as a function of axial position along the 1 kW arcjet centerline. The axial position origin is located at the arcjet throat. Negative axial position corresponds to the converging near-cathode region, while the expanding nozzle flow is designated in the positive axial direction. Figure 4(a) shows the results with all radiative transitions optically thin, while Fig. 4(b) shows the results for fully trapped resonance transitions. The only significant difference in the number densities appears in the expanding plasma region for the $m = 2$ excited state. In this region, where recombination is
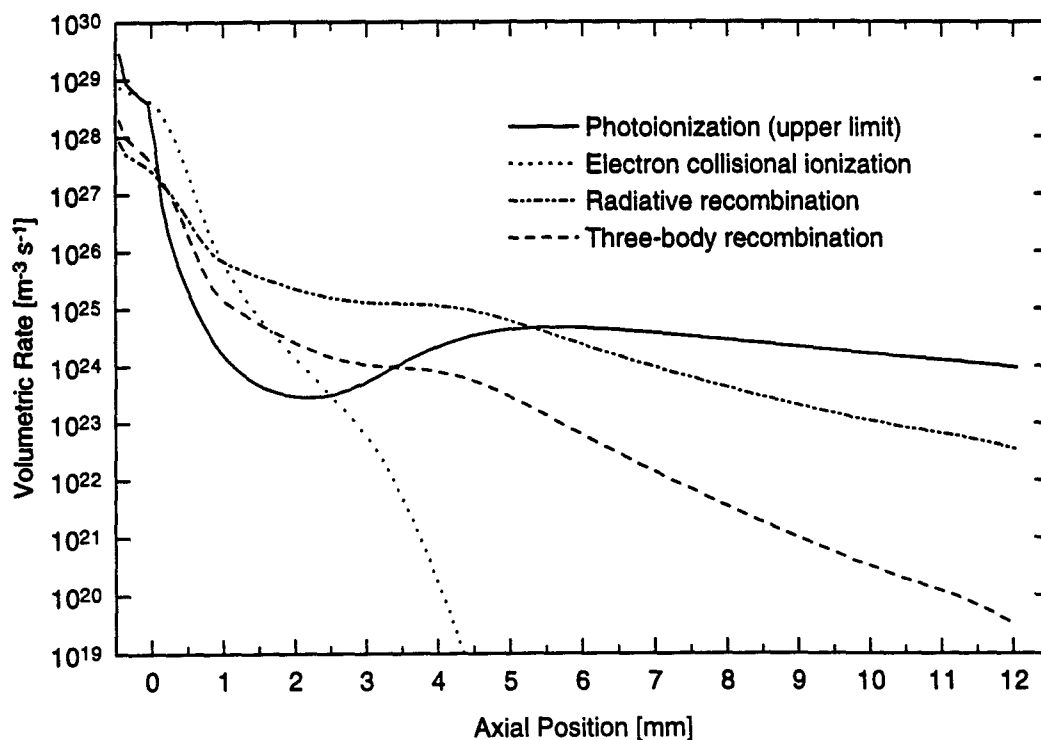
Fig. 3. A comparison between the ionization and recombination rates along the axis of the 1 kW arcjet.
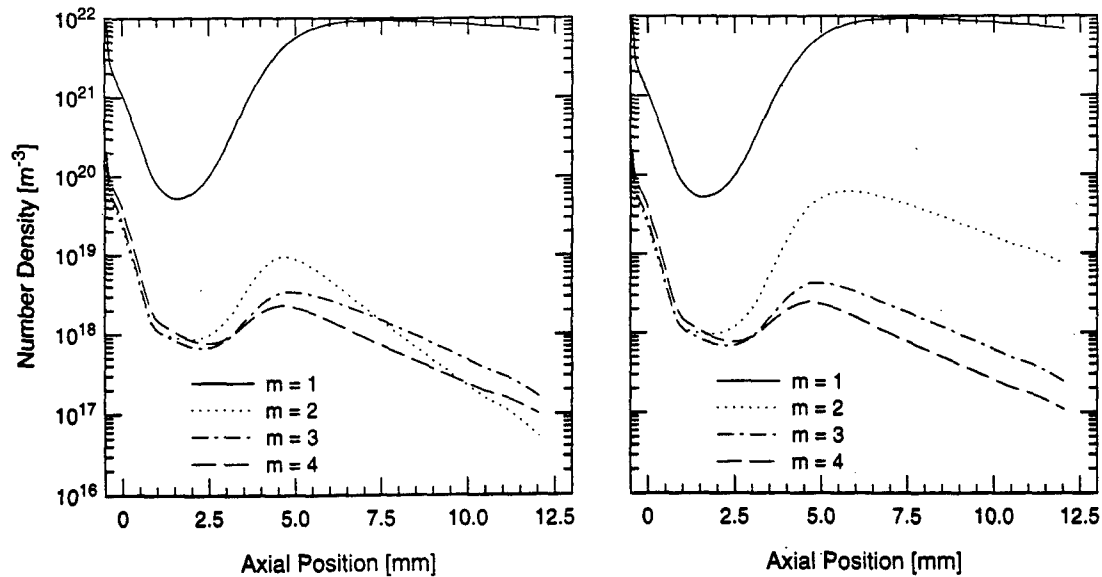
Fig. 4. Calculated axial variation of the number densities of the lowest four atomic hydrogen states in the 1 kW arcjet with (a) optically thin plasma, and (b) fully trapped resonance radiation.

occurring, the trapping of the resonance radiation results in an effective barrier to transitions to the ground state and hence a buildup in the $m = 2$ number density. The other excited states are not significantly affected since they are able to radiate to lower states. As would be expected, the radiation trapping has no effect in the near-cathode region of the flow where the plasma is ionizing. The effect of this population buildup in the $m = 2$ state on the axial emission spectrum is shown in Fig. 5. Here the simulated H_α lineshape at the centerline exit plane is shown for different values of the resonance radiation escape factor from no trapping to fully trapped. The higher Balmer lines display identical trends. The increased $m = 2$ population associated with the trapped resonance radiation results in significant reabsorption of the H_α linecenter radiation. Relative to the broad emission background lineshape, this reabsorption feature is both narrower, due to the lower
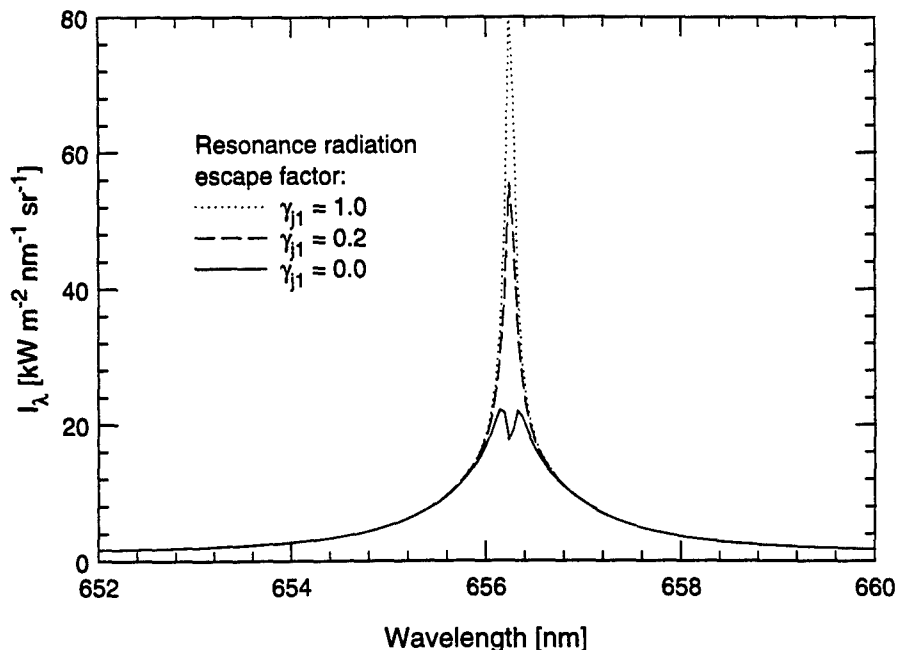
Fig. 5. Simulated H_α axial emission lineshape at the exit plane centerline of the 1 kW arcjet for different values of the resonance radiation escape factor.
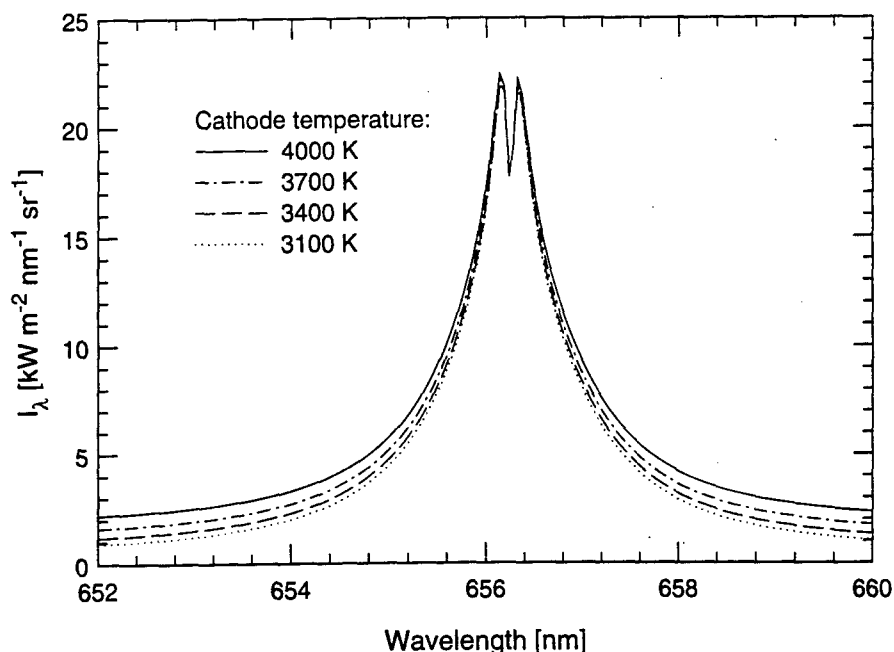
Fig. 6. Simulated H_α axial emission lineshape at the exit plane centerline of the 1 kW arcjet for different values of the cathode temperature.

electron number density in the expansion region, and shifted off-center, due to the lower axial velocity. The shift, however, is small and nearly imperceptible. In the case of optically thin radiation, the lower $m = 2$ number density results in further emission in the expansion region rather than reabsorption, and this emission "spike" is similarly narrowed and shifted. A comparison of these lineshapes with the measured H_α spectrum indicates that the resonance radiation is very nearly fully trapped. Therefore, all of the following calculations assume fully trapped resonance radiation.

Integration of the radiant intensity beyond the exit plane was performed to determine the effect of the plume on the emission spectrum. In a worst case scenario, plume properties were taken to be the properties at the exit plane centerline. With trapped resonance radiation the linecenter reabsorption was essentially complete by the exit plane and little change in the spectrum was seen through the plume. Furthermore, since the plume temperature and electron number density actually drop in the axial direction, the contribution to the emission spectrum from the plume is considered negligible.

The most remarkable feature of Fig. 5 can be found not in the linecenter intensities, but in the wings of the lineshapes. It appears that the linewings are independent of both the resonance radiation escape factor and the axial position in the expansion region. This is to be expected since the broad emission lineshape originates from the ionizing near-cathode region of the flow. It was shown in numerous simulations that the lineshape wings are entirely determined by the plasma properties within approximately 1 mm of the cathode. In this region the electron number density is considerable and the lineshapes are overwhelmingly Stark broadened. The usefulness of this observation as a diagnostic tool lies in the fact that a lineshape fit to the wings of the axial emission spectrum permits the determination of the electron number density in the arc or near-cathode region of the arcjet, independent of other plasma properties in the arc or downstream of the throat. It must be kept in mind, however, that this measurement will be a line-of-sight average in this arc region, but strongly weighted towards the cathode where the number density of emitters is the greatest, as demonstrated in Fig. 4.

Since one of the objectives of this study is to determine the cathode temperature, it is instructive to investigate the dependence of the axial emission on cathode temperature. Figure 6 shows the simulated Balmer alpha emission spectrum for different values of the cathode temperature. The cathode emissivity was fixed at 0.4 and the resonance radiation was assumed optically trapped. As would be expected, the linecenter reabsorption from the expansion flow region is independent of

the cathode temperature, whereas the baseline, determined primarily from the cathode thermal emission, is very sensitive to the cathode temperature.

The complete simulated axial emission spectrum of the 1 kW arcjet in the range of 400–700 nm is shown in Fig. 7. The contributions to the complete spectrum from the cathode emission alone and from cathode emission and continuum radiation by the free electrons are indicated separately. The effect of the free electron radiation is to increase the broadband intensity above that of the cathode emission and thereby essentially obstruct the view of the cathode. Fortunately, however, the continuum radiation is a small fraction of the cathode emission at long wavelengths. A spectral window exists at wavelengths longer than approximately 550 nm, but outside of interference from H_α, for viewing the cathode and obtaining the cathode temperature. This region of the spectrum was therefore used to measure the cathode temperature by fitting the simulated spectrum to the measured spectrum. The cathode temperature was a parameter of the model which could be adjusted until a good fit is obtained. Since the continuum radiation is small and accounted for in the model, the precision of the cathode temperature measurements is primarily limited by the uncertainty in the emissivity of tungsten near its melting point.

The four lowest hydrogen Balmer lines are clearly visible in the simulated spectrum of Fig. 7. These lines are broadened substantially by the high electron number density in the arc region. The integrated line intensities have been calculated and are shown as a function of the transition upper state energy in the Boltzmann plot of Fig. 8. The evident non-linearity may be a result of non-equilibrium in the ionizing arc region or an effect of radiation transfer on the spectral lines. To determine which is the case, the Boltzmann plot is compared to that of an optically-thin, uniform plasma with properties typical of the near-cathode region. Two cases, an LTE plasma and an ionizing plasma, both at $T = 35,000$ K and $p_H = 2 \times 10^5$ Pa, were considered. For the ionizing plasma, the electron number density was taken to be one order of magnitude lower than that which is necessary for the LTE plasma. The excited state number densites were determined using the collisional–radiative model and the integrated line intensities were then calculated using[7]

$$I^{ji} = \int F_\lambda^{ji}(\lambda)\, \mathrm{d}\lambda = \frac{hc}{4\pi\lambda^{ji}}\, n_j A_{ji} l \qquad (11)$$
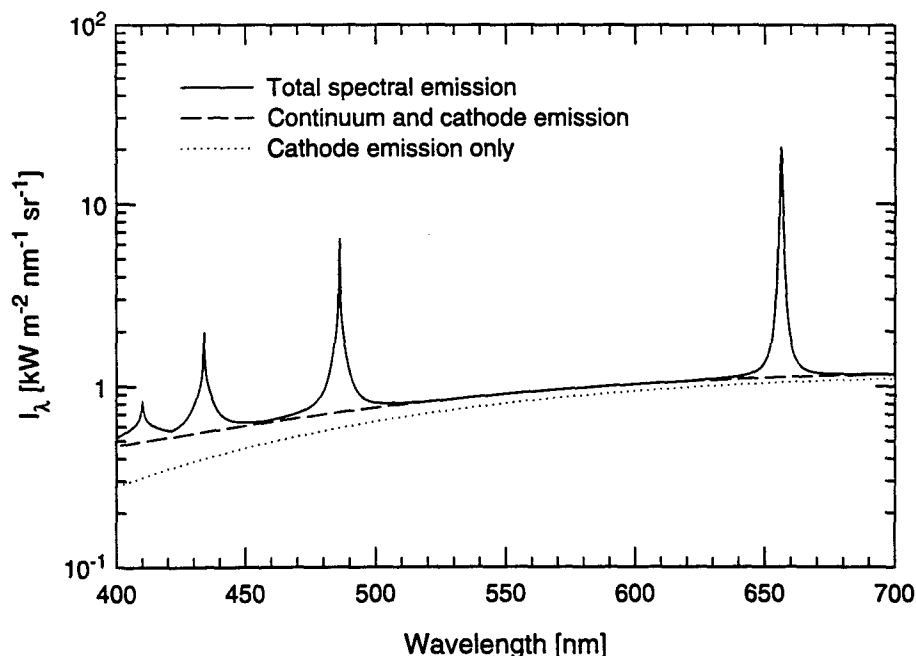

Fig. 7. Simulated axial emission spectrum at the exit plane centerline of the 1 kW arcjet at the operating condition of 1.5 kW and 14.1 mg/sec of hydrogen. The spectrum shows the total axial emission as well as the components due to only thermal emission from the cathode and continuum electron plasma emission plus cathode emission.
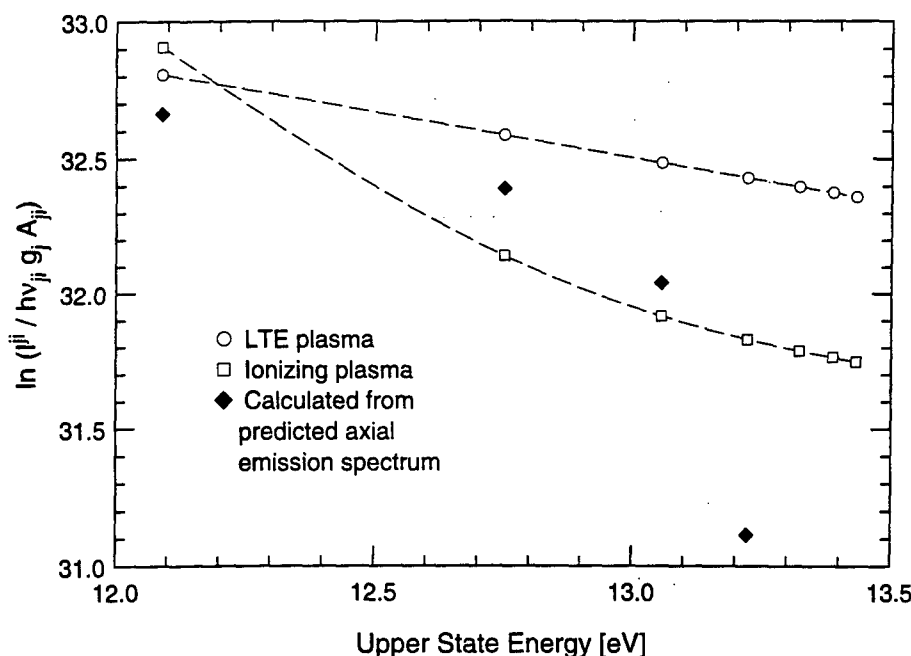
Fig. 8. Boltzmann plot of the simulated axial emission spectrum of Fig. 7. Also shown are Boltzmann plots of an LTE and ionizing plasma at typical conditions in the near-cathode region.

where the effective length, l, was taken to be 1 mm. Since the Boltzmann plot of the predicted emission spectrum displays a trend which is unlike those of the LTE and ionizing plasmas, it is believed that the radiation transfer has a significant effect on the total line intensities. This result is not surprising in light of the discussion concerning radiation trapping. Consequently, radiation transfer effects render the Boltzmann plot of the axial emission ineffective in determining the arc temperature.

EXPERIMENTAL DESCRIPTION

Experiments were undertaken to measure the axial emission spectrum from 1 and 5 kW laboratory type arcjet thrusters. The 5 kW arcjet is shown in cross-section in Fig. 1. Each arcjet consists of a tungsten nozzle having a 20 deg half-angle diverging section and an exit plane area ratio of 225. The tip of the 2% thoriated tungsten cathode sits a short distance upstream of the nozzle constrictor. The constrictor diameter and cathode gap dimensions are respectively 0.64 and 0.45 mm for the 1 kW arcjet, and 0.76 and 0.9 mm for the 5 kW arcjet. The experiments were performed in two different laboratories which necessitated some minor differences in the experimental setup; however, the general set-up can be represented schematically in Fig. 9. For the 1 kW class thruster the vacuum facility consisted of a 1.09 × 0.56 m dia stainless steel chamber maintained at a background pressure of 0.4 torr by two mechanical pumps and blowers. For the 5 kW class thruster the vacuum facility consisted of a 2.34 × 1.22 m dia stainless steel chamber maintained at a background pressure of 0.25 torr by mechanical and diffusion pumps. The details of the experimental setup are given in Refs. 5 and 6 and summarized in Table 1.

A long focal length lens was used to colect light axialy from the arcjet throat and bring it to a focus on a 20 μm diameter field stop. The field stop provided the spatial filtering and defined the spatial resolution in the arcjet constrictor, which was approximately 40 μm in the 1 kW arcjet and 65 μm in the 5 kW arcjet. The image at the field stop was then focused, using a short focal length lens, onto the entrance slit of a monochromator which was used for spectral filtering. A photomultiplier tube was employed as the photodetector, and phase-sensitive detection was performed for background noise rejection using a digital lock-in amplifier. The reference signal was provided by a mechanical beam chopper placed near the intermediate focus at the spatial filter. The digitized output of the lock-in amplifier was transferred to a personal computer for spectral
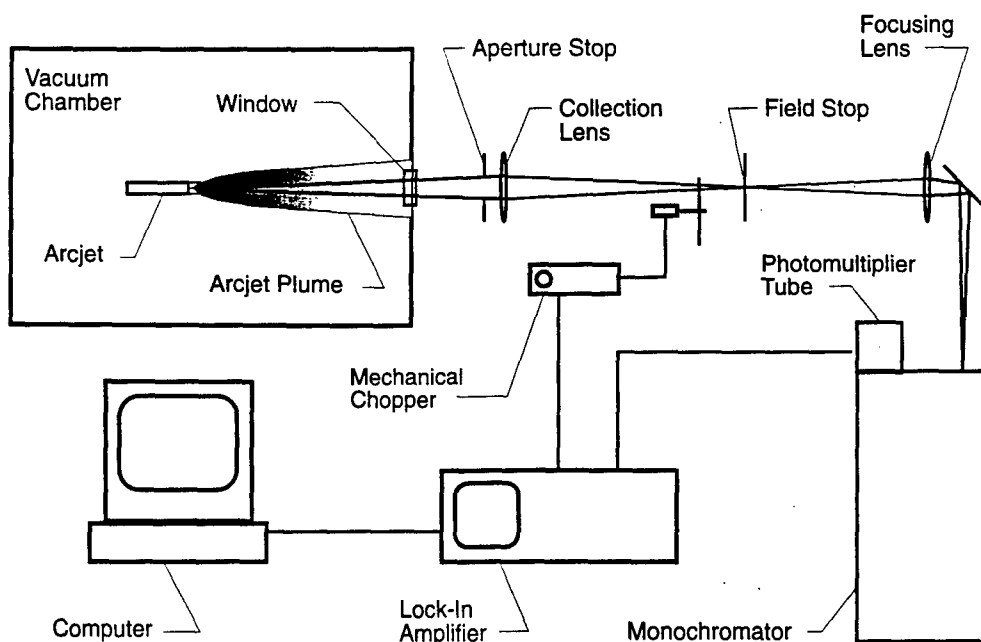
Fig. 9. Schematic diagram of the axial emission experimental set-up.

analysis. To minimize the light colection volume from the arcjet plume and, hence, the molecular hydrogen emission, an aperture stop was placed in front of the collection lens to provide very slow collection optics. Intensity calibration was performed using an 18 A tungsten filament lamp whose temperature was determined with an optical pyrometer.

The experiments were performed under a variety of operating conditions as given in Table 1. Axial emission over the complete visible spectrum was colected on the arcjet centerline to obtain estimates of the cathode temperature from the spectral background. Spectral scans of the H_a line were taken at several power levels and radial positions to determine the specific energy and radial dependence of the electron number density within the arc.

Table 1. Arcjet and experimental details.

Arcjet	1 kW class	5 kW class
Arcjet properties:		
cooling	radiation	radiation
nozzle throat diameter (mm)	0.64	0.76
exit plane diameter (mm)	9.5	12.1
expansion length (mm)	12.1	13.5
cathode gap (mm)	0.45	0.90
Optical setup:		
collection lens f.l. (mm)	400	500
focusing lens f.l. (mm)	150	80
field stop diameter (μm)	20	20
aperture stop diameter (mm)	25.4	12.7
collection f/ #	28	165
spatial resolution (μm)	40	65
monochromator f.l. (m)	0.5	0.64
monochromator grating (gr/mm)	1200	2400
spectral resolution (nm)	0.083	0.016
Operating conditions:		
H_2 mass flow rate (mg/sec)	14.1	18.45
arcjet current (A)	5.6–10.3	18–36
arcjet voltage (V)	146.0–163.8	116.7–120.8
arcjet power (kW)	0.92–1.5	2.2–4.4
specific energy (MJ/kg)	70–115	119–238
tank pressure (torr)	0.4	0.25
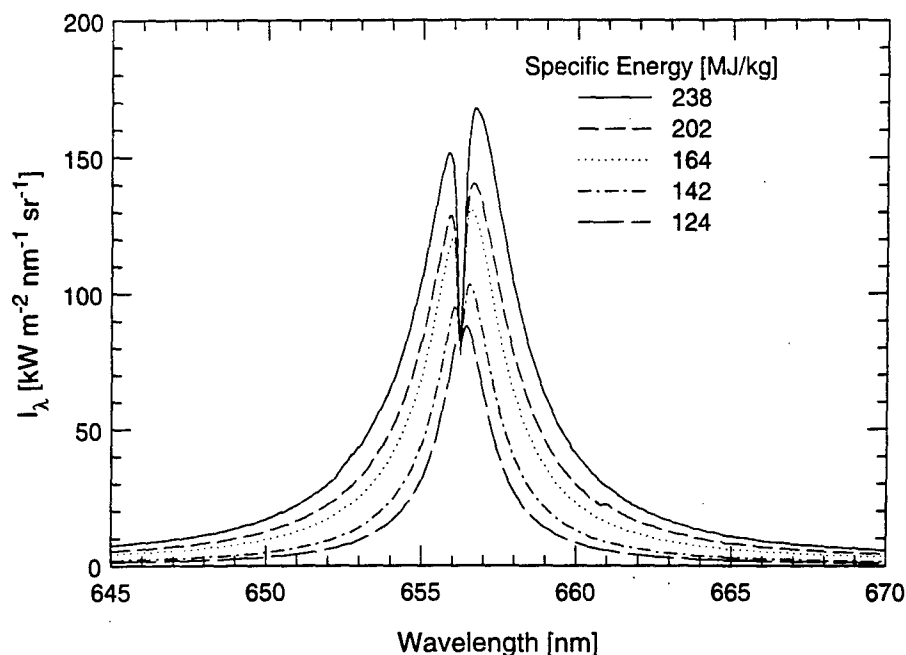
Fig. 10. Measured centerline axial emission spectra of H_α at different specific energies for the 5 kW arcjet showing the reabsorption dip near linecenter.

EXPERIMENTAL RESULTS AND DISCUSSION

Typical measured axial emission H_α lines are shown for the 5 kW arcjet at various specific energy levels in Fig. 10. These lines show clearly the previously mentioned absorption dip near linecenter. At first glance one might suspect that the velocity in the arc region relative to the plasma in the downstream expansion region could be estimated from the Doppler shift of the linewings relative to the reabsorption dip. However, if this were the case then the wings would be blue-shifted relative to the dip and not red-shifted as measured. This red-shift is indeed not a Doppler shift, but a Stark shift which occurs for all hydrogen Balmer lines at large electron number densities. The Stark red-shift of H_α has been documented in the literature[16] for electron densities up to 10^{23} m^{-3}. By linearly extrapolating these measured shifts to typical electron densities near the cathode, say 4×10^{23} m^{-3}, we find a red shift of approximately 0.2 nm, which is larger than the expected Doppler blue shift of approximately 0.03 nm. However, because the Doppler shift is not insignificant and the precise axial velocity in the arc is not known, a measurement of this shift could not be used as an alternative method to obtain the near-cathode electron number density with accuracy. Conversely, the uncertainty in the measured arc electron number density, coupled with the uncertainty in determining the precise shift of the linewings, precluded the measurement of axial velocity in the constricted arc.

Electron number density

As mentioned in the modeling results, the electron number density in the near-cathode region can be determined from the measured H_α linewings. This is accomplished by fitting a Lorentzian lineshape to the linewings, and the FWHM of the fit is a direct measure of the electron number density in the arc by the Stark broadening mechanism. The relationship between the FWHM and the electron number density was obtained by static-ion Stark calculations by Vidal, Cooper and Smith[17] (VCS). Although recent dynamic-ion simulations[18] have shown that the VCS calculations are in error at electron densities typical of the arcjet exit plane, the VCS calculations were considered sufficiently accurate to be used for determining arc region n_e. One difficulty with this measurement, however, is that the best fit Lorentzian is found to be very sensitive to the amount of the linewings to which the fit is performed. This is demonstrated in Fig. 11, where two different fits are shown to the linewings of a typical measured H_α spectrum. The difference between the two fits is the extent of the linewings used in the fit, as indicated by the percentage of the peak intensity

to which the fit is applied. A logarithmic intensity scale has been used to emphasize the linewings. It appears that both Lorentzian curves fit the wings extremely well; however, they differ in FWHM by nearly 25%, corresponding to a discrepancy in electron number density by approximately 40%. This uncertainty constitutes the limiting factor in accurately determining the arc electron number density from the linewings. On the one hand, to ensure that the fit is performed only to the part of the line originating near the cathode, it would be desirable to fit only the very far wings. This will reduce the systematic error associated with the radiation transfer near linecenter. On the other hand, since the noise is larger in the wings of the line, performing a linefit to only the far wings results in a very large statistical error in the determination of the linewidth. Thus, several best fits were performed to varying amounts of the linewings to determine the limits of the electron number density; consequently, the measured densities have considerable uncertainty, by as much as a factor of two.

The measured electron number density in the near-cathode region is shown as a function of specific energy in Fig. 12 for both the 1 and 5 kW arcjets. Despite the large uncertainties, the densities clearly show an increasing trend with specific energy. This trend is consistent with the fact that the arc current increases with increasing arcjet power. At a fixed mass flow rate, it is expected that the plasma conductivity, and hence electron number density, in the arc would increase with current density, and therefore power. The 1 and 5 kW arcjet results cannot be compared directly since the arcjet geometries and the mass flow rates are different. However, the 1 kW results may be compared to peak near-cathode electron densities computed by the 1 kW arcjet model of Butler et al.[14] shown as a dashed line in Fig. 12. The agreement is quite reasonable keeping in mind the approximations and numerical difficulties in modeling the arcjet, and the fact that the model results are peak electron densities while the measurements are line-of-sight averages over a small region near the cathode.

The arc electron number density was also measured as a function of radial position in the 5 kW arcjet at a specific energy of 238 MJ/kg. The results are shown in Fig. 13, along with the radial distribution of electron density at the constrictor (dashes) and the cathode tip (dots) as determined by the arcjet model of Butler et al.[14] The measured densities are larger than the model predictions
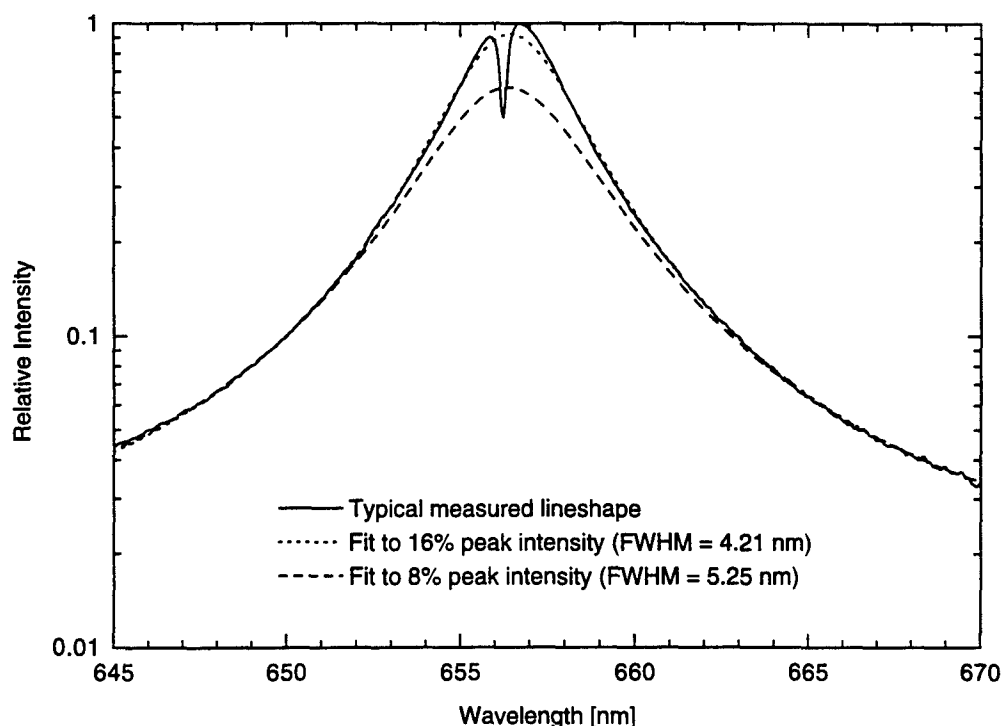
Fig. 11. Typical measured H_a lineshape with best fit Lorentzian functions to the linewings. The best fits differ in how much of the linewings are used in the fitting procedure as indicated by the percentage of the peak intensity used in the fitting.
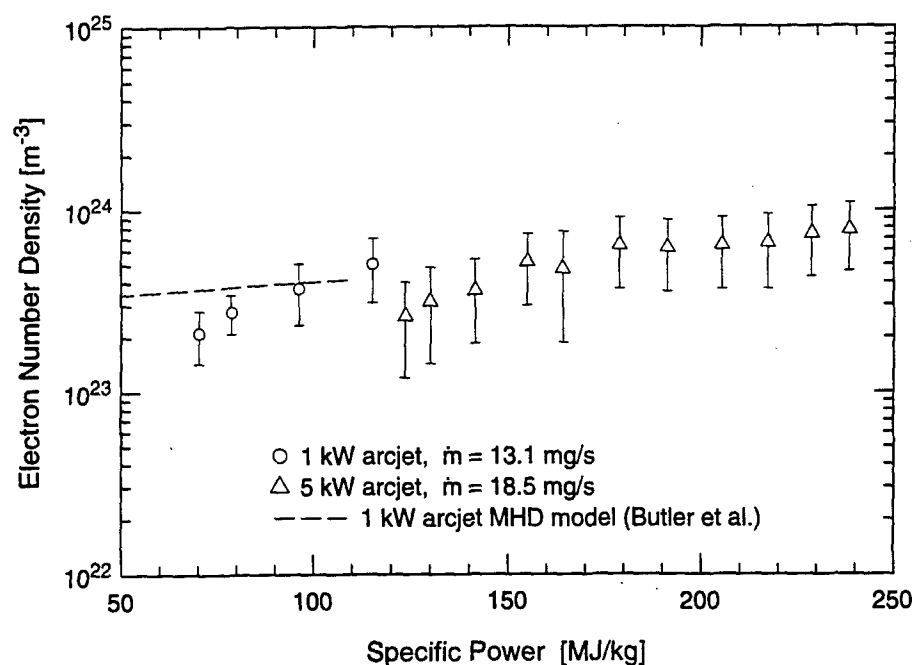
Fig. 12. Measured near-cathode electron number density as a function of specific energy for both the 1 and 5 kW arcjets. The dashed line gives the peak near-cathode electron density in the 1 kW MHD model of Butlet et al.[14]

near the linecenter by a factor of perhaps two to four, while the discrepancy becomes very large away from the arcjet centerline. The measured densities are probably artifically high at large radial positions because of the finite spatial resolution of the collection optics and the transient instabilities in the location of the arc. Nevertheless, the measured electron densities are considerably larger than the model predictions. Since the model does not include species diffusion, this
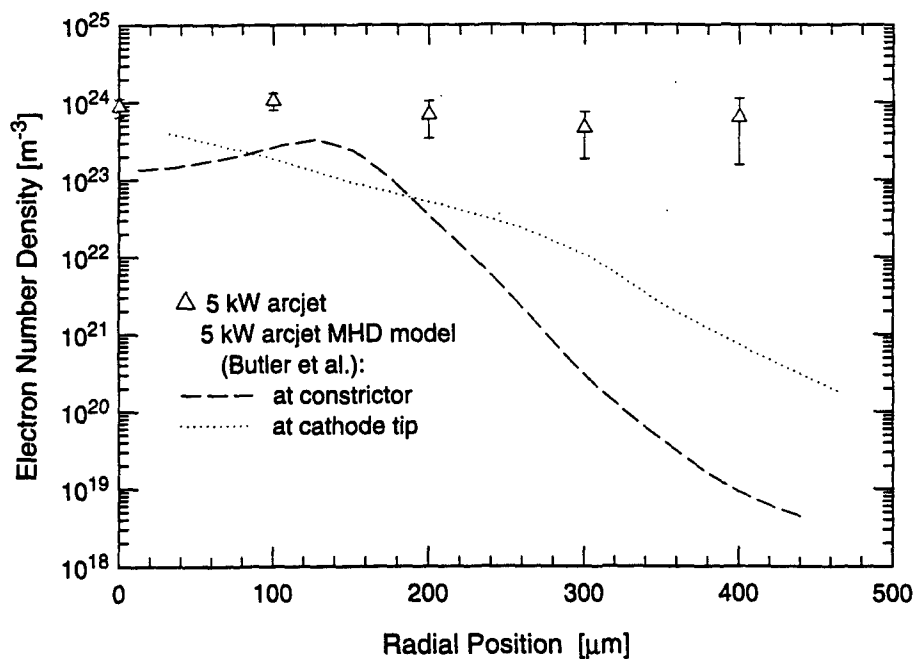
Fig. 13. Measured near-cathode electron number density as a function of radial position for the 5 kW arcjet at a specific energy of 238 MJ/kg. The dashed and dotted lines are model predictions by Butler et al[14] at the arcjet constrictor and cathode tip respectively.
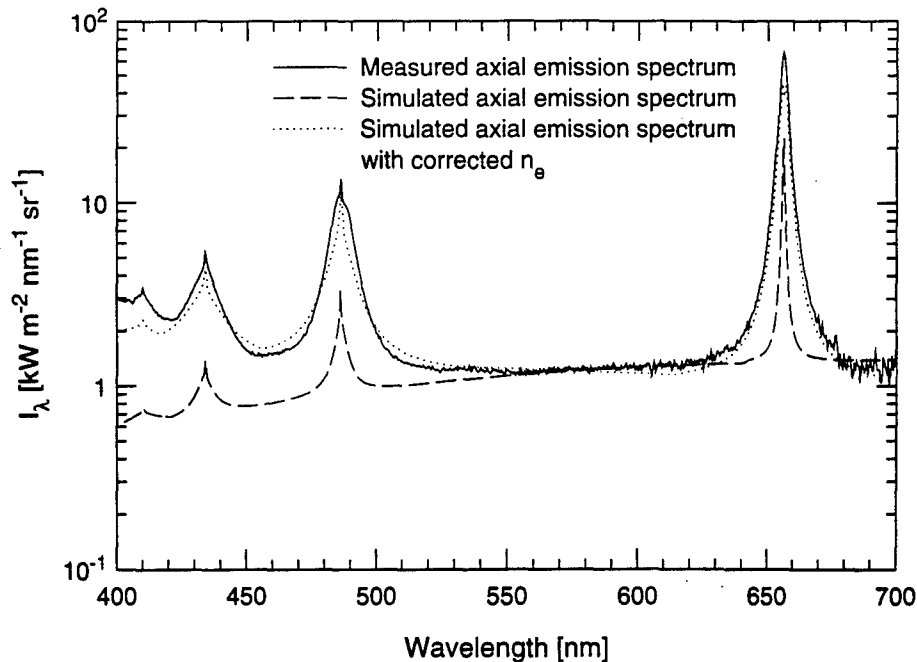
Fig. 14. A comparison between the measured (solid) and calculated (dashes, dots) axial emission spectra of the 5 kW arcjet for a specific energy of 220 MJ/kg. The dashed line is the calculated spectrum using the axial properties from Butler et al[14] and a cathode temperature of 3830 K. The dotted line is a calculated spectrum using a corrected electron number density and a cathode temperature of 3400 K.

discrepancy is likely an indication of the importance of diffusional transport processes in the arc region of the plasma.

Cathode temperature

The complete measured axial emission spectrum in the visible region is shown (solid) in Fig. 14 for the 5 kW arcjet at a specific energy of 220 MJ/kg. The simulated spectrum is also shown (dashed). The baseline or background emission, corresponding to a cathode temperature of 3830 K, is seen to agree well with the measured spectrum above 550 nm. However, the simulated spectrum considerably underpredicts the width and intensities of the four Balmer lines. To understand this discrepancy, an investigation was performed to determine which plasma property has the greatest effect on the line intensities and it was discovered that only an increase in the electron number density could significantly increase these line intensities. Since a discrepancy of a factor of two to four between the measured and modeled electron density has already been noted above, the axial emission was re-modeled using the same plasma properties as before except the electron number density increased in the arc region by a factor of three. This simulation, shown dotted in Fig. 14, agrees remarkably well with the measured spectrum for all of the Balmer lines except perhaps H_δ. (At the short wavelengths the measured spectrum may be inaccurate due to the difficulty in calibrating the intensity.) This remarkable agreement is in accordance with the previous result that the model underpredicts centerline arc electron densities by a factor of approximately two to four in the 5 kW arcjet.

The cathode temperature was measured from the spectral background in the manner described above. However, using the increased electron number densities, the cathode temperature must be reduced by about 10% due to the increased continuum radiation component of the background. Because of this uncertainty, it is preferable to have a means of determining the cathode temperature from the measured spectrum which is independent of the MHD arcjet model. This is achieved by assuming that the effect of the continuum radiation on the background spectrum can be reasonably well approximated by a uniform arc of some unknown length. The electron number density in the arc is taken to be the value measured from the H_α linewings, while the temperature and atomic hydrogen density are assumed to be typical values in the arc. For the 5 kW arcjet results presented here these values were taken to be 50,000 K and 6×10^{21} m^{-3} respectively. The resulting spectrum

is calculated using these plasma properties and the cathode thermal radiative properties. By fixing the cathode spectral emissivity at 0.4, the calculated background is fit to the measured spectrum, with the parameters of the fit being the cathode temperature and the length of the arc. The resulting cathode temperature measurements are shown in Fig. 15. In all cases, an arc length of 0.29 mm was found to give the best fit. The error bars shown in the figure are due only to the uncertainty in fitting the calculated spectrum to the measured spectrum, and not due to systematic errors in the measurement technique.

The measured cathode temperatures show an increasing trend with specific energy. This may be explained by an increase in the current density at the arc attachment with increasing arcjet power, consistent with the measured increase in plasma conductivity, or electron number density, as discussed above. However, the cathode temperatures are found to be somewhat below the melting point of pure tungsten, which is inconsistent with documented cathode erosion measurements inferring the presence of a molten pool of tungsten at the cathode tip.[19] This discrepancy may be accounted for in the uncertainty in the spectral emissivity of molten tungsten at normal incidence. If the emissivity is below the assumed value of 0.4 then the temperatures will be greater than those shown in Fig. 15.

Having obtained a measurement of the cathode temperature, the electric field at the cathode tip and the cathode fall voltage can be estimated. Inspection of the cathode tip of the 5 kW arcjet revealed a small crater of 0.75 mm dia. At 220 MJ/kg the arcjet current is 36.0 A, and assuming that the current is uniformly distributed over the crater, the resulting current density is approximately 8×10^7 A/m². The Shottky-enhanced thermionic emission current density, j_{th}, is given by[20]

$$j_{th} = AT_c^2 \exp\left[\frac{-e}{kT_c}\left(\phi_w - \left(\frac{eE}{4\pi\epsilon_0}\right)^{1/2}\right)\right]$$ (12)

where E is the electric field, T_c is the cathode temperature, ϕ_w is the work function, and the constant A is given by

$$A = 2\left(\frac{2\pi m_e k^2 e}{h^3}\right).$$ (13)
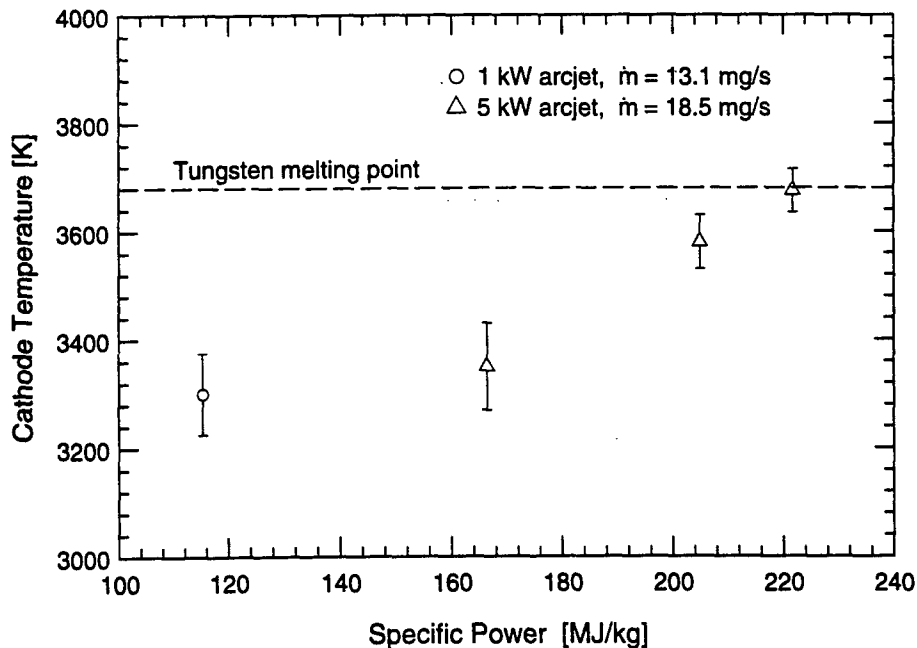

Fig. 15. Measured cathode temperature as a function of arcjet specific energy for both the 1 and 5 kW arcjets. The error bars correspond only to the statistical error of the fitting.

Assuming a work function of 4.5 V for tungsten,[21] and a measured cathode temperature of roughly 3700 K, an electric field of 5×10^8 V/m is required to produce the specified current density. Little experimental data exists on field strengths near cathodes in high pressure arcs; however, calculated values in the 10^8 V/m range have been reported.[22] The sheath thickness is approximately 10^{-8} m, which implies a cathode fall voltage on the order of 5 V. This agrees well with typical high pressure discharges.[23]

It is clear that field enhancement of the thermionic emission must be considered, since neglecting the electric field would necessitate a cathode temperature of approximately 4400 K to sustain the required current density. Such a high cathode temperature is inconsistent with the measured emission spectrum; consequently, the electric field must play a significant role in the emission process at the cathode.

SUMMARY AND CONCLUSIONS

In this study the axial emission of 1 and 5 kW hydrogen arcjet thrusters is investigated. The radiative transfer equation is integrated from the cathode to the arcjet exit plane and beyond to predict the centerline axial emission spectrum. The atomic hydrogen line emission is calculated by a collisional–radiative model using input properties from a single-fluid MHD arcjet code developed by Butler et al.[14] The calculations predict the complete visible spectrum including contributions from atomic hydrogen line emission, continuum emission from the free electrons, and cathode graybody radiation, while radiation from molecular hydrogen and metal vapor are not included. Results from the modeling indicate that a spectral window exists for direct measurement of the cathode temperature by thermal emission. Furthermore, the modeling indicates that the lineshape wings of the atomic transitions depend only on the electron number density in the near-cathode region of the arcjet. Hence, the collisional–radiative model predicts an optical diagnostic technique to directly measure the electron number density in the arc without modification to the arcjet anode. Lastly, the modeling results indicate that the radiation transfer through the arcjet has an effect on the integrated line intensities, thereby rendering a Boltzmann plot incapable of providing a measure of the arc temperature in the near-cathode region.

Experiments were performed to verify the modeling predictions. The measured and simulated axial emission spectra are in excellent agreement when the electron number density is increased in the arc by a factor of three from the MHD model predictions. This indicates that the MHD model is underpredicting the arc electron density. Since the arc is fully ionized, an increase in the modeled electron density would require an increase in pressure. For a fixed mass flow rate this can only be achieved by increasing the arcjet power, resulting in a decrease in efficiency. However, this is desirable since the present MHD model overpredicts the arcjet efficiency.[1]

The near-cathode electron number density was measured from the Stark broadening of the linewings of the H_α line. There is considerable statistical error in this measurement technique which results in uncertainties in number densities by a factor of two or more. Nevertheless, the measurements indicate that the arc electron density increases with specific energy at a constant mass flow rate, which suggests that the arc current density increases with arcjet power rather than, or perhaps in addition to, an increase in the arc cross-sectional area. The radial distribution of the measured electron number density suggests that diffusional transport of electrons plays a significant role in the arc region. This result, however, is inconclusive due measurement uncertainties stemming from the limited spatial resolution and the spatial instability of the arc.

The cathode temperature was measured from the spectral background and found to be in the neighborhood of, but somewhat below, the melting point of pure tungsten, and increasing with arcjet specific energy. The latter result can be realized by an increase in current density at the arc attachment with increasing arcjet power, which is in agreement with the measured increase in plasma conductivity, or electron number density, near the cathode. The former result is inconsistent with observations that the cathode tip is in a molten state during arcjet operation. However, this discrepancy may be attributed to the uncertainty in the spectral emissivity of molten tungsten. Assuming a cathode temperature at the tungsten melting point, a calculation of the Shottky-enhanced thermionic emission from the cathode gives a cathode fall voltage in agreement with that of typical high pressure discharges. The accuracy of the cathode temperature measurements would

be significantly improved with a better knowledge of the spectral emissivity of molten and near-molten tungsten.

REFERENCES

1. M. A. Cappelli, J. G. Liebeskind, R. K. Hanson, G. W. Butler, and D. Q. King, A comparison of hydrogen arcjet plume properties to single and two-fluid model predictions, IEPC-93-220, *23rd AIAA/AIDAA/DGLR/JSASS International Electric Propulsion Conference* (September 1993).
2. T. Moeller, D. Keefer, and R. Rhodes, Comparison of experimental and numerical results for radiation cooled and water cooled hydrogen arcjets, IEPC-93-214, *23rd AIAA/AIDAA/DGLR/JSASS International Electric Propulsion Conference* (September 1993).
3. I. Boyd, M. A. Cappelli, and D. R. Beattie, Monte Carlo and experimental studies of nozzle flow in a low-power hydrogen arcjet, AIAA-93-2529, *29th AIAA/SAE/ASME/ASEE Joint Propulsion Conference* (June 1993).
4. M. A. Cappelli and P. V. Storm, Interior plasma diagnostics of arcjet thrusters, AIAA-94-2654, *25th AIAA Plasmadynamics and Lasers Conference* (June 1994).
5. P. V. Storm and M. A. Cappelli, Axial emission diagnostics of a low power hydrogen arcjet thruster, IEPC-93-219, *23rd AIAA/AIDAA/DGLR/JSASS International Electric Propulsion Conference* (September 1993).
6. P. V. Storm and M. A. Cappelli, Axial emission measurements on a medium power hydrogen arcjet thruster, AIAA-94-2743, *30th AIAA/ASME/SAE/ASEE Joint Propulsion Conference* (June 1994).
7. H. R. Griem, *Plasma Spectroscopy*, McGraw-Hill, New York (1964).
8. A. T. M. Wilbers, G. M. W. Kroesen, C. J. Timmermans, and D. C. Schram, *JQSRT* **45**, 1 (1991).
9. W. G. Vincenti and C. H. Kruger, *Introduction to Physical Gas Dynamics*, Robert E. Krieger, New York (1965).
10. B. van der Sijde, J. J. A. M. van der Mullen, and D. C. Schram, *Beitr. Plasmaphys.* **24**, 447 (1984).
11. T. Holstein, *Phys. Rev.* **83**, 1159 (1951).
12. L. C. Johnson, *Astrophys. J.* **174**, 227 (1972).
13. W. L. Wiese, M. W. Smith, and B. M. Glennon, Atomic transition probabilities: hydrogen through neon, *NSRDS-NBS4* 1 (1966).
14. G. W. Butler, A. E. Kull, and D. Q. King, Single fluid simulations of low power hydrogen arcjets, AIAA-94-2870, *30th AIAA/ASME/SAE/ASEE Joint Propulsion Conference* (June 1994).
15. W. L. Wiese, Line broadening, in *Plasma Diagnostic Technique*, R. H. Huddlestone and S. C. Leonard, eds., Academic Press, New York (1965).
16. W. L. Wiese, D. E. Kelleher, and D. R. Paquette, *Phys. Rev. A* **6**, 1132 (1972).
17. C. R. Vidal, J. Cooper, and E. W. Smith, *Astrophysical J. Suppl. Ser.* **25** No. 214, 37 (1973).
18. D. E. Kelleher, W. L. Wiese, V. Helbig, R. L. Greene, and D. H. Oza, *Phys. Scripta* **T47**, 75 (1993).
19. F. M. Curran, T. W. Haag, and J. F. Raquet, Arcjet cathode phenomenon, NASA Technical Memorandum 102099 (1989)
20. J. K. Koester, Analytical and experimental studies of thermionically emitting electrodes in contact with dense seeded plasmas, Ph.D. thesis, California Institute of Technology (1970).
21. *CRC Handbook of Chemistry and Physics*, 73rd edn, CRC Press, Boca Raton, FL (1992).
22. W. L. Bade and J. M. Yos, Theoretical and experimental investigation of arc plasma-generation technology, Part II, Vol. 1, ASD-TDR-62-729, AVCO Corp. (1962).
23. W. Finkelnburg and H. Maecker, *Electric Arcs and Thermal Plasma*, translation from *Handbuch der Physik*, Bd. **22**, Gasentladungen II (1956).

Interior Plasma Diagnostics of Arcjet Thrusters

Mark A. Cappelli* and P. Victor Storm†

Stanford University, Stanford, California 94305-3032

We review past experimental measurements of internal flow properties of arcjet thrusters. These measurements are generally classified as either intrusive, requiring design changes to prototype thrusters, or nonintrusive, and include measurements of cathode temperature, as well as static pressure, flow temperatures (vibrational, rotational, electronic, translational), electron density, and velocity throughout the interior region extending to the exit plane. Comparisons are made to available model predictions. These measurements, performed on a wide range of thrusters, and operating on variety of propellants, indicate that the nozzle plasma flow may be removed from local thermodynamic equilibrium.

Nomenclature

$\ell n\, \Lambda$ = coulomb logarithm
$\dot{m}$ = propellant mass flow rate, kg s^{-1}
n_e = electron number density, m^{-3}
P = arcjet power, W
p_{stag} = stagnation pressure, Pa
p_{throat} = throat static pressure, Pa
T_{cat} = cathode temperature, K
T_e = electron translational temperature, K
T_{elec} = electronic excitation temperature, K
T_{rot} = rotational excitation temperature, K
T_{tran} = heavy species translational temperature, K
T_{vib} = vibrational excitation temperature, K
σ_{SH} = Spitzer–Harms electrical conductivity, Ω^{-1} m^{-1}

I. Introduction

ARCJET propulsion systems have been successfully employed in stationkeeping applications. To enable other applications such as repositioning or orbit transfer, the arcjet must deliver 1000 s of specific impulse at 35–50% thrust efficiency.[1] However, efficiencies approaching 50% at high specific impulse have not yet been achieved. The future design of more efficient and reliable thrusters requires a better understanding of the physical processes governing arcjet operation. This understanding can be obtained through a combination of experimental diagnostics and analytical modeling. Many studies have been conducted to investigate arcjet performance under different operating conditions, electrical configurations, and geometries.[2] Understanding the physical processes governing the arcjet operation requires a detailed knowledge of the plasma properties everywhere in the flowfield. A great deal of research has been conducted to measure the flow properties in the plume of arcjet thrusters using electrical and optical techniques.[2-4] Much of this work was driven by the need to understand the effect that the partially ionized and chemically reacting plume may have on other spacecraft surfaces and communications. As far back as the early sixties,[5] mass flux probes, impact probes, and enthalpy probes were implemented as exit plane and plume diagnostics to better understand the performance of these devices. More recently, advanced optical diagnostics[6-9] have been developed and implemented to measure the exit plane flow properties and to better understand the

thermal and chemical nonequilibrium nature of arcjet flows. Although much has been learned from these exit plane studies, it is evident that little is known about the plasma properties within the constrictor region and nozzle of the arcjet, yet it is here where the plasma behavior controls the arcjet performance.

In this article, we will review some past measurements made by other researchers and our own recent measurements of flow properties in the nozzle interior and constrictor (near-cathode) region of arcjet thrusters. These measurements can be classified as either intrusive or nonintrusive, depending on whether significant changes were made to the arcjet thruster to carry out the diagnostic. The intrusive measurements reviewed here include the static pressure measurements in both low-power (1-kW) thrusters using simulated hydrazine decomposition products as a propellant[10]; static pressure measurements in high-power (30-kW) thrusters operating with nitrogen as a propellant[11]; current distribution and floating potential measurements conducted using a segmented anode configuration in a 1-kW arcjet[12]; spectroscopic emission measurements of n_e and characteristic temperatures for T_{vib}, T_{elec}, and T_{rot} in the expansion nozzle of 1-kW thrusters using simulated hydrazine decomposition products as a propellant[13]; similar measurements to those described in Ref. 13 in 26-kW thrusters using ammonia as a propellant[14]; spectroscopic imaging of T_e and T_{elec} in a medium-power, water-cooled thruster using hydrogen as a propellant[15]; and n_e and T_{elec} in the constrictor region of a low power (1–3-kW) arcjet operating with helium as the propellant.[16] The nonintrusive measurements reviewed here include spectroscopic emission measurements of the near-cathode region n_e and T_{cat} in low and medium power (1- and 5-kW, respectively) hydrogen arcjet thrusters[17,18]; and laser-induced fluorescence (LIF) measurements of velocities in the nozzle of a low-power hydrogen arcjet thruster.[19] Despite the variations in propellant and differences in operating conditions, there are many common features in flow behavior associated with the various thrusters studied, some of which are discussed in the following sections.

II. Static Pressure Measurements

Static pressure measurements are useful in interpreting internal flow behavior in arcjets. In many cases, they can provide insight into the losses associated with nonideal or viscous effects. In general, static pressure measurements reflect changes in the flowfield characteristics, which are expected to influence arcjet thruster performance and stability.[20]

Harris et al.[11] presented a detailed study of the static pressure variation in a 30-kW water-cooled arcjet thruster operating with nitrogen as a propellant. In that study, the arcjet was

*Associate Professor, High Temperature Gasdynamics Laboratory. Member AIAA.

†Research Assistant, High Temperature Gasdynamics Laboratory. Student Member AIAA.

instrumented with 16 equally spaced pressure taps located in positions ranging from the arcjet plenum, through an extended constrictor, nearly to the exit plane of the nozzle. Such measurements can be classified as intrusive, in that it is not clear how the presence of such features may perturb or alter the internal flow characteristics. It is useful to examine here, nonetheless, some of the conclusions drawn from that study.

An arcjet flow, such as that investigated by Harris et al.,[11] is expected to be far removed from ideal isentropic conditions, and will experience imperfect gas effects. Despite this, it is interesting to note that the ratio of axial static pressure to stagnation pressure (taken to be the pressure measured by the upstream tap in the plenum) is independent of $\dot{m}$ or P as expected from a quasi-one-dimensional analysis, if the entire nozzle flow is choked. For all arc powers and flow rates studied, their measurements further indicated that the sonic point was located beyond the end of the constrictor, suggesting that viscous boundary-layer growth is significant within the constrictor. Up to the sonic point, an ideal quasi-one-dimensional analysis would indicate that the static pressure should increase with the square root of temperature (for a constant $\dot{m}$), reflecting the drop in density with temperature and the choked condition at the sonic point. If the radial pressure gradients are small, then assuming that the plasma is significantly ionized in the arc core, n_e is expected to decrease with the square root of the temperature. As is discussed later, recent measurements do not reflect this trend, strongly indicating a departure from ideal conditions.

Similar measurements have been performed by Talley et al.[10] in a 1-kW laboratory arcjet thruster operating on mixtures of hydrogen and nitrogen to simulate hydrazine decomposition products.[10] In their facility, five pressure taps were machined into the anode housing, providing static pressure measurements at locations of approximately 1.5 mm upstream of the throat, at the throat, and three measurements distributed along the expansion nozzle. Unlike the 30-kW arcjet of Harris et al.,[11] there is no significant constrictor channel in these low-power devices, and so it is more likely that the sonic point will coincide with the location of the throat. This is supported by the critical pressure ratio (ratio of static pressure to p_{stag} under choked conditions) of 0.52 measured in the throat for the arc-ignited low-power thruster,[10] unlike the 0.66–0.9 values measured in the constrictor region of the arc-ignited high-power thrusters.[11] Talley et al.[10] report, however, that their cold-flow p_{throat} is significantly greater than the critical pressure ratio, indicating that the sonic point under cold-flow conditions has moved downstream of the throat. They attribute this behavior to the strong swirl component of velocity in the cold-flow case that is dampened out following arc ignition.

The throat static pressure measurements of Talley et al.[10] combined with an estimate of the temperature in the arc core of 20,000–40,000 K (not atypical for a constricted arc at high pressures), allow an estimate of n_e in the core of the arc near the arcjet throat, provided we assume that the arc is in local thermodynamic equilibrium. Using the static pressure measurements of Ref. 10 (measured near the converging section of the nozzle), which range from 20–50 psia for $\dot{m} = 35$–65 mg/s ($P/\dot{m}$ of 10–30 MJ/kg), and taking $p_{throat}/p_{stag} \sim 0.52$, we estimate throat electron number densities ranging from 6×10^{22}–3×10^{23} m^{-3}. Recently, Zube and Myers[13] measured n_e from Stark broadening of hydrogen spectral lines in the upstream region of the expansion nozzle of a nearly identical arcjet thruster, also operating on simulated hydrazine decomposition products, over a comparable range of $P/\dot{m}$, albeit at much higher $\dot{m}$ (100 mg/s). Despite these different operating conditions, a comparison of the calculated n_e to the measurements of Zube and Myers,[13] reported at a distance of 3 mm downstream of the throat ($\sim 10^{21}$ m^{-3}), indicates that significant axial gradients in n_e exist in the near vicinity of the cathode and throat. Indeed, very strong axial number densities were measured near the throat of a 26-kW ammonia arcjet by
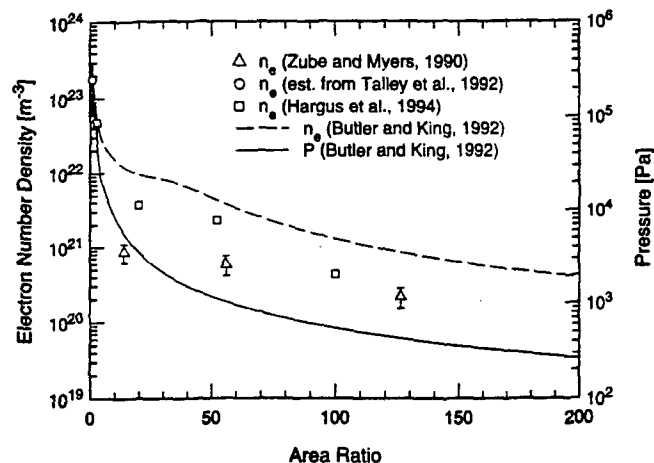
Fig. 1 Axial variation in n_e in a 1-kW class arcjet. The solid and dashed lines are the calculations for a low-power arcjet of Butler and King,[20,23] (see, e.g., Ref. 17) with hydrogen as a propellant. The data points are for a low-power thruster operating on hydrazine decomposition products from Ref. 13 (triangles), a high-power thruster operating on ammonia from Ref. 14 (squares), and, as estimated in the text, from the static pressure measurements of Ref. 10 (circles).

Hargus et al.,[14] using spectroscopic methods similar to those of Zube and Myers.[13] We speculate that such strong axial gradients in n_e contribute to the stability of a diffuse arc attachment at the anode in this region of the nozzle. A lower n_e and cooler plasma will result in a correspondingly lower current density for a given electric field strength. A transition from a diffuse to constricted arc attachment at the anode has been shown to be less favorable at lower attachment current densities.[21,22]

The strong axial variation in n_e in low-power arcjet thrusters has been captured by recent single-fluid magnetohydrodynamic (MHD) models developed by Butler and King.[20,23] In Fig. 1, we graph the model simulations for a (nominal) 1-kW arcjet thruster operating with hydrogen as a propellant ($\dot{m} = 13.1$ mg/s and $P/\dot{m} = 115$ MJ/kg), as well as available experimental data.[10,13,14] Although the results of Refs. 10 and 13 are for an entirely different propellant, and the results presented in Ref. 14 are for much higher powers, we include them on the graph for illustrative purposes. We see that in the hydrogen arcjet thruster, the predicted axial variation in n_e is in qualitative agreement with the observations in essentially the same thruster operating on simulated hydrazine decomposition products, and with the measurements made in the 26-kW ammonia engine.

III.   Electrical Measurements

Until the recent electrical studies of Curran and Manzella,[12] we could only speculate as to the mode and distribution of current attachment along the anode surface in low-power arcjets. In that study, an arcjet of identical geometry to those baselined for use in communications satellites was instrumented with a segmented anode. Although inherently an intrusive diagnostic, this segmented anode design allowed them to estimate the current distribution and floating (plasma) potential as well as the anode fall voltage. In addition, they were able to perturb the attachment (i.e., electrically isolate various segments) to force current to a particular region along the anode.

The anode described in Ref. 12 was divided into five segments. The first consisted of the converging section up to the end of the constrictor/throat. The second, third, and fourth sections were centered approximately 1, 2.5, and 4 mm downstream of the throat, respectively. The last segment consisted of the remaining section of the nozzle. Each segment was separated from the others by thin boron–nitride spacers.

The most interesting finding is that under normal operation (all segments connected together and connected to the power supply) the current was nearly equally distributed to all but the first segment (which collected little or no current under steady operation). This finding indicates that the current density decreases significantly along the axial direction, consistent with the measured drop in n_e.[13] The first segment, when electrically isolated, barely influenced the current attachment at the remaining four segments. This is an important result, in that it indicates that little or no current is collected by this region of the anode. Although the floating potential of this segment was not measured while all others were connected, it was found to be approximately 35 V (relative to the cathode) when the current was forced to the fifth segment.[12] Using 35 V as an estimate of the voltage between the cathode and the end of the constrictor (which is approximately 0.75–1.0 mm from the cathode tip, depending on the gap spacing), we can estimate the extent of arc constriction (arc diameter). To do this, we need the electrical conductivity, which, if the arc core is fully ionized, is given by the Spitzer-Harm expression[24] (in MKS units):

$$\sigma_{SH} = 1.53 \times 10^{-2}(T_e^{3/2}/\ell n\ \Lambda) \qquad (1)$$

Here, $\ell n\ \Lambda$ depends (weakly) on both n_e and T_e. If we assume $T_e = 30,000$ K, $n_e = 10^{23}$ m^{-3}, and that the arc core is highly ionized, we estimate the electrical conductivity to be approximately 16,000 Ω^{-1} m^{-1}. Using a current of 11A, we arrive at an arc diameter of approximately 200 μm. Comparing this to the constrictor diameter of approximately 700 μm indicates that the arc is constricted to about 10% of the throat area. This estimate is within a factor of 2 of what has been measured based on Stark broadened axial line emission from a 1-kW arcjet operating on hydrogen.[17]

Another interesting result of the Curran and Manzella study[12] is that when the last segment is isolated from the power supply (and its current is shifted to the next upstream segment), the voltage on the last segment can be used to estimate the anode fall voltage at the next upstream segment. It is found that when isolated, the voltage of the fifth segment (relative to the cathode) was roughly equal to the voltage on all of the remaining connected segments. If we can assume that this last segment acts as an emissive probe, then it will measure the local plasma potential. This suggests that the anode fall voltage in the distant nozzle may be negligible. This result is not surprising if one considers that the field near the anode consists of both a resistive component balanced by an ambipolar component that is associated with gradients in plasma density:

$$E \approx (J/\sigma) - (kT/e)(\nabla n_e/n_e) \qquad (2)$$

We see that, at sufficiently low current densities, the plasma potential can in fact be greater than the anode potential (giving rise to a negative fall). In the case at hand, it appears that the current densities are sufficiently low near the end of the nozzle that the anode fall is small. Another interesting experiment described in the study of Curran and Manzella[12] involved forcing the current to attach to the first (furthest upstream) segment by isolating the remaining four. The floating potential of the remaining four segments, when compared to the potential difference between the cathode and the first segment, affords an estimate of the anode fall voltage at the first segment. Under these conditions, a high current density ensues and we would therefore expect the anode fall to increase significantly. Indeed this was the case,[12] with the anode fall voltage increasing to approximately 40 V.

IV. Optical Emission Measurements

Much has been learned about the internal flow characteristics of arcjet thrusters by studying the intrinsic plasma emission. One of the first and most thorough investigations of the nozzle flow of a prototype thruster was performed by Zube and Myers[13] using optical emission spectroscopy. In that study, a set of holes were drilled into the anode (nozzle) of a 1-kW arcjet thruster at three axial positions, approximately 3, 6, and 9 mm from the throat of a nozzle that had a maximum area ratio of 225:1. A set of holes were also drilled at various radial positions, approximately 9 mm from the throat of a nozzle similar to that described earlier, and at 9 and 12 mm from the throat of a nozzle of equal half-angle (30 deg), but extended to an area ratio of 400:1. Like the static pressure measurements, these measurements can be considered to be intrusive, in that it is not clear how the presence of such holes perturb or alter the internal flow characteristics. The research presented in Ref. 13 was motivated by the need to better understand the nonequilibrium processes in the nozzle of an arcjet thruster operating on mixtures of hydrogen and nitrogen to simulate hydrazine decomposition products. These nonequilibrium processes include vibrational, rotational, and electronic excitation, as well as finite rate recombination. Hargus et al.[14] extended the Zube and Myers spectroscopic method[13] to the study of a 26-kW ammonia arcjet thruster. Optical access holes were drilled into the sides of the nozzle at distances of 2.5, 12.7, and 22.9 mm downstream of the 2.5-mm constrictor. Their nozzle had an area ratio of 100:1 and a half-angle of 19 deg. The electron number density was measured from the line-of-sight-integrated spectral (primarily Stark broadened) linewidth of the H_β transition in atomic hydrogen. Their measured axial variation in n_e is compared to single-fluid calculations for the 1-kW arcjet (albeit at slightly different operating conditions and for hydrogen as a propellant) in Fig. 1. The differences between model predictions and measurements are within a factor of 2–10, and might be accounted for by the slight differences in operating conditions.

An interesting result of the Zube and Myers study[13] is that extending the nozzle clearly perturbs the upstream current and plasma properties. They found that the n_e that was measured 9 mm from the throat of an arcjet, having a 12-mm-long nozzle, was significantly less (by some 40% or so) than that at the same location in an extended nozzle (15 mm) of equal expansion angle. This result reveals the influence that the nozzle geometry may have on arc behavior. More importantly, it suggests that a nonnegligible fraction of the current extends down into the low-density region of the flow, consistent with the electrical measurements and findings of Curran and Manzella.[12]

Their measured T_{elec} (from the Balmer transition series of atomic hydrogen), T_{rot} and T_{vib} (from the $C^3\Pi_u - B^3\Pi_g$ electronic transition of molecular nitrogen) are displayed in Fig. 2. Also displayed in the figure is the translational temperature computed using the arcjet model of King and Butler[20,23] (see for example Ref. 17) for a similar low-power arcjet operating on hydrogen. Like n_e, the temperatures drop in the expansion zone (beyond an area ratio of about 10), most noticeably for T_{elec}, which is argued to be close to T_e because of rapid thermalization between the free and bound electrons in the high-lying electronic levels.[13] The electron–proton and proton-atomic hydrogen translational energy relaxation times are estimated to be less than the residence times within the expansion nozzle, which is comparable to the hydrogen–molecular nitrogen relaxation time; therefore, Zube and Myers[13] argue that T_{elec} should also reflect the heavy species translational temperature (T_{tran}). This is seen to be supported by the model calculations for the comparable power hydrogen arcjet only very near the throat. It is apparent that translational energy exchange is less efficient downstream where n_e drops significantly. It is also apparent from Fig. 2 that T_{rot} and T_{vib} are less than T_{elec} and T_{trans}. At first, one may conclude the presence of a substantial departure from local thermodynamic equilibrium for these internal energy modes, as suggested by Zube and Myers.[13] However, we remind the reader that these measurements are based on line-of-sight averages of emission, and so

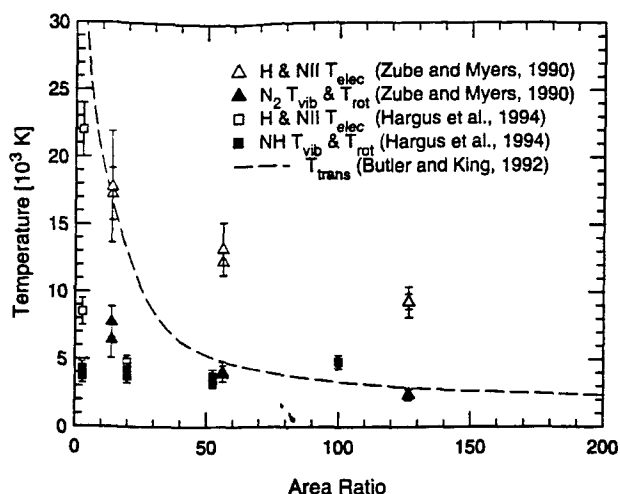**Fig. 2** Comparison of axial variation in temperatures in the expanding nozzle of a low-power arcjet thruster. The dashed lines are the calculations for a low-power arcjet of Butler[20,23] (see, e.g., Ref. 17) with hydrogen as a propellant. The data points are for a low-power thruster operating on hydrazine decomposition products from Ref. 13 (triangles), and a high-power thruster operating on ammonia from Ref. 14 (squares).

the signal from any emitting species reflects the local properties in the region where the density of the emitting species is greatest. Because of the high centerline temperatures, it is possible that molecular emission originates from the cooler boundary region within the nozzle and indicates a lower T_{rot} and T_{vib}.

The measurements of Zube and Myers[13] were limited to positions 3 mm from the throat of the arcjet. Machining holes closer to the constrictor would be more difficult in such a small device. However, prior to the Zube and Myers study,[13] Ishi and Kuriki[16] successfully modified the constrictor region to accommodate optical access into a low-power arcjet operating on helium propellant. In that study, they positioned optical viewports at four locations within the constrictor, which was 8 mm in length for their design. Their results clearly revealed an internal (constrictor) flow that was far removed from ionizational equilibrium, with the plasma seemingly overdense with respect to Saha equilibrium. The departure from Saha equilibrium was found to be more pronounced farther downstream of the entrance to the constrictor. Although no direct measurements of the departure from ionizational equilibrium have been made in the constrictor or nozzle region of a low-power hydrogen arcjet, it is expected that a similar result would ensue. We would expect that the plasma is near ionization equilibrium in the throat or constrictor, and that the departure from Saha equilibrium would be more pronounced in the diverging region of the nozzle, since electron–atom collisions become less frequent as densities fall.

In an attempt to better understand the constrictor flow region of a 6–12-kW water-cooled hydrogen arcjet, Glocker and Auweter-Kurtz[15] machined optical access into the constrictor, which allowed the imaging of the arc plasma emission onto an intensified charge coupled device (CCD) video camera. Radial profiles of T_{elec} and T_r were obtained from the Abel-inverted intensities of continuum emission (at 600 nm), and relative spectral line emission from the H_α and H_β atomic transitions. The measured peak (centerline) temperatures are in agreement, suggesting that the constrictor plasma is in near local thermodynamic equilibrium. However, both methods give peak temperatures in the range of 10,000–13,000 K, which are below their own numerical predictions of approximately 20,000 K,[15] and substantially below the constrictor temperatures predicted in low-power and medium-power radiation-cooled hydrogen arcjets.[17,18] The images captured in Ref. 15 allow for an estimate of the arc diameter within the constrictor. The arc core does not appear to fill the constrictor,

and has a diameter that is roughly one-third of that of the constrictor. This result is consistent with the constrictor arc diameter estimated earlier, and that measured in a medium-power, radiation-cooled hydrogen arcjet.[18]

Recent experimental measurements of n_e were made in the near-cathode region of 1- and 5-kW arcjets by Storm and Cappelli.[17,18] No modifications to the prototype arcjets were made, and so these measurements are nonintrusive. Using hydrogen as propellant, the centerline axial emission spectrum was measured and the near-cathode axial line-of-sight (LOS) electron number density was obtained from the Stark broadening of the wings of the H_α line. Radiative transfer effects on the spectral line are localized to near line-center, whereas the linewings are determined by the properties within approximately 1 mm of the cathode tip.[17] The thoriated tungsten cathode temperature was also measured by the broadband emission away from the Balmer lines, accounting for molecular hydrogen and continuum emission, as necessary.

A typical axial emission spectrum in the visible region is shown in Fig. 3. The broadband background is a combination of thermal radiation from the cathode and continuum emission from the plasma electrons. Molecular hydrogen emission was negligible because of the use of very slow optics.[18] Using axial variations of n_e and T_e that were computed using the single-fluid arcjet model of Butler and King[20] for a 5-kW hydrogen arcjet, the continuum emission in the axial direction was calculated with a one-dimensional radiation transfer model. This continuum emission is shown for comparison (dashed line) in Fig. 3. The background continuum is well approximated by the cathode and continuum emission assuming a T_{cat} of 3730 K. In this manner, T_{cat} was varied in the model so as to reproduce the measured continuum emission over a range of $P/\dot{m}$ values, and the results, shown in Fig. 4, indicate that T_{cat} is very near or above the melting point of pure tungsten (3690 K) and increases with $P/\dot{m}$. These results are consistent with well-documented cathode erosion measurements that infer the presence of a molten pool of tungsten at the cathode tip.[25] The increase in T_{cat} with $P/\dot{m}$ predicts an increase in arc current density at the arc attachment, consistent with the measured increase in conductivity, or n_e, as discussed next. Note that when the electron number densities computed by the model are artificially increased by about a factor of 3, the measured spectrum agree very well with that simulated on the basis of the other computed variables (dotted line in Fig. 3).

For comparison, Zhou et al.[26] measured the temperatures of thoriated tungsten cathodes in a stationary argon discharge using both single- and two-color pyrometry. They recorded tip temperatures between 3500–3800 K, depending on the cathode diameter and increasing with arc current, and hence, P.
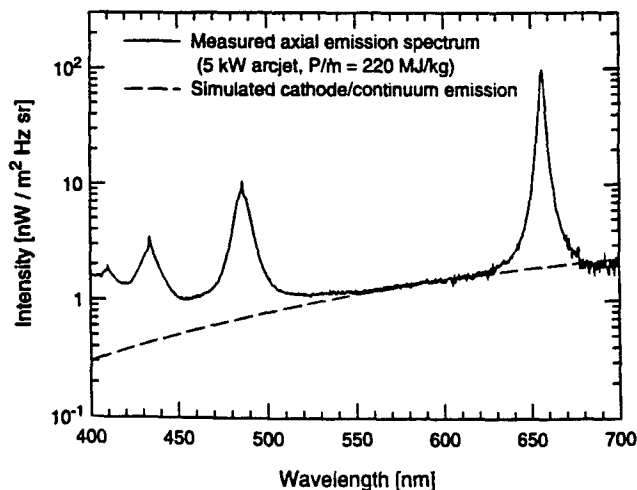

Fig. 3 Axial emission spectrum of a 5-kW hydrogen arcjet (solid line) and the calculated cathode/continuum emission (dashed line) corresponding to a cathode temperature of 3730 K.
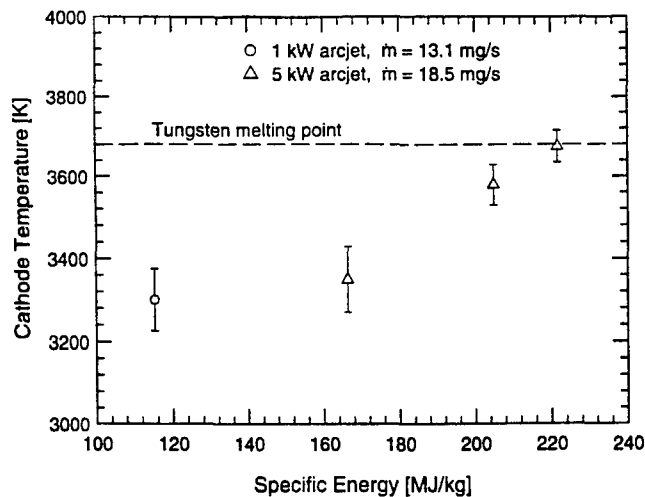
Fig. 4 Measured cathode temperature in 1- (circles) and 5-kW (triangles) arcjets operating on hydrogen propellant.
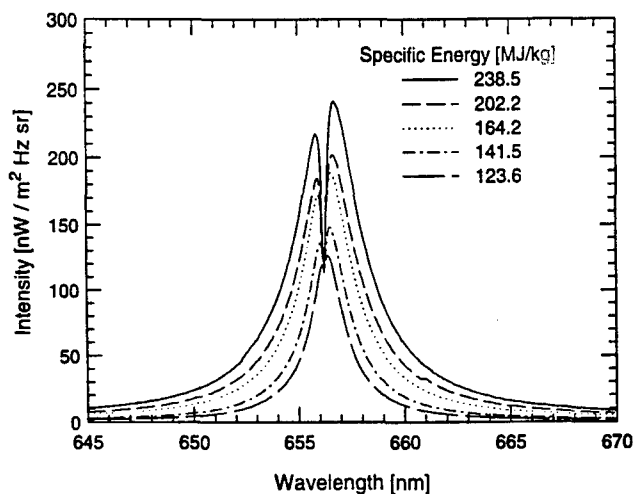
Fig. 5 Axial emission spectra of the H_α line at various specific energy for the 5-kW hydrogen arcjet showing the blue-shifted reabsorption dip near line center.

Although these experiments were performed at much higher currents, the current densities are comparable to those in the hydrogen arcjets, and the cathode temperatures are in good agreement with those measured in the arcjet.

Storm and Cappelli[17,18] measured the near-cathode n_e by the Stark broadening of the linewings of the H_α line. Their analysis is limited to the far wings of the line because the line core is expected to experience significant distortion because of self-absorption. Sample H_α emission spectra from the 5-kW arcjet are shown in Fig. 5. The line is broadened considerably because of the large n_e upstream of the constrictor, and the central dip is caused by reabsorption by the relatively cool plasma in the downstream expansion region and plume.[17,18] Based on the relative Doppler shift between the emitting plasma near the constrictor and the absorbing plasma in the plume, one would expect the central dip to be red-shifted by a small fraction of the width of the linewings, if, in accordance with the linear Stark theory, the hydrogen lines are unshifted and symmetric. However, the exact opposite is observed in Fig. 5. The large blue-shift in the central dip can be accounted for by the asymmetry in the Stark broadening of H_α, which results in an apparent red-shift of the line at large n_e.[27] For $n_e = 2 \times 10^{23}$ m^{-3}, a typical value near the cathode (see Fig. 1), the asymmetric Stark red-shift of H_α linewings is approximately 0.12 nm, which is large compared to a Doppler blue-shift of approximately 0.03 nm. Unfortunately, because of the relatively small size of the Doppler shift and the uncertainty in determining

the precise spectral line center, the axial velocity in the constrictor region could not be determined.

The width of the linewings, however, could be measured accurately, and from the Stark-broadened fullwidth at half-maximum (FWHM), the near-cathode region n_e was determined.[18] Most previous measurements involving Stark broadening of the Balmer lines of hydrogen (including Ref. 17) have made use of the Stark broadening tables compiled by Vidal, Cooper, and Smith (VCS)[28] in the early 1970s, which assumed perturbations to the atomic energy levels by electron collisions while the ions remained static. Recent Monte Carlo simulations by Kelleher et al.,[29] taking into account dynamic ions, have shown that the VCS tables underpredict the linewidths of H_α by a factor of approximately 2 at electron densities typical of the near-cathode region, and as much as a factor of 30 at lower densities. Use of the VCS tables would then result in greatly overestimated n_e from H_α. The present n_e measurements were made using the recent Monte Carlo simulations, whose FWHMs are compared to those of the VCS tables in Fig. 6. However, as these simulations were only performed up to $n_e = 10^{23}$ m^{-3}, electron densities larger than this were obtained by extrapolation.

The measured near-cathode n_e for the 1- and 5-kW arcjets are shown as a function of $P/\dot{m}$ in Fig. 7. The 1-kW results differ from those of Ref. 17 because of the improved Stark broadening calculations and linewing fits. The relatively large

Fig. 6 Stark broadened FWHM for H_α showing the discrepancy between the computations by VCS[28] and the recent Monte Carlo simulations.

Fig. 7 Measured near-cathode n_e in the 1- (circles) and 5-kW (triangles) arcjets, compared to the MHD 1-kW arcjet model of Butler and King[20,23] (see, e.g., Ref. 17) (dashed line).

uncertainties in these measurements are primarily because of the uncertainty in determining precisely which parts of the spectra of Fig. 5 constitute the linewings. In other words, the uncertainty reflects the very nature of th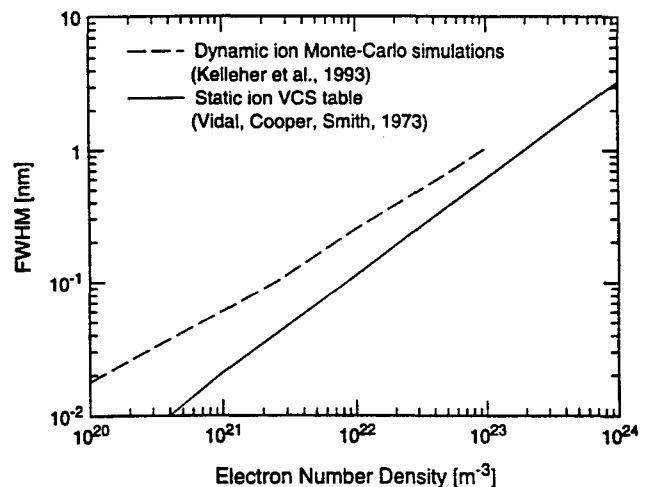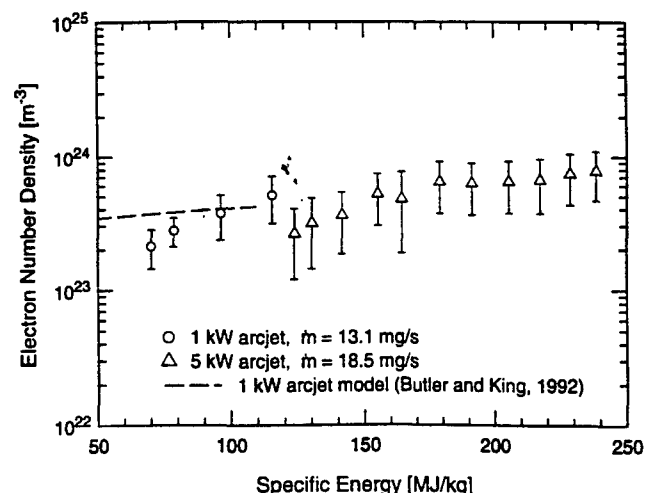ese measurements being axial LOS averages within approximately 1 mm of the cathode tip. Nevertheless, despite the large uncertainties, the increase in n_e, and therefore, plasma conductivity, with P is apparent. This is consistent with the measured increase in T_{cat} with P. Furthermore, the results for the 1-kW arcjet display reasonably good agreement to peak near-cathode n_e predicted by the MHD arcjet model simulations by Butler and King[20,23] (e.g., Ref. 18). The measured densities are somewhat lower than the calculated peak densities because of the fact that they are LOS averages over a small region.

V. LIF Measurements of Velocity

The first measurements of flow velocity in the nozzle interior were recently made using laser-induced fluorescence by Storm and Cappelli.[19] In that study, axial velocity components in a 1-kW hydrogen arcjet were measured from the Doppler shift of the hydrogen Balmer-α line from an unshifted stationary reference. To obtain optical access to the nozzle interior, the laser excitation beam was directed into the arcjet axially, while the fluorescence was collected broadband at an angle of 16 deg to the arcjet centerline. Since this angle was smaller than the 20-deg divergence half-angle of the nozzle expansion, the plasma could be probed everywhere downstream of the arcjet throat. The drawback to this technique, however, was the considerable background signal created by scattered laser light in the nozzle. This signal noise was the limiting factor in restricting the physical domain of the measurements to near the arcjet centerline where the LIF signal was the greatest. Despite this background noise, measurements were obtained along the axis of the nozzle from the exit plane to within 1.5 mm of the throat, and radial scans were obtained at three different axial positions.

The measured axial velocities are given in Figs. 8 and 9. As no other measurements of velocity have been made in the arcjet nozzle interior, the results can only be compared to simulations of the 1-kW hydrogen arcjet using the model of Butler and King.[20,23] The most recent model results of the centerline axial velocity, given as a function of area ratio in Fig. 8, are in very good agreement with the measurements. The centerline velocity is seen to drop monotonically from a peak of approximately 17.5 km/s at 1.3 mm downstream of the throat (area ratio of approximately 6) to around 12 km/s at the exit plane (area ratio of 225). This apparent axial drop in velocity is contrary to what one would expect in a supersonic diverging
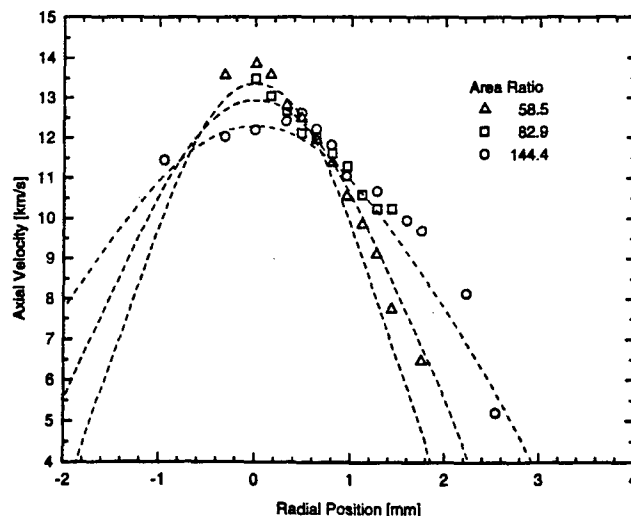
Fig. 9 Radial profiles of axial velocity at three axial locations within the arcjet nozzle. The errors are typically ±0.6 km/s. The dashed lines are results of the Butler and King[20,23] arcjet model (Ref. 19) at the same axial locations as the measurements.

nozzle; however, as the centerline temperature drops rapidly in the axial direction (Fig. 2), the Mach number increases as expected. Since the expansion converts thermal energy into kinetic energy, the mass-average velocity must necessarily increase in the downstream axial direction. The observed drop in centerline velocity must therefore be a result of viscous transport of axial momentum in the radial direction, indicating the importance of viscosity in this flowfield.

As a result of the radial transport of momentum away from the nozzle centerline, the axial velocity far from the centerline should increase with downstream position. This is evident in Fig. 9, which shows radial profiles of the axial velocity measured at three axial positions within the nozzle. (The LIF signal intensity drops off quickly with radial position, indicating a rapid radial decrease in the $n = 2$ excited state number density of atomic hydrogen. This loss in signal restricted the measurement domain to within approximately 2 mm of the nozzle centerline.) The dashed lines in the figure are the model results at the same axial locations as the measurements. The measurements and the model show remarkably good agreement, however, the modeled velocities are somewhat lower than the measurements away from the arcjet centerline. As predicted, the velocities away from the centerline increase with axially position. Since most of the mass convection occurs in this outer region, the total kinetic energy of the flow is increasing downstream, as expected.

VI. Summary

In this article, we have reviewed past measurements of flow properties in the nozzle interior and constrictor (near-cathode) region of arcjet thrusters. Many of the measurements reveal flow behavior that is consistent with recent arcjet simulations. These measurements include static pressure, anode current distribution, plasma density, velocity and temperatures, and cathode temperature. Advances have been made in the use of nonintrusive optical diagnostics to measure arcjet flow properties in the near-cathode and anode throat region, where the arc is greatly constricted and strongly contributes to heat transfer and device performance.

Static pressure measurements in low power arcjets indicate that the sonic point is very near the constrictor, in contrast to similar measurements in higher-power arcjets, where higher aspect-ratio constrictors give rise to boundary-layer growth that moves the sonic point downstream of the constrictor exit. Electron number densities based on static pressure measurements compare favorably to those computed on the basis of resistive MHD simulations. Optical emission measurements in-
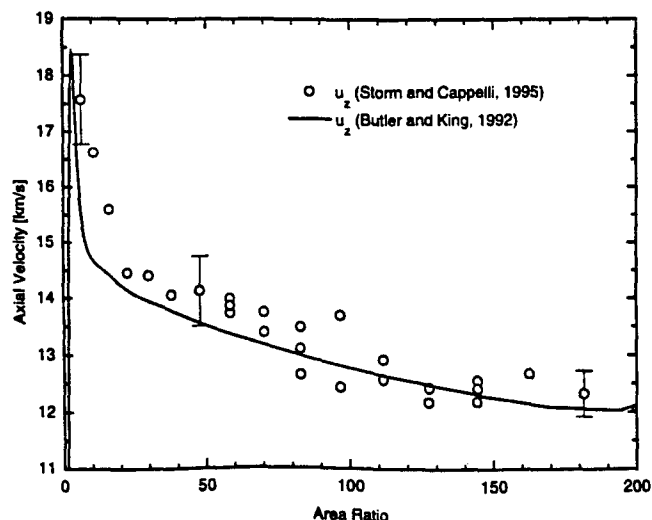

Fig. 8 Measured axial velocity along the arcjet centerline, compared to the MHD 1-kW arcjet mode of Butler and King[20,23] (see also Ref. 19). Typical errors are shown.

dicate that n_e drops downstream of the throat, suggesting a concomitant decrease in the current densities. It is suspected that the drop in current density strongly favors diffuse attachment along the anode.

Electrical measurements using a segmented anode configuration support the notion that the anode arc attachment is diffuse as opposed to constricted. In low-power arcjets, the current appears to be distributed across the anode in a way that is consistent with the observed decrease in plasma density (and, hence, plasma conductivity). Measurements of floating potential permit an estimate of the electric field strength in the throat. From this, we have estimated the extent of arc constriction and have found that the arc cross-sectional area is approximately one-tenth of the constrictor area, consistent with recent estimates based on Stark-broadened axial line emission. It is also apparent, from floating potential measurements, that the anode fall voltage varies dramatically along the anode, being near zero in the region of attachment near the exit plane and close to 40 V at the attachment near the throat.

A range of spectroscopic studies, implemented by collecting plasma emission side-on through holes in the anode, and end on by collecting light axially, support the conjecture that the nozzle flow is removed from thermal equilibrium. The departure from thermal equilibrium is evidenced by an elevated T_{elec}, and is less severe in the upstream plasma near the throat. This is expected, since the higher pressures and plasma densities in that region give rise to a plasma that is close to Saha equilibrium. The expansion process creates an overdense plasma and subsequently overpopulates excited electronic levels.

Near-cathode electron number densities are found to be only weakly dependent on $P/\dot{m}$. This trend is captured by the MHD simulations. An increase in static pressure is therefore expected to reflect an increase in throat temperatures, a result that has yet to be verified by experimental observations. For the first time, direct and nonintrusive measurements of T_{cat} have been made in 1- and 5-kW hydrogen arcjet thrusters. These measurements indicate that cathode temperatures apparently exceed the melting point of tungsten at modest $P/\dot{m}$ (200 MJ/kg) and are apparently below the melting point at lower $P/\dot{m}$.

Measurement of plasma velocities in the nozzle expansion flowfield indicate a viscous diffusion of axial momentum away from the arcjet axis and a corresponding decrease in axial velocity. This observation is also seen in the MHD simulations and is an indication of the highly viscous nature of the plasma flow within the arcjet nozzle.

Despite the progress that has been made in diagnostics of the internal flow, many issues related to performance efficiency and lifetime are still unresolved. Although existing models do well at predicting the exit plane plasma conditions, they seem to still overpredict thrust efficiency. It is the combined effort of modeling and experimental measurements of internal flow properties that will lead to a better understanding of plasma flow behavior, and hence, models with better predictive capabilities.

Acknowledgments

References

[1]Vaughan, C., and Cassady, J., "An Updated Assessment of Electric Propulsion Technology for Near-Earth Space Missions," AIAA Paper 92-3202, July 1992.

[2]Manzella, D. H., Curran, F. M., Myers, R. M., and Zube, D. M., "Preliminary Plume Characteristics of an Arcjet Thruster," AIAA Paper 90-2645, July 1990.

[3]Hoskins, W. A., Kull, A. E., and Butler, G. W., "Measurement of Population and Temperature Profiles in an Arcjet Plume," AIAA Paper 92-3240, July 1992.

[4]Carney, L. M., and Keith, T. G., "Langmuir Probe Measurements of an Arcjet Exhaust," *Journal of Propulsion and Power*, Vol. 5, No. 3, 1989, pp. 287–294.

[5]Van Camp, W. M., Esker, D. W., Checkley, R. J., Duke, W. G., Kroutil, J. C., Merrifield, S. E., and Williamson, R. A., "Study of Arcjet Propulsion Devices," NASA CR-54691, March 1966.

[6]Cappelli, M. A., Hanson, R. K., Liebeskind, J. G., and Manzella, D. H., "Optical Diagnostics of a Low Power Hydrogen Arcjet," 22nd International Electric Propulsion Conf., Paper 91-091, Oct. 1991.

[7]Liebeskind, J. G., Hanson, R. K., and Cappelli, M. A., "Flow Diagnostics of an Arcjet Using Laser-Induced Fluorescence," AIAA Paper 92-3243, July 1992.

[8]Beattie, D. R., and Cappelli, M. A., "Raman Scattering Measurements of Molecular Hydrogen in an Arcjet Thruster Plume," AIAA Paper 95-1956, June 1995.

[9]Crofton, M. W., Welle, R. P., Jansen, S., and Cohen, R. B., "Temperature, Velocity and Density Studies in the 1-kW Ammonia Arcjet Plume by LIF," AIAA Paper 92-3242, July 1992.

[10]Talley, K., Elrod, W., and Curran, F. M., "Static Pressure Measurements of the NASA Lewis 1.2-kW Arcjet," AIAA Paper 92-3111, July 1992.

[11]Harris, W. J., O'Hair, E. A., Hatfield, L. L., Kristiansen, M., and Grimes, M. D., "Static Pressure Measurements in a 30-kWe Class Arcjet," AIAA Paper 91-2457, June 1991.

[12]Curran, F. M., and Manzella, D. H., "The Effect of Electrode Configuration on Arcjet Performance," NASA TM 102346, July 1989.

[13]Zube, D. M., and Myers, R. M., "Thermal Nonequilibrium in a Low Power Arcjet Nozzle," *Journal of Propulsion and Power*, Vol. 9, No. 4, 1993, pp. 545–552.

[14]Hargus, W., Micci, M., and Spores, R., "Interior Spectroscopic Investigation of the Propellant Energy Modes in an Arcjet Nozzle," AIAA Paper 94-3302, June 1994.

[15]Glocker, B., and Auweter-Kurtz, M., "Numerical and Experimental Constrictor Flow Analysis of a 10 kW Thermal Arcjet," AIAA Paper 92-3835, July 1992.

[16]Ishi, M., and Kuriki, K., "Optical and Analytical Studies of Arc Column in DC Arcjet," AIAA Paper 87-1086, May 1987.

[17]Storm, P. V., and Cappelli, M. A., "Axial Emission Diagnostics of a Low Power Hydrogen Arcjet Thruster," 23rd International Electric Propulsion Conf., Paper 93-219, Sept. 1993.

[18]Storm, P. V., and Cappelli, M. A., "Axial Emission Measurements on a Medium Power Hydrogen Arcjet Thruster," AIAA Paper 94-2743, June 1994.

[19]Storm, P. V., and Cappelli, M. A., "Laser-Induced Fluorescence Measurements Within an Arcjet Thruster Nozzle," AIAA Paper 95-2381, July 1995.

[20]Butler, G. W., and King, D. Q., "Single and Two Fluid Simulations of Arcjet Performance," AIAA Paper 92-3104, July 1992.

[21]Yuan, B. P., and Cappelli, M. A., "Linear Stability Analysis of the Ionization Layer of a Diffuse Anode Arc," AIAA Paper 95-3064, July 1995.

[22]Yuan, B. P., and Cappelli, M. A., "Stability of a Near-Thermal Plasma in Contact with an Anode," AIAA Paper 95-1991, June 1995.

[23]King, D. Q., and Butler, G. W., "Modeling and Measurements of N_2 Arcjet Performance," AIAA Paper 90-2616, July 1990.

[24]Mitchner, M., and Kruger, C. H., Jr., *Partially Ionized Gases*, Wiley, New York, 1974.

[25]Curran, F. M., Haag, T. W., and Raquet, J. F., "Arcjet Cathode Phenomenon," NASA TM 102099, May 1989.

[26]Zhou, X., Berns, D., and Heberlein, J., "Arc Electrode Interaction Study," NASA Grant NAG3-1332, Final Rept. June 1994.

[27]Wiese, W. L., Kelleher, D. E., and Paquette, D. R., "Detailed Study of the Stark Broadening of Balmer Lines in a High-Density Plasma," *Physical Review A: General Physics*, Vol. 6, No. 3, 1972, pp. 1132–1153.

[28]Vidal, C. R., Cooper, J., and Smith, E. W., "Hydrogen Stark Broadening Tables," *Astrophysical Journal Supplement Series*, Vol. 25, No. 214, 1973, pp. 37–136.

[29]Kelleher, D. E., Wiese, W. L., Helbig, V., Greene, R. L., and Oza, D. H., "Advances in Plasma Broadening of Atomic Hydrogen," *Physica Scripta*, Vol. T47, 1993, pp. 75–79.

Stark broadening corrections to laser-induced fluorescence temperature measurements in a hydrogen arcjet plume

P. Victor Storm and Mark A. Cappelli

Laser-induced fluorescence of the H_α transition of atomic hydrogen has previously been performed in the plume of a hydrogen arcjet thruster. Measurements of plasma velocity and temperature, based on the Doppler shift and broadening of the H_α line shape, were previously published [Appl. Opt. **32**, 6117 (1993)]. In that paper the Stark broadening of the H_α transition was estimated from static-ion calculations performed in the early 1970's and found to be negligible in comparison with the Doppler broadening. However, more recent dynamic-ion calculations have shown the Stark broadening to be considerably larger than was previously assumed, resulting in inaccurate temperature measurements. We present a reanalysis of the fluorescence data, taking into account the improved Stark broadening calculations. The correct atomic hydrogen translation temperature and electron number density are obtained from the Doppler and Stark broadening components of the measured line shape. The results indicate a substantial drop in temperature from those previously reported. © 1996 Optical Society of America

Key words: Arcjet, laser-induced fluorescence, atomic hydrogen, hydrogen plasma, Balmer alpha. Stark broadening, Doppler broadening, translation temperature, electron number density.

1. Introduction

Arcjet thrusters are devices used to produce low thrust, high-impulse gas flows for satellite station-keeping and are potentially targeted for satellite orbit transfer maneuvers. Thermal energy is supplied to the propellant by joule heating within a constricted arc, stabilized in the throat region of the converging–diverging nozzle. Temperatures within the arc are much higher than those attainable in a conventional chemical thruster; hence, a specific impulse two or three times greater than that of the best chemical rocket can be achieved. Research is currently under way to increase the specific impulse and improve the efficiency of arcjets and to design lower-power versions for onboard propulsion on proposed microsatellites. To aid in the design and development of better arcjets, researchers have developed sophisticated arcjet models.[1,2] These models can be used to predict the operating behavior and scaling laws of the

thruster, leading to a better understanding of the physical processes occurring within the arcjet and especially the energy loss mechanisms. Proper validation of the models, however, requires measurements of thermodynamic and fluid mechanical properties of the plasma within and exhausting from the thruster. To date a considerable number of investigations have been made to measure plasma properties in the arcjet plume. Laser-induced fluorescence has been demonstrated to be ideal for such measurements because of its excellent spatial resolution, specie-specific nature, and abundant signal level.

Recent measurements of velocity and translation temperature were performed by Liebeskind *et al.*,[3] who used laser-induced fluorescence (LIF) on the Balmer-α transition of atomic hydrogen in the plasma plume of a 1-kW-class radiation-cooled hydrogen arcjet thruster. In these experiments the Balmer-α (H_α) transition was spectrally scanned by the laser excitation while the fluorescence signal was collected broadband. The fluorescence line shape obtained was fit with a Gaussian function to determine velocity (from the Doppler shift of the line center relative to a stationary reference source) and atomic translation temperature (from the Doppler broadening of the line). A comparison of these measurements at the arcjet exit plane with results of a

single-fluid continuum arcjet model[4] found the velocities in excellent agreement, but the measured temperatures were considerably higher than the modeled temperatures.[5] Other line broadening mechanisms were considered as a possible explanation for this discrepancy, but they were found to be insignificant.[3] In particular, the maximum contribution to the H_α linewidth caused by Stark broadening was estimated from a previously measured upper limit of the electron number density[6] and static-ion Stark broadening tables based on calculations of electron impact broadening, assuming stationary ions.[7] The estimated maximum Stark linewidth was approximately $0.01\ \mathrm{cm}^{-1}$. By comparison, the Doppler broadening was of the order of $0.70\ \mathrm{cm}^{-1}$; hence, Stark broadening was considered negligible.

Recent Monte Carlo simulations of charged-particle collisional broadening in hydrogen, which include the effects of ion collisions, have revealed that the static-ion calculations underpredict the true Stark broadening of H_α.[8] The error may be as large as a factor of 30 at electron number densities typically found in the plume of the arcjet, indicating that Stark broadening is truly significant and must be taken into account in determining the translation temperature from the linewidth. Plasma emission measurements recently performed in the plume of the arcjet have shown that Stark broadening of H_α is indeed significant at the arcjet exit plane.[9] In this latter study both translation temperature and electron number density were determined as a function of radial position and arcjet power. The temperature measurements were found to be in good agreement with the aforementioned arcjet model. These findings motivated a reanalysis of the LIF measurements, duly taking into account the most recent Stark broadening calculations of the atomic line shape.

2. Analysis

The H_α line of atomic hydrogen corresponds to the transition between the first and second excited electronic states. Both states of this transition are split because of spin-orbit coupling, and the selection rules give rise to five allowable transitions between these states.[3] The resulting line shape therefore consists of five closely spaced fine-structure lines. The strength and relative position of these five lines are given in Table 1. Each of these lines is spectrally broadened by two mechanisms: atomic thermal motion of the emitter and collisions of the emitter with charged particles. The former mechanism is responsible for Doppler broadening and produces a Gaussian line shape when the emitters have a Maxwellian velocity distribution. The Gaussian linewidth FWHM is related to the translation temperature according to the Doppler broadening relation[10]

$$\Delta\lambda_G = \lambda_0 \left(\frac{8\ln 2\, kT}{mc^2}\right)^{1/2},\qquad (1)$$

Table 1. Relative Positions and Intensities of the Fine Structure Component Lines of the Balmer-α Transition of Hydrogen

Upper j	Lower j	Transition	δr (cm^{-1})	Relative Intensity
1/2	3/2	$3S_{1/2} \leftrightarrow 2P_{3/2}$	−0.144	0.05
3/2	3/2	$3D_{3/2} \leftrightarrow 2P_{3/2}$	−0.036	0.28
5/2	3/2	$3D_{5/2} \leftrightarrow 2P_{3/2}$	0.000	2.50
1/2	1/2	$3S_{1/2} \leftrightarrow 2P_{1/2}$	0.220	0.31
		$3P_{1/2} \leftrightarrow 2S_{1/2}$		
3/2	1/2	$3P_{3/2} \leftrightarrow 2S_{1/2}$	0.328	1.96
		$3D_{3/2} \leftrightarrow 2P_{1/2}$		

where m is the atomic mass, c is the speed of light in a vacuum, k is the Boltzmann constant, and λ_0 is the unshifted line-center wavelength.

The broadening mechanism associated with charged-particle collisions is Stark broadening. In general, the Stark-broadened line shape depends strongly on electron number density and the particular electronic transition, and it depends weakly on electron and ion temperatures. The Stark broadening of H_α has been recently calculated by a dynamic-ion Monte Carlo simulation.[8] It has been found[11] that ion collisions play the dominant role in broadening the H_α line for electron number densities below approximately $10^{20}\ \mathrm{m}^{-3}$. At these low electron densities, the ion collision duration is shorter than the coherence time for the transition; hence, the ions can be treated in the impact limit. In this limit the Stark-broadened FWHM of H_α in a pure hydrogen plasma is given by the expression[12]

$$\Delta\lambda_L = 1.55 \times 10^{-4}\frac{\lambda_0^2}{\pi c}n_e\left(\frac{m_i}{2m_e}\right)^{1/2}\frac{1}{\sqrt{T_i}}$$

$$\times\left[27.54 + \ln\left(\frac{2T_DT_im_e}{n_em_i}\right)\right],\qquad (2)$$

where $T_D \equiv T_eT_i/(T_e + T_i)$, n_e is the electron number density in units of inverse cubed centimeters, m_e and m_i are the electron and ion masses, and T_e and T_i are the electron and ion temperatures in degrees Kelvin. The line shape is Lorentzian in the ion-impact limit.[13] The dependence of the linewidth on ion temperature is $\sim T^{-1/2}$, while the dependence on electron temperature is considerably weaker.

When both Doppler and Stark broadening mechanisms exist simultaneously, the resulting line shape is a convolution of a Gaussian and a Lorentzian, producing a Voigt line-shape function. The measured H_α line shape was fit by a sum of five Voigt functions, one for each of the fine-structure lines. However, because of the known relationships between the relative line positions and strengths, the fit contained only five parameters: the amplitude, line-center position, baseline offset, Gaussian width, and Voigt a parameter, which is defined as

$$a \equiv \frac{\sqrt{\ln 2}\,\Delta\lambda_L}{\Delta\lambda_G}.\qquad (3)$$
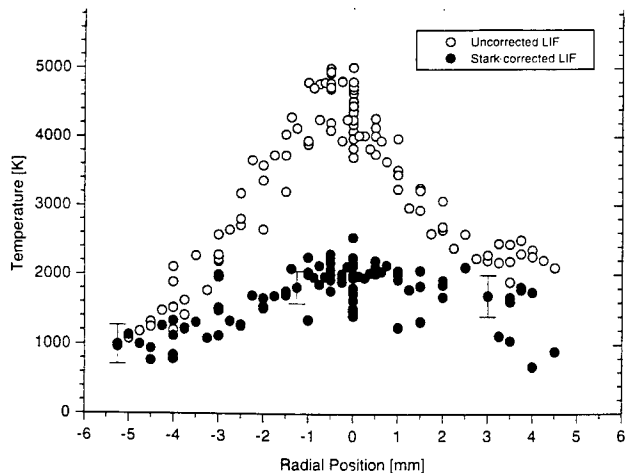
Fig. 1. Translation temperature at the arcjet exit plane at an arcjet power of 1.43 kW.

Fig. 2. Translation temperature at the arcjet exit plane center line as a function of arcjet power.

Atomic translation temperature and electron number density were determined from the best-fit Gaussian and Lorentzian widths according to Eqs. (1) and (2), respectively. For the electron number density to be calculated by using Eq. (2), the ion and electron temperatures were obtained as follows. Thermal equilibrium was assumed between the ion and atom species; hence, the ion temperatures were taken to be the measured atom translation temperatures. Previous emission measurements at the exit plane of the arcjet have shown that the electrons are not in equilibrium with the atoms.[9] Electron temperatures in the range of 0.8 to 1.3 eV were measured in that study, depending on the radial position and the arcjet power. Because the dependence on electron temperature is very weak, an average value of 1.0 eV was assumed throughout the analysis.

3. Results

As mentioned above, the velocity measurements are not affected by the Stark broadening and are therefore considered correct. The corrected translation temperature results are shown in Figs. 1–3. In these figures the open circles represent the original temperature measurements while the filled circles are the Stark-corrected temperatures. The original temperature measurements can be found in Ref. 3 (Figs. 9, 11, and 12, respectively).

Figure 1 shows the translation temperature as a function of radial position at 0.4 mm downstream of the arcjet exit plane at an arcjet power of 1.43 kW and a H_2 mass flow rate of 13 mg/s. The selected error bars on the corrected temperatures are representative of the uncertainty in the best-fit Doppler widths, as discussed below. The true error, caused by the scatter in the data, is evidently somewhat larger. By accounting for Stark broadening, the temperature profile has been considerably reduced from a peak of approximately 4500 K in the original data to approximately 2000 K. Near the edge of the plume the temperature has also decreased somewhat. This
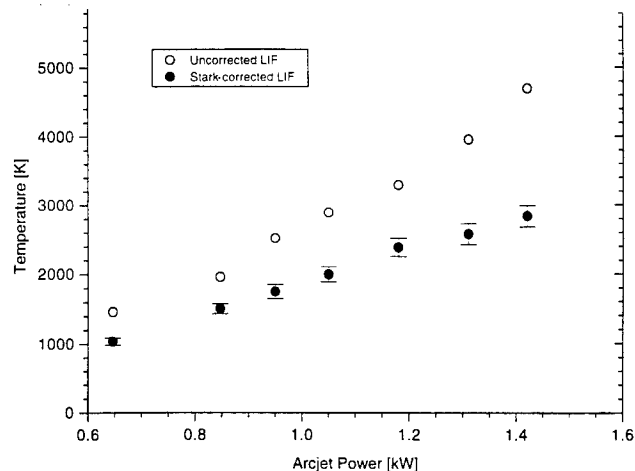
temperature drop represents a significant decrease in exhausting enthalpy, implying that the arcjet is operating more efficiently than was previously thought. The apparent radial shift of approximately 0.5 mm in the peak of the temperature profile was due to the difficulty in establishing the plume center line, and it was not due to flow asymmetry.[3] (A preliminary Stark correction to these data was presented in Ref. 9, Fig. 11, with a peak center-line temperature of approximately 3500 K. This preliminary correction did not account for spin-splitting of the transition, resulting in the erroneously high temperatures reported in that paper.)

The center-line translation temperatures are shown in Fig. 2 as a function of arcjet power at a fixed mass flow rate of 13 mg/s. The corrected temperatures still increase approximately linearly with arcjet power, although with a lower slope than the uncorrected temperatures. This increase with arcjet power is indicative of the increase in enthalpy con-
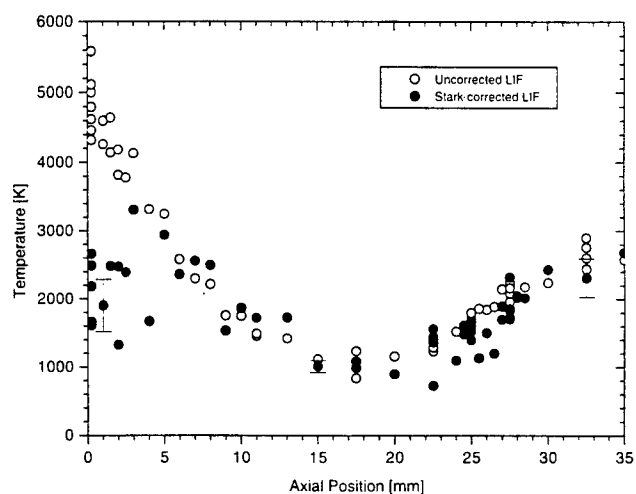
Fig. 3. Translation temperature along the plume center line at an arcjet power of 1.43 kW.
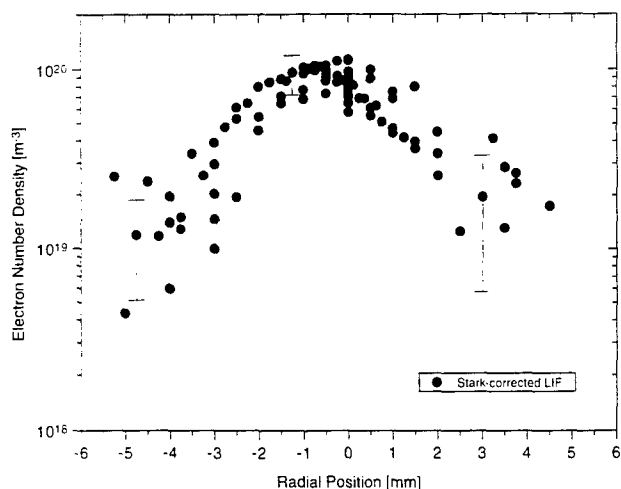
Fig. 4. Electron number density at the arcjet exit plane at an arcjet power of 1.43 kW.
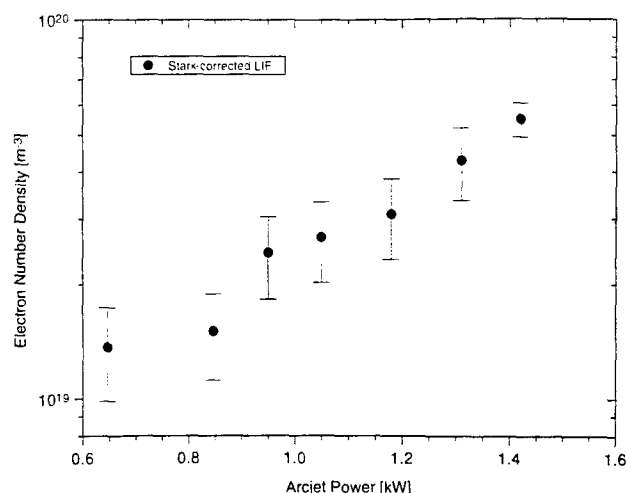
Fig. 5. Electron number density at the arcjet exit plane center line as a function of arcjet power.

vected out of the thruster and is consistent with the observed decrease in arcjet efficiency with specific energy. The lower slope, however, indicates that the decrease in efficiency with power is less extreme than was previously believed.

Figure 3 shows the variation of temperature with axial position along the center line of the plume under the same operating conditions as in Fig. 1. As in the previous figures, the error bars, given on a few selected points, are determined by the uncertainty in the Doppler component of the best-fit line shape and underestimate the true uncertainty in the temperature measurements. Having an additional parameter, the Voigt fit is less precise than a Gaussian fit; hence, the scatter is larger in the corrected temperatures than in the uncorrected temperatures. It is interesting to note that the only significant difference between the uncorrected and the corrected data occurs within a few millimeters of the nozzle exit. In this region the electron number density is substantial enough to produce a significant Stark-broadening component, resulting in lower corrected temperatures. Beyond approximately 5 mm from the exit plane the Stark broadening is considerably less important and the corrected and uncorrected temperatures are nearly identical. The initial drop in temperature with axial position is due to the fact that flow is underexpanded at the arcjet exit plane. The rise in temperature evident at approximately 22 mm downstream of the exit plane occurs as a result of a compressive shock, indicative of a diamond shock structure in the plume.[3]

The electron number densities were calculated from the Lorentzian components of the Voigt fits and are presented in Figs. 4–6, analogous to the temperatures of Figs. 1–3. The radial profile (Fig. 4) is very symmetric and peaks at approximately 10^{20} m^{-3}, confirming the ion-impact criterion for the Stark broadening. As in the temperature results, a few typical error bars are given on selected data points. It is evident that there is considerably more scatter in

the data away from the arcjet center line than near the center line. This is due to the greatly reduced LIF signal intensity far from the center line and the consequential increased noise in the fluorescence scans. The presence of electrons convecting out of the arcjet constitutes an ionization energy loss. With the assumption of no slip velocity between the electrons, ions, and atoms, and with the use of the measured axial velocity profile given in Ref. 3, the ionization energy flux at the exit plane was calculated to be less than 40 W. Representing less than 3% of the arcjet power, this ionization energy flux does not contribute significantly to the total energy loss.

The center-line electron number density, given in Fig. 5, increases approximately exponentially with arcjet power. An increase in the electron density by a factor of 4 is evident in less than a twofold increase in arcjet power from 0.85 to 1.43 kW. This constitutes a significant change in the ionization energy flux; however, as stated above, the ionization energy
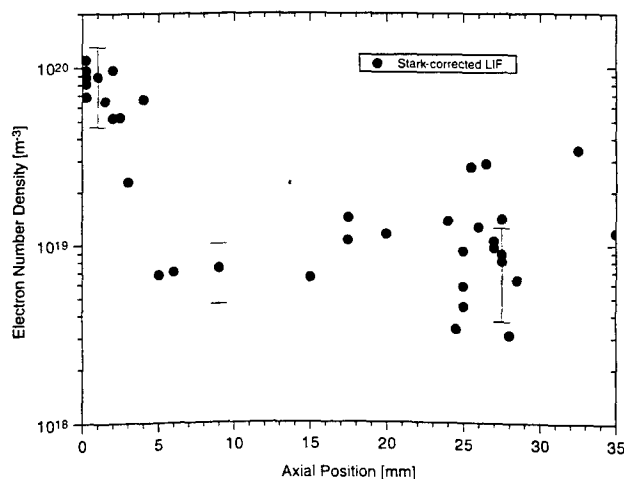
Fig. 6. Electron number density along the plume center line at an arcjet power of 1.43 kW.
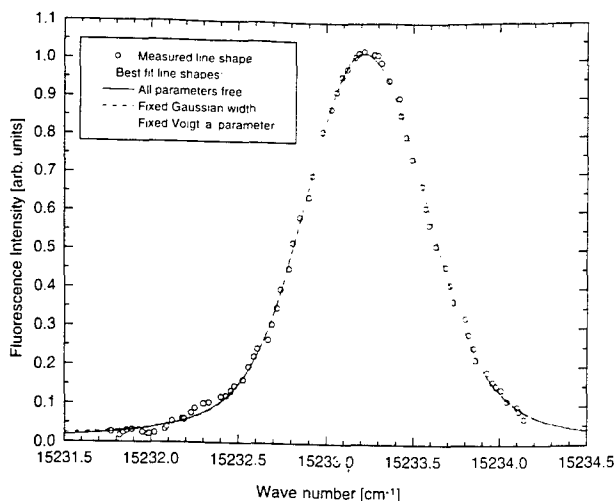
Fig. 7. Typical measured H_α line shape and best fits. The fits are nearly indistinguishable, explaining the large uncertainties in the temperatures and electron number densities given in the previous figures.

loss does not have a large effect on the overall efficiency of the thruster.

Finally, the axial dependence of the center-line electron number density is shown in Fig. 6. The density drops an order of magnitude in the first 5 mm and then rises slowly thereafter. The initial drop is consistent with the decrease in temperature seen in Fig. 3 and fact that the plasma is in a recombining state as it is exhausting from the arcjet. Beyond 25 mm downstream the scatter in the data is quite significant and the electron number density is difficult to determine accurately.

A note on the fitting accuracy and error bars is in order. In a multiparameter fit, as is the case with a Voigt function, the fitting parameters are sensitive to each other as well as to the noise in the data. To demonstrate the accuracy of the measured temperatures and electron number densities, Fig. 7 shows a typical measured H_α line shape at the arcjet exit plane center line and a power of 1.43 kW. The best fit to the data, allowing all parameters to vary freely, is shown as the solid curve and has the values of $T = 1947 \pm 372$ K and $n_e = (8.2 \pm 3.7) \times 10^{19}$ m^{-3}. The other two curves show the best fits determined by fixing either the Gaussian width or Voigt a parameter at one standard deviation from their optimal values while letting the other parameters vary. The three fits are almost identical and are only slightly distinguishable far from the line center. With the Gaussian width fixed at $\pm\sigma$ from its value determined in the free fit, the electron density is found to be 6.5×10^{19} m^{-3} ($+\sigma$) and 9.5×10^{19} m^{-3} ($-\sigma$). With the Voigt a parameter fixed at $\pm\sigma$ of its optimum value, the temperature is found to be 1570 K ($+\sigma$) and 2350 K ($-\sigma$). These ranges of values are of the order of the measured uncertainties of n_e and T, as expected.

4. Conclusions

A reanalysis of the laser-induced fluorescence measurements presented in Ref. 3 has been performed, taking into account recent dynamic-ion Stark broadening calculations for the H_α line of hydrogen. The original translation temperature measurements are in error because they did not account for Stark broadening. The velocity measurements presented in Ref. 3 are based on the Doppler shift of the line and are believed to be correct. The reanalysis has permitted an accurate determination of both atomic hydrogen translation temperature and electron number density from the Gaussian and Lorentzian components of the line shape, respectively. The translation temperatures are reduced considerably from those presented in Ref. 3, indicating less enthalpy loss and therefore a more efficient arcjet operation than was previously believed. The measured electron number densities display trends that correlate well with the measured temperatures. The total ionization energy loss has been estimated from the radial profiles of velocity and electron number density, and it has been found to be less than 3% of the total arcjet power.

References

1. G. W. Butler, A. E. Kull, and D. Q. King, "Single fluid simulations of low power hydrogen arcjets," presented at the 30th AIAA Joint Propulsion Conference, Indianapolis. Ind., 27–29 June 1994, paper AIAA 94-2870.
2. I. D. Boyd, D. R. Beattie, and M. A. Cappelli, "Numerical and experimental investigations of low-density supersonic jets of hydrogen," J. Fluid Mech. **280**, 41–67 (1994).
3. J. G. Liebeskind, R. K. Hanson, and M. A. Cappelli. "Laser-induced fluorescence diagnostic for temperature and velocity measurements in a hydrogen arcjet plume," Appl. Opt. **32**, 6117–6127 (1993).
4. G. W. Butler. B. A. Kashiwa, and D. Q. King, "Numerical modeling of arcjet performance," presented at the 21st AIAA Fluid Dynamics. Plasmadynamics and Lasers Conference, Seattle, Wash., 18–20 June 1990, paper AIAA 90-1474.
5. M. A. Cappelli. J. G. Liebeskind, R. K. Hanson, G. W. Butler, and D. Q. King, "A comparison of arcjet plume properties to model predictions," presented at the 31st AIAA Aerospace Sciences Meeting. Reno, Nev., 11–14 January 1993, paper AIAA 93-0820.
6. D. H. Manzella, F. M. Curran, R. M. Myers, and D. M. Zube. "Preliminary plume characteristics of an arcjet thruster." presented at the 21st AIAA International Electric Propulsion Conference, Orlando, Fla., 18–20 July 1990, paper AIAA 90-2645.
7. C. R. Vidal. J. Cooper, and E. W. Smith, "Hydrogen Stark broadening tables," Astrophys. J. Suppl. Ser. **25**, 37–136 (1973).

8. D. E. Kelleher, W. L. Wiese, V. Helbig, R. L. Greene. and D. H. Oza. "Advances in plasma broadening of atomic hydrogen," Phys. Scr. T **47**, 75–79 (1993).

9. P. V. Storm and M. A. Cappelli, "High spectral resolution emission study of a low power hydrogen arcjet plume," presented at the 26th AIAA Plasmadynamics and Lasers Conference. San Diego, Calif., 19–22 June 1995, paper AIAA 95-1960.

10. W. Demtröder, *Laser Spectroscopy* (Springer-Verlag, Berlin, 1981).

11. D. H. Oza, R. L. Greene, and D. E. Kelleher. "Collisional broadening of the Balmer-α transition of H and He$^-$ in plasmas," Phys. Rev. A **37**, 531–536 (1988).

12. C. Stehlé and N. Feautrier. "Stark broadening of the H_α line of hydrogen at low densities: quantal and semiclassical results." J. Phys. B **17**, 1477–1489 (1984).

13. D. H. Oza. R. L. Greene. and D. E. Kelleher, "Dependence of the half widths of plasma-broadened hydrogen lines on reduced mass, temperature and density," Phys. Rev. A **38**, 2544–2551 (1988).

14. J. A. Pobst, I. J. Wong. and R. A. Spores, "Laser-induced fluorescence of ground state hydrogen atoms at the nozzle exit of an arcjet thruster." presented at the 31st AIAA Plasmadynamics and Lasers Conference, San Diego, Calif., 19–22 June 1995, paper AIAA 95-1973.

Fluorescence Velocity Measurements in the Interior of a Hydrogen Arcjet Nozzle

P. Victor Storm and Mark A. Cappelli

Fluorescence Velocity Measurements in the Interior of a Hydrogen Arcjet Nozzle

P. Victor Storm* and Mark A. Cappelli†
Stanford University, Stanford, California 94305-3032

Introduction

A S arcjet thrusters have advanced from laboratory devices to in-flight operational thrusters for satellite north-south station-keeping, there has been an increase in interest in improving arcjet efficiency and operating range. These improvements will be obtained primarily through advanced analytical modeling of arcjets; however, validation of the models can be performed only by comparison with experimental measurements of operating parameters and plasma properties. During the past several years, a number of optical diagnostics have been developed to investigate properties in the plasma plume of the arcjet. Primary among these diagnostics is laser-induced fluorescence (LIF), which has proven very useful because of its abundant signal level, very good spatial resolution, and specie-specific nature. Plasma properties in the plume of an arcjet thruster operating on a variety of propellants have been measured using LIF. Liebeskind et al.[1] measured atomic hydrogen translational temperature and velocity at the exit plane of a 1-kW hydrogen arcjet thruster, and investigated slip velocity by the fluorescence of helium in a helium-seeded hydrogen arcjet.[2] Ruyten and Keefer[3] measured velocity in an argon plume of a 0.3-kW arcjet, and Ruyten et al.[4] performed LIF on atomic hydrogen and nitrogen to measure velocity in a 1-kW arcjet plume using simulated ammonia as the propellant. Recently, Pobst et al.[5] measured ground-state atomic hydrogen density, temperature, and velocity profiles at the exit plane of a 1-kW hydrogen arcjet using pulsed two-photon LIF.

Although LIF has been successfully applied to arcjet thrusters as a plasma plume diagnostic, it has not been used previously to investigate plasma properties within the nozzle because of geometric constraints and reduced signal-to-background noise ratios. Optical studies of the plasma in the interior of the arcjet were performed

previously only in emission.[6] An analysis based on collisional-radiative modeling suggests the feasibility of applying laser-induced fluorescence to the plasma in the interior of a low-power hydrogen arcjet.[7] The first use of laser-induced fluorescence for spatially resolved plasma velocity measurements within an arcjet nozzle are described. The arcjet was operated on a propellant of pure hydrogen. The Balmer-α transition of atomic hydrogen was scanned by the excitation laser source while simultaneously detecting the spectrally integrated resonance fluorescence. Velocity was determined from the Doppler shift in the peak of the laser excitation spectrum relative to a stationary reference. The arcjet operating conditions were chosen to facilitate a comparison between these measurements and arcjet modeling results of Butler et al.[8,9]

Experiment

The arcjet thruster used in this experiment was a 1-kW-class radiatively cooled laboratory-type thruster. The tungsten nozzle (Fig. 1) consisted of a 0.635-mm-diam, 0.25-mm-long throat and a 12.1-mm-long conical diverging section at a half angle of 20 deg. With a design area ratio of 225, the exit plane diameter was 9.53 mm. The tip of the 2% thoriated tungsten cathode was originally set approximately 0.45 mm upstream of the nozzle constrictor; however, with erosion of the cathode, this value may be somewhat larger. The arcjet was operated at a current and voltage of 9.8 ± 0.1 A and 151 ± 1 V, respectively, and a fixed H_2 mass flow rate of 14.2 mg/s. The vacuum facility consisted of a 1.09 × 0.56 m diam stainless-steel chamber, that was maintained at background pressure of approximately 0.35 torr by two 590-l/s blowers.

The fluorescence excitation was provided by a continuous-wave ring dye laser pumped by an argon-ion laser. The dye laser was operated with DCM dye that has a broad emission band centered around 650 nm, making this dye particularly suitable for the Balmer-α excitation of hydrogen at 656.28 nm. Dye laser output up to 200 mW was obtained with a pump laser power of 4 W. Scanning of the ring dye laser across the Balmer-α transition was performed with a tunable, piezoelectrically driven intracavity etalon. The scanning range was limited by laser mode instability to approximately 50 GHz, or 0.075 nm, which was on the order of the linewidth of the Balmer-α line at the conditions in the nozzle. The laser beam was directed axially into the plasma to probe the interior of the arcjet and to use the nozzle as a beam dump. Consequently, the axial-velocity component was measured from the Doppler shift of the line. The fluorescence was collected through a window on the vacuum chamber end plate at an angle of 16 deg from the arcjet axis, and detected broadband with a photomultiplier tube. The spatial resolution was approximately 0.6 mm in the axial direction and 30 μm in the transverse directions, as determined by the laser beam waist and the collection optics. The spectral resolution of the laser was 4×10^{-4} nm. By translating the arcjet axially and radially, velocity measurements were obtained along the arcjet centerline as well as radially at a few axial positions, as indicated by the crosshatches in Fig. 1. A fraction of the excitation laser beam from the dye laser was split off and sent to a photodiode detector and a wavemeter to monitor the laser intensity and wavelength. The fluorescence signal was normalized by the laser intensity, but was not corrected for possible fluctuations in laser wavelength, which were believed to be negligible.

Since the fluorescence signal was considerably smaller than the background emission, phase-sensitive detection was performed by mechanically chopping the excitation beam at a frequency of 1.5 kHz and detecting the signal with a digital lock-in amplifier. Noise at the chopping frequency, due mainly to scattered laser light in the arcjet, was the primary limitation in obtaining a significant signal in regions of weak fluorescence. Velocity measurements were taken from the nozzle exit plane to within 1.5 mm of the throat, at which point the LIF signal was overwhelmed by the background of scattered laser light.

Analysis

The recorded fluorescence signal was normalized by the photodiode output to account for variations in the laser power during the scanning of the spectral line. The wavelength was obtained from the wavemeter, an instrument that determines absolute wavelength by the interference of the input laser signal with an internal reference. The Doppler shift of the line center was accurately determined by fitting the normalized line shape with a Gaussian profile. The Balmer-α transition of atomic hydrogen is an electronic transition between the first and second excited states, i.e., $n = 2 \rightarrow n = 3$. This transition comprises five fine-structure components formed because of spin-orbit coupling; however, because the fine-structure splitting was considerably smaller than the line broadening at the conditions encountered in the arcjet plasma, it was therefore neglected. Although non-Gaussian broadening mechanisms of the spectral line, such as Stark broadening, were believed to be present and comparable with the Doppler broadening, a simple Gaussian fit was sufficient to determine the spectral line center. A Voigt fit was unnecessary and less accurate, given the scarcity of data in the line wings. Since the scanning was performed on the laser excitation and not on the fluorescence collection, the Doppler shift is only associated with the component of the velocity in the direction of the laser excitation, namely, in the direction parallel to the nozzle axis. This axial velocity component u_z was determined from the shift of the spectral line center Δv from a stationary reference frequency v_0 according to

$$u_z/c = \Delta v/v_0$$

The stationary reference was obtained from previous LIF measurements performed on the same arcjet at the same facility by Liebeskind et al.[1] The pressure shift of the spectral line is negligible in comparison with the Doppler shift.

Results and Conclusions

Measurements of axial velocities along the nozzle centerline and along three diameters are given in Figs. 2 and 3, respectively. The axial position is defined as zero at the exit plane and negative into the nozzle. Hence, the nozzle throat is located at −12.1 mm. The centerline velocity drops monotonically from a peak of approximately 17.5 km/s at 1.3 mm downstream of the throat to around 12 km/s at the exit plane. Since no other measurements of velocity have been made within the arcjet nozzle, the results can only be compared to the modeling work of Butler et al.[8] The results of two versions of this model are shown in Fig. 2. One version includes mass diffusion terms in the species momentum equation, whereas the other does not include such terms. There is remarkably good agreement between the measurements and the former model, clearly indicating the importance of including diffusional processes to correctly model the transport of heavy species in the plasma. This is not surprising considering the large radial gradients in plasma properties within the nozzle.[9] The only significant discrepancy between the model results and measurements are in the three data points closest to the throat of the arcjet. However, in this region the measurements have the largest uncertainty because of the reduced LIF signal and the increased background noise.

Figure 3 displays radial profiles of the axial velocity measured at three axial positions within the nozzle (2.54, 5.08, and 6.35 mm
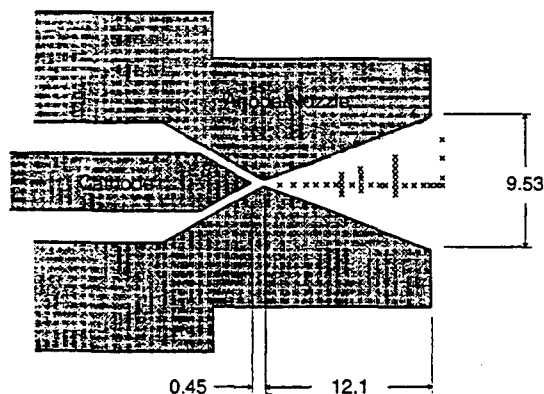
Fig. 1 Schematic cross section of the 1-kW arcjet thruster nozzle (not to scale). All dimensions are in millimeters. Crosshatches indicate the positions where the measurements were taken.

9.53

0.45 —— 12.1 ——
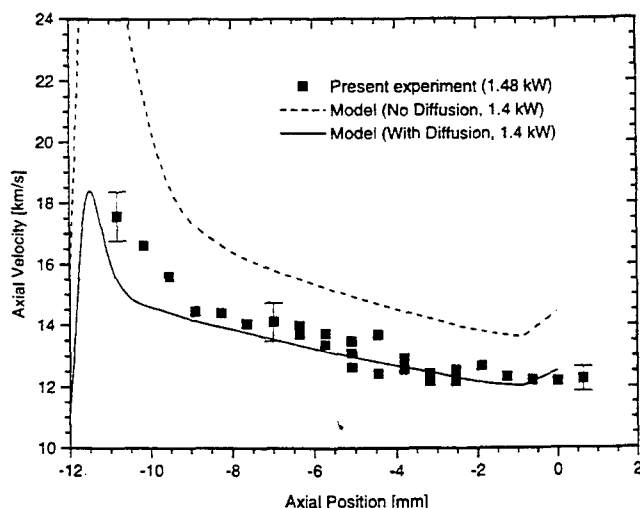
Fig. 2 Measured axial velocity along the arcjet centerline. Typical errors are shown. The measurements are compared to results of an arcjet model incorporating mass diffusion and without mass diffusion.
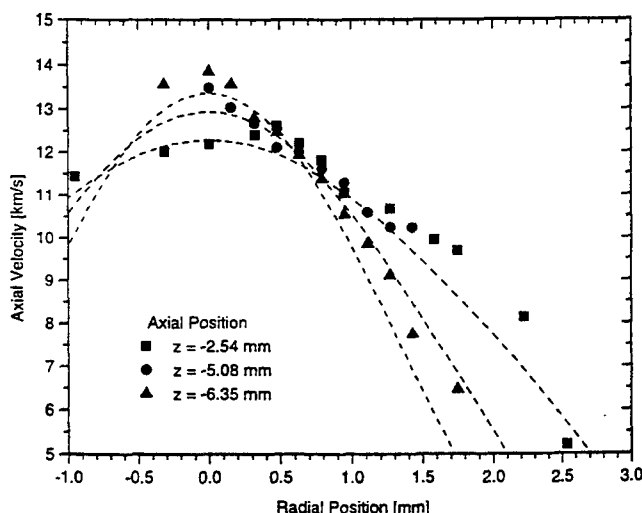
Fig. 3 Radial profiles of axial velocity at three axial locations within the arcjet nozzle. Errors are typically ±0.6 km/s. The dashed lines are results of the arcjet model (with diffusion) at the same axial locations as the measurements.

References

[1] Liebeskind, J. G., Hanson, R. K., and Cappelli, M. A., "Laser-Induced Fluorescence Diagnostic for Temperature and Velocity Measurements in a Hydrogen Arcjet Plume." *Journal of Applied Optics.* Vol. 32, No. 30, 1993, pp. 6117–6127.

[2] Liebeskind, J. G., Hanson, R. K., and Cappelli, M. A., "Experimental Investigation of Velocity Slip Near an Arcjet Exit Plane." *AIAA Journal,* Vol. 33, No. 2, 1994, pp. 373–375.

[3] Ruyten, W. M., and Keefer, D., "Characterization of Electric Thruster Plumes Using Multiplexed Laser-Induced Fluorescence Measurements," AIAA Paper 92-2965, July 1992.

[4] Ruyten, W. M., Burtner, D., and Keefer, D., "Laser-Induced Fluorescence Measurements on the Plume of a 1 kW Arcjet Operated on Simulated Ammonia," International Electric Propulsion Conf., Seattle, WA, Paper 93-127, Sept. 1993.

[5] Pobst, J. A., Wysong, I. J., and Spores, R. A., "Laser Induced Fluorescence of Ground State Hydrogen Atoms at Nozzle Exit of an Arcjet Thruster," AIAA Paper 95-1973, June 1995.

[6] Cappelli, M. A., and Storm, P. V., "Interior Plasma Diagnostics of Arcjet Thrusters," AIAA Paper 94-2654, June 1994.

[7] Storm, P. V., and Cappelli, M. A., "Laser-Induced Fluorescence Measurements Within an Arcjet Thruster Nozzle," AIAA Paper 95-2381, July 1995.

[8] Butler, G. W., Kashiwa, B. A., and King, D. Q., "Numerical Modeling of Arcjet Performance," AIAA Paper 90-1474, June 1990.

[9] Butler, G. W., Boyd, I. D., and Cappelli, M. A., "Nonequilibrium Flow Phenomena in Low-Power Hydrogen Arcjets," AIAA Paper 95-2819, July 1995.

upstream from the exit plane). The LIF signal intensity dropped off quickly with radial position, indicating a rapid radial decrease in the $n = 2$ excited-state number density of atomic hydrogen. This loss in signal restricted the measurement domain to within approximately 2 mm of the nozzle centerline. The dashed lines in the figure are the model results at the same axial locations as the measurements. The measurements and the model show remarkably good agreement; however, the measured velocities are somewhat greater than those of the model away from the arcjet centerline. Although the centerline velocity decreases axially, the velocities away from the centerline increase with axially position. Because most of the mass convection occurs in this outer region, the total kinetic energy of the flow is clearly increasing downstream, as is expected in a supersonic diverging nozzle.

At present, experiments are under way to perform a more comprehensive study to map the velocity flowfield at various arcjet specific energies for both hydrogen and simulated hydrazine propellants.

Arcjet nozzle flow-field characterization by laser-induced fluorescence

P. Victor Storm and Mark A. Cappelli

Laser-induced fluorescence of the Balmer–alpha (H_α) transition of atomic hydrogen was performed within the nozzle of a 1-kW class radiatively cooled arcjet thruster operating on hydrogen and synthesized-hydrazine propellants. Axial velocities were determined from the Doppler shift of the H_α line center relative to a stationary reference, whereas translational temperatures and electron number densities were determined from a line-shape analysis of the H_α transition. The results are compared with a numerical model and indicate excellent agreement with the velocities, as well as temperatures near the nozzle exit. There are discrepancies, however, in the temperatures far upstream of the exit and in the electron densities, suggesting needed improvements in the modeling of the recombination chemistry. © 1998 Optical Society of America

OCIS codes: 300.2530, 020.0020, 020.6580.

1. Introduction

With the successful deployment of space-qualified arcjet thrusters for satellite north–south station keeping, there has been a recent increase in interest both in improving arcjet performance and efficiency and in extending the operating range to include other potential applications, such as satellite repositioning and orbit transfer. Such developments will be facilitated through advanced numerical simulations of arcjets; however, the validation of these simulations can be performed only by a comparison with experimental measurements of operating parameters and plasma properties. A number of optical diagnostics have been developed recently to measure the plasma properties in the interior and the exhaust plume of the arcjet nozzle. Primary among these diagnostics is laser-induced fluorescence (LIF), which has proved useful because of its abundant signal level, good spatial resolution, and specie-specific nature. Plasma properties in the exhaust plume flow have been measured by LIF techniques in several arcjet thrusters operating with a variety of different propellants.[1–4] Until recently, only emission spectroscopy has been used as an optical diagnostic to probe the plasma in the nozzle interior. The first such emission studies were performed either by observing the plasma through small holes or quartz windows in the anode[5–7] or observing the emission emanating axially from the nozzle.[8] A summary of these emission studies and other nonoptical investigations of the arcjet nozzle interior, including pressure and current density measurements, is given in Ref. 9.

LIF was only recently demonstrated by the authors to be useful as a diagnostic tool to investigate plasma properties within an arcjet nozzle.[10] Overcoming problems associated with geometric constraints and reduced signal-to-noise ratios made it possible to obtain measurements of axial velocity in a 1-kW hydrogen arcjet nozzle from the Doppler shift of the hydrogen Balmer–alpha (H_α) line relative to a stationary reference. Following the initial success of these measurements, the technique was refined to include temperature and electron-density determination from a spectral line-shape analysis, and measurements were performed over a wide range of arcjet operating conditions.

We present the results of LIF measurements of axial velocity, atomic hydrogen translational temperature, and electron number density in a 1-kW arcjet nozzle flow field operating on propellants of pure hydrogen and a 1:2 volumetric mixture of nitrogen and hydrogen to simulate the dissociation products of hydrazine. Resonance fluorescence was performed on the H_α transition of atomic hydrogen. Spatially resolved measurements were obtained along the arcjet

The authors are with the High Temperature Gasdynamics Laboratory, Department of Mechanical Engineering, Stanford University, Stanford, California 94305-3032.

centerline to within a few millimeters of the nozzle throat. The arcjet operating conditions were chosen to facilitate a comparison with a numerical hydrogen arcjet model.[11]

2. Theory

LIF involves the excitation of an atomic or molecular transition by the absorption of laser radiation with a subsequent emission of radiation. The measured fluorescence signal is proportional to the rate at which fluorescence photons arrive at the detector, N_p, which for low laser intensity is given by

$$N_p \approx nV\eta \, \frac{\Omega}{4\pi} \frac{A_{ul}}{A_{ul}+Q_u} B_{lu,\lambda} \, \Phi(\lambda)I_{\text{laser}}, \qquad (1)$$

where n is the number density of the absorbing state; V is the fluorescence collection volume; η is the efficiency of the collection optics; Ω is the solid angle subtended by the collection optics; A_{ul} and $B_{lu,\lambda}$ are the Einstein coefficients for the transition between lower state l and upper state u; Q_u is the quenching rate of the emitting state; $\Phi(\lambda)$ is the line-shape overlap integral, the convolution of the transition line shape, and the laser line shape; and I_{laser} is the laser intensity. For low laser power, the fluorescence signal is clearly proportional to the laser intensity and is detrimentally affected by collisional quenching.

At higher laser power, as the stimulated emission rate approaches the spontaneous emission or the quenching rates, an additional factor of $(1 + I_{\text{laser}}/I_{\text{sat}})^{-1/2}$ appears in Eq. (1), with the saturation intensity given by

$$I_{\text{sat}} = \frac{\pi}{2} \, \Delta\lambda \, \frac{g_u}{g_u+g_l} \frac{A_{ul}+Q_u}{B_{lu,\lambda}}, \qquad (2)$$

where $\Delta\lambda$ is the transition linewidth, and g_u and g_l are the degeneracies of the upper and lower states of the transition. As the laser intensity approaches the saturation intensity, the fluorescence signal loses its linear dependence on the laser intensity. However, quenching of the transition has the benefit of increasing the saturation intensity, thereby permitting the use of a higher laser power while remaining in the linear fluorescence regime.

The H_α spectral line of atomic hydrogen consists of transitions between the $n = 2$ and $n = 3$ principal quantum numbers. Coupling of the spin and orbital angular momenta gives rise to fine-structure splitting of both of these states according to the total angular-momentum quantum number j. These spin–split energy levels are shown schematically in Fig. 1. Quantum-mechanical selection rules give rise to seven allowable transitions between these states; however, if one neglects hyperfine splitting and quantum-electrodynamic effects, only five of these transitions are nondegenerate. These nondegenerate transitions are indicated in Fig. 1, and their relative spacing and intensities are given in Table 1.[12]

There are two significant line-broadening mecha-
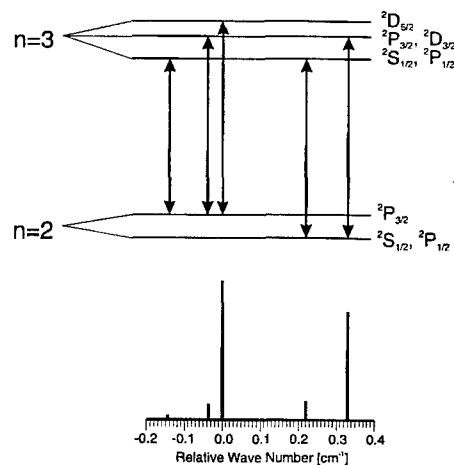
Fig. 1. Energy-level diagram of the atomic hydrogen $n = 2$ and $n = 3$ states showing the spin-orbit splitting and the allowable transitions constituting the H_α spectral line.

nisms under the plasma conditions typically found within the arcjet nozzle: Doppler and Stark. For radiating dipoles in translational equilibrium, Doppler broadening takes a Gaussian line-shape profile with a Doppler FWHM given by[13]

$$\Delta\lambda_D{}^{\text{FWHM}} = \lambda_0 \left(\frac{8kT\ln2}{mc^2}\right)^{1/2}, \qquad (3)$$

where m is the atomic mass and T is the atomic translational temperature.

Stark broadening arises from disturbances in the atomic energy levels through collisions with charged particles, namely, electrons and hydrogen ions. Because of their large difference in mass, and hence velocity in a thermal plasma, calculations of the Stark-broadening line shape normally treat the electrons in the impact limit and the ions as stationary. However, Monte Carlo simulations of the Stark broadening of the H_α transition, taking into account nonstatic ions, have shown much better agreement with measurements than previous static-ion calculations.[14]

In the impact approximation, the Stark-broadening line shape is Lorentzian and the FWHM is generally a strong function of the electron–ion density, the particular electronic transition, and a weak function of electron and ion temperatures. Although the true Stark

Table 1. Components of the H_α Transition and Their Properties[a]

Upper j	Lower j	Transition	$\delta\nu$ (cm^{-1})	Relative Intensity
1/2	3/2	$3s\,{}^2S_{1/2} \leftrightarrow 2p\,{}^2P_{3/2}$	−0.144	0.05
3/2	3/2	$3d\,{}^2D_{3/2} \leftrightarrow 2p\,{}^2P_{3/2}$	−0.036	0.28
5/2	3/2	$3d\,{}^2D_{5/2} \leftrightarrow 2p\,{}^2P_{3/2}$	0.000	2.50
1/2	1/2	$3s\,{}^2S_{1/2} \leftrightarrow 2p\,{}^2P_{1/2}$ $3p\,{}^2P_{1/2} \leftrightarrow 2s\,{}^2S_{1/2}$	0.220	0.31
3/2	1/2	$3p\,{}^2P_{3/2} \leftrightarrow 2s\,{}^2S_{1/2}$ $3d\,{}^2D_{3/2} \leftrightarrow 2p\,{}^2P_{1/2}$	0.328	1.96

[a]Data are from Ref. 12.

Fig. 2. Schematic diagram of the experimental setup.

line shape of the H_α transition is not precisely Lorentzian, it is closely approximated as such, particularly near the line center where the impact approximation most appropriately applies. To avoid any potential uncertainty in the Stark-broadening calculations, we use instead a Stark-broadening relation obtained experimentally in a low-pressure wall-stabilized arc that had a similar plasma density and temperature to that within the arcjet nozzle.[15] The best fit to this experimental data gives the relationship

$$\log \Delta\lambda_S{}^{FWHM} = 0.0272\, n_e{}^{0.090} - 3.29, \qquad (4)$$

where n_e is in units of inverse cubic meters and $\Delta\lambda_s$ is in units of nanometers. This relationship is applicable in the range of electron density from 10^{19} to 10^{23} m^{-3}.

The simultaneous existence of both inhomogeneous Doppler broadening and homogeneous Stark broadening gives rise to a Voigt line-shape function.[13] Since the broadening mechanisms apply independently to all five fine-structure transitions constituting the H_α line, the complete line shape is a sum of five Voigt functions whose relative positions and intensities are given in Table 1.

The shift of the line-center wavelength $\Delta\lambda_0$ relative to a stationary reference $\lambda_{0,ref}$ is related to plasma velocity u according to the Doppler shift equation

$$\frac{u}{c} = \frac{\Delta\lambda_0}{\lambda_{0,ref}}, \qquad (5)$$

where c is the speed of light in the medium, which can be taken to be the vacuum speed of light with sufficient accuracy.

3. Experiment

The experimental setup is shown schematically in Fig. 2. The fluorescence excitation laser beam was supplied by pumping a continuous-wave ring dye laser by a Spectra Physics Stabilite 2016 argon-ion laser in the multiline mode. The dye laser was originally a Spectra Physics Model 380A but was replaced in the middle of the experiments with a Coherent Model 699-21. The dye laser contained DCM dye, which has broad absorption and fluorescence bands centered around 500 and 650 nm, respectively, making it particularly suitable for Ar$^+$ pumping at 488 and 514.5 nm and hydrogen H_α excitation at 656.28 nm. Dye-laser output of as much as 200 mW was achieved with a pump laser power of 4 W in all the lines. Spectral scanning of the ring dye laser was accomplished with a tunable, piezoelectrically driven intracavity etalon. In the Spectra Physics 380A, the high-voltage scanning signal was supplied by a Burleigh Model RC-43 programmable ramp generator. The maximum scanning range was nominally 75 GHz; however, in practice, the scans were limited to approximately 50 GHz or 0.07 nm owing to laser mode instability. Scanning of the dye laser could not be performed continuously; instead, the laser would mode-hop axial modes, at 200-MHz spacing, as the etalon was being scanned. This however was inconsequential since the axial-mode spacing was considerably less than 1% of the H_α linewidth, which was at least 30 GHz FWHM. In the Coherent 699-21, spectral scanning was performed with the laser-scanning electronics, which provided control over the piezoelectrically driven intracavity etalon. The maximum scanning range was 30 GHz or approximately 0.04 nm at the H_α wavelength. By use of optical feedback, we used the laser electronics to adjust the ring-cavity length to provide continuously smooth scanning over the entire 30 GHz. For both dye lasers, the specifications indicate a maximum laser linewidth of 20 MHz, which was established by the frequency jitter.

The fluorescence laser beam from the dye laser was expanded to approximately 40 mm in diameter by a -25-mm focal-length (f.l.) plano-concave lens and then collimated by use of a 750-mm f.l. achromat lens. We then focused the collimated beam into the arcjet using a 700-mm f.l. achromat lens. Optical access to the vacuum chamber was provided by a 76-mm-diameter quartz window on the end plate, aligned axially with the arcjet. By expanding the beam before focusing, we reduced the Gaussian beam waist to 15 μm, and the depth of focus was approximately 0.50 mm. The laser was directed axially into the nozzle to probe the interior flow field and to use the nozzle itself as a beam dump. A fraction of the excitation laser beam from the dye laser was split off and directed to a Thorlabs Model PDA50 photodiode detector and a Burleigh Model WA-10 wavemeter to monitor the laser intensity and the wavelength. In addition, with the Coherent 699-21 dye laser the intensity was monitored by a photodiode detector built into the laser head and recorded by the laser-control electronics.

Fluorescence collection was performed through a second 76-mm-diameter quartz window on the chamber end plate, adjacent to the window used for the excitation laser beam. In this configuration, the optical axis was aligned at 16° to the excitation beam and the arcjet axis. Collection and focusing of the fluorescence signal were performed with a single 400-mm f.l. achromat lens. The fluorescence was focused onto a 100-μm-diameter pinhole, which was

used as a field stop or spatial filter. With a transverse magnification of 0.84, determined by the position of the collection lens, the spatial resolution at the arcjet in the axial direction was approximately 0.4 mm. The resolution in the transverse directions was determined by the laser beam waist, which was approximately 15 μm.

Detection of the fluorescence was accomplished immediately after the field stop with a Hamamatsu R928 photomultiplier tube (PMT) at a cathode supply of 1000 V, enclosed in a lighttight housing. A 10-nm bandwidth H_α interference filter was mounted to the entrance of the PMT housing to eliminate unwanted background light at other wavelengths. Furthermore, to prevent saturation of the PMT, a neutral density filter of 2.0 optical density was placed in front of the field stop.

Since the fluorescence signal was considerably smaller than the background emission, phase-sensitive detection was performed with a Stanford Research Systems SR850 digital lock-in amplifier. The excitation laser beam was mechanically chopped near the dye laser at a frequency of 1.5 kHz, and the chopper provided the reference signal to the lock-in amplifier. Signal noise away from the chopping frequency was digitally filtered in the lock-in amplifier by use of a low-pass filter with a time constant in the range of 0.3–1.0 s and a roll-off of 24 dB/octave. Scans across the H_α line were taken in a minimum of 62.5 s, and the data were sampled at a rate of 8 Hz, resulting in a minimum of 500 data points per scan. Noise at the chopping frequency, resulting primarily from laser light scattered in the arcjet nozzle, could not be filtered and was therefore the limiting factor in obtaining a clean fluorescence signal. Outputs of the high-voltage etalon scanning signal and photodiode detector were simultaneously recorded through analog input channels of the lock-in amplifier to calibrate for wavelength and to normalize the scans by laser intensity.

The vacuum facility consisted of a 1.09 m × 0.56 m diameter stainless-steel chamber. Two mechanical pumps and two 590-l/s (1250-CFM) blowers pumped the chamber through a 15-cm-diameter steel pipe.
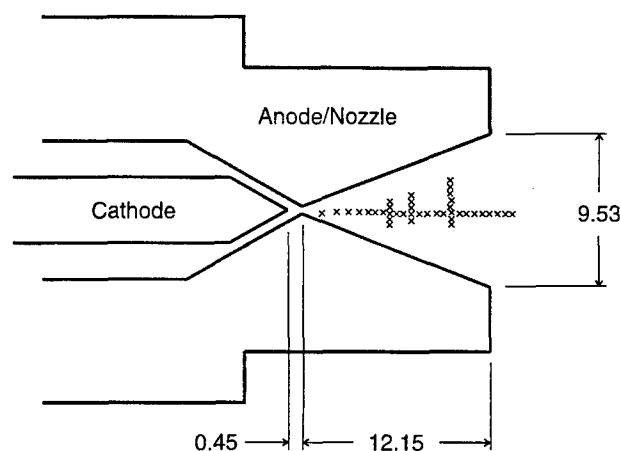

Fig. 3. Schematic cross section of the 1-kW arcjet thruster nozzle. All the dimensions are in millimeters. The cross hatching indicates the positions where the measurements were taken.

With the arcjet operating, the chamber back pressure was typically 50 Pa (5.0×10^{-4} atm). The arcjet used in these experiments was a 1-kW radiation-cooled laboratory model that was designed and built at the NASA Lewis Research Center. The arcjet's thoriated-tungsten nozzle, shown schematically in Fig. 3, consisted of a 0.635-mm-diameter, 0.25-mm-long throat and a 12.15-mm-long conical diverging section at a half angle of 20°. With a design area ratio of 225, the exit plane diameter was 9.53 mm. The tip of the 2% thoriated-tungsten cathode was originally set approximately 0.45 mm upstream of the nozzle constrictor; however, with erosion of the cathode, this value could be somewhat larger. The arcjet is mounted on translation stages with two degrees of freedom. By translating the arcjet axially and radially, we obtained measurements along the arcjet centerline as well as radially at a few axial positions, as indicated by the cross hatching in Fig. 3.

Several arcjet operating conditions were investigated and are summarized in Table 2. Most of the experiments were performed with a pure hydrogen propellant at three different mass flow rates and several power levels. Of particular importance were

Table 2. Summary of Arcjet Operating Conditions, Laser Scan Ranges, and Measurements

Propellant	Flow Rate (mg/s)	Current (A)	Voltage (V)	Power (kW)	Scan Range (GHz)	Measurement
Hydrogen	9.47	4.89	162	0.79	30	u_z on axis
Hydrogen	11.8	4.80	169	0.81	30	u_z on axis
		6.56	155	1.01	30	u_z on axis
		8.11	149	1.21	30	u_z on axis
Hydrogen	14.2	4.51	176	0.80	30	u_z on axis
		6.04	164	0.99	30	u_z on axis
		7.84	155	1.21	30	u_z on axis
		8.94	151	1.35	30	u_z on axis
		9.80	151	1.48	50	u_z axial and radial
		7.85	155	1.22	70	u_z, T_{tr}, n_e on axis
Synthesized Hydrazine	40.9 N_2 5.95 H_2	9.00	133	1.20	70	u_z, T_{tr}, n_e on axis

the operating conditions of 14.2-mg/s flow rate and the 1.2–1.5-kW power level, as these conditions matched those of the numerical simulations.[11] In addition to the pure hydrogen operation, a propellant consisting of a 1:2 volumetric mixture of nitrogen to hydrogen was used to simulate the dissociation products of hydrazine. Measurements were performed with this propellant at a total mass flow rate of 46.85 mg/s and a 1.2-kW power level. This operating condition was chosen to match closely that used in Ref. 5 but unfortunately permits only a qualitative comparison of the results with those of the pure hydrogen operation.

4. Data Analysis

The recorded fluorescence signal from the lock-in amplifier was normalized with respect to laser intensity to account for variations in the laser power during each scan. The wave-number scale was ascertained from the linear etalon drive voltage and the scan end points recorded by the wavemeter. The linewidth of the H_α transition, given the plasma temperature and density in the arcjet nozzle, was of the order of 30 GHz or greater. Hence the 30- and 50-GHz scans, obtained using the Coherent 699-21 and Spectra Physics 380A dye lasers, respectively, were not sufficiently wide to capture the wings of the transition line shape. The line center, however, could be accurately resolved by fitting the measured trace with either a Gaussian or a Lorentzian profile. In determining the line-center position only, the fine structure did not need to be taken into account. Since the scanning was performed on the laser excitation and not on the fluorescence collection, the measured shift is associated only with the component of the velocity in the direction of the laser excitation, which corresponds to the arcjet axial direction. This axial velocity component u_z was determined from the shift of the spectral line center from a stationary reference according to the Doppler shift equation [Eq. (5)]. The stationary reference wavelength was determined previously in a low-pressure microwave discharge as well as by recording the H_α fluorescence at the nozzle exit plane centerline with a laser excitation in the radial direction.[1] The only other potential spectral line-shift mechanism pertaining to the H_α line at the conditions found in the arcjet plasma is the Stark shift. However, calculations based on the arcjet model results confirm that the Stark redshift of H_α is important only in the arc region within approximately 1 mm of the nozzle throat.[16] Throughout most of the nozzle, the Stark shift is at least an order of magnitude smaller than the Doppler shift.

To determine atomic hydrogen translational temperature and electron number density from Doppler and Stark broadening of the H_α line shape, three partially overlapping 30-GHz scans were pieced together to produce traces with a total width of 70 GHz. These concatenated scans were obtained only for the two operating conditions specified in Table 2, and a typical example is shown in Fig. 4 along with the best-fit line shape. The precise broadening param-
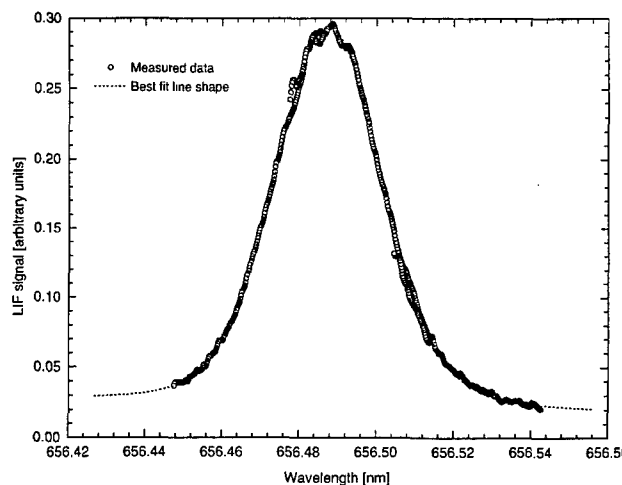

Fig. 4. Typical LIF scan of the H_α transition at the arcjet exit-plane center line, obtained by piecing together three overlapping 30-GHz scans. Also shown is the best-fit line shape consisting of a sum of five Voigt functions.

eters were determined by fitting the measured line shape with a sum of five Voigt functions, whose relative positions and strengths are given by the fine-structure parameters of Table 1. In this manner, the Doppler- and Stark-broadening contributions to the line shape could be deconvolved, and the plasma temperature and electron number density could be determined by use of Eqs. (3) and (4).

5. Results and Discussion

The fluorescence saturation behavior was first investigated to determine the maximum practical laser intensity. The peak line-center fluorescence signal at the exit plane centerline is plotted as a function of laser intensity in Fig. 5. The fluorescence signal exhibits a linear dependence with a laser power to at least 100 mW, indicating that the transition is not saturating. A numerical study of the fluorescence signal in the interior of the arcjet, by use of a
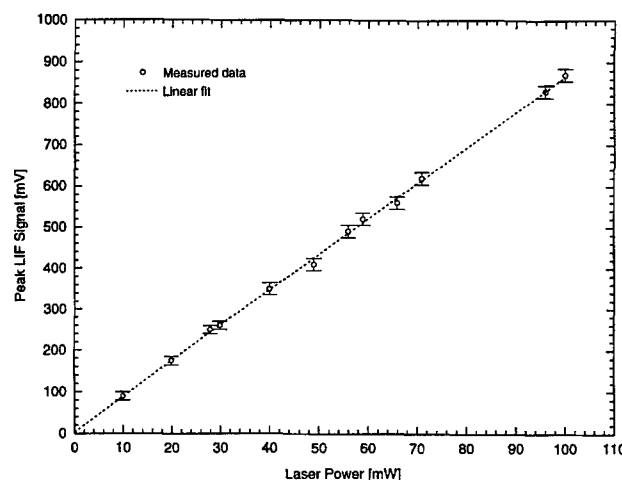

Fig. 5. Fluorescence saturation behavior at the arcjet exit-plane center line.

collisional-radiative model, demonstrated that the plasma in the interior of the nozzle is less disposed to fluorescence saturation than that at the exit plane, because of the increased quenching rates.[17] Thus to ensure that saturation would not be detrimental anywhere in the measurement domain, the measurements were performed below 100 mW of laser power.

The results of axial velocity, temperature, and electron number density are presented separately below. A few general issues concerning the presentation of the results must be addressed first. In the figures presenting measurements along the centerline of the arcjet nozzle, the axial position is defined as zero at the nozzle exit plane and as positive in the flow direction. Hence the interior region of the nozzle is assigned negative axial coordinates. With this definition, the nozzle throat is located at approximately −12.15 mm.

The measurement domain was limited by the signal-to-noise ratio of the LIF detection. The considerable plasma temperature and pressure in the nozzle interior result in significant collisional quenching rates with a consequent poor LIF signal compared with the background emission and the scattered laser light. The signal-to-noise ratio became progressively smaller farther into the arcjet nozzle from the exit plane. Moreover, the signal rapidly decreased away from the nozzle centerline as the population in the $n = 2$ pumping state decreased. As a result of these considerations, the measurement domain was limited to within a few millimeters of the nozzle centerline, and several millimeters downstream of the throat. At one operating condition only, LIF detection was successfully achieved within 2 mm of the arcjet throat; however, for the most part, signal detection could be accomplished only within 6–8 mm upstream of the exit plane.

Error bars have been omitted from the figures to avoid a cluttered appearance. The typical uncertainty in the axial velocity measurements was approximately ±0.4 km/s. Since the velocity uncertainty was primarily governed by the accuracy of the wavemeter rather than errors introduced by the data-fitting procedure, this uncertainty was relatively uniform throughout the entire measurement domain. This was not the case, however, for the temperature and electron-density measurements. These properties were determined from the line-shape fit and were therefore largely dependent on the noise in the measured fluorescence scan. As the scans became progressively noisier farther into the nozzle away from the exit plane, the measurement uncertainties increased significantly. The typical uncertainties were ±15% at the exit plane and double this value at approximately $z = -4$ mm.

A. Axial Velocity

Axial velocity measurements were obtained along the nozzle centerline at eight different operating conditions with the pure hydrogen propellant (indicated by the 30-GHz scans in Table 2). To present all this data in one figure, the axial velocities were nondi-
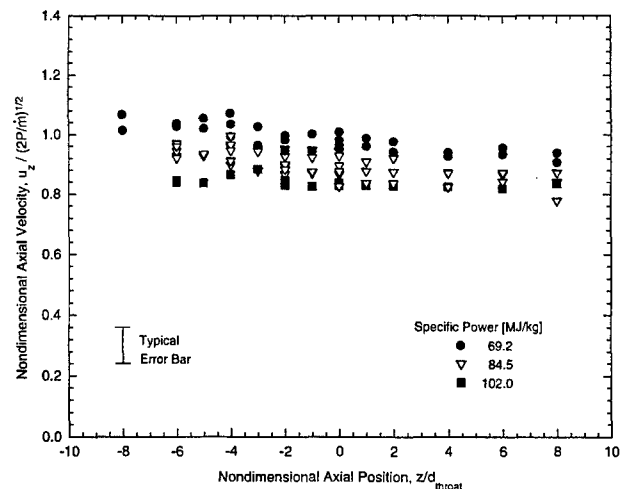

Fig. 6. Center-line axial velocity in the arcjet nozzle plotted in nondimensional form.

mensionalized by the square root of twice the specific power, $(2\ P/\dot{m})^{1/2}$, whereas the axial position was nondimensionalized by use of the nozzle throat diameter. The results are shown in Fig. 6. The operating conditions were specifically chosen to match the specific power at the three different flow rates. Thus although there are eight different operating conditions shown in this figure, these constitute only three different specific power levels. The most striking result displayed in Fig. 6 is that the nondimensionalized axial velocities nearly collapse to a single line, indicating the significant influence of the specific power on the velocity distribution. Given that the specific power is a measure of the energy deposition per unit mass, this strong dependence is not unexpected. In fact, neglecting losses, a simple energy balance for a uniform flow gives

$$\dot{m}h_i + P = \dot{m}\left(h_e + \frac{1}{2}u_e{}^2\right), \qquad (6)$$

where h_i and h_e are the inlet and the exit specific enthalpy and u_e is the exit velocity. Neglecting the inlet enthalpy compared with the electrical power, and neglecting the exit enthalpy compared with the exit kinetic energy, the exit velocity of this one-dimensional flow would be given by

$$u_e = (2P/\dot{m})^{1/2}. \qquad (7)$$

In such a perfect lossless flow, this scaling would hold precisely and one would expect the data to collapse perfectly to a single line whose value would approach unity at the nozzle exit. However, considerable energy losses are present in the arcjet nozzle flow, the dominant of which include viscous and frozen flow losses, thermal conduction through the nozzle wall, and radiation emanating out of the exit. In addition, the exhausting enthalpy could be significant in comparison with the flow kinetic energy. For these reasons the data do not collapse precisely to a single line, and a residual dependence on specific power and
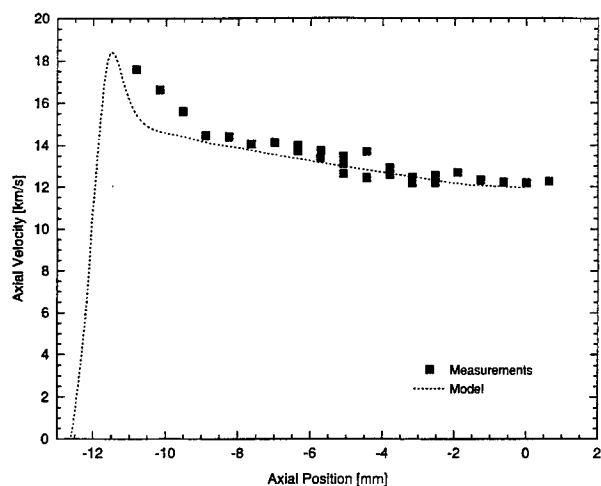
Fig. 7. Comparison of the modeled and measured axial velocities along the nozzle center line with hydrogen propellant at a mass flow rate of 14.2 mg/s and an arcjet power of 1.4 kW. The model results are from Ref. 11.

Fig. 8. Radial profiles of axial velocity at three axial locations within the hydrogen nozzle at the same conditions as in Fig. 7. The dashed curves give the results of the arcjet model described in Ref. 11.

other possible flow parameters is apparent. (Note that, although the nondimensional velocity data presented in Fig. 6 is of the order of unity, this does not imply negligible losses, since it is the peak centerline velocity being plotted. The mass-average velocity is expected to be considerably lower, reflecting the energy losses.)

It is interesting to observe that the centerline axial velocity decreases in the downstream axial direction. This is contrary to expectation, as a supersonic expansion in a diverging nozzle normally generates a flow acceleration. The observed deceleration is a consequence of the action of viscosity. The high plasma temperatures in this nozzle flow give rise to a highly viscous laminar flow field. The centerline velocity decreases in the flow direction because of viscous dissipation and, more importantly, viscous transport of axial momentum in the radial direction.

The measured centerline axial velocity at one operating condition (14.2 mg/s and 1.4 kW) is compared in Fig. 7 with the results of a numerical arcjet model at the same condition.[11] With the exception of the three measurement points closest to the nozzle throat, the agreement between the model and the measurements is excellent. The discrepancy near the throat might be a result of measurement uncertainty associated with the loss of the LIF signal discussed above. In accordance with the measurements, the numerical model predicts a decreasing centerline axial velocity with an increasing axial position. The evidence that viscous transport is responsible for this behavior is best seen in Fig. 8, which presents radial profiles of axial velocities at three different axial positions ($z = -6.35$, -5.08, and -2.54 mm) within the arcjet nozzle. When the centerline velocity decreases axially, a crossover takes place within 1 mm of the centerline beyond which the flow accelerates downstream. This flattening of the radial profile is indicative of the radial transport of the axial momentum away from the nozzle
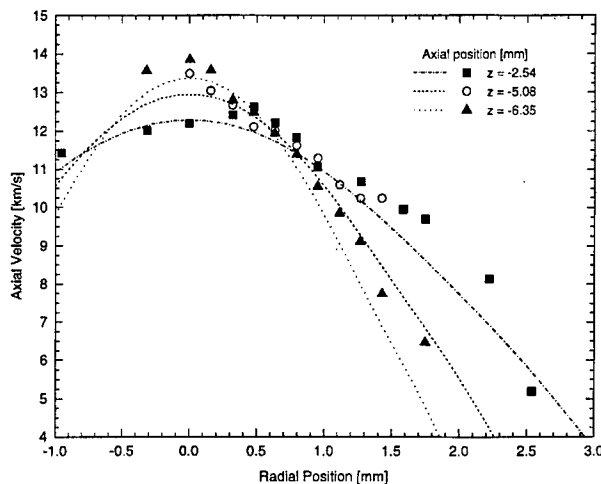
centerline. Since most of the mass convection occurs in the outer regions of the flow, the total kinetic energy is expected to increase downstream, despite the results of Fig. 7, which suggest the contrary. The model results at the same axial locations, presented as dashed curves, are in good agreement with the measurements, except far from the centerline where the LIF signal-to-noise ratio was poor. As mentioned above, the LIF signal intensity dropped off quickly with radial position because of a rapid drop in the $n = 2$ excited-state number density of atomic hydrogen.

The centerline axial velocities for pure hydrogen and synthesized-hydrazine propellants at an arcjet power of 1.2 kW are compared in Fig. 9. Also shown in this figure are the hydrogen arcjet model results, at a 1.2-kW power level, which are in good agreement with the hydrogen measurements. Since the mass flow rates of the two propellants were quite different,

Fig. 9. Comparison of axial velocity along the arcjet nozzle center line for hydrogen and synthesized-hydrazine propellants at an arcjet power of 1.2 kW.

only a qualitative comparison of these results is meaningful. There are two striking differences in the measured axial velocities between the two propellants: the upstream velocities are much greater and the exit-plane velocities are much lower with the synthesized-hydrazine propellant than with the hydrogen propellant. Although the slope is quite uniform in the hydrogen results, the axial velocitie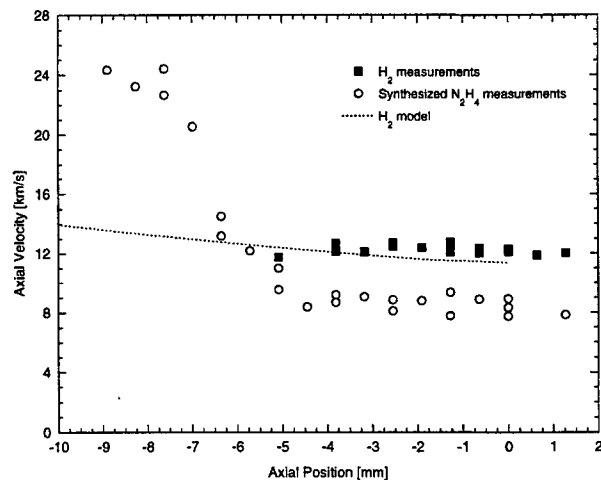s exhibit a rapid decrease between 8 and 5 mm upstream of the exit plane, followed by a near-uniform downstream region. The precise reason for this behavior is not well understood, but could be analogous to the observed change in the slope, evident in the hydrogen velocities much farther upstream, as indicated by the model results in Fig. 7.

It is not surprising that the axial velocity at the exit plane is lower with the synthesized-hydrazine propellant. This can be explained in part by the considerably lower specific power with synthesized hydrazine (25.6 MJ/kg) rather than with hydrogen operation (84.5 MJ/kg). However, in addition, the presence of atomic nitrogen in the plasma substantially increases the viscosity of the flow and hence the consequential viscous losses. This fact was supported by an observed increase in the axial pressure drop as measured between the propellant inlet and the chamber. This pressure drop was approximately 50 psi (absolute) for pure hydrogen and more than 80 psi (absolute) for synthesized-hydrazine operation. Since the nozzle flow is laminar and viscous, the axial pressure drop can be determined to a large extent by the flow viscosity.

What is more notable in these results, however, is the large flow velocity far upstream of the nozzle exit with the synthesized-hydrazine propellant. This observation is somewhat more difficult to understand. We speculate that it is related to a downstream shift of the sonic point from the nozzle throat because of viscous, or perhaps boundary layer, effects, coupled with a substantially hotter arc (and therefore higher sonic velocity) associated with the addition of nitrogen atoms to the plasma. The latter conjecture is substantiated by two observations. First, using optical pyrometry, the exterior of the nozzle was observed to operate hotter with the synthesized-hydrazine propellant. The peak exterior temperature was 1450 K for synthesized hydrazine at 1.2 kW (25.3 MJ/kg), but only 1300 K for hydrogen at the higher power level of 1.5 kW (106 MJ/kg). (Unfortunately, pyrometric measurements were not taken with the hydrogen propellant at 1.2 kW; however, one would naturally expect a lower nozzle temperature.) Second, the voltage drop across the arcjet decreased from approximately 155 V with pure hydrogen to 133 V with synthesized hydrazine. This decrease in voltage is indicative of an increase in the plasma conductivity. In the fully ionized arc, the plasma conductivity is given by the Spitzer–Härm relation, which in mks units is

$$\sigma_{SH} = 1.53 \times 10^{-2} \frac{T_e^{3/2}}{\ln \Lambda},\qquad(8)$$
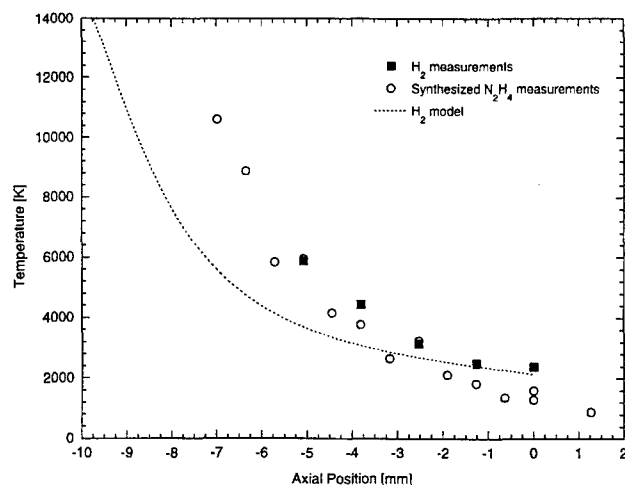

Fig. 10. Comparison of plasma translational temperature along the arcjet nozzle center line for hydrogen and synthesized-hydrazine propellants at an arcjet power of 1.2 kW.

where $\ln \Lambda$ is the Coulomb logarithm, a weak function of electron density and temperature.[18] The observed decrease in arc voltage must therefore be accompanied by an increase in the arc temperature. These two observations support the hypothesis that the arc is substantially hotter, and therefore the sonic velocity is greater, in the synthesized-hydrazine operation. A numerical model of the arcjet with hydrazine propellant would be instructive for our understanding of the fundamental physics and gasdynamics of the nozzle flow and would help to clarify the observed behavior.

B. Temperature

The atomic hydrogen translational temperature along the arcjet nozzle centerline is given in Fig. 10 for both the propellants and the hydrogen arcjet model, all at a power of 1.2 kW. The model and the hydrogen measurements display good agreement to within a few millimeters of the nozzle exit, but diverge farther upstream. Although the measurement uncertainty increases upstream of the exit plane, the discrepancy with the model is larger than the experimental error. This suggests a needed improvement in the model, as, for example, a fine tuning of the recombination chemistry or the calculation of transport coefficients.

The measured translational temperatures for the two different propellants are in remarkable agreement. However, in light of the discussion in Subsection 5.A concerning the comparison of axial velocities, it is surprising that the temperatures are lower for the synthesized-hydrazine propellant than for pure hydrogen. As discussed above, other evidence suggests the opposite behavior should exist, at least in the arc region of the flow. In fact, had the hydrogen measurements exhibited the same behavior as the hydrogen model results, a more reasonable concordance with the synthesized-hydrazine measurements would have resulted. It would therefore be benefi-
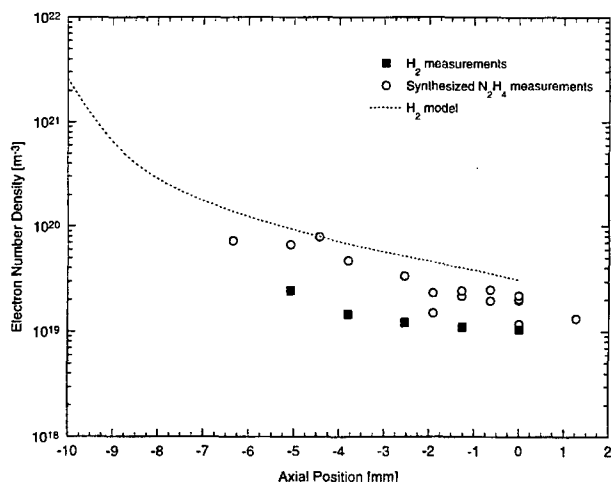
Fig. 11. Comparison of plasma-electron number density along the arcjet nozzle center line for hydrogen and synthesized-hydrazine propellants at an arcjet power of 1.2 kW.

cial to refine the pure hydrogen temperature measurements through further experimentation, particularly in the region further upstream into the nozzle.

C. Electron Density

A comparison of the modeled and measured centerline electron number densities at 1.2 kW is shown in Fig. 11. In all three cases there is a near-exponential increase in the electron density upstream from the nozzle exit, with a doubling approximately every 3 mm. Although the trends are remarkably similar, there are evident discrepancies in the overall magnitudes of the model and the two measurements.

The difference between the two sets of measurements is not significant and can be easily explained by differences in the extent of ionization in the arc region upstream. As discussed above in Subsection 5.A, the pressure upstream of the nozzle throat is greater with the synthesized-hydrazine propellant than with the pure hydrogen propellant. In the fully ionized arc region the electron density is proportional to the static pressure. Since the recombination rates of atomic nitrogen and hydrogen are similar, it is reasonable to expect a greater electron density downstream of the nozzle throat with the synthesized-hydrazine propellant.

On the other hand, the discrepancy between the hydrogen measurements and the model is quite significant. The model predicts densities three to four times greater than the measurements, which may indicate that the simulation does not model the recombination chemistry accurately. A faster recombination rate several millimeters upstream of the exit would decrease the modeled electron-density results, producing better agreement with the measurements. Moreover, this change would supply additional thermal energy to yield better agreement with the measured temperature. Certainly this could be a

possible explanation for the observed discrepancies; however, it would be instructive to validate the hydrogen measurements by additional experiments, particularly in the region as close to the nozzle throat as possible. Such measurements could be performed using a laser system with a greater power and scanning range.

6. Conclusions

Laser-induced fluorescence measurements on the H_α transition of atomic hydrogen were performed in the nozzle interior of a 1-kW arcjet operating on hydrogen and synthesized-hydrazine propellants. Centerline axial velocities were obtained over a wide range of operating conditions from the Doppler shift of the line center relative to a previously determined stationary reference source. Atomic hydrogen translational temperatures and electron number densities were determined for a limited number of operating conditions by concatenating three 30-GHz scans, thereby permitting a line-shape analysis of the H_α transition.

The axial velocity measurements in the hydrogen arcjet are in excellent agreement with a recently developed numerical model of the arcjet.[11] These measurements suggest a highly viscous laminar flow field. The results indicate a centerline deceleration caused by the viscous dissipation and the radial transport of axial momentum; however, given the radial profiles of the axial velocity, the total flow-axial momentum at any cross section is expected to increase downstream, consistent with the behavior of a supersonic expansion. A nondimensionalization of the data suggests that the specific power plays a dominant yet nonexclusive role in the determination of the axial velocity. Other parameters, such as viscosity, density, and sound speed, are expected to have an influence on the velocity distribution within the nozzle. The centerline axial velocities measured in the synthesized-hydrazine arcjet exhibit different behavior from those of the pure hydrogen propellant, although the differences could be reasonably explained, or at least postulated, by differences in the operating conditions and the plasma properties with the introduction of nitrogen atoms into the propellant.

The modeled and measured hydrogen translational temperature display good agreement near the nozzle exit but diverge upstream. This suggests a needed adjustment in the model recombination chemistry, although additional measurements of the hydrogen temperature, particularly farther upstream into the nozzle, would be useful to resolve this apparent discrepancy. The measured centerline temperatures in the synthesized-hydrazine thruster are somewhat lower than, but in surprisingly good agreement with, those in the pure hydrogen arcjet.

The centerline electron number density measurements are also remarkably similar with both propellants. The slight difference in magnitude could be reasonably explained by consideration of the plasma density in the upstream arc region and the relative ionic recombination characteristics of nitrogen and

hydrogen. In contrast, a large discrepancy was found between the hydrogen measurements and the model results. As with the temperature discrepancy, we speculate that a refinement in the model recombination rate could ameliorate this disparity; however, validation of the measurements through further experimentation would be beneficial.

The use of hydrogen H_α LIF as a diagnostic for measuring velocity, temperature, and electron density within the nozzle of an arcjet thruster has been demonstrated. Recommendations for further work would include improving the laser power and the scanning range to permit measurements closer to the arcjet throat where model validation would still be desirable.

References

1. J. G. Liebeskind, R. K. Hanson, and M. A. Cappelli, "Laser-induced fluorescence diagnostic for temperature and velocity measurements in a hydrogen arcjet plume," Appl. Opt. **32**, 6117–6127 (1993).
2. W. M. Ruyten and D. Keefer, "Two-beam multiplexed laser-induced fluorescence measurements of an argon arcjet plume," AIAA J. **31**, 2083–2089 (1993).
3. J. G. Liebeskind, R. K. Hanson, and M. A. Cappelli, "Experimental investigation of velocity slip near an arcjet exit plane," AIAA J. **33**, 373–375 (1994).
4. J. A. Pobst, I. J. Wysong, and R. A. Spores, "Laser induced fluorescence of ground state hydrogen atoms at nozzle exit of an arcjet thruster," *AIAA-95-1973, 26th AIAA Plasmadynamics and Lasers Conference* (American Institute of Aeronautics and Astronautics, New York, 1995).
5. D. M. Zube and R. M. Myers, "Thermal nonequilibrium in a low power arcjet nozzle," J. Propuls. Power **9**, 545–552 (1993).
6. W. Hargus, M. Micci, and R. Spores, "Interior spectroscopic investigation of the propellant energy modes in an arcjet nozzle," Paper AIAA-94-3302, *AIAA/ASME/SAE/ASEE 30th Joint Propulsion Conference* (American Institute of Aeronautics and Astronautics, New York, 1994).
7. H. Tahara, K. Komiko, T. Yonezawa, Y. Andoh, and T. Yoshikawa, "Thermodynamic nonequilibrium nitrogen plasmas in a direct-current arcjet engine nozzle," IEEE Trans. Plasma Sci. **24**, 218–225 (1996).
8. P. V. Storm and M. A. Cappelli, "Radiative emission analysis of an expanding hydrogen arc plasma—I. Arc region diagnostics through axial emission," J. Quant. Spectrosc. Radiat. Transfer **56**, 901–918 (1996).
9. M. A. Cappelli and P. V. Storm, "Interior plasma diagnostics of arcjet thrusters," J. Propuls Power **12**, 1070–1076 (1996).
10. P. V. Storm and M. A. Cappelli, "Fluorescence velocity measurements in the interior of a hydrogen arcjet nozzle," AIAA J. **34**, 853–855 (1996).
11. G. W. Butler, A. E. Kull, and D. Q. King, "Single fluid simulations of low power hydrogen arcjets," Paper AIAA-94-2870, *30th AIAA/ASME/SAE/ASEE Joint Propulsion Conference* (American Institute of Aeronautics and Astronautics, New York, 1994).
12. H. A. Bethe and E. E. Salpeter, *Quantum Mechanics of One and Two-Electron Atoms* (Springer-Verlag, Berlin, 1957) Sec. 64, p. 274.
13. H. R. Griem, *Spectral Line Broadening by Plasmas* (Academic, London, 1974).
14. D. H. Oza, R. L. Greene, and D. E. Kelleher, "Collisional broadening of the Balmer-α transition of H and He⁺ in plasmas," Phys. Rev. A **37**, 531–536 (1988).
15. H. Ehrich and D. E. Kelleher, "Experimental investigation of plasma-broadened hydrogen Balmer lines at low electron densities," Phys. Rev. A **21**, 319–334 (1980).
16. P. V. Storm and M. A. Cappelli, "LIF characterization of arcjet nozzle flows," Paper AIAA-96-2987, *32nd AIAA/ASME/SAE/ASEE Joint Propulsion Conference* (American Institute of Aeronautics and Astronautics, New York, 1996).
17. P. V. Storm and M. A. Cappelli, "Laser-induced fluorescence measurements within an arcjet thruster nozzle," Paper AIAA-95-2381, *31st AIAA/ASME/SAE/ASEE Joint Propulsion Conference* (American Institute of Aeronautics and Astronautics, New York, 1995).
18. M. Mitchner and C. H. Kruger, *Partially Ionized Gases* (Wiley, New York, 1973).

Thermodynamic Analysis Based on Measurements of Flowfield Properties in Low Power Hydrogen Arcjet Thrusters

Mark A. Cappelli[†], Darren H. Berns[††], William A. Hargus, Jr.,[††] and P. Victor Storm[††]

High Temperature Gasdynamics Laboratory
Department of Mechanical Engineering
Stanford University
Stanford, California, USA

Abstract

We review our past and recent measurements of plasma and flowfield properties in low power hydrogen arcjet thrusters. These include measurements of exit plane mass flux profiles, species temperature and velocity at the exit plane, within the nozzle, and near the cathode region, as well as constrictor and cathode surface temperatures during arcjet operation. In past papers, our experimental measurements have been shown to compare favorably to available numerical model predictions, and in some cases, have been instrumental in guiding the model development process. However, in addition to serving as testbeds for advanced simulations of arcjet performance, our detailed property measurements permit us to question the global performance of these devices, within the framework of simple thermodynamic constraints. We briefly describe the use of our experimental findings to understand the behavior and performance limitations of an arcjet when viewed as a simplified thermodynamic system.

I. Introduction

There is little doubt that future arcjet thruster designs will build on the increasing knowledge base that has been constructed over recent years, of the fundamental physical processes that control arcjet performance. In many cases, progress in this technology will be made by incorporating these physical processes into advanced numerical simulations of arcjet operation, which can then be used as tools to design next generation thrusters. It is hoped that these next generation thrusters will extend the envelope of low power arcjet operation to higher specific impulse, and possibly, higher thrust efficiencies.

To date much effort has been made to model arcjet thrusters.[1-7] However, the accuracy of a model can be judged only by comparison with a large body of experimental data. There now exists a substantial collection of experimental data on a standard geometry, low power arcjet operating on hydrogen, [8-20] and several direct comparisons have been made to detailed model predictions.[21-23]

The experimental data include laser induced fluorescence (LIF) measurements of atomic hydrogen velocity, number density, and translational temperature,[8-13] Raman measurements of molecular hydrogen density and rotational temperature,[14] emission measurements of electron number density and temperature at the exit plane, and within the constrictor,[15-17] cathode and anode surface temperatures during operation.[18] as well as impact pressure measurements[19] and mass flux[20] at the exit plane and in the arcjet plume. When combined, these measurements provide an unparalleled collection of information on a single thruster, which serves as a testbed for model development, and, together with available thrust and efficiency data,[24] serves as a means of evaluating the overall arcjet flow behavior and performance.

Details on the measurements and results can be obtained from the above referenced publications. It is not the intention here to review the measurements in any detail. Instead, we shall draw from these results to question the global performance of these devices, within the framework of simple thermodynamic constraints. In this paper, we describe the use of these experimental findings to understand the behavior and performance limitations of an arcjet when viewed as a simplified thermodynamic system.

[†] Associate Professor, Member AIAA

[††] Research Assistant, Student Member AIAA

II. Experimental Measurements

During the past five years, we, and others, have collected an extensive set of data on the flow behavior of low power hydrogen arcjets. The particular data discussed in this paper was collected on a 1 kW class radiatively-cooled laboratory type thruster designed and built by NASA Lewis Research Center.[24] The tungsten nozzle consisted of a 0.64 mm diameter constrictor and a 20 degree half-angle diverging section to an exit plane area ratio of 225. The 2% thoriated tungsten cathode was set approximately 0.45 mm from the nozzle constrictor. Details of this arcjet have been given previously.[24] This arcjet is of particular interest in that it has become a standard testbed for diagnostics and model development as many "identical" arcjets of this type have been widely distributed for laboratory testing and flowfield diagnostics.

Although we have collected data over a wide range of operating conditions, our most extensive data set collected is at or very near the operating conditions of 13 mg/s of hydrogen propellant and an arcjet power of 1.4 kW. As discussed in Section III, these measurements provide us with a means of evaluating the transport of thermodynamic flow properties such as the average specific enthalpy and average specific entropy, and in evaluating the individual contributions of various losses (i.e., profile losses), which impact the overall thermodynamic performance of these devices.

Using laser-induced fluorescence (LIF), we have mapped out the axial velocity profile at the exit plane and within the nozzle region.[8-12] Recent results for the axial and radial variation in the axial component of velocity are depicted in Figs. 1 and 2. Also shown in these figures are the results from two-photon LIF studies of Pobst et al.,[13] and the single-fluid calculations of Butler.[23] Note that the central core of the flow at the exit of the arcjet nozzle is well approximated by a parabolic profile. Note also that the axial velocity decreases with increasing distance downstream of throat. A detailed mapping of the velocity within the nozzle[12] indicates that viscous radial transport of axial momentum from the core is significant in these flows. It is apparent that the single-fluid model does a very good job at capturing the core flow velocity, but appears to underpredict the velocities for radial positions greater than about 2.5 mm. The data in Fig. 2 represent the first velocity measurements within an arcjet nozzle, and the first

direct evidence of the important role that viscosity plays in developing the nozzle flow.

Using optical emission[17] and LIF,[10,11] we have measured the translational temperature at the arcjet exit plane and along the flow centerline within the thruster. The results are summarized in Figs. 3 and 4, along with the two-photon LIF measurements of Pobst. et al.,[13] and the single fluid model predictions of Butler.[23] There is general agreement between the measurements, with that of Ref. 13 being somewhat lower than the measurements of our group. Overall, the temperatures peak in the 2000-2500K range at the exit plane of the thruster, indicative that a considerable enthalpy is convected out of the nozzle, despite the relatively large area ratio.

The general agreement that is obtained between the measured and predicted velocity and temperature distributions, although significant, is not a sufficient test of the overall model capability. While this agreement is encouraging, the model predicts a specific impulse that is approximately 15% greater than that measured under comparable operating conditions.[23]

In order to better understand the source of this discrepancy, we have recently employed Raman scattering as a means of measuring the exit plane molecular hydrogen density.[14] These measurements are shown in Fig. 5, along with the measurements of Pobst et al.,[14] of the atomic hydrogen number densities obtained using two-photon LIF, as well as the single-fluid model predictions.[23] We see that the model overpredicts the measured molecular hydrogen number densities, while seemingly underpredicting the atomic hydrogen number density. Although at first, one might attribute this discrepancy to the incorrect prediction of the exit plane dissociation fraction, we shall see later that the calculated dissociation fraction (H-atom mole fraction) of nearly 45% as inferred from the measured number densities in this figure is inconsistent with an overall energy balance on the propellant.

In an attempt to resolve this inconsistency, we have recently designed and implemented a probe for measuring the distributed exit plane mass flux.[20] A typical exit plane mass flux profile is shown in Fig. 6. For comparison, we also show the mass flux profile predicted by the single-fluid model.[23] We see from these measurements that the model overpredicts the mass flux in the core of the

flow, while underpredicting the mass flux at larger radii. This result is qualitatively consistent with the overprediction of the molecular hydrogen density across the exit plane (if we assume that the flow is only weakly dissociated), while underpredicting the velocity at larger radii. In Fig. 6, we also plot the inferred molecular hydrogen number density (assuming weak dissociation), calculated from the mass flux profile and measured axial velocity profile. We see that the inferred molecular hydrogen number density is in reasonable agreement with the measured molecular hydrogen number density. This agreement supports the conjecture that the flow is only weakly dissociated, a conclusion also drawn from the model simulations. More importantly, it suggests that the potential source of error in the simulations is in the modeling of the pressure field in the nozzle, a result that may be very sensitive to the selection of the transport properties (i.e., viscosity) of the dissociated hydrogen mixture.

In a series of studies aimed at understanding the near-cathode behavior of these arcjets, we have viewed the axial plasma and cathode emission along a direction opposite the plasma flow through the nozzle. As described in detail in Ref. 16, the spectral line intensity of the Balmer series transitions, when viewed along this direction, originates mainly from the first millimeter volume of plasma immediately in front of the cathode within the constrictor region. The predominantly Stark-broadened spectral lineshape in the distant wings of the H_α transition was used to measure the near-cathode (constrictor) electron number density. This data, for a range of operating powers, is shown in Fig. 7. Also shown in Fig. 7 is the inferred arc temperature, based on the assumption that the arc centerline is fully ionized, and that the flow is sonic (choked) at the point of maximum emission ($P_{throat} \approx 0.53 P_{feed}$). Recent measurements of static pressure in the constrictor of a 1kW arcjet operating on simulated hydrazine[25] indicate that the flow is choked very near the arcjet constrictor. The temperatures that are arrived at from this analysis are in quantitative agreement with those measured spectroscopically in a water-cooled helium arcjet.[26] However, the trend is opposite to what is expected; that the arc temperatures should increase with increasing specific energy. We attribute this apparent anomaly to two possible sources: (i) the optical emission measurements of electron density do not sample from a region of the flow close to the sonic point, and (ii) the uncertainty in the electron densities. Although we expect electron densities to increase with increasing specific energy, the limitations of our measurements do not permit us to determine if they increase at a rate greater or less than the feed pressure. For the purposes of our thermodynamic analysis, we shall therefore assume that the arc temperature is nominally 20000K.

In order to arrive at a measure of the cathode and anode temperature during arcjet operation, axial emission originating from the inner arcjet surfaces was collected by a long distance-microscope through a series of redirecting mirrors and imaged onto a CCD camera.[18] A 700nm, 10 nm bandwidth, and an 810nm, 10 nm bandwidth interference filter, were chosen such that the cathode and anode emission could be isolated from the hydrogen lines and the continuum emission due to free electrons in the plasma. An absolute intensity calibration was performed with a tungsten filament lamp, so as to convert the measured intensity distribution to temperatures, assuming an appropriate emissivity of 0.4 for the tungsten surfaces.

It is important to note here that no corrections to these data have been made for the re-radiation of cathode emission that is reflected off of the anode surfaces. The effects of surface reflections will be more significant downstream of the constrictor for these geometries, and the inferred temperatures should be interpreted as upper bounds on the actual anode temperatures.

Fig. 8 depicts a typical result of the inferred temperature verses radial position as projected onto the direction of observation. The location of the throat (constrictor) edge, and nozzle edge (ID and OD) are illustrated for a convenient reference. The large central peak (off scale in this figure) is associated with the molten cathode spot, discussed in detail in Ref. 18. Note that the anode temperature appears to be relatively uniform and at a value of approximately 1400 - 1500 K throughout most of the nozzle, and then rises sharply to approximately 1700-2500 K very near the arcjet constrictor. The inferred anode temperatures are consistent with measurements made of the outer surface of the anode using two-color pyrometry.

Although it is appropriate to undertake a detailed comparison between the collected arcjet data and predictions from physical models of arcjet operation, in the section that follows, we instead use these data to understand the global arcjet

performance. The analysis below provides a means of checking for self consistency, and for critically assessing the realistic performance limits within the framework of simple thermodynamic constraints.

III. Simple Arcjet System Model

In many ways, an arcjet can be thought of as an open thermodynamic system, which processes a fluid from one equilibrium thermodynamic state to another. Like all thermodynamic systems, there are limits associated with such state-changing processes imposed by the first and second law balances. Often, these thermodynamic limitations are far from reached because of the irreversibility associated with entropy production during one or more process paths. Although the end states between process paths in real systems may be somewhat removed from thermodynamic equilibrium, it is nonetheless useful to undertake such thermodynamic equilibrium analyses, as they can provide insight as to how far removed an actual process may be from an ideal process (no entropy production), and possible directions for design changes so as to be closer in performance to the ideal case.

The Arcjet Flow as a Thermodynamic Process

The fluid within an arcjet, as an open thermodynamic system, can be thought of, in a simplified way, as undergoing a sequence of thermodynamic processes. Unlike many multi-component thermal systems, the analysis of an arcjet is not straightforward, in that it cannot be easily decomposed into a subset of components, each of which can be analyzed using first and second law balances. In a global sense however, an arcjet does have the characteristics of a broader class of thermal systems, as illustrated in Fig. 9, in which mass can flow into and out of the system (open system) at a rate $\dot{m}$ (assuming a steady process), carrying with it various energy modes, as well as flow work and entropy. When work is done on the system at a rate $\dot{W}$, such a system can release heat to the environment, and convert some fraction of this work to a desired form of energy (kinetic energy, thermal energy, potential energy, work, or mixtures thereof).

Although there are no clean demarcations within an arcjet system separating well defined processes on the working fluid, it is nonetheless instructive to carry out a thermodynamic analysis that makes use of the fundamental energy and entropy balances. The recent plethora of measurements that have been made on a particular arcjet thruster (the NASA Lewis 1 kW class laboratory model arcjet thruster operating on hydrogen) provides an unparalleled opportunity to analyze such a complex system using these basic laws.

As a starting point, we will define the primary system of analysis, by way of the control volume illustrated in Fig. 9, to include both the propellant within the arcjet nozzle, (contained within the exit plane, and upstream of the cathode where it is at a known temperature) and the tip of the cathode. In steady-state, the propellant enters the control volume at a rate $\dot{m}$ equal to that at which it is discharged, carrying with it an average specific enthalpy, $\bar{h}_i$, and average specific entropy, $\bar{s}_i$ It is discharged with an average specific enthalpy $\bar{h}_o$, and specific entropy, $\bar{s}_o$ (generally greater than $\bar{h}_i$ .and $\bar{s}_i$ respectively), having a mass-associated kinetic energy transfer rate of $\frac{1}{2}\int \rho v^2 \vec{v} \cdot d\vec{A}$ (here, $\vec{v}$ is the exit plane velocity, which can vary over the exit area of the nozzle). The electrical supply does work at a rate $\dot{W}$ (this is also the input arcjet power from the power supply), on the electrons, to overcome the potential barrier in the discharge. Heat is transferred to the anode, which is at a temperature of T_A, at a rate $\dot{Q}_A$, equal to the rate that the anode radiates heat to distant space.

An arcjet operating in space is *necessarily irreversible* (i.e., entropy must be produced), in that the propellant can never be heated by the distant environment, while still discharging out of the nozzle at a temperature higher than that of the propellant flowing in. To illustrate this, consider the entropy balance applied to the control volume indicated in Fig. 9:

$$\dot{P}_s = \dot{m}\left(\bar{s}_o - \bar{s}_i\right) + \frac{\dot{Q}_A}{T_A} \qquad (1)$$

The balance states that entropy must be produced in this system at a rate $\dot{P}_s$, as long as heat is transferred from the propellant to the anode, and as along as the propellant entropy is increasing, both of which are true in the case of an arcjet.

It is of little use then to define the "ideal performance" as that in which a reversible process takes place (no entropy production) since this

would imply heat transfer from the environment to the propellant, which is not physically possible here.

In order to better understand how close to "ideal" arcjet operation we may be by present arcjet design, our approach here is to analyze the arcjet system further, by dividing it into two idealized subsystems. The first is one which includes the cathode tip and arc, on which work, at a rate $\dot{W}$ is performed by the electric field on the electrons. The arc is defined by a stationary volume of propellant, maintained at a temperature, T_{arc}, by ohmic heating, and heat is transferred from the arc to the surrounding flowing propellant at a rate $\dot{Q}_H$. This subsystem is identified in Fig. 10. Certainly, this interpretation is greatly simplified, since in practice, the propellant heated by the arc is indeed convected through the nozzle. However, the approximation made here is justified by the fact that the viscosity of the arc fluid increases with temperature, producing a low density, highly viscous region around which most of the propellant flows.

The second subsystem is the flowing propellant within the nozzle surrounding the arc. This is also illustrated in Fig. 10. In this subsystem, the propellant enters the control volume at a rate $\dot{m}$, carrying with it an average specific enthalpy, $\bar{h}_i$, and average specific entropy, $\bar{s}_i$, computed using a known inlet flow temperature, which, along with the velocity, is assumed to be uniform. The propellant is discharged from the nozzle with an average specific enthalpy $\bar{h}_o$, and average specific entropy, $\bar{s}_o$, defined as:

$$\bar{h}_o = \int \rho u_z(r) h_o(r) dA / \dot{m}$$
$$\bar{s}_o = \int \rho u_z(r) s_o(r) dA / \dot{m} \quad (2)$$

Heat is transferred to the anode, which is at a temperature, T_A, at a rate $\dot{Q}_A$, and heat is transferred to the propellant from the arc at a rate $\dot{Q}_H$.

An entropy balance on the arc subsystem indicates that entropy must be produced at a rate $\dot{P}_{s(arc)} = \dot{Q}_H / T_{arc}$. This same amount of entropy is transferred to the propellant subsystem by way of heat transfer. An energy and entropy balance on the propellant subsystem gives the rate of kinetic energy out of the exit of the nozzle:

$$\frac{1}{2} \int \rho v^2 \bar{v} \cdot d\bar{A} = \frac{1}{2} \int \rho u_z^3 dA + \frac{1}{2} \int \rho u_r^2 u_z dA$$
$$= \dot{W} - \dot{W}\frac{T_A}{T_{arc}} + \dot{m}(\bar{h}_i - \bar{h}_o) \quad (3)$$
$$- T_A(\bar{s}_i - \bar{s}_o) - T_A \dot{P}_{s_{prop}}$$

Here, we have expressed the outflow of kinetic energy as the sum of two terms; the axial and radial energy component. The latter can be interpreted as the "profile loss," which does not contribute to the thrust power of the arcjet. The last term on the right hand side (RHS) of Eqn. 3 represents the *irreversibility rate* associated with entropy production in the propellant subsystem, where the propellant is heated and expanded. Note also that the second term on the RHS is the entropy transfer from the arc to the propellant. We can express this relation in terms of the mean jet velocity, $\bar{u}$, by defining the *kinetic energy coefficient*, α_E:

$$\alpha_E = \frac{1}{2}\int \rho u^3 dA / \frac{1}{2}\dot{m}\bar{u}^2 \quad (4)$$

(which has a value of 2 for a uniform density flow with a parabolic velocity profile, close to the case here).

We can also introduce the momentum coefficient, α_M:

$$\alpha_M = \int \rho u_z^2 dA / \dot{m}\bar{u} = T/\dot{m}\bar{u} \quad (5)$$

(which has a value of 4/3 for a uniform density flow and a parabolic velocity profile). Note that we have defined the thrust, T as just the momentum flux, and we are neglecting the force associated with a finite expansion pressure.

The output of kinetic energy derived above can be expressed in terms of the thrust, T:

$$\frac{T^2 \alpha_E}{2\dot{m}\alpha_M^2} = \dot{W} - \dot{W}\frac{T_A}{T_{arc}} + \dot{m}(\bar{h}_i - \bar{h}_o)$$
$$- P_{PL} - T_A\dot{m}(\bar{s}_i - \bar{s}_o) - T_A\dot{P}_{s_{prop}} \quad (6)$$

where we have introduced $P_{PL} = \frac{1}{2}\int \rho u_r^2 u_z dA$ as the profile loss. We can go further and define the *thrust efficiency*, $\eta_T = \frac{T^2}{2\dot{m}\dot{W}}$:

$$\eta_T = \left\{ 1 - \frac{T_A}{T_{arc}} + \frac{\dot{m}}{\dot{W}} \left(\bar{h}_i - \bar{h}_o \right) - \frac{\dot{m} T_A}{\dot{W}} \left(\bar{s}_i - \bar{s}_o \right) \right.$$
$$\left. - \frac{T_A}{\dot{W}} \dot{P}_{s_{prop}} - \frac{P_{PL}}{\dot{W}} \right\} \frac{\alpha_M^2}{\alpha_E} \qquad (7)$$

The *adiabatic thrust efficiency* is defined here to be the thrust efficiency when the increase in propellant entropy is supported by the production of entropy in the heating and expansion of the propellant, and the entropy transfer from the arc to the propellant, i.e.,

$$0 = -\dot{W} \frac{T_A}{T_{arc}} - \dot{m} T_A \left(\bar{s}_i - \bar{s}_o \right) - T_A \dot{P}_{s_{prop}} \qquad (8)$$

Within this adiabatic limit, the adiabatic thrust efficiency is then:

$$\eta_{T(adiabatic)} = \left(1 - \frac{\dot{m}}{\dot{W}} \left(\bar{h}_i - \bar{h}_o \right) - \frac{P_{PL}}{\dot{W}} \right) \frac{\alpha_E}{\alpha_M^2} \qquad (9)$$

as expected, since maximum thrust is achieved when there is no energy loss to the anode via heat transfer. It instructive to compare the actual efficiency measured under typical arcjet operating conditions, to that of the "ideal" case for expansion of the propellant to an known exit temperature, T_E, and a known exit plane fractional dissociation (which for hydrogen, is equal to the atomic hydrogen mass fraction):

$$\theta_D = \frac{\dot{m}_H}{\dot{m}}. \qquad (10)$$

Here, $\dot{m}_H$ represents the mass flow rate of atomic hydrogen at the arcjet exit plane. For the purpose of this calculation, we shall assume that the total density and mole fractions of atomic and molecular hydrogen are uniform at the exit plane. This assumption is justified by the relatively weak radial dependence on the measured molecular hydrogen number densities. Also, the exit plane enthalpy of the mixture (atomic and molecular hydrogen) is calculated assuming fully excited rotational and vibrational energy modes that are in thermal equilibrium with the local translational temperature. Using the measured radial variation in translational temperature and axial velocity, we can compute the average exit plane specific enthalpy, as defined in Eqn. 2. From the measured exit plane axial and radial velocity, we can also calculate the momentum and kinetic energy coefficients, as well as the profile loss, P_{PL}.

Fig. 11 shows the calculated variation in the adiabatic thrust efficiency with exit plane fractional dissociation (atomic hydrogen mass fraction), assuming an exit pressure of 2 Torr, inlet pressure of 2 atm, inlet propellant temperature of 300K (the results are not very sensitive to the selection of these conditions), and nominal operating conditions of 1.4 kW and 13mg/s. As expected, we see a decrease in the adiabatic thrust efficiency with increasing fractional dissociation of the propellant. This is attributed primarily to the frozen flow losses in the propellant. For example, at a fractional dissociation of 0.25, the centerline exit plane propellant is calculated to be twice the equilibrium dissociation at the local (peak centerline) temperature.

It is emphasized that the adiabatic thrust efficiencies depicted in Fig. 11 are expected to be significantly higher than the actual thrust efficiencies, since, by definition, anode heat transfer is not included in the calculation. This calculation therefore allows us to put an upper bound on the dissociation fraction, since the adiabatic thrust efficiencies must not be greater than the actual thrust efficiencies that have been measured. Performance measurements on an arcjet of the same design operating on hydrogen under similar conditions place the thrust efficiencies in the 0.28-0.3 range.[24]

Clearly, this result implies that the actual dissociation fractions are expected to be considerably less than 0.18 and much lower than the values estimated from the combined measurements of the atomic[13] and molecular hydrogen[14] number densities alone. As discussed earlier, the agreement between the molecular hydrogen number densities measured by Raman scattering and the total densities measured by the mass flux probe are consistent with this overall energy balance, and so we must conclude that the atomic hydrogen number densities are somewhat higher than that which can be accounted for on the basis of an energy balance. This conclusion is also supported by the fact that the measured atomic hydrogen number densities seem to be greater than the measured total densities, over a significant portion of the exit plane.

It is of further interest to note that for the conditions used to generate the results depicted in Fig. 11, the profile loss associated with the radial component of velocity at the exit plane, P_{PL},

accounts for approximately 35W, and the overall adiabatic efficiency is reduced by 90% as a result of the exit plane axial profile factor α_E / α_M^2.

The overall conclusions derived from the results shown Fig. 11 are not strongly affected by uncertainties in the exit plane temperature. In Fig. 12, we plot the adiabatic thrust efficiency against the peak exit plane temperature (constraining the exit temperature profiles to have the same general shape and near-wall' temperatures that were measured). In this figure, we fix the fractional dissociation at a value of $\theta_D = 0.15$. We see that significant (500K) uncertainties or differences in the measured temperature do not strongly affect the above interpretation, although it is true that an overestimate of the actual exit temperature would reduce the upper limit imposed on the dissociation fraction.

In many thermodynamic systems, it is appropriate to define the "ideal efficiency" to be the efficiency determined for a system operating under certain thermal constraints (heat transfer to and from thermal reservoirs) when the production of entropy in the system is zero. Considering the propellant subsystem, we can define the *ideal thrust efficiency* as:

$$\eta_{T_{(ideal)}} = \left\{ 1 - \frac{T_A}{T_{arc}} + \frac{\dot{m}}{\dot{W}}\left(\bar{h}_i - \bar{h}_o\right) \right.$$
$$\left. - \frac{\dot{m}T_A}{\dot{W}}\left(\bar{s}_i - \bar{s}_o\right) - \frac{P_{PL}}{\dot{W}} \right\} \frac{\alpha_M^2}{\alpha_E} \quad (11)$$

However, we find that if we impose the constraint that the heat transfer to the anode must be positive, we arrive at physically significant efficiencies only for very low arc temperatures (2000 - 3000K), values that are considerably less than what is estimated experimentally.

A more appropriate measure of the limiting efficiencies attainable in an arcjet, is the case of an isentropic (constant entropy), reversible (no entropy production) flow that is one-dimensional and uniform at the arcjet exit plane, and expanded to negligible temperature:

$$\eta_{T_{(isentropic)}} = 1 - \frac{T_A}{T_{arc}} + \frac{\dot{m}}{\dot{W}}\bar{h}_i \quad (12)$$

From Eqn. 12, one can see the benefit of regeneratively cooling the propellant. If the injected propellant has a negligible enthalpy, then the limiting efficiency approaches the *Carnot efficiency:*

$$\eta_{T_{(Carnot)}} = 1 - \frac{T_A}{T_{arc}} \quad (13)$$

which depends only on the ratio of the anode and arc temperatures. As usual, this limiting result implies that the efficiency of this thermodynamic expansion process increases when the temperature at which heat is extracted from the system decreases, and the temperature at which heat is transferred to the system increases. It further implies that small gains might be made in thruster performance efficiency by designing an anode that operates at lower temperatures, or, by operating the arcjet to maximize arc temperature. At nominal operating conditions, the Carnot efficiency is expected to be close to unity, since in general, the ratio of the anode to arc temperature is $\ll 1$.

IV. Summary

In this paper, we have reviewed the past and recent measurements of plasma and flowfield properties in low power hydrogen arcjet thrusters. The collective set of data, from various experiments under a narrow range of arcjet operation, has provided us with an opportunity to look closely at the overall performance of an arcjet thruster, within the context of a thermodynamic system. We have defined ideal performance limitations from a first and second-law perspective, and have used the overall balances to identify possible uncertainties in measured plasma properties, such as H-atom concentrations and exit temperatures. Finally, the second-law analysis has shown that in certain limiting cases, the arcjet can be viewed as a simple Carnot engine, the efficiency of which scales as the ratio of the anode to arc temperature.

Acknowledgments

References

1. G.W. Butler, B.A. Kashiwa, and D.Q. King; "Numerical Modeling of Arcjet Performance"; AIAA-90-1474; 21st Fluid Dynamics, Plasma Dynamics and Lasers Conference, June 1990.

2. G.W. Butler and D.Q. King; "Single and Two Fluid Simulations of Arcjet Performance"; AIAA-92-3104, 28th Joint Propulsion Conference, July 1992.

3. G.W. Butler, A.E. Kull, and D.Q. King, "Numerical Simulation of Hydrogen Arcjet Performance," IEPC-93-249, 23rd International Electric Propulsion Conference, September 1993.

4. T.W. Megli, H. Krier, and R.L. Burton, "A Plasmadynamics Model for Nonequilibrium Processes in N_2/H_2 Arcjets," AIAA 95-1961, 26th Plasmadynamics and Lasers Conference, June, 1995.

5. R. Rhodes and D. Keefer; "Modeling Arcjet Space Thrusters"; AIAA-91-1994; 27th Joint Propulsion Conference, June 1991.

6. S. Miller, and M. Martinez-Sanchez, "Nonequilibrium Numerical Simulation of Radiation-Cooled Arcjet Thrusters," IEPC-93-218, 23rd International Electric Propulsion Conference, September, 1993.

7. V. Babu, S. Aithal, and V.V. Subramaniam, "Vibrational Nonequilibrium in Arcjet Flows," IEPC-93-129, 23rd International Electric Propulsion Conference, September, 1993.

8. J.G. Liebeskind, R.K. Hanson, and M.A. Cappelli, "Flow Diagnostics of an Arcjet Using Laser-Induced Fluorescence," AIAA 92-3243, 28th Joint Propulsion Conference, July , 1992.

9. J.G. Liebeskind, R.K. Hanson, and M.A. Cappelli, "Laser-Induced Fluorescence Diagnostic For Temperature and Velocity Measurements in a Hydrogen Arcjet Plume," *Journal of Applied Optics*, Vol. 32, No. 30, Oct., 1993.

10. P.V. Storm and M.A. Cappelli, "Stark Broadening Corrections to Laser-Induced Fluorescence Temperature Measurements in a Hydrogen Arcjet Plume," *Applied Optics*, in press, 1996.

11. P.V. Storm and M.A. Cappelli, "LIF Characterization of Arcjet Nozzle Flows," AIAA-96-2987, 32nd Joint Propulsion Conference, July, 1996.

12. P.V. Storm and M.A. Cappelli, "Fluorescence Velocity Measurements in the Interior of an Arcjet Nozzle," *AIAA Journal*, 34, 853, 1996.

13. J.A. Pobst, I.J. Wysong, and R.A. Spores, "Laser-Induced Fluorescence of Ground State Hydrogen Atoms at the Nozzle Exit of an Arcjet Thruster, AIAA 95-1973, 26th Plasmadynamics and Lasers Conference, June, 1995.

14. D.R. Beattie and M.A. Cappelli, "Raman Scattering Measurements of Molecular Hydrogen in an Arcjet Thruster Plume," AIAA 95-1956, 26th Plasma- dynamics and Lasers Conference, June, 1995.

15. W. Hargus, M. Micci, and R. Spores, "Interior Spectroscopic Investigation of the Propellent Energy Modes in an Arcjet Nozle," AIAA 94-3302, 30t Joint Propulsion Conference, June, 1994.

16. P.V. Storm and M.A. Cappelli; "Axial Emission Diagnostics of a Low Power Hydrogen Arcjet Thruster," IEPC-93-219, 23rd International Electric Propulsion Conference, September 1993.

17. "High Spectral Resolution Emission Study of a Low Power Hydrogen Arcjet Plume," P.V. Storm and M.A. Cappelli, AIAA-95-1960, 26th Plasmadynamics and Lasers Conference, June, 1995.

18. D. Berns, P.V. Storm, and M.A. Cappelli, "Spectral Imaging of the Arcjet Electrode Region," AIAA 95-1957, 26th AIAA Plasmadynamics and Lasers Conference, San Diego, June, 1995.

19. W.A.Hargus, Jr., and M.A. Cappelli, "Pressure Measurements in the Plume of a Low Power Arcjet Nozzle," AIAA-95-2818, 31st Joint Propulsion Conference, July, 1995.

20. W.A.Hargus, Jr., and M.A. Cappelli, "Mass Flux Measurements in the Plume of a Low Power Arcjet Nozzle," AIAA-96-3190, 32nd Joint Propulsion Conference, July, 1996.

21. M. A. Cappelli, J.G. Liebeskind, R.K. Hanson, G.W. Butler, and D.Q. King; "A Comparison of Hydrogen Arcjet Plume Properties to Single and Two-Fluid Model Predictions" IEPC-93-220 23rd International Electric Propulsion Conference, September,1993.

22. M. A. Cappelli, J.G. Liebeskind, R.K. Hanson, G.W. Butler, and D.Q. King "A Comparison of Arcjet Plume Properties to Model Predictions" AIAA 93-0820, 31st Aerospace Sciences Meeting, January, 1993.

23. G.W. Butler, I. D. Boyd, and M.A. Cappelli, "Nonequilibrium Flow Phenomenon in Low Power Hydrogen Arcjets" AIAA -95-2819, 31st Joint Propulsion Conference, July, 1995.

24. F.M. Curran, S.R. Bullock, T.W. Haag, C.J. Sarmiento, and J.M. Sankovic, "Medium Power hydrogen Arcjet Operation," AIAA 91-2227, 27th Joint Propulsion Conference, June, 1991.

25. K. Talley and W. Elrod, "Static Pressure Measurements of the NASA-Lewis 1.2 kW Arcjet," AIAA 92-3111, July, 1992

26. M. Ishii and K. Kuriki, "Optical and Analytical Studies of Arc Collumn in DC Arcjet," AIAA-87-1086, 19th International Electric Propulsion Conference, May, 1987.

DOPPLER-FREE LASER-ABSORPTION MEASUREMENTS OF ELECTRON DENSITY IN A 1-KW HYDROGEN ARCJET

P.V. Storm[†], Q. Walker[†], and M.A. Cappelli[‡]
Mechanical Engineering Department
Thermosciences Division
Stanford University
Stanford, CA 94305

Abstract

Doppler-free absorption spectroscopy (DFAS) of the Balmer-alpha (H_α) transition in atomic hydrogen was performed at the exit plane of a 1-kW class radiatively-cooled arcjet thruster operating on hydrogen as a propellant. Counter-propagating pump and probe beams provided by an Ar^+-pumped continuous-wave (cw) tunable ring-dye laser isolate a zero-velocity class of excited hydrogen atoms that interact with both laser beams. The pump beam produces a Bennet hole in the $v = 0$ velocity class atoms that reduces the absorption of the probe beam. The Doppler-free homogeneously-broadened (Stark broadened) probe absorption is used to determine the upper-bound in the electron number density. The measured electron number density variation across the exit plane and variation with arcjet power behave as expected and demonstrate good agreement when compared to arcjet model predictions and also when compared to previous measurements when experimental measurements of Stark broadening rates extrapolated to higher plasma densities are used. Use of the theoretical broadening rates assuming dynamical ion impacts [C. Stehle and N. Feautrier, *J. Phys. B* **17**, 1477 (1984)] results in a lesser agreement between the measured and predicted electron densities. These results demonstrate the need for improved measurements and validation of Stark broadening rates in these intermediate density ranges ($n_e = 10^{17} - 10^{20}$ cm^{-3}) common to the exit plane and nozzle flow regions of arcjet thrusters.

I. Introduction

The successful deployment of arcjet thrusters for north-south stationkeeping on tele-communication satellites has spawned a considerable interest in extending arcjet operating conditions to other potential applications such as re-positioning and orbit transfer. Such developments will be guided by advanced numerical simulations; however, critical to the development of such simulations is the accumulation of experimental data that characterizes the performance of these arcjets. This characterization includes, in addition to thrust and efficiency measurements, detailed measurements of plasma flow properties throughout the arcjet flowfield. Because of the high enthalpies and high velocities encountered in these devices, conventional flowfield diagnostics such as pressure, mass flux, and electrostatic probes, are difficult to interpret, somewhat intrusive, and often give ambiguous results. For this reason, many researchers have developed and applied non-intrusive optical diagnostics to measure plasma flowfield properties in both the plume and interior of these arcjets.

The most common optical diagnostic used to study arcjet thrusters is optical emission spectroscopy (OES). OES has been used to measure electron number density and temperatures in the nozzle-flow,[1] near-cathode,[2] and exit plane[3] of low-power (1-kW) arcjet thrusters. In addition to OES, a number of laser-based diagnostics have been developed and applied to the characterization of arcjet thrusters.[4-12] Primary among these laser diagnostics is single-photon laser-induced fluorescence (LIF). LIF has proven to be very useful in arcjet studies due to its abundant signal level, good spatial resolution, species-specific nature. Liebeskind et al.[4] measured atomic hydrogen velocities and translational temperature in the plume of a 1-kW hydrogen arcjet thruster, and investigated multi-component velocity slip by seeding the same arcjet with helium.[5] Ruynten and Keefer[6] measured velocities in the plume of a 0.3-kW argon arcjet, and Burtner et al.[7] have reported on hydrogen and nitrogen atom velocities in the plume of a 1-kW arcjet thruster operating on a propellant mixture simulating ammonia. More recently, Storm and Cappelli have reported on the LIF measurements of velocities, temperatures, and electron number densities in the

plume and interior of a 1-kW hydrogen arcjet,[8,9] and velocities and temperature in the interior of a 1 - kW arcjet operating on simulated hydrazine.[10]

In addition to single-photon LIF, both spontaneous Raman scattering[11] and two-photon LIF[12] have been used to characterize 1 - kW hydrogen arcjet thrusters. Together, the studies described in Refs. 2-5,8-12 form a relatively complete data set that describes exit plane hydrogen arcjet flowfield properties under virtually identical operating conditions. This experimental data base has been and continues to be used to critically evaluate the predictive capabilities of both compressible magneto-hydrodynamic (MHD) and direct simulation Monte Carlo calculations of arcjet performance.[13]

Despite the accumulation of a wide range of flowfield property data on low-power hydrogen arcjet thrusters, the spatial variation in exit-plane plasma electron number density has been one of the least documented plasma properties. Electrostatic probe-based measurements of electron number density have been made in 1-kW arcjet thrusters operating on simulated hydrazine propellant.[14] As far as we know, no other probe-based measurements have been made on 1-kW hydrogen arcjet thrusters. Although optical emission[3] and LIF spectroscopy[8] has been used to measure the electron number density in hydrogen arcjets from the Stark-broadened component of the H_α transition in atomic hydrogen, the accuracy of such methods is limited because the total broadening rate of the transition is dominated by the Doppler width. For condition expected at the exit plane of a Hydrogen arcjet thruster, the Doppler component to the total spectral width of the H_α transition can be as large as two to three times that of the Stark width. Also, we have shown previously that although Stark broadening of the H_α transition is believed to be less significant than Doppler broadening, not accounting for its affect on the overall broadening of the LIF excitation spectrum can lead to highly inaccurate measurements of the translational temperature9. These uncertainties are compounded by the lack of reliable Stark broadening rates available for atomic hydrogen in the $n_e = 10^{17}$ - 10^{20} cm^{-3} plasma density range, which extends beyond the conditions expected near the exit region of arcjet thrusters.

In this paper, we report on the preliminary results of experiments aimed at further quantifying the electron number density at the exit plane of a 1-kW hydrogen arcjet thruster. In order to overcome the problems related to the dominance of Doppler broadening in the LIF excitation of the H_α transition, a Doppler-free absorption spectroscopy (DFAS)

method is employed. This DFAS method, which is also laser-based, is used to extract the pure Stark-broadened component in the H_α absorption spectrum and hence the electron number density at the exit of a hydrogen arcjet thruster. The results presented here are preliminary in that an extensive analysis of the DFAS spectral line shape is not performed, and an exhaustive study over a wide range of arcjet operating conditions is not carried out. However, reliable upper limits to the plasma density are measured for operating conditions at which other plasma properties have been obtained, and for which MHD and DSMC modeling results[13] are available.

II. Theory

The DFAS used here is more commonly referred to as Doppler-free laser saturation spectroscopy (DFLSS) in the literature.[15] We purposely avoid the use of this description here because we employ laser-intensities that are well below the spectral transition saturation limits, which greatly simplifies the interpretation of the laser absorption lineshapes.

DFLSS has been developed primarily to, make high-resolution measurements of the transition energies of fine and hyperfine structure components in complex electronic spectra of atoms and simple molecules.[15] One of its first uses was to measure the Rydberg constant by making accurate measurements of the fine-structure splitting in the H_α transition in atomic hydrogen - the transition employed in the study presented here.[16] A partial energy diagram including the two principle quantum levels involved in the H_α transition and their fine structure is shown in Figure 1. Its use as a means of making detailed Doppler-free collision-broadened lineshape measurements is relatively new, and has not yet been extensively applied. In DFLSS, an intense laser is used to saturate an electronic transition of a particular species of interest, in this case, within a multi-component plasma. If the laser is incident onto a purely heterogeneously-broadened (Doppler-broadened) class of absorbers, then the laser photons, of frequency ν_ℓ (or wavelength, λ_ℓ) are only absorbed by that velocity class of absorbers that have a velocity such that in their moving reference frame, the photon energy, $h\nu_\ell$ equals the energy associated with the electronic transition, $h\nu_0$ (or hc/λ_0). If in the stationary (or laboratory) reference frame, $\nu_\ell = \nu_0$, then only absorbers having a laboratory frame velocity of $v = 0$ will interact with this laser beam. As a result, a saturating laser beam of frequency $\nu_\ell = \nu_0$ creates a "hole" in the otherwise Maxwellian population of $v = 0$ absorbers, greatly depleting the

electronic ground state density of these v=0 absorbers, and increasing the excited electronic state density to levels that are above their undisturbed values. This "hole" in the velocity distribution of absorbers is known as the "Bennett" hole.

The saturating laser in essence modifies the absorption coefficient of the medium by the creation of this Bennett hole. A second "probe" laser can be used to study the extent of the creation of a Bennett hole. If a second counter-propagating laser of wavelength equal to λ_0 and equal to that of the saturating laser is directed into the medium (see Figure 2 - top), then only absorbers with $v = 0$ can potentially interact with both laser photons. As a result, the probe beam will experience a reduced attenuation due to the Bennett hole in the $v = 0$ population produced by the saturating laser. On the other hand, for an absorber moving with $v \neq 0$ (see Figure 2- bottom), neither the saturating or probe beam interact with the absorber, and both pass through the medium unattenuated.

In practice, the absorbers in a Doppler broadened medium experience homogeneous broadening mechanisms such as natural broadening and both impact and quasi-steady collision broadening, and the spectral absorption characteristics of the probe beam will reflect these additional broadening mechanisms. The intense (now non-saturating) beam produces a Bennett hole that gives rise to a spectral absorption coefficient that has a Voigt profile.[15] In the homogeneously-broadened case, the counter-propagating probe beam of equal wavelength to the weak pump beam can interact with non-zero velocity absorbers, however, the wavelength dependence of the interaction will always follow the homogeneously broadened lineshape. As a result, the spectral absorption of the probe beam in the weak pump limit is expected to track the homogeneous broadened component in the spectral absorption lineshape, which for the H_α transition in atomic hydrogen at conditions near the arcjet exit plane, is primarily a result of collisional interactions with the electrons and ions, i.e., Stark broadening.

III. Experiment

The experimental setup is shown schematically in Figure 3. Both the pump and counter-propagating probe scanning excitation laser beams were produced by pumping a continuous-wave Coherent 699-21 ring dye laser by a Spectra Physics Stabilite 2016 argon-ion laser in multi-line mode. The dye laser contained DCM dye which has broad absorption and fluorescence bands centered around 500 nm and 650 nm, respectively, making it particularly suitable for Ar^+ pumping at 488 nm and 514.5 nm, and hydrogen H_α excitation at 656.28 nm. Dye laser output in excess of 300 mW was achieved with a pump laser power of 5.2 W in all lines. Continuous spectral scanning of the ring dye laser was accomplished with a tunable, piezoelectrically-driven intracavity etalon. The maximum scanning range was 30 GHz (1.0 cm^{-1}), or approximately 0.04 nm at the H_α wavelength. The laser specifications indicate a maximum laser line width of 20 MHz, established by the frequency jitter. The laser intensity was monitored by a photodiode detector built into the laser head.

The beam from the dye laser was split into three beams using a quartz window beamsplitter with non-parallel faces. The transmitted beam, accounting for approximately 92% of the incident intensity, constituted the pump beam, while one of the two reflected beams, at 4% intensity, was used as the probe beam. The other reflected beam was directed to a Burleigh WA-1000 wavemeter to monitor the laser wavelength. Using several flat mirrors, the probe and pump beams were aligned collinear in counter-propagating directions through the exhaust plume of the arcjet, within 1.0 mm of the exit plane. Two 76-mm diameter quartz windows on opposite sides of the vacuum chamber permitted optical access to the arcjet plume. A 750-mm biconvex lens was used to focus the pump beam to a calculated waist diameter of approximately 300 μm at the arcjet centerline. The focusing of the pump beam was performed to allow, if desired, a sufficient intensity to saturate the atomic transition. A 50-50 cubic-prism beamsplitter was used to spatially separate the pump and probe beams. Absorption of the probe beam was detected with a photodiode, while background light was rejected using a 10-nm-bandwidth H_α interference filter placed immediately in front of the photodiode detector.

To discriminate the Doppler-free signal from the absorption of the probe beam, the pump beam was chopped mechanically at a chopping frequency of approximately 1.6 kHz, and phase-sensitive detection was performed using a Stanford Research Systems SR-850 digital lock-in amplifier. The integration time of the low-pass filter was set to 3.0 s with a 24 dB/oct roll-off. Hence, signal amplification was performed within a bandwidth of 0.3 Hz centered on the 1.6 kHz reference frequency. A noise signal offset by only 5 Hz was therefore filtered by nearly 100 dB. This level of filtering permitted nearly complete rejection of plasma emission noise, as well as laser amplitude and frequency jitter noise on the probe beam. However, scattered light from the (chopped) pump beam could not be distinguished from true signal, and as the intensity of the pump

beam was great compared to the probe beam, this constituted a significant component of the frequency-independent background noise in the recorded spectra. Much of this signal occurred as a result of backscattering of the pump beam off of the chamber windows and the outer surfaces of the cubic-prism beamsplitter. Hence to minimize this background noise, or at least reduce it enough that the Doppler-free signal could be detected, the beam path was carefully misaligned with respect to the optical surfaces, while maintaining the collinearity of the two beams. This produced an angular separation between the probe beam and the back-scattered pump beam (not shown in Figure 3) of a few degrees. The probe beam was then spatially selected for detection using an aperture stop set at a diameter on the order of 1.0 mm.

Although a dye laser power greater than 300 mW was achieved, the experiments were performed at a nominal laser power of 150 mW to improve laser amplitude stability. At this laser power level, the pump and probe beam powers at the arcjet plume are approximately 60 mW and 5 mW respectively. To determine the extent of power broadening of the spectral lines, during one scan a neutral density filter of optical density 1.0 was placed in the pump beam immediately before the chopper. This filter reduced the pump beam power to approximately 6 mW.

The 30-GHz laser scans were performed in 625 seconds, giving rise to a total of 5000 data points per scan by sampling at 8 Hz. Outputs of the high-voltage etalon-scanning signal and the laser-head photodiode detector were simultaneously recorded through analog input channels of the lock-in amplifier in order to calibrate for wavelength and normalize the scans by laser intensity.

The vacuum facility consisted of a 1.09 m × 0.56 m diameter stainless-steel chamber. Two mechanical pumps and two 590-l/s (1250-CFM) blowers pumped the chamber through a 15-cm diameter steel pipe. With the arcjet operating, the chamber back pressure was typically 50 Pa (5.0×10^{-4} atm). The arcjet used in these experiments was a 1-kW radiation-cooled laboratory model which was designed and built at NASA's Lewis Research Center. The arcjet, which has been describe previously[9], is mounted on translation stages permitting adjustment of the position of the plasma plume with respect to the laser beams. The experiments were performed with hydrogen propellant at a flow rate of 10 SLM (approx. 14 mg/s) and an arcjet electrical power ranging from 0.8 to 1.5 kW.

The recorded Doppler-free signal from the lock-in amplifier was normalized with respect to laser intensity to account for variations in the laser power during each scan. The wave number scale was ascertained from the linear etalon drive voltage and the scan endpoints recorded by the wavemeter.

IV. Results

Table 1 provides, for reference, the state designations, frequencies, and relative intensities of the fine-structure components of the H_α transition probed by DFAS in this study. Figure 4 shows representative DFAS profiles of the H_α transition as measured through the arcjet centerline at the exit plane, and through a low-pressure weakly-ionized microwave-sustained hydrogen discharge. For comparison, we also include in this figure, a representative LIF excitation scan (shifted by approximately 1 cm^{-1} so that the peak co-incides with the DFAS scan). Note that the arcjet LIF spectrum is significantly broader than the corresponding DFAS spectrum. This is expected, as the DFAS eliminates the Doppler broadening component to the spectral absorption. Additional features in this figure are noteworthy: (i) the peaks associated with the two strongest fine structure components (the expected location and relative intensities of which are designated by the vertical lines in the figure) are clearly visible in the microwave discharge spectra, and are washed out in the arcjet spectra, presumably due to the greater Stark broadening; (ii) apparent in the microwave plasma DFAS spectrum is the presence of a "cross-over resonance",[15,16] despite the fact that the two peaks have different lower and upper states in the associated transitions; and (iii) the arcjet DFAS spectrum seems to reflect only the stronger of the two fine-structure peaks, with an apparent absence of signal associated with the 3p $^2P_{3/2} \leftrightarrow$ 2s $^2S_{1/2}$ and 3d $^2D_{3/2} \leftrightarrow$ 2p $^2P_{1/2}$ components. This apparent anomaly has yet to be resolved, and will require a further theoretical analysis of the expected DFAS spectral lineshape. The presence of the weak cross-over resonance in the microwave discharge scans is presumably due to a strong collisional coupling between the split states comprising the lower levels in the transition. If so, then such a coupling and cross-over resonance, although a minor affect on the overall spectral lineshape, should be accounted for in any detailed model of the spectral lineshape. In any case, a conservative upper limit in the electron number density can be obtained from the width of the DFAS spectrum if we assume that the measured DFAS spectrum is that of only the strongest fine-structure component. The data presented in the following

figures should therefore be construed as upper bounds to the exit plane plasma density.

Figure 5 compares the measured centerline DFAS spectra at taken at laser powers of 6 mW and 60 mW. Although more noisy than the 60 mW case, the 6 mW spectra is not considerably broader, indicating that the spectral absorption coefficient resulting from the pump beam is not significantly power broadened.

The measured DFAS spectra resulting from absorption along various chords across the exit plane is shown in Figure 6. Although absorption takes place along the line of sight, the measured spectrum is expected to weighted by the conditions where there is a greater number of v = 0 absorbers in the excited (n=2) electronic state. Because of the relatively peaked electron temperature, the greatest number of absorbers is near r = 0, and falls monotomically with increasing radius. As a result, we expect that the variation in the absorption spectral width with lateral position in fact qualitatively reflects the variation in the width of the spectral absorption profile (and hence, electron number density) with radius, r.

The variation in centerline DFAS spectra with arcjet power is shown in Figure 7. A peculiar feature in this figure is the apparent shift in the peak of the DFAS spectra with increasing arcjet power (and hence plasma density). At this point, we cannot explain this anomalous behavior, although it may be a result of an increased collisional coupling between lower states with increasing exit plane plasma temperature. The overall width of the spectra does not seem to be very sensitive to changes in the arcjet operating power.

Using the calculated Stark broadening rates of Stehle and Feautrier[17] for the individual fine-structure components in the spectrum, these data presented in

Figures 6 and 7 can be reduced to plots of the electron number density dependence on the exit-plane radial position and arcjet power. These results are presented in Figures 8 and 9. We see that there is a vary weak dependence of the electron number density with radial position and arcjet power over the ranges investigated. Also shown in Figures 7 and 8 are the calculated results based on simulations using the MHD model of Butler et al.[18] The measured electron number densities are in remarkable agreement with those predicted by the model simulations. It should be noted that previous comparisons of measured hydrogen velocities, temperatures, atomic hydrogen and molecular hydrogen densities also gave very good agreement with the MHD model predictions at or very near these arcjet operating conditions.

A point should be made here about the use of the Stark broadening rates calculated by Stehle and Feautrier.[18] Like the electron collisions, these rates treat the ion perturbing collisions in the impact limit. This approach is valid in the low plasma density limit, and when extrapolated to higher densities, the results agree well with the dynamic ion Monte Carlo simulation of Stark broadening of the Hα transition by Oza et al.[19] These computed rates seem to be in significant disagreement with the measured low-density ($<10^{17}$ cm^{-3}) Stark broadening rates of Weber and Humpert.[20] Use of the Weber and Humpert broadening rates (extrapolated to higher densities) in the interpretation of our data would give rise to inferred electron number densities that are lower than those predicted by the simulation by nearly one order of magnitude. It is apparent that further validation of the computed Stark broadening rates are needed over the plasma density ranges encountered in this study.

Upper$j$	Lower$j$	Transition	δv (cm^{-1})	Relative Intensity
1/2	3/2	3s $^2S_{1/2} \leftrightarrow$ 2p $^2P_{3/2}$	-0.144	0.05
3/2	3/2	3d $^2D_{3/2} \leftrightarrow$ 2p $^2P_{3/2}$	-0.036	0.28
5/2	3/2	3d $^2D_{5/2} \leftrightarrow$ 2p $^2P_{3/2}$	0.000	2.50
1/2	1/2	3s $^2S_{1/2} \leftrightarrow$ 2p $^2P_{1/2}$ 3p $^2P_{1/2} \leftrightarrow$ 2s $^2S_{1/2}$	0.220	0.31
3/2	1/2	3p $^2P_{3/2} \leftrightarrow$ 2s $^2S_{1/2}$ 3d $^2D_{3/2} \leftrightarrow$ 2p $^2P_{1/2}$	0.328	1.96

Table 1. Components of the Hα transition and their properties.

V. Summary

Doppler-free measurements are made of the Balmer-alpha absorption lineshapes through the exit plane region of a low-power hydrogen arcjet. Exit plane electron number densities are extracted from the primarily Stark-broadened spectra. The results obtained in this study are consistent with previous results obtained from a re-analysis of LIF data[8]. In these prior LIF studies, the laser excitation fluorescence lineshapes were interpreted as Voigt profiles, and the Lorentzian (Stark) and Gaussian (Doppler) widths were extracted from theoretical fits to the convoluted spectra. The DFAS results thus confirm the electron number density obtained by LIF, and provide a means of making measurements of higher accuracy. The results presented in this study, however, constitute upper limits to the electron number densities, as detailed DFAS lineshape analysis that include collision-enhanced cross-over resonances have not been performed. These detailed analyses will be the subject of a future paper.

Acknowledgement

References

1. D.M. Zube and R.M. Myers, "Thermal Nonequilibrium in a Low Power Arcjet Nozzle," *Journal of Propulsion and Power* 9, 545, 1993.

2. P.V. Storm and M.A. Cappelli, "Radiative Emission Analysis of an Expanding Hydrogen Arc Plasma I: Arc Region Diagnostics Through Axial Emission," *JQSRT* 56, 901, 1996.

3. P.V. Storm and M.A. Cappelli, "Radiative Emission Analysis of an Expanding Hydrogen Arc Plasma II: Plume Region Diagnostics Through Radial Emission," *JQSRT* 56, 919, 1996.

4. J.G. Liebeskind, R.K. Hanson, and M.A. Cappelli; "Laser-Induced Fluorescence Diagnostic for Temperature and Velocity Measurements in a Hydrogen Arcjet plume," *Applied Optics* 32, 6117, 1993.

5. J.G.Liebeskind, R.K.Hanson, and M.A.Cappelli, "Experimental Investigation of Velocity Slip Near an Arcjet Exit Plane," *AIAA Journal* 33, 373, 1995.

6 W. M. Ruyten and D. Keefer, "Characterization of Electric Thruster Plumes using Multiplexed Laser-Induced Fluorescence Measurements," AIAA-92-2965, 28th Joint Propulsion Conference, July, 1992.

7. D.Burtner, D.Keefer, and W.M. Ruyten, "Experimental and Numerical Studies of a Low Power Arcjet Operated on Simulated Ammonia," AIAA-94-2869, 30th Joint Propulsion Conference, June, 1994.

8. P.V.Storm and M.A. Cappelli, "Stark Broadening Corrections to Laser Induced Fluorescence Temperature Measurements in a Hydrogen Arcjet Plume", *Applied Optics* 35, 4913, 1996.

9. P.V. Storm and M.A. Cappelli, "Fluorescence Measurements of Atomic Hydrogen Velocity in the Interior of an Arcjet Nozzle," *AIAA Journal* 34, 853, 1996.

10. P.V. Storm and M.A. Cappelli, "LIF Characterization of Arcjet Nozzle Flows," AIAA-96-2987, 32nd Joint Propulsion Conference, July, 1996.

11. D.R. Beattie and M.A. Cappelli, "Raman Scattering Measurements of Molecular Hydrogen in an Arcjet Thruster Plume," AIAA-95-1956, 26th AIAA Plasmadynamics and Lasers Conference, June, 1995.

12. J.A. Pobst, I.J. Wysong, and R. A. Spores, "Laser-Induced Fluorescence ground State Hydrogen Atoms at the Nozzle Exit of an Arcjet Thruster, AIAA-95-1973, 31st Plasmadynamics and Lasers Conference, June, 1995.

13. G.W. Butler, I.D. Boyd, and M.A. Cappelli, "Nonequilibrium Flow Phenomenon in Low Power Hydrogen Arcjets," AIAA-95-2819, 31st Joint Propulsion Conference, July , 1995.

14. Burton, R. L. and Bufton, S. A., "Exit-Plane Electrostatic Probe Measurements of a Low-Power Arcjet," Journal of Propulsion and Power Vol. 12, No. 6, pp. 1099-1106, Nov.-Dec., 1996.

15. W. Demtröder, *Laser Spectroscopy*, Springer-Verlag, Berlin, 1981.

16. T.W. Hansch, A.L. Shawlow, and G.W. Series, "The Spectrum of Atomic Hydrogen, *Scientific American* 240, 94, 1979.

17. C. Stehle and N. Feautrier, "Stark Broadening of the H_α Line of Hydrogen at Low Densities:Quantal and Semiclassical Results," *J. Phys. B* 17, 1477, 1984.

18. G.W. Butler, A.E. Kull, and D.Q. King, "Single Fluid Simulations of Low Power hydrogen Arcjets," AIAA-94-2870, 30th Joint Propulsion Conference, June, 1994.

19. D.H. Oza, R.L. Greene, and D.E. Kelleher, "Dependence of the Half-Widths of Plasma-Broadened Hydrogen Lines on Reduced Mass, Temperature, and Density," *Phys. Rev. A* 38, 2544, 1988.

20. E.W. Weber and H.J. Humpert, "Plasma Shift and Broadening of Single Hydrogen Balmer-Alpha Fine-Structure Lines," *Physics Letters A*, 83A, 386, 1981.

n=3

$^2D_{5/2}$

$^2P_{3/2}$, $^2D_{3/2}$

$^2S_{1/2}$, $^2P_{1/2}$

$^2P_{3/2}$

n=2

$^2S_{1/2}$, $^2P_{1/2}$

λ_0 v=0 λ_0

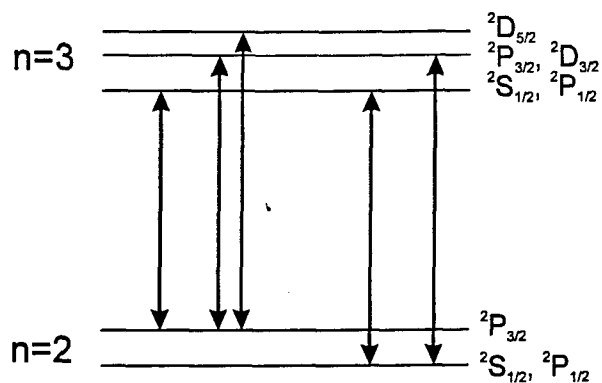$\lambda > \lambda_0$ v>0 $\lambda < \lambda_0$

Figure 1. Energy level diagram of the atomic hydrogen Balmer-alpha line showing the allowable fine-structure transitions.
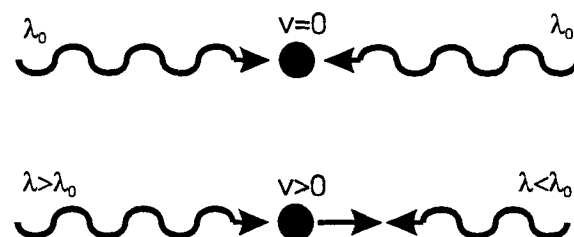
Figure 2. Schematic demonstration of the Doppler-free absorption. The signal arises from the reduced absorption experienced for the v=0 velocity class as a result of saturation by the pump beam.

Ar-Ion Pump Laser

Beam chopper
Pump beam
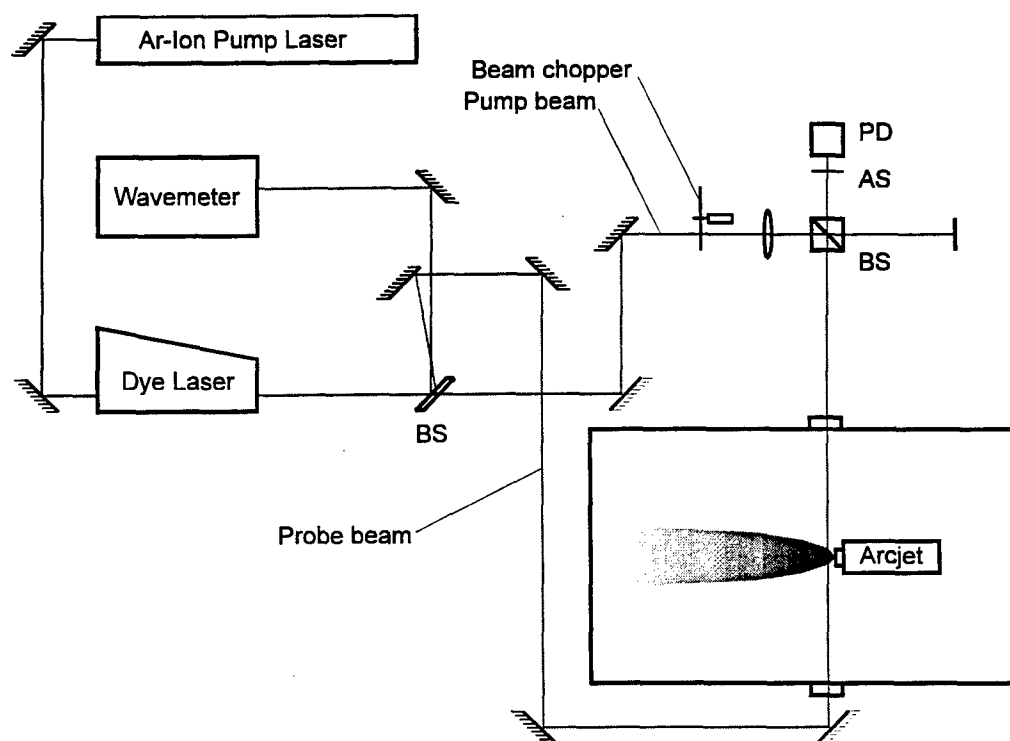
PD

AS

Wavemeter

BS

Dye Laser

BS

Probe beam

Arcjet

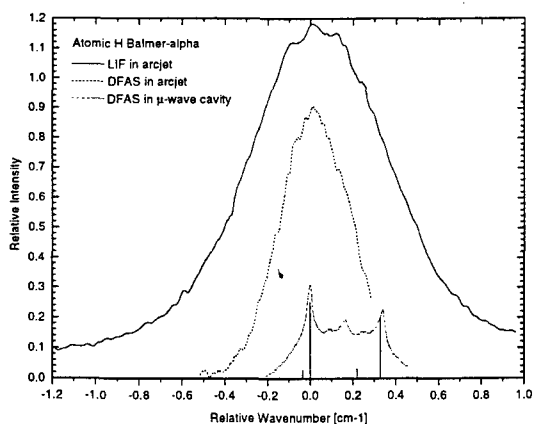Figure 3. Schematic diagram of the Doppler-free absorption experimental setup.

Figure 4. A comparison of measured H_α lineshapes, including Doppler-broadened LIF and Dopper-free absorption spectroscopy (DFAS).
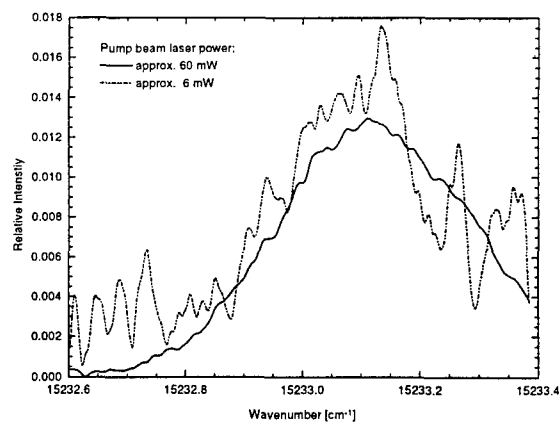

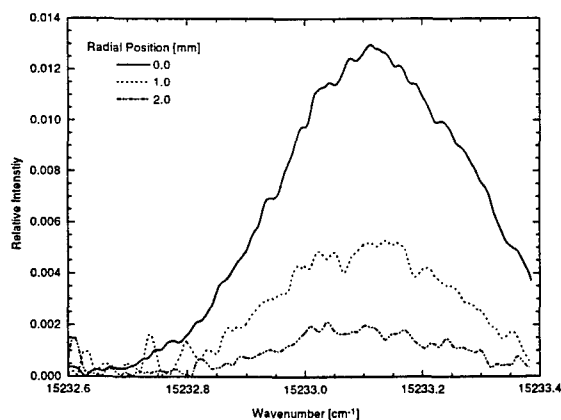Figure 5. A comparison of measured spectra at two different laser power levels.

Figure 6. Typical measured Doppler-free spectra as a function of radial position at the arcjet exit plane.
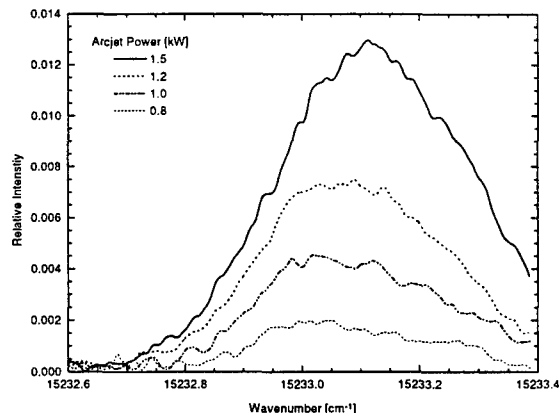

Figure 7. Typical measured Doppler-free spectra at the arcjet centerline for different arcjet power levels.
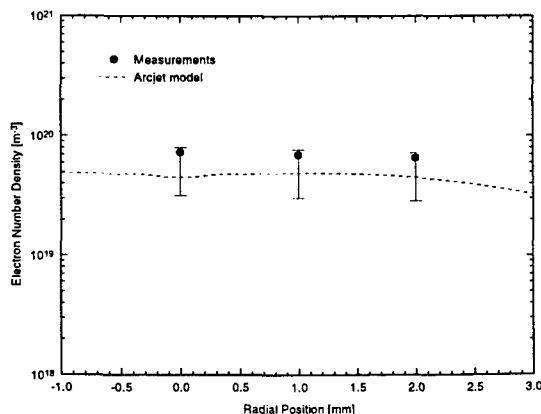

Figure 8. A comparison of the measured and modeled electron number density as a function of radial position at the arcjet exit plane.
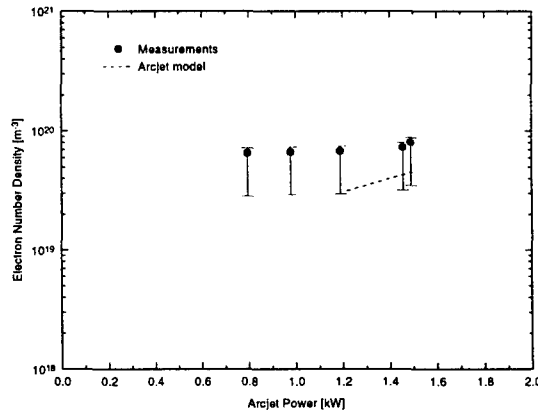

Figure 9. A comparison of the measured and modeled electron number density at the arcjet centerline as a function of arcjet power level.

Laser-induced fluorescence measurements of resonance broadening in xenon

R. J. Cedolin, R. K. Hanson, and M. A. Cappelli

High Temperature Gasdynamics Laboratory, Stanford University, Stanford, California 94305-3032

(Received 16 October 1995; revised manuscript received 15 December 1995)

Resonance broadening in atomic xenon has been studied by using laser-induced fluorescence of two excited-state electronic transitions. The impact theory result for resonance broadening is verified to be accurate and the onset of the breakdown of the theory is chronicled. The spectral broadening of the $6s[3/2]_1^o(^3P_1) \rightarrow 6p[1/2]_0$ (828-nm) transition by the resonant interaction of its lower level with ground-state xenon was investigated for densities of $4 \times 10^{21} - 2 \times 10^{24}$ atoms m^{-3}. The predominantly Doppler-broadened $6s[3/2]_2^o(^3P_2) \rightarrow 6p[3/2]_2$ (823-nm) transition was analyzed for similar conditions, primarily to establish the kinetic temperature of the neutral xenon. Tunable narrow-linewidth semiconductor diode lasers were used to probe the excited states, which were produced by a direct-current glow discharge. The intricate hyperfine structure of the measured profiles was taken into account by summing constituent Voigt profiles to construct model line shapes. The $6s[3/2]_1^o \rightarrow 6p[1/2]_0$ broadening constant at low densities and at 311 K was found to be $6.04(\pm 0.66) \times 10^{-21}$ MHz m^3 atom^{-1}. This result is in agreement with the value predicted by the impact theory for resonance broadening. The $6s[3/2]_1^o \rightarrow 6p[1/2]_0$ Lorentzian width extrapolated to zero density, 43 ± 15 MHz, is in accord with the natural linewidth. At densities above 6×10^{23} atoms m^{-3} the recorded line shapes of this transition exhibited an asymmetry, providing clear evidence of the breakdown of the impact approximation. The measured Lorentzian broadening for the $6s[3/2]_2^o \rightarrow 6p[3/2]_2$ transition was $8.3(\pm 1.8) \times 10^{-22}$ MHz m^3 atom^{-1} at 311 K. [S1050-2947(96)01807-0]

PACS number(s): 32.70.Jz, 32.10.Fn, 32.70.Cs

I. INTRODUCTION

The use of spectroscopic line-shape analysis for the determination of parameters of the environment of an atom or molecule is a common and valuable diagnostic technique. This technique is critically dependent on the accuracy and validity of the prevailing theoretical understanding of the physical processes involved in spectral line broadening. The strong resonant transitions of the noble gases allow for the study of pure resonance broadening, uncomplicated by nonresonant collisional interactions. As the resonant transitions are deep in the ultraviolet and are subject to considerable radiative trapping, experimental work has focused on spectral lines with the resonance level as the lower level [1–13]. These previous studies have concentrated on the lighter inert gases.

We present here an investigation into the resonance broadening of xenon using analyses of the spectral line shapes of two excited-state transitions. As shown in Fig. 1, xenon's $6s[3/2]_1^o(^3P_1)$ level is resonantly coupled to the ground state. The $^3P_1$ level appears as a second resonance level in the inert gases as Russell-Saunders coupling breaks down at the higher atomic numbers. For xenon, as opposed to the lighter inerts, the $^1S_0 \rightarrow {}^3P_1$ transition is slightly stronger than the $^1S_0 \rightarrow {}^1P_1(6s'[1/2]_1^o)$ line [14]. Thus resonance broadening is an important broadening mechanism for the $6s[3/2]_1^o \rightarrow 6p[1/2]_0$ transition. In contrast, the $6s[3/2]_2^o \rightarrow 6p[3/2]_2$ transition is broadened mainly by the Doppler effect as the $6s[3/2]_2^o(^3P_2)$ level is metastable. In a demonstration of the capabilities of diode lasers, Pine, Glassbrenner, and Kafalas [15] recorded absorption line shapes of these severely hyperfine-split transitions. A combination of isotopic and nuclear-spin splitting makes these line shapes a complex conglomeration of individual lines. Stacey and

Thompson [1] have shown with neon that the resonance broadening interaction between unlike isotopes is commensurate with that between identical ones. Also, the effect of the nuclear spin of the odd isotopes is predicted to not be significant if the collisions are diabatic with respect to the nuclear spin splitting (i.e., the inverse of the collision duration must be much larger than the hyperfine splitting) [16,17]. Calculations show that the diabatic assumption is reasonable for the transitions of interest. These considerations, combined with a complete understanding of the un-
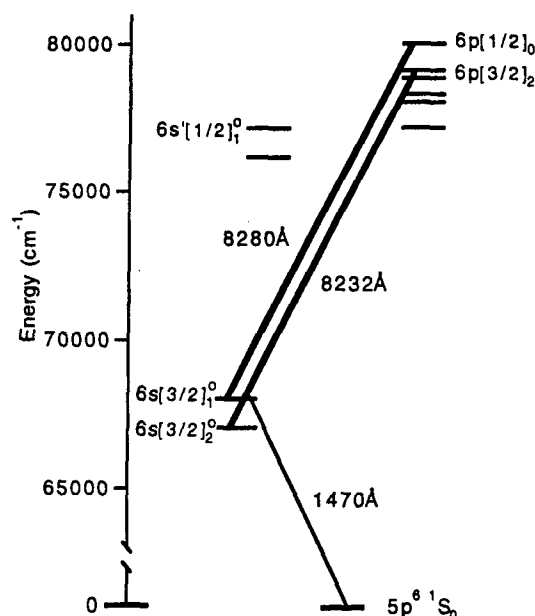

FIG. 1. Partial energy-level diagram of xenon. Energy-level values are from [47].

<u>54</u>   335

derlying hyperfine structure, have permitted our investigation into the line broadening.

Theoretical calculations for resonance broadening in the impact regime produce a simple result for the resonance full width at half maximum (FWHM) [18]:

$$\Delta \nu_{res} = \frac{c r_e}{8} k_{jj'} f_{res} \lambda_{res} N. \tag{1}$$

Here the classical electron radius is represented by r_e, c is the speed of light, λ_{res} is the wavelength of the resonant transition, and $k_{jj'}$ is a constant determined by the quantum numbers j and j' of the ground and resonance levels. For all noble gases, $j = 0$ and $j' = 1$. The theoretical value for this case is $k_{01} = 1.53$ [17,19]. The FWHM is predicted to be temperature independent and to have a linear dependence on the species number density N and on the resonant oscillator strength f_{res}.

Other Lorentzian broadening mechanisms of $6s[3/2]_1^o \rightarrow 6p[1/2]_0$ are not significant for the conditions of interest. The dispersion or van der Waals contribution to the broadening can be safely neglected for strong resonant transitions. Lewis [20] has shown that the dispersion contribution does not simply add to the resonance broadening. For a resonant component more than three times as great as what the dispersion component would be if acting alone, the dispersion contribution to the line shape is entirely negligible. The van der Waals interaction is of the same order across transitions between the same manifolds of fine-structure levels [21]. So the magnitude of the van der Waals broadening of the $6s[3/2]_2^o \rightarrow 6p[3/2]_2$ transition can serve as a check on the assumption to neglect the dispersion contribution to the $6s[3/2]_1^o \rightarrow 6p[1/2]_0$ line shape. Stark broadening data is unavailable for these transitions. It is estimated to be negligible from rough calculations [22] and from extrapolation of data from other noble-gas species [23].

Emission studies of resonance broadening have been complicated by non-Gaussian velocity distributions of highly excited states in the direct-current (dc) discharge plasmas employed [1–7]. One result of this difficulty was the disagreement of the Lorentzian width extrapolated to zero density with the natural linewidth. This "extrapolation anomaly" has recently been investigated in detail for neon [24].

Absorption studies of the resonance broadening have proven more reliable. First, they sidestep the problem of incomplete thermalization of the higher-lying levels. Emission line shapes are affected by the velocity distribution in the upper, emitting, state, whereas absorption probes the lower, resonance, level. Higher-lying states are more likely to be formed by dissociative recombination of molecular ions with electrons, which gives rise to neutral atoms with excess kinetic energy. As a result, these states are not thermalized at the gas kinetic temperature. Lower-lying states are predominantly populated by electron-impact excitation and radiative cascade [24]. These levels are then better thermalized into a velocity distribution closer to a Gaussian. The second advantage of absorption studies is that the use of a narrow-linewidth laser can reduce the complications of the instrumental contribution to the line shape. Using helium [8] and neon [9,10], laser absorption experiments have been used to

verify the resonance broadening theory [Eq. (1)]. However, little work has been done with the heavier inert gases.

The technique we use in this study, laser-induced fluorescence (LIF), effectively measures the absorption line shape by monitoring the fluorescence from a small region following absorption of the probe laser beam. To our knowledge, our measurements are the first test of the low-density resonance broadening theory for xenon and are the first to extend the measurements of absorption line shapes in helium and neon [8,9] to heavier inert gases. Furthermore, Lindsay, Nicol, and Stacey [9] detect a nonlinearity in the dependence of the FWHM on the number density at the high-number-density end of their data set. They suggest that it may be caused by the onset of the breakdown of the impact approximation. An earlier emission study of krypton showed a similar indication [2]. A nonlinearity in the FWHM versus number density for the resonance broadening of an excited level is predicted by Srivastava and Zaidi [25] in the transition from the impact to the static limit. Vaughan could not detect asymmetries at the high densities where a nonlinearity in krypton was observed [2]. In our investigation, measurements were extended to high enough densities to allow for the observation of statistical collision behavior in the form of asymmetric line shapes. As reviewed in Refs. [26] and [27], asymmetric line shapes signal a departure from the impact limit.

This study also demonstrates how knowledge of the underlying hyperfine structure and an understanding of the appropriate broadening mechanisms can enable the use of spectral-line shapes as a diagnostic tool in xenon plasmas. As a rare gas with low ionization potential and high molecular weight, xenon is being used extensively as a propellant in the study of ion thrusters [28] and Hall thrusters [29] for satellite propulsion. Single-point LIF has been shown in studies of electrothermal hydrogen arc-jet thrusters to be a valuable diagnostic tool by offering measurement capabilities of kinetic temperatures and atomic velocities for comparison to physical models [30]. LIF provides the high spatial resolution essential in probing the nonuniform plasma environments encountered in electric propulsion devices. An extension of the LIF line-shape analysis to xenon transitions should prove to be as valuable in the study of xenon plasma thrusters.

II. EXPERIMENT

The plasma source for excited xenon atoms was a room-temperature hollow-cathode dc discharge. The xenon (SpectraGases 99.999% pure) was metered at 0.5 to 1 SCCM, where SCCM denotes cubic centimeter per minute at STP, through the discharge tube, which had a 1-cm-square cross section. The pressure was measured just downstream of the discharge by capacitance manometers (MKS Baratron, 0–10 and 0–100 torr) of 0.5% accuracy. A mechanical pump reduced the system pressure to 10 mtorr and the system was flushed with xenon a few times before the experiment was performed. Line shapes were measured for pressures from 0.13 to 52 torr. For each line-shape measurement, the pressure was recorded and verified to have remained within ±1% of the nominal pressure throughout. A thermocouple bead of 0.6 mm diameter was positioned against the glass to monitor the temperature on the outer wall of the discharge. A nomi-
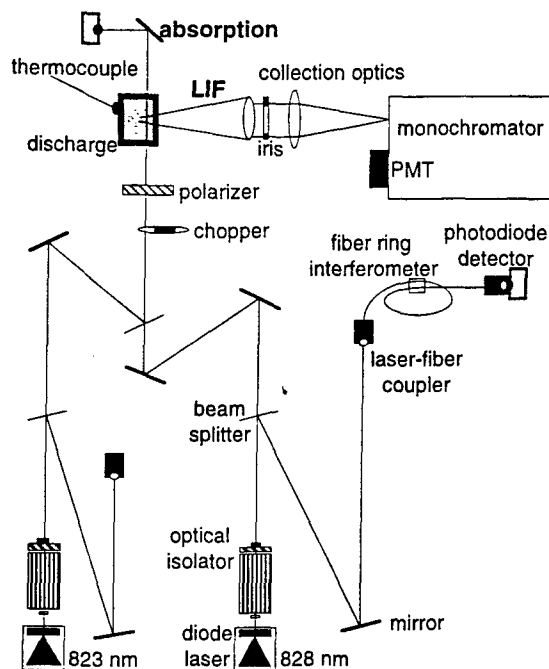
FIG. 2. Experimental setup.

nal discharge current of 0.36 mA was used at densities below 3×10^{23} atoms m^{-3}. The discharge could not be sustained with this current at higher densities so 1 mA was used for the remaining measurements. A sample measurement at 9×10^{22} atoms m^{-3} was taken with a discharge current of 1 mA and it was found to be consistent with the low-density 0.36-mA results. Other research has also demonstrated an insensitivity of the results to the discharge current [3,4,8]. This insensitivity lends credence to our assumption of the insignificance of Stark broadening.

A schematic of the experiment is shown in Fig. 2. The light sources were AlGaAs semiconductor diode lasers, which have Lorentzian emission profiles with a typical linewidth of 10 MHz [31]. The lasers were tuned by current modulation. Both beams first passed through optical isolators to prevent backreflections from affecting laser operation. A portion of each beam was then split off to enable the frequency to be monitored. The monitoring was performed by a fiber ring interferometer [32]. This interferometer was calibrated with a 2-GHz solid confocal étalon and found to have a free spectral range of 178.4±0.4 MHz. The remainder of each beam was joined onto a coincident path through the discharge.

The beam entering the discharge was mechanically chopped at 1 kHz to allow for phase-sensitive detection. A motorized rotating polarizer was used to keep the intensity far below the saturation intensity appropriate to the specific transition and discharge conditions. The saturation intensities were found experimentally to be about 0.2 mW mm^{-2} for the 823-nm transition and about 3 mW mm^{-2} for the 828-nm transition at 1 torr. To avoid complications from power broadening of the line shape, the laser intensity was kept at a level calculated to give only about a 1% reduction in the peak absorption from saturation.

The 5×2 mm^2 laser beam entered the discharge near the LIF collection side to minimize radiative trapping, with the 5-mm side parallel to the collection side of the discharge. A

silicon photodiode monitored the beam intensity that passed through the discharge, providing a measure of the absorption. The spectrally resolved fluorescence was collected at right angles to the incident beam. A half-meter monochromator was used as a spectral filter, passing light over the entire transition while the laser frequency was varied. The LIF was detected by a photomultiplier tube. Lock-in amplifiers were used for both the LIF and absorption signals. LIF excitation scans using the 823- and 828-nm lasers were taken consecutively with the discharge continually operating at the same conditions. Each single trace recorded took from 10 to 240 s depending on the LIF signal strength at the given conditions. Multiple traces were recorded and separately analyzed at each pressure.

III. ANALYSIS

The line shapes for each of the two transitions investigated are composed of a number of hyperfine lines. Xenon has nine stable isotopes, three with natural abundances greater than 20% (^{132}Xe,^{131}Xe,^{129}Xe) [33]. The isotopic shifts required to construct model line shapes were taken from measurements in Refs. [34] and [35]. The isotopes ^{131}Xe and ^{129}Xe with odd atomic mass number have nonzero nuclear-spin angular momenta, which give rise to further hyperfine splitting. The nuclear-spin shifts from the origins of the hyperfine multiplets (given by the isotopic shift) were calculated using parameters that have been measured for each of the levels involved in the relevant transitions [36,37]. The isotopic abundance ratios were used for the relative intensities of the separate isotopic lines (summed over hyperfine components). Any effect discharge mechanisms could have on the relative density distributions of the isotopes was assumed to be small because of the small mass differences between the predominant isotopes. For the isotopes possessing a nuclear magnetic moment, the intensity was distributed between the hyperfine components according to quantum-mechanical sum rules [38]. The positions and relative intensities of the 21 hyperfine components contributing to the $6s[3/2]^o_2 \rightarrow 6p[3/2]_2$ line shape are shown within a sample LIF trace in Fig. 3. The $6s[3/2]^o_1 \rightarrow 6p[1/2]_0$ transition is composed of 12 hyperfine components. Each hyperfine component was individually broadened into a Voigt profile. Atomic velocity correlation effects were estimated to be negligible [39] so the contributing hyperfine line shapes could be accurately represented by Voigt profiles, which convolve Gaussian (Doppler) and Lorentzian contributions. The relative broadening of the hyperfine-split lines was fixed according to the relative masses of the isotopes. The resulting intensities were added to construct an excitation spectrum to model the reduced recorded line shapes.

The recorded absorption trace was used to calculate the intensity incident on the LIF collection volume to normalize the LIF data. The absorption never exceeded 1% for the $6s[3/2]^o_1 \rightarrow 6p[1/2]_0$ transition and was less than 8% for $6s[3/2]^o_2 \rightarrow 6p[3/2]_2$. The recorded interferometer data were then used to transform the LIF data into frequency space to give the reduced line shape.

No correction was made to the LIF spectra to account for the approximately 10-MHz Lorentzian linewidth of the diode lasers. As it contributed an equal amount to each detected
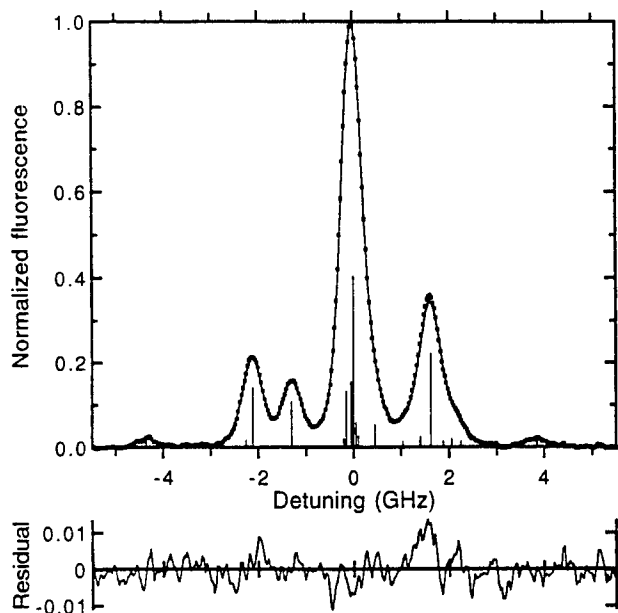
FIG. 3. $6s[3/2]_2^o \rightarrow 6p[3/2]_2$ line shape: •, reduced LIF excitation data with only every fifth point plotted for clarity and Voigt $a = 0.33$; |, hyperfine lines contributing to the line shape; —, curve fit result from sum of Voigt broadened hyperfine lines with residual.

LIF line shape, the slope of a plot of the Lorentzian broadening versus number density would not be affected by it. The laser linewidth would influence only the intercept of the data. Furthermore, if the laser emission profile had any Gaussian component it would have had a negligible affect on the Doppler FWHM of the recorded LIF line shape. As Gaussian components add according to their squares, even a fully Gaussian laser linewidth of 10 MHz would have had a small effect when convolved with the 400-MHz Doppler broadening of the xenon transitions at room temperature.

The reduced LIF line shape was introduced to a χ^2-minimization curve-fitting procedure that optimized the kinetic temperature T_{kin} (which determined the Doppler FWHM) and the Lorentzian FWHM $\Delta \nu_L$ to most closely match the data. This Lorentzian FWHM should be almost entirely composed of the $\Delta \nu_{res}$ of Eq. (1) for the $6s[3/2]_1^o \rightarrow 6p[1/2]_0$ transition. The line positions and relative intensities were fixed in the fitting procedure. The overall amplitude, a linear base line, T_{kin}, and $\Delta \nu_L$ were the parameters to the fit. Figure 3 shows a reduced $6s[3/2]_2^o \rightarrow 6p[3/2]_2$ line shape with the corresponding curve-fit result overlaid onto the data and the fit residual displayed below it. This line shape was mainly Doppler broadened as indicated by the Voigt a parameter value of 0.33. The ability to accurately fit the reduced line shape demonstrates that the hyperfine-splitting data from the literature has proven to be of adequate accuracy for this study. A fit residual within 1–2 % of the peak height was representative of all analyzed line shapes. For the $6s[3/2]_1^o \rightarrow 6p[1/2]_0$ transition, T_{kin} was fixed to the value measured from the $6s[3/2]_2^o \rightarrow 6p[3/2]_2$ line shapes to allow the fit to more accurately find $\Delta \nu_L$.

An alternate analysis procedure involved removal of the background from the data before the curve-fitting procedure. The background was then no longer a parameter to the fit. The signal background was composed of laser reflections from the discharge glass and discharge emission that corresponded in frequency to the lock-in amplifier detection bandwidth. The background signal was recorded before and after each LIF measurement. Thirteen representative line shapes for each transition underwent both analysis methods. There were no significant differences in the results.

IV. RESULTS

The kinetic temperature measured from the Doppler widths of the $6s[3/2]_2^o \rightarrow 6p[3/2]_2$ transition was used to convert the measured discharge pressures to number densities. Thirteen $6s[3/2]_2^o \rightarrow 6p[3/2]_2$ line shapes were recorded and analyzed at six different discharge conditions. The Voigt a parameters of these line shapes varied from 0.02 to 0.36. The kinetic temperatures measured in this way showed no systematic dependence on the discharge operating conditions. Once the lack of pressure dependence was established, $6s[3/2]_2^o \rightarrow 6p[3/2]_2$ line shapes were no longer recorded and the average of T_{kin} over all measurements was used. The 311 ± 33 K average was slightly higher than the discharge wall temperature of around 300 K. Because of the low discharge current used, the thermocouple measurement of the outer discharge wall was unchanged from the ambient room temperature by discharge operation.

Kinetic temperatures were also derived from the Doppler width of the $6s[3/2]_1^o \rightarrow 6p[1/2]_0$ line shapes. At densities below 10^{23} atoms m^{-3} (Voigt $a < 1.4$), these measurements were consistent with the 311 K average of the $6s[3/2]_2^o \rightarrow 6p[3/2]_2$ measurements. Above this density though, the increased Lorentzian component made the $6s[3/2]_1^o \rightarrow 6p[1/2]_0$ line shape less sensitive to the Doppler width and the derived temperatures became more erratic.

Figure 4 displays reduced $6s[3/2]_1^o \rightarrow 6p[1/2]_0$ LIF spectra demonstrating the evolution of the resonance-broadened line shape with increasing pressure. The corresponding curve-fit results are included. The lowest-density measurement is shown in Fig. 4(a). The discharge could not be sustained at substantially lower densities and the Doppler broadening, which was constant over all densities, was becoming predominant. The 12 hyperfine components are shown within the line shape in Fig. 4(a). This transition's hyperfine splitting was only beginning to be resolved at this density. Thirty-five of these line shapes were recorded at seventeen operating conditions.

The resulting Lorentzian FWHM's are plotted against number density in Fig. 5. The theoretical predictions of the resonance broadening from Eq. (1) using previous measurements of f_{res} are displayed with the data over a reduced density range. The full density range is shown in the inset. The error bars on the data display the uncertainty in the number density arising from the uncertainty in the measured neutral kinetic temperature. The low-density end of the error bars were derived from the full +33 K uncertainty found above. The high-density side was cut off at the measured wall temperature for the specific discharge operating condition: The kinetic temperature of the neutral xenon could not be less than the ambient room temperature. The vertical error bars are less than the size of the markers as the statistical uncertainties from the curve fits were not significant.

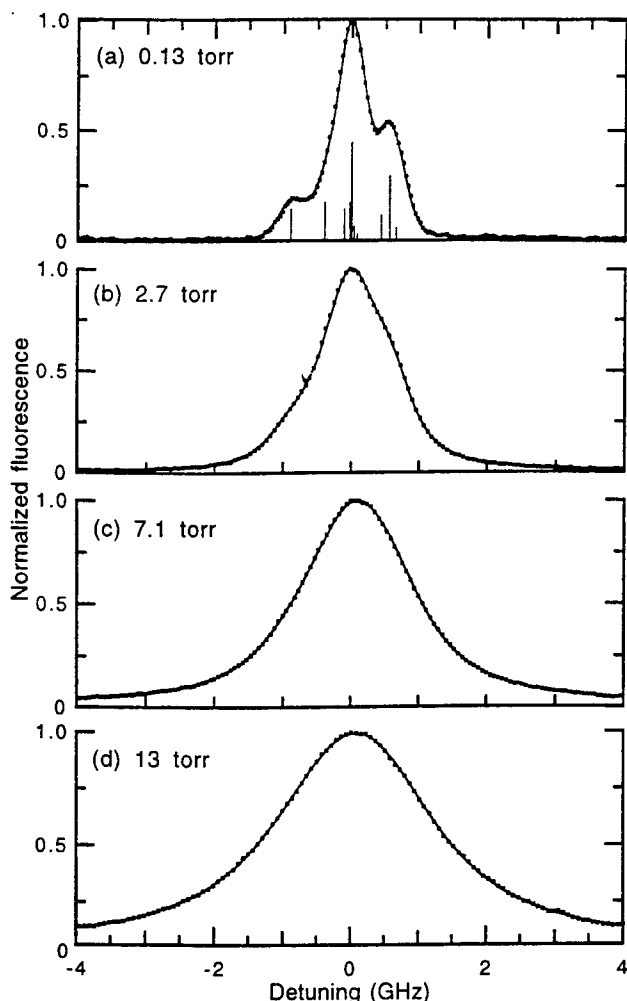As predicted by Eq. (1), the $\Delta \nu_L$ results were linear with

uncertainty in the kinetic temperature. This intercept should be composed of the natural linewidth plus the Lorentzian contribution of the laser linewidth. The laser linewidth has not been measured. To be conservative, we allow for a range of ± 5 MHz around a nominal laser linewidth of 10 MHz. The result is then 43 ± 15 MHz for the natural linewidth.

The recorded $6s[3/2]_1^o \rightarrow 6p[1/2]_0$ line shapes for densities above 6×10^{23} atoms m^{-3} were not symmetrical. Two such line shapes are presented in Fig. 6. Also displayed on Fig. 6(b) is a line shape constructed of summed Voigt profiles, with their broadening determined by the measured low-density broadening constant for the 2×10^{24} atoms m^{-3} density of the measured spectrum. It is readily apparent that, as well as having a broadening reduced from that of the theory, the profile was no longer of the Voigt shape.

The predominance of Doppler broadening for the $6s[3/2]_2^o \rightarrow 6p[3/2]_2$ transition made the line shape less sensitive to the Lorentzian component. However, sufficient line shapes were recorded to allow for a measure of the broadening constant. Figure 7 shows $\Delta \nu_L$ plotted against N for this transition. The horizontal error bars again reflect the uncertainty in the temperature. The vertical error bars are the statistical uncertainties from the line shape curve fits. The linear fit of the $\Delta \nu_L$ measurements is also displayed. It gave $2\gamma/N = 8.3(\pm 1.8) \times 10^{-22}$ MHz m^3 atom^{-1} with the total uncertainty being evenly split between the statistical uncertainty of the fit and the experimental contribution from the uncertainty of T_{kin}. Extrapolation to zero density gave 2.4 ± 11 MHz with the uncertainty being almost entirely statistical.

V. DISCUSSION

The measured broadening constant for $6s[3/2]_1^o \rightarrow 6p[1/2]_0$ can be used to calculate a value for the oscillator strength f_{res} of the resonant transition $5p^6\,^1S_0 \rightarrow 6s[3/2]_1^o$. This calculation facilitates a comparison to the theory embodied in Eq. (1). The value $2\gamma/N = 6.04(\pm 0.66) \times 10^{-21}$ MHz m^3 atom^{-1} yields $f_{res} = 0.255 \pm 0.028$. The most recent measurements of this oscillator strength are 0.264 ± 0.016 [40], 0.273 ± 0.014 [14], 0.222 ± 0.027 [41], and 0.260 ± 0.05 [42]. The direct total absorption measurement described in Ref. [40] assumes that Eq. (1) is valid. Recent semiempirical calculations gave 0.223 and 0.208 ± 0.027 with the difference in the results arising from the approximations employed [43]. Calculations of the $6s[3/2]_1^o \rightarrow 6p[1/2]_0$ resonance broadening from Eq. (1) using each of the above previous f_{res} measurements are displayed in Fig. 5 along with the measured Lorentzian FWHM's. The density range is reduced to the linear region with the full density range shown in the inset. Our data lie most closely to the theoretical broadening based on Ferrell, Payne, and Garrett's 0.260 measurement of f_{res} [42]. Although the uncertainty range of the present measurement overlaps that of Suzuki *et al.* [41], the value 0.222 of Suzuki *et al.* is notably lower than the other measurements. It is also lower than most of the other experimental values compiled in [14]. Suzuki *et al.* point out that a similar situation occurred for their measurements of the corresponding oscillator strength in krypton. Although the most recent f_{res} measurements span a wide range, the compiled values indicate a

FIG. 4. Evolution of reduced $6s[3/2]_1^o \rightarrow 6p[1/2]_0$ LIF excitation line shapes (•) and curve-fit results (—) with density: (a) 3.9×10^{21} atoms m^{-3} with contributing hyperfine lines ($|$) with only every sixth point plotted for clarity and Voigt $a = 0.16$; (b) 8.4×10^{22} atoms m^{-3} with every tenth point plotted and $a = 1.2$; (c) 2.2×10^{23} atoms m^{-3} with every tenth point plotted and $a = 2.8$; (d) 4.0×10^{23} atoms m^{-3} with every twenty-fifth point plotted and $a = 4.9$.

number density N for low N, as seen in Fig. 5. However, a nonlinearity at higher N is clearly evident in the Fig. 5 inset. To obtain the broadening constant $2\gamma/N$, where γ is the half collision width at half maximum, a line was fit to the linear range of data. Consecutive high-density points were excluded from the fit until an exclusion resulted in less than a 1% change in the slope of the fit. The final result, shown in the Fig. 5 inset, was then based on the 19 measurements below densities of 1.5×10^{23} atoms m^{-3} for which the Voigt a ranged from 0.16 to 2.0. The linear fit result was 6.04×10^{-21} MHz m^3 atom^{-1}. The scatter of the data gave a statistical uncertainty (two standard deviations) of 0.01×10^{-21}. Using $T_{kin} = 344$ K as the temperature uncertainty limit gave a value 0.65×10^{-21} higher than that using $T_{kin} = 311$ K. The total statistical plus experimental uncertainty on $2\gamma/N$ was then 0.66×10^{-21} MHz m^3 atom^{-1}. Extrapolating the linear fit to zero density gave 53 MHz with a total uncertainty of 10 MHz arising almost entirely from the
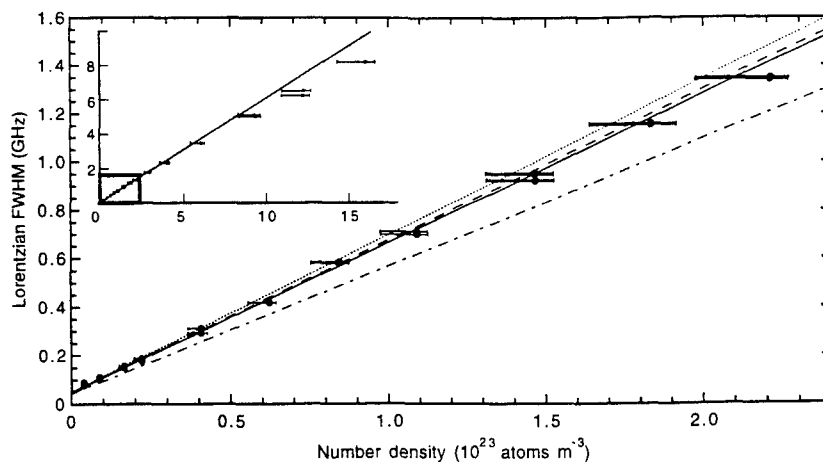
FIG. 5. Plot of $6s[3/2]_1^o \rightarrow 6p[1/2]_0$ $\Delta\nu_L$ versus number density and comparison of measured $\Delta\nu_L$ (•) in the low-density range to impact theory [Eq. (1)] using $\cdots$, $f=0.273$ [14]; $---$, $f=0.264$ [40]; $---$, $f=0.222$ [41]; and $—$, $f=0.260$ [42]. The inset shows the full density range with the expanded region indicated; $—$, linear fit to low-density points.

consensus around 0.260 [14]. Our data are in remarkable agreement with this value. The agreement of the calculated f_{res} with other measurements demonstrates that the impact approximation resonance broadening theory [Eq. (1)] is equally applicable to heavy inert gases. It also shows that any complications introduced by collisional interactions between different isotopes or with atoms in different hyperfine levels is not substantial.

From Fig. 6(b) it is clear that the Voigt model does not adequately represent the recorded line shapes at the higher densities. These asymmetric profiles make it definite that the nonlinearity of $\Delta\nu_L$ with N of resonance broadened transitions is from the breakdown of the impact approximation. The forced fitting of the Voigt model to the asymmetric

high-density line shapes gives an unreliable measure of the FWHM. Thus the nonlinearity of the FWHM with number density in Fig. 5 may be from a combination of a reduction in resonance broadening, as calculated by Srivastava and Zaidi [25] and from the inadequacy of fitting the Voigt model to the asymmetric profile. In any case, the range of validity of Eq. (1) is evident from Fig. 5. The beginning of the nonlinearity defines the breakdown of the impact limit. At the low-density end, measurements become difficult for conditions where the Doppler FWHM becomes much greater than the resonance broadening FWHM. For the conditions of a room-temperature dc discharge, the resonance broadening can be accurately measured roughly from 0.1 to 6 torr.

The impact approximation is often used at significantly higher pressures than encountered in this study for broadening from van der Waals forces. However, the resonance interaction is a longer-range interaction. The validity criterion for the impact approximation $\Delta\nu_L \ll N^{1/3}\bar{v}$ can be used to roughly calculate where the approximation should break down [18]: where $\Delta\nu_L = (2\gamma/N)N \approx (N^{1/3}\bar{v})/10$. Here $\bar{v}$ is
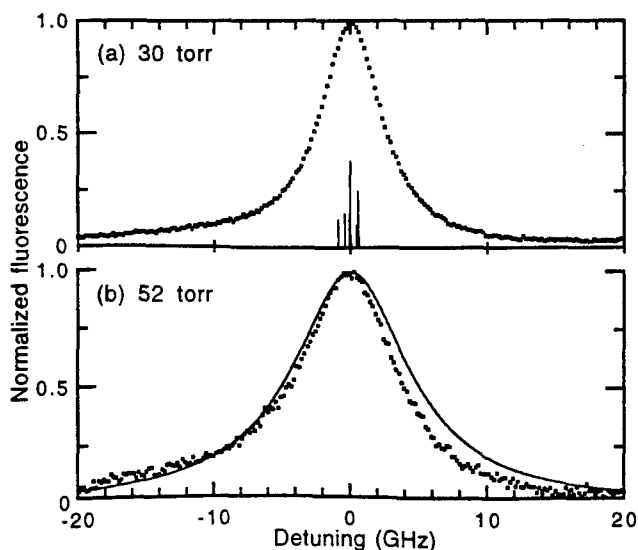

FIG. 6. Asymmetric reduced $6s[3/2]_1^o \rightarrow 6p[1/2]_0$ LIF excitation line shapes (•) at high densities with only every second point plotted for clarity: (a) 9.3×10^{23} atoms m^{-3} with contributing hyperfine lines (|); (b) 1.6×10^{24} atoms m^{-3} with the calculated line shape ($—$) from the sum of Voigt broadened hyperfine lines using the measured 6.04×10^{-21} MHz m^3 atom^{-1} broadening constant to show the departure from low-density theory; Voigt $a=21$.
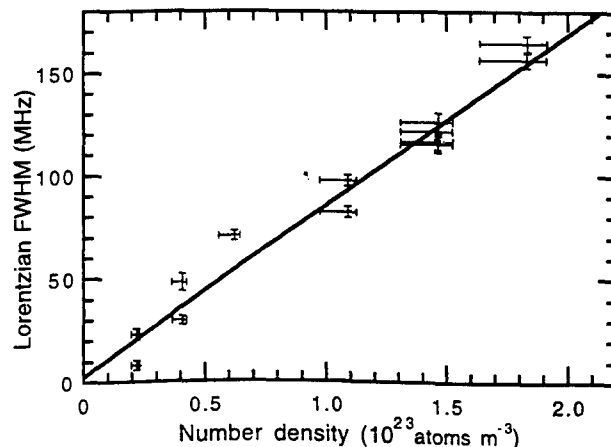

FIG. 7. Plot of $6s[3/2]_2^o \rightarrow 6p[3/2]_2$ $\Delta\nu_L$ versus number density; +, from an analysis of measured line shapes; $—$, linear fit.

the average relative speed. Using $f_{res}=0.260$ to calculate $2\gamma/N$ from Eq. (1) leads to $N\approx2\times10^{23}$ atoms m^{-3} as the estimate for the density at which the impact approximation should begin to break down for the situation considered. This estimate coincides with the beginning of the nonlinearity in our experimental results. The impact approximation also does not apply at frequencies far from line center, even at low densities. However, the portions of the line shapes important to the curve fits do not extend further than a few FWHM's from line center, well within the frequency range of validity except at the highest densities investigated.

As with the previous absorption line-shape measurements [8–10], our data do not show an extrapolation anomaly. The extrapolation of the $6s[3/2]_1^o\rightarrow6p[1/2]_0$ Lorentzian broadening to zero density should give the natural linewidth plus the laser linewidth. This provides a check of the self-consistency of the measurement of f_{res}. Using our measured $f_{res}=0.255$ value along with a radiative lifetime of the $6p[1/2]_0$ level of 26.8 ns [44] gives 48 MHz for the natural linewidth. This value lies well within the range of uncertainty of our measured 43 ± 15 MHz result.

The average T_{kin} derived from the measured $6s[3/2]_2^o\rightarrow6p[3/2]_2$ line shapes was a few percent higher than the ambient room temperature. The small amount of discharge heating measured over all discharge conditions is consistent with calculations based on the work of Grimblatov, Mikhailovskaya, and Suniga [45] and with the findings of others [4,9,10]. The T_{kin} extracted from the curve fit was very sensitive to small disagreements in the positions and relative heights of the secondary peaks in the $6s[3/2]_2^o\rightarrow6p[3/2]_2$ line shape. So, deriving a temperature with an 11% uncertainty is satisfactory considering the complexity of the line shapes. Establishing T_{kin} for the neutral atoms, however, is the main source of uncertainty in our measurements of the resonance broadening.

The Lorentzian component extracted from the $6s[3/2]_2^o\rightarrow6p[3/2]_2$ curve fit was even more sensitive to slight anomalies in the measured line shapes leading to the large uncertainty in the measurement of the broadening constant. Our $8.3(\pm1.8)\times10^{-22}$ MHz m^3 atom^{-1} measurement, though, is in agreement with a previous report of 8.2×10^{-22} MHz m^3 atom^{-1} [46]. As expected, the $6s[3/2]_2^o\rightarrow6p[3/2]_2$ van der Waals broadening is considerably smaller than the Lorentzian broadening of the $6s[3/2]_1^o\rightarrow6p[1/2]_0$ transition. This justifies the entire neglect of the dispersion contribution to the $6s[3/2]_1^o\rightarrow6p[1/2]_0$ line shape. The natural width for the $6s[3/2]_2^o\rightarrow6p[3/2]_2$ transition is 5 MHz [44]. This value again falls within the uncertainty range of the measured Lorentzian width extrapolated to zero density.

ACKNOWLEDGMENTS

[1] D. N. Stacey and R. C. Thompson, J. Phys. B **16**, 537 (1983).

[2] J. M. Vaughan, Phys. Rev. **166**, 13 (1968).

[3] J. M. Vaughan, Proc. R. Soc. London Ser. A **295**, 164 (1966).

[4] A. R. Malvern, A. C. Pinder, D. N. Stacey, and R. C. Thompson, Proc. R. Soc. London Ser. A **371**, 259 (1980).

[5] A. R. Malvern, J. L. Nicol, and D. N. Stacey, J. Phys. B **7**, L518 (1974).

[6] A. Atiola, B. C. Gibson-Wilde, A. C. Lindsay, J. L. Nicol, and I. B. Whittingham, J. Phys. B **21**, 249 (1988).

[7] R. Damaschini, A. Malvern, and J. Verges, Phys. Lett. **69A**, 4 (1978).

[8] A. C. Lindsay, J. L. Nicol, D. N. Stacey, and P. E. G. Baird, J. Phys. B **22**, L303 (1989).

[9] A. C. Lindsay, J. L. Nicol, and D. N. Stacey, J. Phys. B **24**, 4901 (1991).

[10] P. E. G. Baird, K. Burnett, R. Damaschini, D. N. Stacey, and R. C. Thompson, J. Phys. B **12**, L143 (1979).

[11] D. N. Stacey and J. M. Vaughan, Phys. Lett. **11**, 105 (1964).

[12] H. G. Kuhn and J. M. Vaughan, Proc. R. Soc. London Ser. A **277**, 297 (1964).

[13] W. R. Hindmarsh and K. A. Thomas, Proc. Phys. Soc. London **77**, 1193 (1961).

[14] W. F. Chan, G. Cooper, X. Guo, G. R. Burton, and C. E. Brion, Phys. Rev. A **46**, 149 (1992).

[15] A. S. Pine, C. J. Glassbrenner, and J. A. Kafalas, IEEE J. Quantum Electron. **9**, 800 (1973).

[16] A. Omont, J. Phys. (Paris) **26**, 26 (1965).

[17] P. R. Berman and W. E. Lamb, Jr., Phys. Rev. **187**, 221 (1969).

[18] H. G. Kuhn and E. L. Lewis, in *Polarisation, Matière et Rayonnement*, edited by La Societé Francaise de Physique (Presses Universitaires de France, Paris, 1969), p. 341.

[19] C. G. Carrington, D. N. Stacey, and J. Cooper, J. Phys. B **6**, 417 (1973).

[20] E. L. Lewis, Proc. Phys. Soc. London **92**, 817 (1967).

[21] D. F. T. Mullamphy, G. Peach, and I. B. Whittingham, J. Phys. B **24**, 3709 (1991).

[22] A. Schwabedissen and W. Bötticher, J. Phys. B **26**, 3467 (1993).

[23] J. Purić, S. Djeniže, J. Labat, A. Srećković, and M. Platiša, Contrib. Plasma Phys. **31**, 63 (1991).

[24] R. Ciurylo, A. Bielski, J. Domyslawska, J. Szudy, and R. S. Trawiński, J. Phys. B **27**, 4181 (1994).

[25] R. P. Srivastava and H. R. Zaidi, Can. J. Phys. **53**, 84 (1975).

[26] S.-Y. Ch'en and M. Takeo, Rev. Mod. Phys. **29**, 20 (1959).

[27] A. O. Vyrodov, J. Heinze, and U. E. Meier, J. Quant. Spectrosc. Radiat. Transfer **53**, 277 (1995).

[28] F. M. Curran, J. S. Sovey, and R. M. Myers, Acta Astron. **29**, 651 (1993).

[29] L. H. Caveny, F. M. Curran, and J. R. Brophy, in *Proceedings of the 23rd International Electric Propulsion Conference, Seattle, 1993* (Ohio State University, Columbus, 1993), Vol. 1, p. 12.

[30] J. G. Liebeskind, R. K. Hanson, and M. A. Cappelli, Appl. Opt. **32**, 6117 (1993).

[31] J. C. Camparo, Contemp. Phys. **26**, 443 (1985).

[32] L. F. Stokes, M. Chodorow, and H. J. Shaw, Opt. Lett. **7**, 288 (1982).

[33] E. Browne et al., in Table of Isotopes, 7th ed., edited by C. M. Lederer and V. S. Shirley (Wiley, New York, 1978).

[34] D. A. Jackson and M.-C. Coulombe, Proc. R. Soc. London Ser. A 338, 277 (1974).

[35] W. Fischer, H. Hühnermann, G. Krömer, and H. J. Schäfer, Z. Phys. 270, 113 (1974).

[36] D. A. Jackson, F. R. S., and M.-C. Coulombe, Proc. R. Soc. London Ser. A 327, 137 (1972).

[37] H. Geisen, T. Krümpelmann, D. Neuschäfer, and Ch. Ottinger, Phys. Lett. A 130, 299 (1988).

[38] H. E. White, Introduction to Atomic Spectra (McGraw-Hill, New York, 1934), p. 439.

[39] P. L. Varghese and R. K. Hanson, Appl. Opt. 23, 2376 (1984).

[40] H. M. Anderson, S. D. Bergeson, D. A. Doughty, and J. E. Lawler, Phys. Rev. A 51, 211 (1995).

[41] T. Y. Suzuki et al., Phys. Rev. A 43, 5867 (1991).

[42] W. R. Ferrell, M. G. Payne, and W. R. Garrett, Phys. Rev. A 35, 5020 (1987).

[43] D. Bessis, A. Haffad, and A. Z. Msezane, Phys. Rev. A 49, 3366 (1994).

[44] M. R. Bruce, W. B. Layne, C. A. Whitehead, and J. W. Keto, J. Chem. Phys. 92, 2917 (1990).

[45] V. M. Grimblatov, L. V. Mikhailovskaya, and L. Suniga, Opt. Spektrosk. 77, 887 (1994) [Opt. Spectrosc. 77, 797 (1994)].

[46] K. Tachibana, N. Kitagawa, and H. Harima, in Proceedings of the Third Workshop on Radiation Detectors and Their Uses, Ibaraki, Japan, 1988, edited by M. Miyajima, S. Sasaki, and T. Doke (National Laboratory for High Energy Physics, Tsukuba, 1988), p. 45.

[47] C. E. Moore, Atomic Energy Levels, Natl. Bur. Stand. (U.S.) Circ. No. 467 (U.S. GPO, Washington, DC, 1958), Vol. III, p. 113.

Laser-induced fluorescence study of a xenon Hall thruster

R.J. Cedolin, W.A. Hargus, Jr., P.V. Storm, R.K. Hanson, M.A. Cappelli

Thermosciences Division, Department of Mechanical Engineering, Stanford University, Stanford, CA 94305-3032, USA
(rcedolin@navier.stanford.edu; cap@leland.stanford.edu)

Abstract. Laser-induced fluorescence of the neutral-xenon $6s[3/2]_2^0 \rightarrow 6p[3/2]_2(^3P_2 - {}^1D_2)$ transition at 823.2 nm and the xenon-ion $5d[3]_{7/2} \rightarrow 6p[2]_{5/2}^0(^4D_{7/2} - {}^4P_{5/2})$ transition is used to measure plasma parameters in the plume of a laboratory-model xenon Hall thruster. The Hall discharge operates nominally at 62 V, 4.2 A, and 3.2 mg s^{-1} xenon flow, with an overall thruster power of 320 W. A tunable semiconductor diode laser and an Ar$^+$-pumped dye laser are used to probe the respective excited-state transitions. Axial velocity measurements are made at a number of axial and radial locations up to 4.5 cm downstream of the thruster-exit plane and under a variety of thruster operating conditions. Neutral velocities from 100 m s^{-1} to 400 m s^{-1} and ion velocities as high as 12 km s^{-1} are calculated from measured Doppler shifts. The charge-exchange phenomenon evidently does not significantly affect the xenon neutrals. The spectral-line shapes of the ion indicate a spread in ion energies through a non-Maxwellian distribution of axial velocities. Neutral kinetic temperatures of 500 ($\pm$200) K are observed under standard operating conditions. Zeeman and Stark effects on the spectral-line shapes, from the thruster's magnetic and electric fields, are not substantial. The measured line center of the ion transition is 16521.23 ($\pm$0.02) cm^{-1}.

PACS: 52.70.Kz; 32.70.Jz; 52.75.-d

The use of xenon as a propellant for satellite electric propulsion has stimulated a growing interest in the use of laser diagnostic techniques for xenon plasmas. These techniques are being developed for application to both Kaufman-type ion thrusters and Hall accelerators such as the stationary plasma thruster and the anode layer thruster. Nonintrusive measurements of parameters in the plumes and within the discharge channels of these satellite thrusters are needed to give an insight into the physical processes controlling their operation. Optical diagnostic measurements have been employed successfully in the past to study various plasma properties in electric propulsion devices. The hydrogen arcjet, for example, has been extensively studied using lasers as probes to measure velocity, temperature, and electron number density [1].

Laser-induced fluorescence (LIF) has proven to be a particularly valuable tool in these studies. The high spatial resolution of single-point laser-induced fluorescence is essential in probing nonuniform plasma environments, such as those encountered in electric propulsion devices. Extensive studies of Hall thrusters using this nonintrusive technique should be equally valuable.

We report LIF velocity measurements of singly-ionized and neutral xenon in the plume of a laboratory-model Hall thruster. Spectroscopic diagnostic techniques for xenon are complicated, in general, by the intricate hyperfine structure of xenon spectral transitions. The complicated spectroscopy of xenon does not, however, prevent the use of LIF as a velocity diagnostic. Measurements of xenon-ion velocities from Doppler-shifted LIF spectra have been made previously in a stationary plasma thruster [2]. A tunable AlGaAs semiconductor diode laser and a tunable dye laser are used here to interrogate the plasma downstream of the annulus exit of the Hall thruster operating at 320 to 680 W. Measurements of neutral velocities, ion velocities, as well as other neutral and ion parameters, are important to the validation of physical models [3]. In addition, these measurements are helpful in gaining qualitative information on the performance of the specific thruster being investigated.

We discuss also the effects of plasma properties on the xenon spectral-line shapes, namely the velocity distribution and kinetic temperature, and the magnetic field. Knowledge of the constituent transitions contributing to a spectral-line shape is required to gain insight into the plasma environment through its effect on the spectral distribution of the collected fluorescence. The spectroscopy of two transitions of neutral xenon are well understood. The spectral broadening of the $6s[3/2]_1^0 \rightarrow 6p[1/2]_0(^3P_1 - {}^3P_0)$ transition at 828.0 nm has been developed into a number density diagnostic, and the Doppler broadening of the $6s[3/2]_2^0 \rightarrow 6p[3/2]_2(^3P_2 - {}^1D_2)$ transition at 823.2 nm has been employed successfully as a kinetic temperature diagnostic in a room-temperature direct-current (dc) glow discharge [4]. Knowledge of the isotopic and nuclear-spin splitting of xenon-ion transitions is more limited. The xenon-ion

$5d[3]_{7/2} \rightarrow 6p[2]^0_{5/2}(^4D_{7/2} - ^4P_{5/2})$ transition at 605.1 nm is the only transition of the xenon ion for which isotopic and hyperfine structure measurements have been reported [5–7].

1 Theory

The interaction of a laser beam with a plasma may involve the excitation of some atoms to a higher quantum state. Monitoring the fluorescence from these higher states as the laser is tuned over the transition provides a measure of the fluorescence-excitation-line shape, allowing for a nonintrusive reconstruction of a spectral-line shape representative of the plasma conditions. If the species absorbing the laser light has a velocity component along the axis of the laser beam, it absorbs the light at a frequency different from that of stationary absorbers because of the Doppler effect. The magnitude of this frequency shift $\delta\nu_{12}$ depends on the velocity v along the laser beam axis as follows:

$$\delta\nu_{12} = \nu_{12}\frac{v}{c}. \tag{1}$$

The Doppler shift of a species' fluorescence profile away from the line center ν_{12} of stationary absorbers is thus a direct measure of the species velocity.

A partial energy level diagram for neutral xenon is shown in Fig. 1. The energy-level values are from [8]. The excited-state, neutral transition probed in this work, arising from the metastable $6s[3/2]^0_2$ level, is indicated. The levels shown on the energy-level diagram are the fine-structure components resulting from electron-spin–orbit interactions. Transitions between these energy levels are hyperfine split into several components from nuclear-spin effects and from isotopic effects. This splitting decomposes the 823.2-nm transition into 21 lines. A model line shape can be constructed by

broadening the 21 lines into Voigt profiles and subsequently adding the individual components [4]. The assumption of a Maxwellian velocity distribution of the absorbing atoms within the probe volume allows the modelling of the line shape using a Gaussian component to a Voigt profile. This assumption is reasonable for a dc discharge. However, the assumption of a Maxwellian velocity distribution in the plume of the Hall thruster is not necessarily valid given the highly nonequilibrium nature of this plasma.

As is the case with neutral xenon, the ground state of the xenon ion is not easily accessible to LIF. The excited-state, xenon-ion transition probed is the 605.1-nm transition arising from the metastable $5d[3]_{7/2}(^4D_{7/2})$ state, as shown in Fig. 2. The energy-level values in the figure are from [9]. This transition has 19 isotopic and hyperfine components contributing to its line shape. Nonresonant fluorescence at 529.2 nm is collected from the $6p[2]^0_{5/2}(^4P_{5/2})$ upper state.

The measured LIF signal is given by [10]

$$S_f = \eta_d\alpha_c h\nu_{12}AN_2. \tag{2}$$

where η_d is the efficiency of the detection system. α_c takes into account factors involving the collection system, and A is the Einstein coefficient for spontaneous emission of the detected radiation. A two-level rate-equation analysis yields the following result for the upper-level population at steady state [11]:

$$N_2 = \frac{N_1 + N_2}{1 + \frac{g_1}{g_2} + (A + Q)\frac{c}{B_{12}\Phi_H I_\nu}}. \tag{3}$$

Here I_ν is the spectral irradiance (intensity) at frequency ν, and B_{12} is the Einstein stimulated absorption coefficient, $B_{12,\nu} = B_{12}\Phi_H$ with Φ being the transition's spectral-line
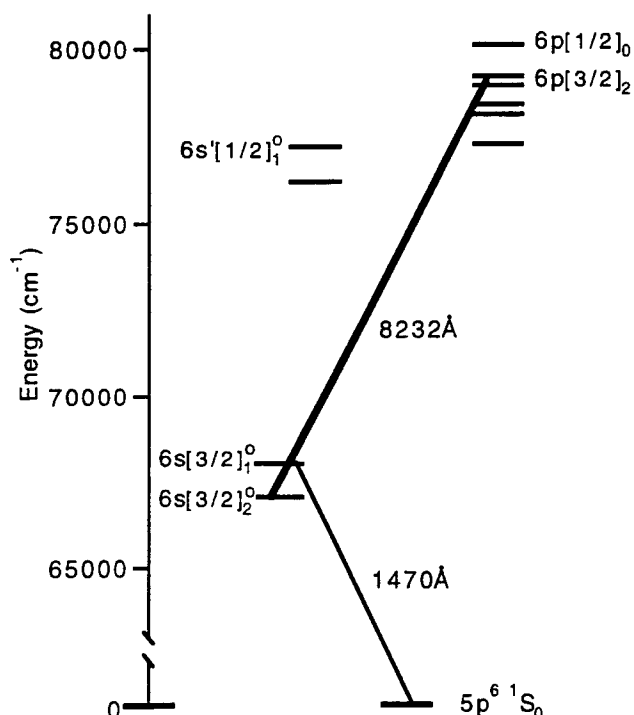

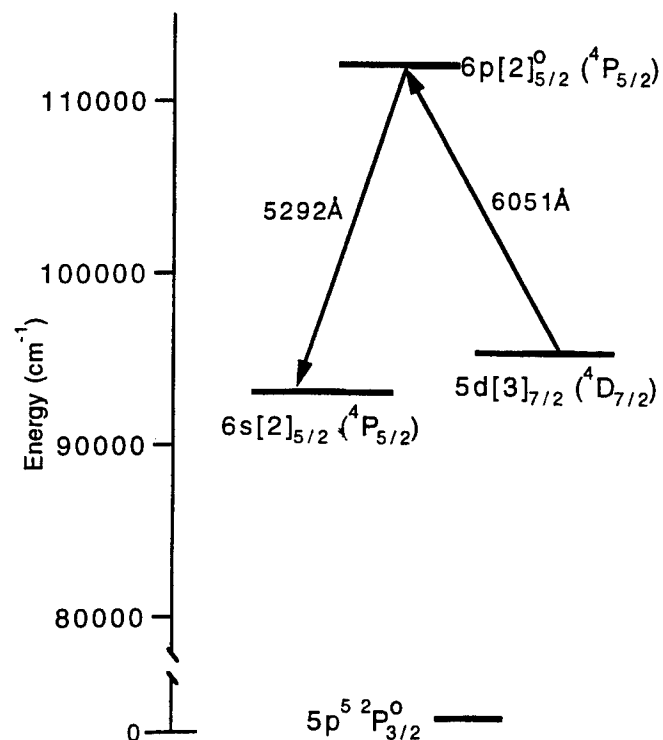Fig. 1. Partial energy-level diagram of xenon

Fig. 2. Partial energy-level diagram of singly-ionized xenon

shape, which accounts for the variation of absorption with laser frequency. The spectral-line shape is determined by the plasma environment of the absorbing atoms. The homogeneous contribution to the line shape Φ_H, from collisional interactions between the probed absorbers and other particles and from the inherent uncertainty in assigning an energy to the energy states involved, is the Lorentzian contribution to the Voigt profile. The lower and upper state degeneracies are represented by g_1 and g_2, and Q is the collisional quenching coefficient from the upper state. Assuming a Maxwellian velocity distribution and integrating over all spectral packets [12, 13] to account for a Gaussian, inhomogeneous broadening component results in

$$S_f = \eta_d \alpha_c h \nu_{12} \frac{A}{A+Q} \frac{B_{12}}{c}$$
$$\times \frac{I_\nu}{\sqrt{(1+I_\nu/I_{sat})}} (N_1 + N_2) \Phi_\nu(a_S, w) ,$$
(4)

with I_{sat} the saturation intensity:

$$I_{sat} = \frac{\pi c \Delta\nu_L}{2} \frac{A+Q}{B_{12}} \frac{g_2}{g_1+g_2} .$$
(5)

and $\Phi_\nu(a_S, w)$ the Voigt-line shape with parameter a_S [14]. The Voigt w parameter is a nondimensional detuning from line center and the usual Voigt a parameter is defined as

$$a \equiv \sqrt{\ln 2} \frac{\Delta\nu_L}{\Delta\nu_G} ,$$
(6)

with $\Delta\nu_L$ and $\Delta\nu_G$ being the Lorentzian and Gaussian full widths at half maximum (FWHM). The parameter a_S is then

$$a_S = a\sqrt{1 + \frac{I_\nu}{I_{sat}}} .$$
(7)

For low laser intensities, I_{sat} drops out of the above analysis ($I/I_{sat} \to 0$) and a line shape can be accurately modelled using (4) by summing the Voigt profiles with the a parameter, not a_S. A demonstration of the model and fitting procedures for this case can be found in [4]. The different line intensities arise only from different isotopic abundances and different B_{12} values for each nuclear-spin-split component. The relative broadening is only slightly different from the differences in isotopic mass, which affect the Doppler component. The kinetic temperature can, in this case, be extracted easily from the Doppler component supplied by the curve fit of the model.

For higher laser intensities the situation is considerably more complicated. The relative hyperfine-line intensities and their relative broadening in the detected fluorescence are then affected by different I_{sat} values. Saturation or power broadening occurs as there is preferential absorption, and therefore saturation of the signal, when the laser is tuned to one of the line centers. The proximity in energy of the nuclear-spin-split levels would require that a multilevel model be considered in the saturated case; however, Berg and Shackleford [11] find that in an analysis of a four-level model the general behaviour turns out to be the same as for the simpler two-level model. Also, I_{sat} only depends on the collisional quenching from the collection of upper nuclear-spin-split states to the lower collection of states if the collisional transfer rates between

the laser-coupled levels and nearby levels are much greater than the quench rate from the upper levels down to the lower levels. The saturated-line shape still contains information on the kinetic temperature and other plasma parameters but this information is not so easily extracted. Other assumptions embodied in (4) are constant laser intensity across the probe volume, negligible radiative trapping – the absorption of the probe volume fluorescence before reaching the detector – and negligible upward collisional excitation.

Local electric and magnetic fields can further affect the spectroscopy of a transition. A magnetic field splits each fine or hyperfine line into a number of lines through Zeeman splitting. An extremely strong electric field can also cause a splitting, as well as a shifting, of spectral lines through Stark effects. Furthermore, perturbations of an atom's energy levels by nearby charged particles lead to a Stark shift as well as Stark broadening of a spectral line.

2 Facility

The Hall-thruster test facility consists of a nonmagnetic, stainless-steel tank approximately 1 m in diameter and 1.5 m in length. Two 50-cm diameter oil-diffusion pumps together provide a nominal pumping speed in air of $35\,000\,\mathrm{l\,s^{-1}}$ and are backed by a $425\text{-}\mathrm{l\,s^{-1}}$ mechanical pump. All pressure measurements are made with an ionization gauge which is not corrected for gas species. The base pressure reading of the system is 10^{-7} torr. While firing the thruster at nominal run conditions with a total of $3.2\,\mathrm{mg\,s^{-1}}$ flow of xenon, the tank pressure reading is 2×10^{-4} torr. These values correspond to a xenon pumping speed of $2000\,\mathrm{l\,s^{-1}}$. The thruster is mounted on a two-axis translation mount within the tank.

The thruster used in this study is a laboratory model based on the design of thrusters being considered for high specific-impulse station-keeping missions. The operating principles of the Hall and related closed-drift thrusters are discussed extensively in the literature [15–20]. Excluding the cathode, the thruster body has an overall width of 95 mm and a height of 120 mm. The thruster body also serves as the magnetic-field circuit. As shown in Fig. 3, there is an inner north magnetic pole and outer south pole surrounding an insulated, annular channel, which is 10 mm wide and 14 mm in depth. Four outer solenoids and one central solenoid generate the magnetic field. The solenoid cores are constructed of mild steel while the front plates (Fig. 3) are made from commercially pure iron. The solenoids consist of cores 6.5 mm in diameter wrapped with 22-gauge, insulated copper magnet wire. The resulting magnetic induction field has a maximum value of 120 G, which occurs at a solenoid current of 2.5 A. The magnetic field strength limitations result from the design of the central core; however, resistive heating in the solenoid coils reduces the maximum continuous current to 2.0 A from the 200-°C temperature limit imposed by the magnet-wire insulation.

The alumina insulator supports the 90-mm diameter, nonmagnetic, stainless-steel anode, which also distributes the propellant into the annulus. Propellant distribution is accomplished by 32 evenly spaced holes each with a diameter of 0.5 mm. The cathode current is produced by an Ion Tech HCN-252 hollow-cathode neutralizer capable of supporting a maximum of 5 A. The neutralizer is mounted on the thruster
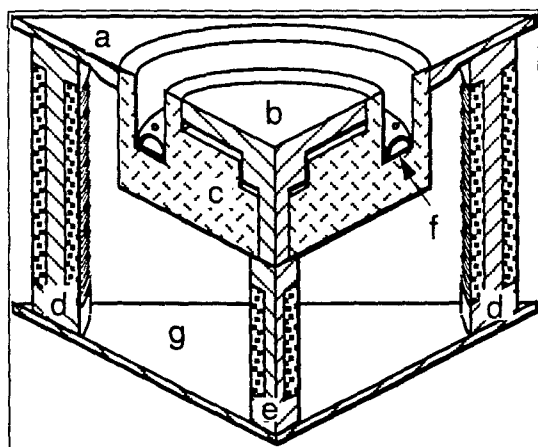
462

Fig. 3a–g. Laboratory-model Hall thruster: a south magnetic pole (front plate); b north magnetic pole; c alumina plasma insulator; d outer solenoids; e central solenoid; f propellant distribution system and anode; g back plate

Fig. 4. Current–voltage characteristic for an anode mass-flow rate of 2.9 mg s^{-1} and cathode mass flow of 0.29 mg s^{-1}

by a stainless-steel bracket which positions the electron beam to intercept the ion beam at a 30° angle downstream from the vertical approximately 70 mm from the exit of the thruster.

The main discharge is nominally powered by a current-controlled power supply. The cathode requires two power supplies. A variable transformer powers the heating element, supplying 8.5 A at startup and 4.0 A during normal operation. The cathode keeper is supplied with 250 V for startup and approximately 7 V and 250 mA during thruster operation. A current-controlled power supply furnishes power to the solenoids.

Figure 4 shows the current–voltage characteristic of the Hall thruster for nominal operation at 2.9 mg s^{-1} xenon flow through the anode and 0.29 mg s^{-1} through the cathode. The typical voltage knee is evident at a current of approximately 4.3 A [15]. This condition corresponds to approximately 50% of the emitted electrons neutralizing the ion beam, with the remainder supporting the electric field in the channel. The current-equivalent mass flow from the annulus, assuming full ionization, is 2.2 A.

Standard operating conditions for the thruster are as shown in Table 1. Because of limitations in the allowable heat flux to the alumina insulator, power levels are generally limited to below 400 W for the nominal flow rates. This power level allows the thruster to run near the base of the voltage knee of the thruster which according to Kaufman [15] is the optimum operation point for Hall thrusters.

3 Experiment

3.1 Neutral-xenon measurements

A schematic of the diagnostic setup for the neutral-xenon measurements is shown in Fig. 5. A tunable AlGaAs semiconductor diode laser is the excitation source for the neutral-xenon measurements. Diode lasers are capable of providing typical lasing linewidths of about 10 MHz [21]. The beam first passes through an optical isolator. The laser beam then encounters a beam splitter. The main portion of the beam passing through the beam splitter is redirected into the thruster plume in the axial direction and focused near the thruster exit. The beam is expanded and then brought down
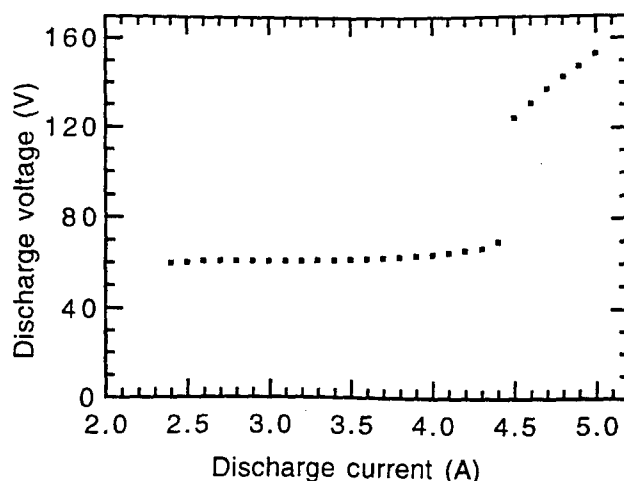
Table 1. Steady state conditions – after 10 run hours

Power to main discharge	260 W	(4.2 A, 62 V)
Power to cathode keeper	1.7 W	(250 mA, 6.9 V)
Power to cathode heater	21 W	(4.15 A, 5 V)
Power to magnetic circuit	38 W	(2.0 A, 19.2 V)
Total power	321 W	
Mass-flow rate to anode	2.9 mg s^{-1}	(30 SCCM)
Mass-flow rate to cathode	0.29 mg s^{-1}	(1.0 SCCM)
Background pressure	2×10^{-4} torr	
Solenoid temperature	206 °C	
Front plate temperature	208 °C	

to a submillimeter focus by 1000-mm and 750-mm focal-length lenses. About 15 to 20 mW of laser power reaches the probe volume, far exceeding the saturation intensity for the 823-nm transition [4]. This level of laser power is required to provide a reasonable signal level from the neutral xenon in the highly ionized thruster plume. The laser probes the exit of the channel of the thruster on the side opposite the cathode.

The probe volume at the beam focus is imaged onto the entrance slit of a half-meter monochromator by 600-mm and 280-mm focal-length lenses. An iris matches the collection system $f/\#$ to that of the monochromator. The plasma emission and LIF are collected at right angles to the laser beam. The intersection of the collection volume with the laser beam defines the probe volume. A photomultiplier tube detects the LIF along with the background plasma emission. The monochromator is used as a spectral filter, transmitting light over the entire transition while the laser frequency is varied to produce the LIF line shape. The monochromator's slit height determines the extent of the probe volume along the beam axis, which is also the axial plume direction. For one set of neutral-xenon measurements, light was collected over a 10-mm length of the laser beam. For a subsequent set of measurements, this length was reduced to 6 mm. A portion of the laser beam large enough to provide an adequate fluorescence signal needs to be imaged onto the monochromator slit.
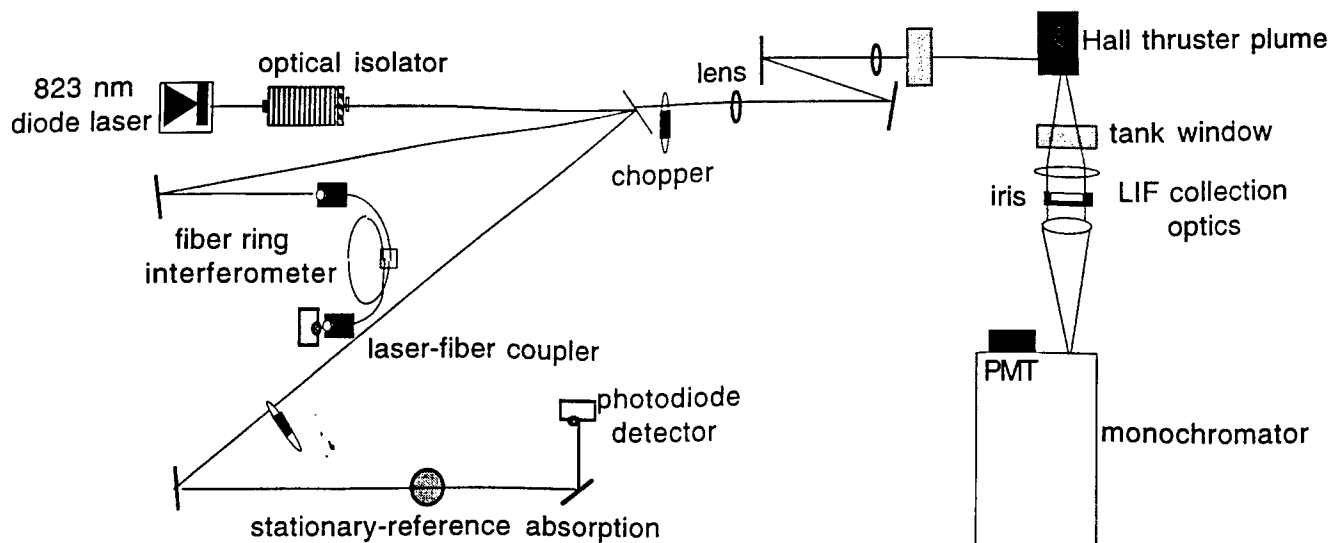
Fig. 5. Schematic of diagnostics setup

A dc discharge in a xenon spectrum tube serves as a stationary xenon-plasma source. One of the two reflections from the beam splitter is redirected through this discharge. A silicon photodiode monitors the beam intensity that passes through the discharge to record the absorption profile as the laser is tuned. The absorption-line shape is recorded simultaneously with the LIF profile from the thruster plume to provide an unshifted, zero-velocity reference.

Phase-sensitive detection is used to discriminate between the fluorescence and the background emission. A lock-in amplifier is locked to the frequency of a mechanical chopper operating at 2–3 kHz. The highly ionized nature of the plasma results in a low signal-to-background ratio requiring the use of a long time constant ($\tau = 1$ or 3 s) and scan times from 15 to 30 min for the 12-GHz scans. Phase-sensitive detection is also used for the spectrum-tube absorption.

The laser frequency is monitored by a fiber ring interferometer [22] with a 178.4 ± 0.4 MHz free spectral range. A laser-fiber coupler focuses the second beam-splitter reflection into a single-mode fiber connected to the interferometer. Another laser-fiber coupler focuses the interferometer output onto a detector.

3.2 Xenon-ion measurements

Since the 605-nm transition is inaccessible with readily available diode lasers, a tunable dye laser pumped by an argon-ion laser is used for the ion measurements. The dye laser provides linewidths on the order of MHz. As with the above measurements, 1000-mm and 750-mm focal-length lenses focus the 605-nm laser light to a probe volume at the annulus exit of the thruster opposite the cathode. Calculations show the beam waist to be about 50 μm. The approximately 100 mW of laser power that reaches the probe volume again saturates the transition.

The laser beam enters the thruster's annular channel axially and reflects off the anode propellant ring within the thruster. The anode propellant ring is carefully positioned so that the laser beam reflects back on itself through the probe volume. The incoming and reflected beams are then counter-propagating through the probe volume. The resultant fluorescence from the probe volume has two peaks shifted in opposite directions by the Doppler shift. The two profiles are centered around the line center of stationary absorbers. In this situation, a measure of the unshifted line center at the probe volume conditions is provided automatically, and there is no need for an external zero-velocity reference. The reflection is not fully specular. However, as the transition is strongly saturated, the LIF from the reflected beam is comparable to that from the incoming beam.

The same apparatus used for the neutral measurements collects the fluorescence at 529 nm from the probe volume at right angles to the counter-propagating beams. Light is collected over a 1-mm length of the incident and reflected laser beams. The beam diameter determines the other dimensions of the probe volume. The mechanical chopper modulates the probe-beam intensity at 3 kHz, and the lock-in amplifier uses a 3-s time constant. Scan times are 10 min for the 30-GHz scans. The laser frequency is determined by the scan rate of the dye laser's intracavity etalon, with the scan end points obtained by a wavemeter.

4 Results

4.1 Neutral velocities

Figure 6 shows sample simultaneous LIF and absorption traces for the neutral-xenon 823-nm transition. Both measured line shapes have been normalized by the laser intensity and then by their peak values. The LIF is from a probe volume at the center of the Hall-thruster annulus opposite the cathode, 1.5 cm downstream of the exit plane. The absorption is from the xenon spectrum tube serving as the zero-velocity reference. From (1), the line shift of $0.015\,\mathrm{cm}^{-1}$ in Fig. 6 corresponds to a neutral-xenon velocity of $380\,\mathrm{m\,s}^{-1}$ into the laser beam. For a sample condition, the diode laser was tuned up to $0.5\,\mathrm{cm}^{-1}$ from the unshifted or zero-velocity frequency to investigate the possibility of the existence of other collections of neutrals at higher velocities. No signal above the noise level of a few percent of the peak LIF was found.
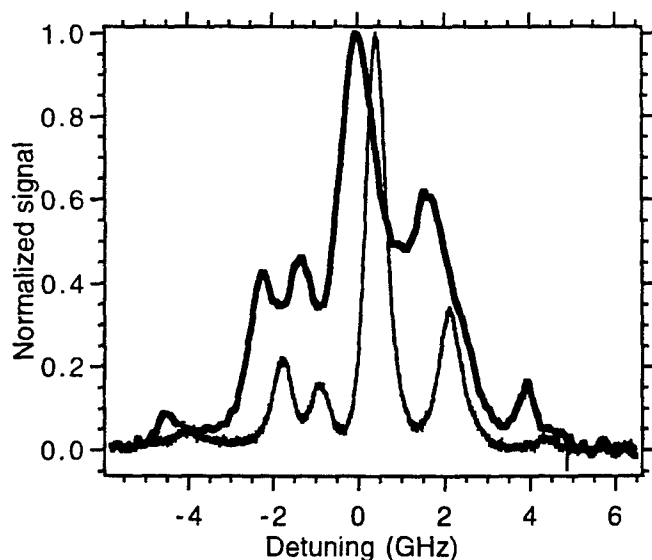
Fig. 6. Frequency shift of neutral-xenon 823-nm-line shape: |. LIF from Hall-thruster plume, 1.5 cm from exit plane; |. absorption from dc-discharge unshifted-reference source

Fig. 7. Neutral-xenon axial velocity at different axial locations: ▼. 6 mm axial probe length: ■. 10 mm axial probe length

Axial neutral velocity calculations from measured line shifts, such as those in Fig. 6, were made at several axial and radial locations under standard thruster operating conditions (see Table 1). The results for the different axial locations, all at the center of the annular channel, are shown in Fig. 7. The exit plane is the position where half of the probe volume is blocked from the collection optics by the edge of the thruster. The location of the probe volume relative to the thruster was measured to within a 1-mm accuracy. The axial velocity was 240 m s^{-1} at the exit plane and peaked near 400 m s^{-1} at 1.0 to 1.5 cm downstream. Two sets of data are shown in Fig. 7, one where the probe volume was 10 mm in the axial direction and one where it was 6 mm. This length is displayed on one point for each data set. The axial velocity measurements for different radial positions were from an axial position 5 mm downstream of the exit plane. These data were all taken with a 6-mm probe length along the laser-beam axis, and the probed locations spanned a 9-mm radial range across the annular channel. The resultant axial velocities were nearly constant, being within 8% of the average value of 330 m s^{-1}.

The Hall thruster was run at different powers to investigate the velocity as a function of discharge current at a point at the center of the annulus 5 mm downstream of the exit plane. The results are shown in Fig. 8. With no solenoid current, a glow discharge could be maintained with 46 mA between the anode and the hollow cathode. As the plasma in a glow discharge is very weakly ionized, the neutral-xenon flow characteristics for this condition are effectively the same as for simple propellant flow with no discharge. The glow discharge is needed, however, to produce the excited-state neutrals required for the LIF measurement. An axial velocity of 100 m s^{-1} was measured in the glow discharge. The thruster body temperature, which was monitored by thermocouples, remained at room temperature throughout this measurement. A measurement was also taken with the thruster running at a power above that of the standard conditions, on the upper part of the $V-I$ curve at 4.7 A and 122 V (see Fig. 4). This elevated power produced a neutral-velocity result significant-
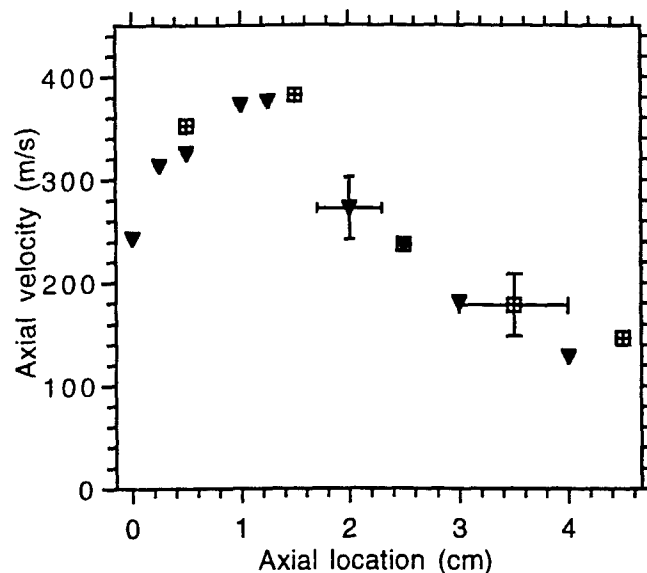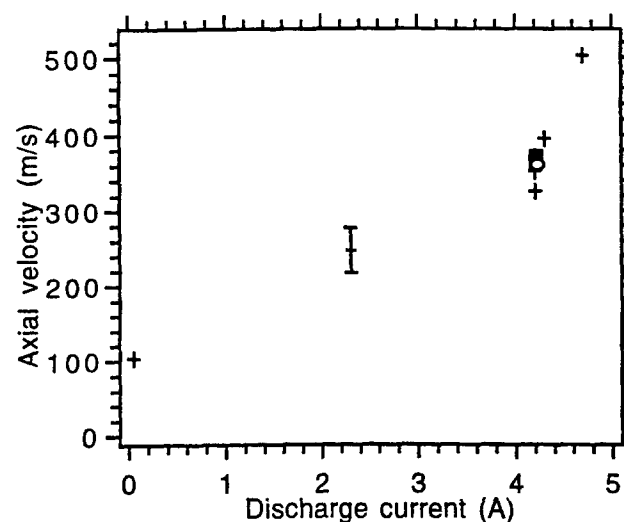

Fig. 8. Neutral-xenon axial velocity 5 mm from exit plane at different operating conditions: +. 2.0 A solenoid current; o. 1.5 A solenoid current; ■, 1.0 A solenoid current

ly higher, reaching 500 m s^{-1}. This operating condition was close to an unstable operating regime.

Included in Fig. 8 are the axial neutral-velocity results for solenoid currents different from the standard conditions. Measurements were made with solenoid currents of 1.0 and 1.5 A as well as with the standard 2.0 A. These solenoid currents correspond to peak magnetic field strengths of 88, 93, and 97 G. The lower magnetic field strengths resulted in line shifts not significantly different from that from the nominal 2.0-A condition. Furthermore, the recorded LIF line shapes for these three different conditions were indistinguishable, within experimental uncertainty.

The main contributing factor to the uncertainty in the axial neutral velocities arises from the determination of the peak position of the recorded LIF data. Noise in the data can cause the maximum measured signal to be slightly offset from where it would have been in a perfectly smooth trace. The frequency locations of the measured LIF traces are found by

matching the overall line shape to a calculated line shape, instead of simply using the peak location. The uncertainty in the placement of the peak location was ± 30 m s^{-1}. The axial velocity results at different radial positions were consistent with this uncertainty, being constant with a scatter of about this magnitude. The uncertainty is displayed on a sample point for each data set in Figs. 7 and 8. Other contributions to the uncertainty included changes in thruster operation over the scan time, as well as between scans, and the magnitude of the Stark shift. The collisional Stark shift has a linear dependence on the electron number density n_e at the probe volume [23]. An estimate of the Stark shift for the neutral-xenon 823-nm transition can be taken from the line shift versus pressure data of Schwabedissen and Bötticher [24]. If the line shift at the zero-pressure intercept in their data is attributed entirely to a Stark effect, an estimate of the Stark shift can be made. An upper bound of 0.01 cm^{-1} is obtained at an n_e of 0.8×10^{15} cm^{-3}. For the smaller n_e values expected at most probed locations in the Hall thruster, the Stark shift arising from interactions with charged particles is anticipated to be small.
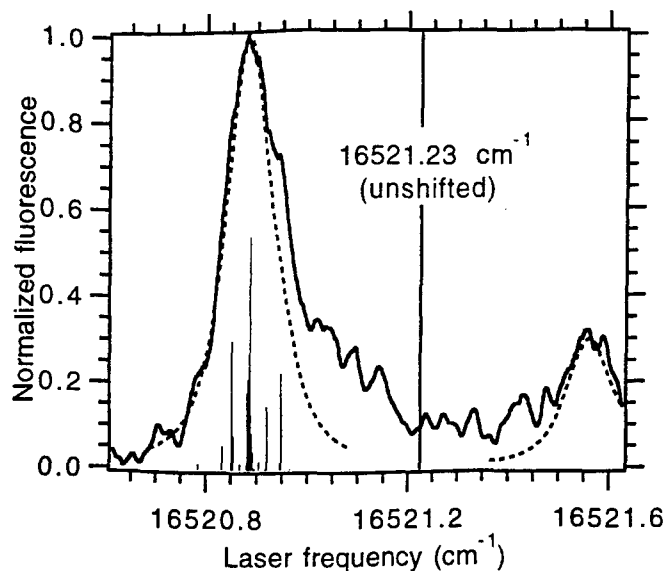

Fig. 9. Frequency shift of xenon-ion 605-nm-line shape: —, LIF from Hall-thruster plume: - - -, constructed profiles: |, lines contributing to the line shape

4.2 Ion velocities

Figure 9 shows a sample trace of the xenon-ion 529-nm fluorescence collected as the laser was tuned over the 605-nm transition. The data has been normalized by the laser intensity and then by the peak value. The LIF is from a probe volume at the center of the thruster channel opposite the cathode, 1.5 cm downstream of the exit plane. The incoming laser beam gave rise to the main fluorescence peak, while the reflection of the beam from the anode propellant ring caused the fluorescence peak at the right side of Fig. 9. The counter-propagating beams produced LIF Doppler shifted in opposite directions. For convenience, profiles for the low laser-power limit were used to establish the peak positions. These constructed profiles are shown with each LIF peak. The hyperfine and isotopic lines contributing to the LIF are shown within one of these profiles. From (1), the line shift in Fig. 9 of 0.34 cm^{-1} (0.68 cm/2) corresponds to a xenon-ion velocity of 6.2 km s^{-1} in the axial direction. For higher velocities, the two LIF peaks could not be captured in one trace. In this case, two consecutive traces, each recording one of the peaks, were linked using the wavemeter reading. At some of the axial positions far downstream of the exit plane, the reflected beam had diverged to the point where a peak could not be detected clearly. In this case, the peak position of LIF from the incoming beam was compared to the unshifted line center, using an average of all the measurements, to calculate a velocity.

Ion axial velocity data were taken at several axial and radial locations. The thruster was operated near the conditions shown in Table 1. As a consequence of using a current-controlled power supply, however, the discharge voltage varied significantly. Figure 10 shows the results for the different axial locations, all at the center of the annular channel. These velocities correspond to the shifts of the main peaks of LIF. Three sets of data are shown. The first set of data was taken with the main discharge driven by a current-controlled power supply. As indicated on the figure, the discharge voltage drifted from 85 V at the beginning to 78 V for the last measurement. The ion velocity was near 1 km s^{-1} at the exit plane, increasing to near 7 km s^{-1} at 3.0 cm downstream
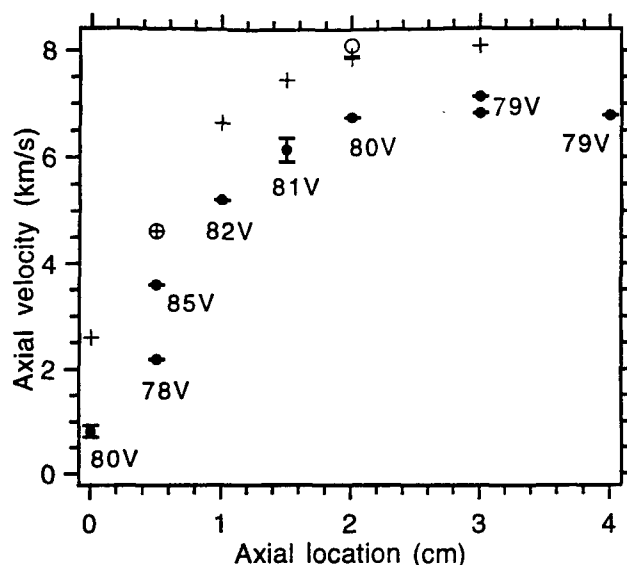
Fig. 10. Xenon-ion axial velocity at different axial locations: •, current-controlled power supply, 4.2 A. voltages as shown: +, voltage-controlled power supply, 88 V. 4.1–4.2 A: o, current-controlled power supply, 4.2 A. 87 V

before levelling off. The second set of data was taken using a voltage-controlled power supply for comparison. The voltage was set at 88 V in order to match the standard operating current of 4.2 A. This data shows the same trend. The difference in operating voltage resulted from day-to-day changes in the operating conditions of the thruster. Two data points were taken immediately after the second set using the current-controlled power supply at 4.2 A and 87 V for a comparison under more closely matched current-voltage conditions. These conditions gave velocity results similar to the second set, in which the discharge voltage was controlled. Moving radially at a position 0.5 cm from the exit plane, measurements were taken 2, 4, and 5 mm from the center of the annular channel, as well as at the center of the channel. The thruster was operating at 4.2 A and 78 V. The corresponding veloci-

ty results at these different radial positions were within 15% of the 2.2 km s^{-1} value found at the channel center, with no significant trend.

Measurements were also taken at other operating conditions. Using the current-controlled power supply, the thruster was run at higher currents. The results of these measurements are shown in Fig. 11. Measurements were taken at 4.2 and 4.55 A in one session and at 4.2 and 4.73 A in another session. The voltages, which varied from session to session, are shown with each data point. The results at both axial locations show the similar trend of increasing ion velocity with discharge voltage. In another experiment, the thruster was run with decreased xenon-flow rates through the anode, with the voltage-controlled power supply set at a discharge voltage of 155 V. The reduced flow rates allowed for higher discharge voltages and higher resultant ion velocities. Measurements were made at 1.7 mg s^{-1} (2.4 A discharge current), 1.9 mg s^{-1} (2.8 A), 2.1 mg s^{-1} (3.3 A), 2.3 mg s^{-1} (3.7 A), and 2.5 mg s^{-1} (4.4 A) at a position 2.0 cm from the exit plane. The measured velocities were uniform with flow rate, in a range from 11.7 to 12.7 km s^{-1}.

As before, there is an uncertainty in the velocity measurements from the reading of the peak positions of the recorded LIF data. Constructed line shapes are used to help determine where the peak in the data would have been if the trace were perfectly clean. The uncertainty in determining peak locations was ±100 m s^{-1}. For most measurements, this uncertainty was small relative to the large velocities measured. The wavemeter accuracy also contributes an uncertainty of ±2 % to each measurement. A sample error bar accounting for these two uncertainties is displayed on two points in Fig. 10 and on one point on Fig. 11. These uncertainties are small compared to changes in ion velocity from changes in thruster operation between different scans. When the thruster operating conditions were carefully matched, the velocity results at a given position were consistent. This result can be seen in Fig. 10 at 0.5 cm and 2.0 cm for the matched conditions. Stark or other shifts of the line center do not contribute to the uncertainty for the ion measurements: The simultaneous recording of LIF from counter-propagating beams automatically calibrates the measurements to account for any non-Doppler line shifts.

4.3 Additional results

The LIF from the counter-propagating beams in the ion velocity measurements provided a measure of the line center, unshifted by the Doppler effect, of the xenon-ion 605-nm transition. This line center corresponds to the point midway between the LIF from the incoming and reflected peaks, as seen in Fig. 9. Twenty-two measurements in total were taken which captured both peaks. There was no discernible trend in the line-center locations with axial position, with radial position, or with discharge operation. The line center from these measurements was found to be 16521.23 cm^{-1} with a statistical uncertainty (two standard deviations) of 0.01 cm^{-1}. The wavemeter accuracy contributes another 0.01 cm^{-1} to the uncertainty of this value.

The spectral distribution of the measured LIF, or the spectral-line shape, contains information on the velocity distribution of the probed species. To extract information on
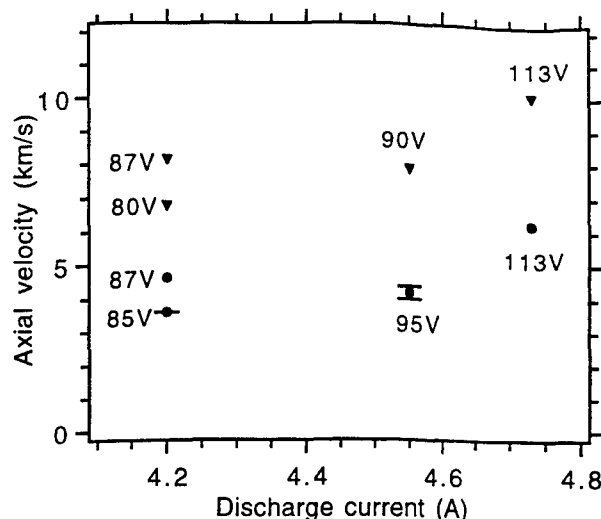

Fig. 11. Xenon-ion axial velocity at different operating conditions: •, 0.5 cm from exit plane: ▼, 2.0 cm from exit plane

the kinetic temperature from a Doppler broadening component, an attempt to model the line shape can be made using (4) and the known positions and relative intensities of the isotopic and hyperfine-split lines. For the neutral-xenon-line shapes the kinetic temperature T_{kin} is used as a parameter, along with Δv_L and a saturation parameter I/I_{sat}. The kinetic temperature determines Δv_G. The saturation parameter mainly affects the relative peak heights in the line shape. The kinetic temperature and Δv_L affect the width. The saturation parameter needs to be multiplied by factors specific to each of the hyperfine lines through the definition of I_{sat} in (5). These complications, combined with the extensive isotopic and hyperfine splitting, make a full-scale numerical fit intractable: consequently, the parameters are adjusted while comparing the model result to a data trace.

A sample neutral-xenon line shape recorded under standard thruster operating conditions was compared to the model. The sample data was taken at the center of the annular channel 1.0 cm downstream of the exit plane. The I/I_{sat} was adjusted to best match the relative peak heights of the three secondary peaks surrounding the main central peak in the 823-nm line shape. Subsequently, Δv_L and T_{kin} were adjusted to match the width and shape. The model result for an I/I_{sat} of 3.3, a T_{kin} of 500 K, and a Δv_L of 0.014 cm^{-1} was found to match most closely the experimental spectrum. The results are shown in Fig. 12, in which the data trace from the thruster operating as a glow discharge is also included for comparison. The neutral-xenon kinetic temperature is known to be slightly above room temperature for this low-current glow-discharge condition [4]. Slightly changing Δv_L from 0.014 cm^{-1} greatly affected the resultant model line shape in comparison to the sample measured spectrum. At T_{kin} values above 700 K, the model-line shape's width became clearly greater than that of the data for a Δv_L of 0.014 cm^{-1}. The lower temperature boundary is set by the glow-discharge temperature so the neutral-xenon kinetic temperature under standard conditions was 500 ± 200 K.

The neutral-xenon line shapes recorded at standard thruster operating conditions did not show much variation
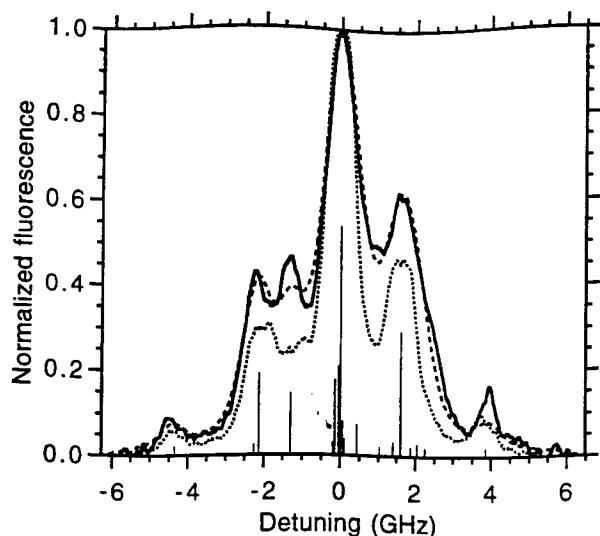
Fig. 12. Neutral-xenon 823-nm saturated-line-shape modelling: —. LIF for standard Hall-thruster operation, 1.0 cm from exit plane: - - -. model result for $T_{kin} = 500$ K. $I/I_{sat} = 3.3$. $\Delta\nu_L = 0.014$ cm^{-1}; ⋯⋯. LIF from Hall thruster operating as a glow discharge

in width. The line shape recorded at a higher thruster power was significantly different, however, having a width corresponding to a temperature that was at least 1000 K. At this condition, 4.7 A and 122 V, the line shape showed no evidence of any underlying structure making it difficult to derive a more definite measure of the neutral kinetic temperature.

From Fig. 9, it is evident that the xenon ions do not have a Maxwellian velocity distribution. No combination of input parameters would construct Voigt profiles to match the recorded LIF data, given the relative locations of the isotopic and hyperfine lines. The non-Maxwellian nature of the distribution is particularly evident on the low-velocity side of the peak LIF signal. Furthermore, constructed profiles that include the effects of saturation cannot possibly replicate this tail in the LIF distribution. The symmetry of the shapes of the LIF peaks about the unshifted line center, accounting for the differences in signal intensities from the incoming and reflected beams, suggests that the non-Voigt shape of each peak arises from a spread in ion velocities rather than from a further splitting of the contributing lines.

A spread of velocities consistently appeared in the recorded xenon-ion data traces. The effect became more apparent for the data taken further from the exit plane, with secondary peaks appearing. The data recorded furthest from the exit plane, 4.0 cm downstream, had a secondary peak of ion LIF comparable to the main peak in signal intensity, at approximately half the peak velocity. The data recorded at different thruster operating conditions were similarly affected, the phenomenon being more a function of location than of power or propellant-flow rate. Substantial secondary peaks were reproduced in data taken consecutively at the same location. Such was the case for the two traces recorded at 2.0 cm from the exit plane with the voltage-controlled power supply, along with the series of traces recorded at 2.0 cm downstream at different flow rates.

5 Discussion

5.1 Velocities

The key information concerning the general operation of Hall thrusters gained from this study is that charge-exchange between accelerated ions and slow-moving neutrals is not substantial. The xenon ions exit the thruster at far higher velocities than the neutrals. The lack of fast-moving neutrals indicates that the ions do not interact significantly with the neutrals exiting the thruster or that low-energy, background neutrals are being entrained into the flow in adequate numbers to thermalize high-velocity neutrals. The insensitivity to thruster operating conditions of the neutral velocities relative to that of the ion velocities is further evidence of the insignificance of the ion-neutral interaction.

Peak ion velocities as high as 12 km s^{-1} are noteworthy for a laboratory-model thruster. The 1.5-kW SPT-100, a thruster nearing space qualification, has ion velocities around 16 km s^{-1} [2]. This thruster was operated at a discharge voltage of 300 V, compared to the 155-V maximum applied to the Hall thruster in this study. For the laboratory-model thruster, the ion acceleration is seen in Fig. 10 to occur mainly over the first 2 cm from the exit plane. This result may be a consequence of the particular design of the magnetic field circuit coupled with the placing of the cathode. These observations demonstrate how these types of measurements can provide insight into thruster operation and aid in an ongoing design process.

The neutrals also accelerate after exiting the Hall thruster, reaching a peak 1.0 to 1.5 cm downstream (Fig. 7). To understand the flow of neutrals, the possibility of momentum-transfer collisions with high-velocity ions and of thermalizing collisions with stationary, background neutrals must be considered. The flow of neutrals is possibly choked at the thruster exit plane. A neutral kinetic temperature of 550 K corresponds to a sonic velocity for xenon of 240 m s^{-1}. The neutral velocity may increase after the exit plane from expansion or through collisions with ions. The velocity reduction 1.5 cm downstream might occur because of a shock process or collisions with slower, entrained neutrals. The qualitative observation of the neutral kinetic temperature being axially invariant, however, is evidence against a shock process.

The good agreement between the data sets in Fig. 7 permits two observations. First, the variation in operation of the thruster between the two runs did not noticeably affect the neutral velocities. This result is contrary to that which occurs with the ion velocity, further indicating only a small interaction between the ions and the neutrals. The ion velocities are very sensitive to changes in thruster operation, specifically the discharge voltage. Secondly, there are no steep gradients in the density of excited neutrals. The measured line shift and corresponding velocity are skewed to those in the region of the highest density of absorbers within the probe volume, because that region dominates the fluorescence. High density gradients would cause disagreement in the measured velocity at some axial locations between data taken with probe volumes of different sizes.

The neutral flow is affected by significant changes in the power input to the thruster, but not notably by changes in magnetic field. With xenon flowing through the thruster when it is not operating, the measured velocity of 100 m s^{-1}

at 5 mm downstream of the exit plane is subsonic. The xenon sonic velocity in a room-temperature glow discharge is 180 m s^{-1}. In contrast, for the standard operating conditions it was shown above that the flow is possibly sonic at the exit plane and increases downstream. When the thruster is pushed to operate at a point further up from the voltage knee, the velocity 5 mm downstream increases significantly. The higher velocity may result from the increase in the velocity of the ions interacting with the neutrals; alternatively, it may be from an increase in the heating of the neutrals, resulting in higher velocities independent of a more direct interaction of neutral velocities with the ions. Changing the magnetic field should affect thruster performance. Therefore, the observed insensitivity of the neutral axial velocities to the applied magnetic field further suggests a lack of interaction of the neutrals with the ions.

As discussed previously, changes in the discharge voltage as a result of the unsteady thruster operation must be considered. The ion velocity results are reproducible for conditions where the voltage is matched. The data in Fig. 10 for 87–88 V at 0.5 and 2.0 cm demonstrate this observation. Differences between the data sets taken with the current- and voltage-controlled power supplies are attributable to differences in discharge voltage. As seen in Fig. 11, increasing the current affects the ion velocity through its relation to the discharge voltage. In contrast, the ion velocity is not sensitive to radial position, nor to the investigated changes of as much as 50% in flow rate. The ion acceleration being external to the channel may serve to make these factors unimportant.

5.2 Velocity distributions

The effect of saturation on the line shapes obtained in this study limits the accuracy of the determination of plasma parameters from line-shape analysis. Many of the assumptions implicit in (4) become disputable for saturated-line shapes and for the conditions of interest. A more refined model for a saturated-line shape would require a better knowledge of the plasma conditions. Changes in thruster operation which may affect the excited-state neutral-xenon populations over the long scan times also contribute to discrepancies between a measured spectrum and a model. Further, a significant assumption in the model is that of a Maxwellian velocity distribution of the neutrals in the probe volume. The assumption of translational equilibrium at a point in the plasma may be questionable in itself, but the assumption that the neutrals throughout the probe volume have an equilibrated velocity distribution is idealistic. The probe volume being larger than the region over which there is a substantial velocity change, or change in Doppler shift, can result in a blended line shape. This complication makes the model's applicability to the line shape recorded at higher thruster powers more questionable as there are larger velocity gradients in the probe volume.

It is, nevertheless, possible to extract some information on the neutral-xenon kinetic temperature. From Fig. 12, it can be seen that the width of the recorded spectrum from Hall thruster operation is slightly greater than that of the spectrum from glow-discharge operation. Thus, the 500 ± 200 K result is reasonable because, as previously discussed, the kinetic temperature in the glow-discharge case is known to be near room temperature. From calculations for the 823-nm transition, Stark broadening of 0.014 cm^{-1} is predicted to correspond to an electron number density on the order of $10^{14}-10^{15}$ cm^{-3} [24, 25], which is a possibility for some locations in the Hall discharge. This value for $\Delta \nu_L$ of the line shape is thus not unreasonable for use in the determination of the kinetic temperature.

An examination of the xenon-ion line shapes leaves no doubt that the ion-velocity distribution is non-Maxwellian. A kinetic temperature cannot be defined. The majority of ions travel at the peak velocity; however, the remainder apparently leave the thruster with a range of velocities mainly below this peak velocity. The xenon ions accelerate across the potential drop in the discharge from the location where they are created. The LIF spectrum reflects, in part, the distribution of the potential drops over which the ions accelerate, and in turn reflects the locations where they are created. The spectrum reveals that the majority of ions are created at one axial location, with some being created downstream from this point. Collisions may slightly affect this distribution. Plasma oscillations in the thruster may also contribute to the distribution of ion velocities. Prior research has found that ions may not exit Hall thrusters at a constant velocity. Plasma oscillations in the tens of kHz modulate the velocity of the ions [26, 27]. As the LIF measurements made here do not have that time resolution, the effect of the oscillations on the measurements would be a spreading of the line shape in the observed velocity space. Charge-exchange of fast-moving ions with slow-moving, background neutrals could be another possible explanation for a spread in ion velocities. The neutral data, however, show ample evidence to discount this possibility.

As discussed, the validity of the assumption of a Maxwellian velocity distribution is an important consideration in the analyses of the neutral- and ionic-xenon line shapes. This assumption comes into question for the axial measurements made here because of distributions in the axial velocity. Probing the plasma circumferentially may circumvent these difficulties. Velocity gradients across the probe volume would be small because of small circumferential velocities. There would be no difference in acceleration from different potential drops that the ions had encountered. The ions would still have a modulated velocity due to plasma oscillations, but probably not on the same scale as in the axial direction. The distribution of velocities in the probe volume would be predominantly determined by thermal considerations, not by gradients, varied potential drops, or plasma oscillation effects. Thus, to better assess the kinetic temperature of either species, measurements should be made with the laser probing the thruster plume circumferentially. However, this arrangement would yield circumferential – not axial – velocity information.

5.3 Additional spectroscopic details

Previously published values for the line center of the probed xenon-ion transition are 16 521.22 cm^{-1} [9] and 16 521.24 cm^{-1} [8]. The value found in this study is 16 521.23(± 0.02) cm^{-1}, in agreement with the values from the literature. This result shows the Stark shift to be negligible for this ion transition under the plasma conditions in the thruster plume, particularly in relation to the magnitude of the observed Doppler shifts. The lack of a trend in the line-center locations further enforces this observation.

As discussed earlier. the Stark shift arising from interactions with charged particles for the neutral-xenon transition is also not expected to be significant. It is possible, though. that a Stark shift has a slight effect on the velocities calculated at some locations. The measured line shift is slightly. but not significantly, higher for the lower applied magnetic fields. The lower solenoid currents may result in lower local electric field. E. and n_e values in the probe volume and thus smaller Stark shifts. If this observation is attributable to an actual occurrence and not just to the uncertainty in the measurement. it would indicate a Stark shift of the main lines of the 823-nm transition in the opposite direction in frequency from that of the Doppler shift. A Stark shift in this direction would offset some of the Doppler shift. resulting in a slight underestimate of the velocity. However. the neutral-xenon line shapes give no evidence of a Stark shift. As seen in Fig. 12. the relative locations of the nuclear-spin-split lines agree with their unshifted relative positions: There is no indication that these components are shifted by different amounts or in opposite directions by the Stark effect. Furthermore. no change is observed in the overall measured line shape due to different relative Stark shifts as the local E and n_e change with the different applied magnetic fields.

The spectral distribution of the fluorescence from the thruster plume contains information on other plasma parameters besides the kinetic temperature. such as the electron number density and magnetic field. The electron number density determines the Lorentzian width of the transitions through Stark broadening: however. the broadening rate and confidence in the model result for $\Delta \nu_L$ are both lacking. The effects of the magnetic field are not readily apparent. The qualitative observation of the replication of the recorded neutral-line shape at different magnetic field strengths indicates that the Zeeman splitting is not significant for the given operating conditions. The Zeeman splitting is also negligible for the ion as it is of similar magnitude to that of the neutral.

References

1. P.V. Storm, M.A. Cappelli: Appl. Opt., submitted for publication (Mar. 1997)
2. D. Manzella: AIAA-94-3141. 30th Joint Propulsion Conference. Indianapolis. IN, USA (June 1994)
3. M.S. Rhee. M.J. Lewis: AIAA-95-2928. 31st Joint Propulsion Conference. San Diego. CA. USA (July 1995)
4. R.J. Cedolin. R.K. Hanson. M.A. Cappelli: Phys. Rev. A **54**. 335 (1996)
5. C.R. Bingham. M.L. Gaillard. D.J. Pegg. H.K. Carter. R.L. Mlekodaj. J. Cole. P.M. Griffin: Nucl. Instrum. Methods **202**. 147 (1982)
6. C. Borghs. P. De Bisschop. R.E. Silverans. M. Van Hove. J.M. Van den Cruyce: Z. Phys. A **299**. 11 (1981)
7. S.D. Rosner. T.D. Gaily. R.A. Holt: Phys. Rev. Lett. **40**. 851 (1978)
8. C.E. Moore: *Atomic Energy Levels*. National Bureau of Standards Circular 467 (U.S. GPO. Washington 1958). Vol. III. p.113
9. J.E. Hansen. W. Persson: Physica Scripta **36**. 602 (1987)
10. R.P. Lucht. in *Laser Spectroscopy and its Applications*. edited by L.J. Radziemski et al. (Marcel Dekker. Inc.. New York 1987). pp.623–7
11. J.O. Berg. W.L. Shackleford: Appl. Opt. **18**. 2093 (1979)
12. A. Yariv: *Quantum Electronics*. 3rd ed. (Wiley. New York 1989). pp.168–70
13. A.E. Siegman: *Lasers* (University Science Books. Mill Valley. CA 1986). pp.207–295
14. M. Mitchner. C.H. Kruger. Jr.: *Partially Ionized Gases* (Wiley. New York 1973). p.70
15. H.R. Kaufman: AIAA Journal **23**. 78 (1985)
16. H.R. Kaufman. R.S. Robinson. M.L. Day. T.W. Haag: AIAA-90-2595. 21st International Electric Propulsion Conference. Orlando. FL. USA (July. 1990)
17. J. Ashkenazy. Y. Raitses. C. Appelbaum: AIAA-95-2673. 31st Joint Propulsion Conference. San Diego. CA. USA (July 1995)
18. J.J. Szabo. J.E. Pollard: AIAA-95-2926. 31st Joint Propulsion Conference. San Diego. CA. USA (July 1995)
19. A. Bober. N. Maslennikov: IEPC-93-001. 23rd International Electric Propulsion Conference. Seatlle. WA. USA (Sept. 1993)
20. E.A. Pinsley. C.O. Brown. C.M. Banas: J. Spacecraft **1**. 525 (1964)
21. J.C. Camparo: Contemp. Phys. **26**. 443 (1985)
22. L.F. Stokes. M. Chodorow. H.J. Shaw: Opt. Lett. **7**. 288 (1982)
23. H.R. Griem: *Spectral Line Broadening by Plasmas* (Academic Press. New York 1974). p.320
24. A. Schwabedissen. W. Bötticher: J. Phys. B **26**. 3467 (1993)
25. J. Purić. S. Djeniže. J. Labat. A. Srećković. M. Platiša: Contrib. Plasma Phys. **31**. 63 (1991)
26. G.S. Janes. R.S. Lowder: Phys. Fluids **9**. 1115 (1966)
27. Y.B. Esipchuk. A.I. Morozov. G.N. Tilinin. A.V. Trofimov: Zh. Tekh. Fiz. **43**. 1466 (1973) [Sov. Phys. Tech. Phys. **18**. 928 (1974)]

A Study of a Low Power Hall Thruster Transient Behavior

W.A. Hargus, Jr.[†], N.B. Meezan[†], and M. A. Cappelli[‡]
Mechanical Engineering Department
Thermosciences Division
Stanford University
Stanford, CA 94305

Abstract

Characterization of the transient behavior of a co-axial xenon Hall accelerator is presented. Electrostatic probes, including floating, grounded, emissive (plasma potential), and swept Langmuir probes, are used to measure the time-average and spectral properties of the plasma both outside and within the acceleration channel. The measurements confirm the existence of low-frequency (< 100kHz) coherent azimuthal drift waves and more stochastic disturbances within the channel. The properties of these disturbances depend on the location within the channel, and where in the current-voltage characteristics the thruster is operating, in agreement with observations in other Hall thrusters documented in the literature. Measurements of the time-average plasma potential indicates that in this particular Hall thruster, the largest axial electric field exists between the channel exit and cathode plane, consistent with recent laser-induced fluorescence measurements in the same device, and coincident with the region of the thruster where there is a negative gradient in the magnetic field. The average azimuthal wave speeds are measured and compared to the $E \times B$ drift velocity. The electron temperature is relatively uniform along the discharge, and in the range of 5-10 eV, in qualitative agreement with the observed potential differences between the floating potential and floating emissive probes.

Introduction

Proposals to use crossed-field Hall accelerators as high-performance, high specific impulse electric thrusters for satellite propulsion date back to the early 1960's [1]. Numerous experimental and developmental programs were initiated in the United States shortly afterwards [2-4]. These programs established the basic operating principles of the device. In a crossed-field Hall accelerator, electrons (a large fraction of which are emitted by an external cathode) are magnetized by an applied radial magnetic field (in contrast, the ions, with a significantly lower Hall parameter, are not) and the ions, generated by volume ionization, are accelerated by the electrostatic fields established by the retarded electron flow. In a co-axial Hall thruster design, there is an imposed axial electric field and an applied radial magnetic field. In this configuration, the electrons are constrained to move along the azimuthal coordinate, in the direction of the closed $E \times B$ drift (hence the name "closed electron drift accelerator"). It was recognized early on, however, that the electron current comprised too large a fraction of the total discharge current than can be accounted for by classical collisional diffusion and that an "anomalous" cross-field diffusion of electrons was necessary in order to account for the enhanced plasma conductivity. An extensive experimental study by Janes and Lowder [5] drew attention to the presence of weakly turbulent density and field fluctuations which give rise to the cross-field transport. These experiments were subsequently followed by the several studies of Morozov and colleagues in the former Soviet Union [6-8], in which the nature and structure of this turbulent plasma was further resolved and in which the first theoretical analysis of the wave dispersion relations were presented.

The nature of the instabilities that give rise to the unsteady behavior in these co-axial Hall accelerators is strongly dependent on the sign of the axial gradient in the applied magnetic field [6]. There appear to be at least

three principle oscillatory modes present in modern Hall thrusters: (i) relatively low frequency (20-60 kHz) traveling azimuthal drift waves (often mislabeled as "ionization waves") in the regions of the thruster where the axial gradient in the applied magnetic field $dB_r/dz<0$. These waves are predominant when operating along the ionization portion of the I-V curves and are seemingly damped in the current saturation operating regime, except for regions very near the anode [6] where the wave is excited even in cases where $dB_r/dz>0$; (ii) moderate frequency (~70-500 kHz) largely turbulent axial waves in the regions where $dB_r/dz>0$, with frequencies centered at approximately the inverse ion transit times (hence these waves are often referred to as transit-time oscillations in the literature [7]); and (iii) high frequency (~MHz) azimuthal waves, evident very near the "optimum magnetic field," defined as where the discharge current is a maximum for a fixed voltage and mass flow rate [8]. These and other oscillatory characteristics of Hall discharges are reviewed and discussed in a recent paper by Choueiri [9].

The precise role played by the oscillatory and turbulent behavior characteristic of these Hall discharges is qualitatively understood [9]. However, a quantitative mapping of the plasma in terms of the regions of instability and their influence on electron transport requires further careful examination of the time-average and temporally-resolved plasma properties within the ionization and acceleration regions of the discharge. Such knowledge gives physical insight into a range of performance-limiting factors in modern-day thrusters [10].

In this paper, we report on preliminary results of experiments aimed at verifying the transient operating characteristics of a Hall thruster designed and fabricated in our laboratory. The primary goal of our research is to develop and apply spatially-resolved plasma diagnostics for the ionization and acceleration regions in Hall thrusters. Recently, we have reported on the application of laser-induced fluorescence (LIF) to measure the neutral xenon and singly-ionized xenon velocities at the exit plane of a laboratory thruster [11,12]. The development and

---

application of advanced diagnostics can provide the data needed to further validate models and detailed simulations of Hall thruster operation. These models are expected to be important in the development of the next generation of thrusters that extend the performance envelope. In the study reported here, we have used a variety of electrical probes to characterize the time-average plasma properties and low-frequency (<100 kHz) disturbances in a laboratory Hall accelerator. Complementary thrust measurements allow for the characterization of thruster performance at the conditions examined. The Hall discharge studied here is not intended to be a prototype for an operational thruster and serves only as a test bed for the development of plasma diagnostic tools. Such tools can yield general, quantitative information on the plasma behavior and can be extended for use on prototype thrusters.

Experimental Description

Hall Accelerator and Test Facility

A detailed description of the Hall accelerator studied here and the facility in which these experiments are carried out is provided in another paper [13]. We provide only a brief description in this paper. The test facility consists of a non-magnetic stainless steel tank approximately 1 m in diameter and 1.5 m in length pumped by two 50 cm diffusion pumps. The base pressure of the facility is approximately 10^{-6} Torr. The background pressure during thruster testing at a xenon flow rate of 2-3 mg/sec is typically 10^{-4} Torr. Although this pressure is an order of magnitude lower than that of Janes and Lowder [5], it is still considerably higher than chamber pressures that are generally acceptable for the collection of reliable thruster performance data [14], and it is expected that the ingestion of background gas very near the exit of this discharge may influence the transient discharge characteristics. The possibility of this effect was a partial motivation for this study.

The Hall accelerator used in this study was constructed in 1995 and is the first attempt at Stanford to build a laboratory model Hall thruster [12]. A detailed description of its design is provided in Ref. 13. The thruster consists of inner and outer magnetic pole-pieces surrounding an insulated acceleration channel annulus 10 mm wide and 15 mm in depth. The radial magnetic field has a maximum value of approximately 100 G at a winding current of 2.0 A, the nominal operating conditions for this study. The cathode, required to neutralize the ion beam and support the necessary electric field, is a commercial hollow cathode (Ion Tech, Inc. model HCN-252). The plane of the cathode is approximately 2 cm downstream of the exit of the discharge. Propellant flow to the thruster anode and cathode sections is controlled by two factory calibrated Unit Instruments 1200 series mass flow controllers.

The accelerator channel has a region in which $dB_r/dz>0$ (z<9mm) and $dB_r/dz<0$ (z>9mm) [13,15]. As discussed by Morozov [6], the axial variation in the magnetic field has a significant affect on the transitory response of these discharges. In addition, his studies revealed that for discharges in which $dB_r/dz\geq0$ over the entire channel, the ratio of the average ion current (I_i) to total average discharge current (I_d), $\xi=I_i/I_d$ can exceed 60%. In contrast, when $dB_r/dz<0$, $\xi\leq0.4$. The enhanced electron current conductivity is attributed to the instabilities associated with the low-frequency traveling azimuthal drift waves predominant in the region of the discharge where $dB_r/dz<0$. These disturbances give rise to
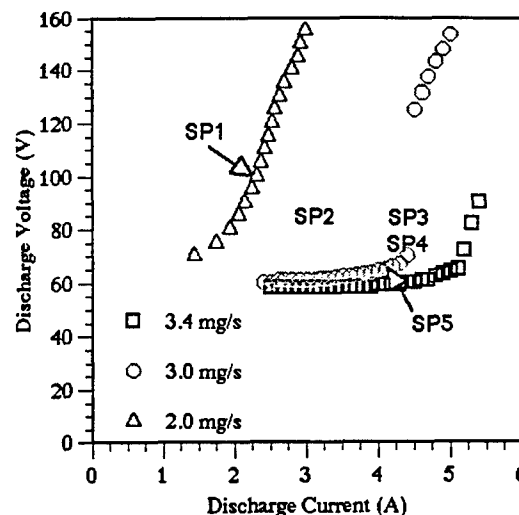

Figure 1. I-V characteristics of the Hall thruster operating on xenon.

equipotential surfaces that connect the exit plane to the anode along which the electrons can migrate [6]. As discussed below, the magnetic field distribution present in our discharge supports the growth of such waves, and gives rise to values of $\xi\sim0.4$ at the cathode plane under nominal operating conditions. This relatively low value indicates that the thruster is operating at below optimum performance. This is attributed to the shape and strength of the applied magnetic field.

Figure 1 shows a the I-V characteristics typical of this thruster. Unlike the I-V response seen in space-qualified thrusters, we see that the current continues to rise significantly beyond the region of the "knee". In many cases, we do not observe a distinct current saturation region. Two possible explanations for the absence of a distinct saturation in the discharge current are (i) the relatively high background pressure ($\sim10^{-4}$ Torr), which gives rise to continuous and incomplete ionization resulting from the ingestion of background gas in the chamber; and (ii) the shape and magnitude of the magnetic field. The latter issue is discussed in more detail in Ref. 13, where the performance of this thruster is compared to that of a thruster with a significantly different magnetic field distribution.

Also indicated in Figure 1 are five operating conditions for which a more extensive set of data is gathered. Operating set point SP1 ($V_d = 100V$, $I_d = 2.3A$, $\dot{m} = 2$ mg/sec anode flow rates) represents operation in a near-current saturation mode. Set point SP2 ($V_d = 85V$, $I_d = 3.1A$, $\dot{m} = 2.5$ mg/sec anode flow rates) represents operation just above the knee at a moderate xenon flow rate (entire I-V curve not shown). Set point SP3 ($V_d = 85V$, $I_d = 4.5A$, $\dot{m} = 3$ mg/sec anode flow rates) represents operation at the same voltage as SP2 but at the highest mass flow investigated. Set point SP4 ($V_d = 75V$, $I_d = 3.7A$, $\dot{m} = 3$ mg/sec anode flow rates) and SP5 ($V_d = 65V$, $I_d = 3.35A$, $\dot{m} = 3$ mg/sec anode flow rates) represent operation along the same I-V curve as SP3, but at lower power, closer to and just below the "knee" respectively.

Floating Potential Probes

A number of measurements are made of the floating potential of the plasma along the axial and azimuthal coordinates of the thruster both outside and within the accelerator channel. The floating potential probes consist of a 0.5 mm diameter tungsten wire surrounded by an alumina sleeve oriented such that the axis of the exposed
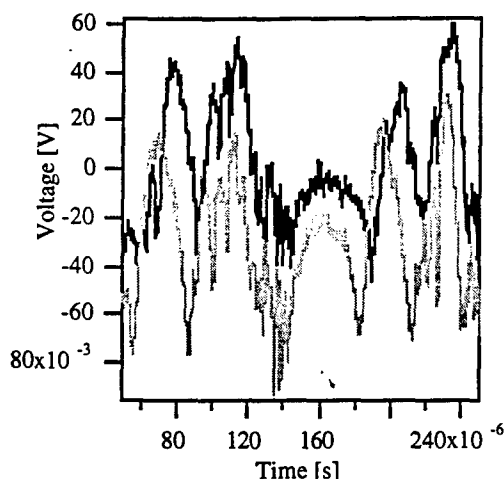
Figure 2. Oscilloscope traces of the signal from two floating potential probes placed 45° apart along the azimuthal direction at the exit of the Hall thruster.

portion of the probe was perpendicular to the axial coordinate of the thruster. The exposed length of the probe was 0.3 cm providing a total probe area of approximately 5 mm². The probe leads were attached to the center pin of a 50Ω co-axial cable, with a grounded outer shield. Co-axial transmission line feedthroughs provided the transfer of the signal through the chamber into a Tektronix model TDS-210 oscilloscope.

For evaluation of DC component and the low frequency (<50kHz) AC oscillations in the floating potential, the signals were terminated with the internal 1 MΩ impedance of the oscilloscope. We note that this termination is likely to make the detection of phase shifts unreliable since the 1 MΩ termination on the oscilloscope causes the co-axial cable to act as a low-pass filter, compromising the frequency response of the system. Verification that the system was adequately capturing the low frequency (<50kHz) AC structure in the signal was performed by comparing the transient signal obtained with a 1 MΩ impedance to that obtained with a 75kΩ and 50Ω terminator on the oscilloscope.

The time-variation in the floating potential is not a measure of the time-variation in the plasma potential. However, it has been shown by Esipchuk et al. [7] that the time-varying component of a floating potential probe is equal to that of a hot emissive (floating) probe in a Hall accelerator. As pointed out in Ref. 7, this implies that the disturbances giving rise to time-varying potentials are isothermal since the differences between the floating and plasma potential are in general proportional to the electron temperature (ϕ_p-ϕ_f~2kTe). We therefore interpret the transient oscillations on the floating potential probes to reflect the spectra associated with transient oscillations in the local plasma potential on the basis of these prior findings.

Azimuthal Wave Speed Detection Probes

The same type of probes described above to detect the floating potential were used to determine the average phase velocity of the azimuthal waves. Two probes were separated by 45° along the azimuthal coordinate midway between the inner and outer insulating walls. In order to achieve a high degree of sensitivity to a wide spectral range, the signals to the oscilloscope were terminated by 50Ω in order to match the impedance of the co-axial transmission line. As a result of this low impedance

termination, the signals do not represent the floating potentials. Instead, the exposed wires behave more like grounded probes. It is therefore difficult to directly relate the amplitude of the fluctuations to the time-variation in a particular plasma property (i.e., plasma potential, density, etc..). It is noteworthy however, to mention that the oscilloscope trace was nearly identical in structure to that of the signal from a probe terminated with 75kΩ, the time average signal of which was close to the floating potential. As a result, we believe that oscillatory signal in these low-impedance traces reflects the oscillatory variation in the floating or plasma potential. Regardless, the primary intention of these measurements was to detect the time delay between the arrival of the disturbances on the two probes. The power spectra from these probes was used to qualitatively interpret the spatial characteristics of the disturbances within the discharge channel.

An example of the oscilloscope traces from the two probes (separated by 45° in the azimuthal direction) placed at the exit plane of the Hall accelerator operating at the set point SP1 is shown in Figure 2. A distinct time delay between the two probe traces is apparent. However, it is also apparent that at this operating set point the disturbance is not of a pure wave, and that the phase delay is not consistent across the entire trace, indicative of a degree of turbulence. In the results presented in the next section, a cross-correlation of the two traces is used to obtain a representative average of the phase delay between the two signals, from which an estimate of the traveling azimuthal wave speed can be derived. The cross-correlation is also used to qualitatively determine the coherence of the waves.

The calculated wave speed, v_p, is expected to be considerably less than the azimuthal drift velocities, v_d = E_z/B_r . In prior studies of Hall discharges, measured values of v_p range from 0.2 to 0.8v_d. This is in agreement with the theoretical analysis of Esipchuk and Tilinin [8] as shown by Choueri [9]. The source of excitation of these waves is the electron drift velocities associated with gradients in the magnetic field and/or plasma density [9].

Hot Probes for Plasma Potential Measurements

Two probes were constructed to measure plasma potentials in the plasma produced by the Hall thruster. The first probe consisted of tungsten wire 0.50 mm in diameter and 5.0 mm in length placed perpendicular to the ion flow. The lead immediately behind the probe was insulated by 1.6 mm diameter alumina tube and shielded instrumentation cable through a vacuum feedthrough and connected to a digital voltmeter.

The first probe is only used to verify the floating potential measurement of the second probe and extends the measurements of the floating potential of the second probe to within a few millimeters of the anode. The second probe is designed to measure plasma potential by heating a 5 mm long tungsten wire filament using a 12V stepdown transformer. The transformer electrically isolates the probe from line voltage (110V) yet allows the probe to be heated such that the thermionic emission of the probe overcomes the impedance of the probe sheath. The probe therefore floats at near the true plasma potential. When the transformer is unpowered, the probe is cold and the entire circuit remains at the local floating potential. The filament was suspended perpendicular to the ion flow by two sections of 22 gauge copper wire sheathed in 1.6 mm diameter alumina tubing. Plasma and floating potentials were measured at the center tap of the

transformer by a digital voltmeter relative to the thruster ground.

<u>Langmuir Probe for Temperature Measurements</u>

A Langmuir probe consisting of a tungsten wire 0.50 mm in diameter and 5.0 mm in length was placed in parallel to the plasma flow. It was swept using a Kepco Instruments BOP72-3 four quadrant power supply. Current flow through the probe was measured using a 10 Ω shunt. The voltage across the shunt was measured using a unity gain high common mode rejection Burr-Brown AN-117 differential amplifier.

The measured current-voltage traces were analyzed using planar probe theory as outlined in Ref. 16. Near the floating potential, the total current collected by a driven probe is given by:

$$I = I_e e^{-e(\phi_p - \phi)/kT_e} - I_i \qquad (1)$$

where I is the measured current, ϕ is the probe potential, ϕ_p is the plasma potential, T_e is the electron temperature, I_e is the electron saturation current, I_i is the ion saturation current, k is Boltzmann's constant, and e is the electron charge. The above equation can be rearranged to express the temperature as the inverse of the slope of the measured voltage-current trace.

The interaction between probes and magnetic fields is not well understood. It has been recognized that probes with lengths on the order of the Larmor radius are less affected by magnetic fields, and so the probe length was intentionally short. The probe was further constrained by the length to diameter ratio so that end effects could be neglected.

<u>Thrust Measurements</u>

The thrust stand used in this study has been discussed extensively in the literature [13,14]. It is an inverted pendulum type thrust stand built by the Jet Propulsion Laboratory and loaned to Stanford for the duration of this work by the U.S. Air Force Phillips Electric Propulsion Laboratory. Thrust is determined from the pendulum displacement measured by a linear voltage differential transducer. Calibration is provided by four 5.0 g weights. Thermal drift is minimized by water cooling surfaces exposed to the thruster plume and the portion of the stand that supports the thruster.

For each thrust measurement, the thruster was run for a period of 10-15 minutes to stabilize the thruster operation and to allow the thrust stand reach thermal equilibrium. Subsequently, 3 to 5 measurements of the thrust stand displacement were made, interspersed with induced oscillations to minimize stiction of the thrust stand. All power to the thruster was then turned off and a calibration of the thrust stand followed. Further details on these thrust measurements can be found in Ref. 13.

Results

Measurements of the time-variation in the floating potential were made with low frequency resolution (<50 kHz) within the accelerator channel for the four operating set points described above. A relative measure of intensity of the disturbances along the channel is the probe *voltage modulation*, defined here as twice the calculated standard deviation in the signal traces, ΔV. Figure 3 gives the variation in ΔV along the accelerator channel. We see that in all cases, the low frequency disturbances are uniformly distributed throughout the channel, with the exception of set point SP1, where there

is a noticeable increase in the amplitude of the disturbance (to about 16% of the peak) in the vicinity of the peak in the radial magnetic field. The nature of these disturbances, i.e., whether they are traveling waves or transient, uncorrelated (turbulent) disturbances are determined from the low-impedance terminated probes, as discussed below. The frequency spectra of the disturbances (as detected with the probes terminated with a 50 ohm impedance to match the co-axial line) at various axial positions within the channel are plotted as contour diagrams in Figure 4.

For the set point SP1, which corresponds to the thruster operation in the current saturation regime of the I-V curve, we see that the frequency spectrum is quite broad, with enhanced excitation of relatively low-frequency oscillations (~17kHz) coincident with the region of maximum magnetic field. This result is consistent with the high impedance terminated floating potential data. The relatively low frequencies appear to be characteristic of the so-called "loop" or "circuit" instabilities [9]. The origin of such instabilities are poorly understood, and are known to be quite sensitive to the power supply characteristics. The coincidence between the activity of this mode and the region of highest magnetic field suggests that this instability is associated with the ionization process, and indeed it has been referred to as the "instability in the position of the zone of ionization," in the previous Russian literature as described in Ref. 9. The contour plot for SP1 shows some excitation of frequencies in the 27kHz range.

For set point SP2, which corresponds to operating just above the knee of the I-V curve, we see the emergence of instabilities in the 27kHz frequency range, characteristic of traveling azimuthal drift waves often described in the literature. As mentioned above, this disturbance is slightly
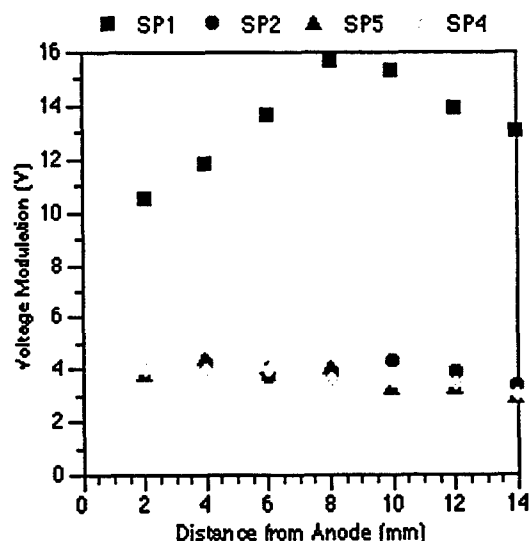

Figure 3. Variation in the voltage modulation as detected from the floating potential probe: squares-SP1; circles-SP2; diamonds-SP4; triangles-SP5.

evident in the case of SP1, although it is masked by the presence of the 17kHz mode. We also note that for this operating condition, that the activity is concentrated mainly near the exit plane (z>9 mm), where the gradient in the magnetic field is negative, i.e., $dB_r(z)/dz < 0$.

The frequency of this apparent azimuthal mode shifts slightly towards higher values (~27-35 kHz) at even higher mass flow rates, as indicated in the contour plot for set

point SP3. Furthermore, we see that this oscillation appears to have spread throughout the entire discharge channel of the thruster. There is little evidence of activity at frequencies < 20kHz.

At the lowest voltage and highest mass flow rates studied (set point SP5), the disturbances in this frequency range are not as strong, are perhaps shifted to slightly lower frequencies, and, are predominantly active near the anode. More interesting is the appearance of a harmonic at approximately 42 kHz.

The nature of these disturbances can be further resolved by use of the two azimuthally separated probes to study the coherence of these waves in the azimuthal direction. Figure 5 shows a cross-correlation of the two signal traces given in Figure 2, taken with two probes separated by 45° in the azimuthal direction at the exit plane of the thruster operating at the set point SP1. The shift in the peak of the correlated spectrum is apparent,

indicating an average phase shift of 4.1 ± 0.3 μsec. This phase shift corresponds to a wave speed of 8.6 km/sec, in the direction of the **E x B** drift. The easily discernible phase shift indicates that these disturbances are highly correlated, indicative of a coherent traveling azimuthal wave.

Table 1 gives the measured time delay, τ_d, between the signal traces and the calculated variation in the azimuthal wave speed, with axial position for four of the operating set points. In almost all cases, the azimuthal phase shift is difficult to prescribe with certainty in the axial region between 2 and 6 mm from the exit anode (where $dB_r/dz>0$), as the coherence in the signals is poor. Furthermore, with the exception of set point SP4, the traveling azimuthal wave is clearly excited near the exit plane, where $dB_r/dz < 0$. For set point SP4, the only discernible phase shift is near the exit plane, where there is a fair degree of coherence in the signals.
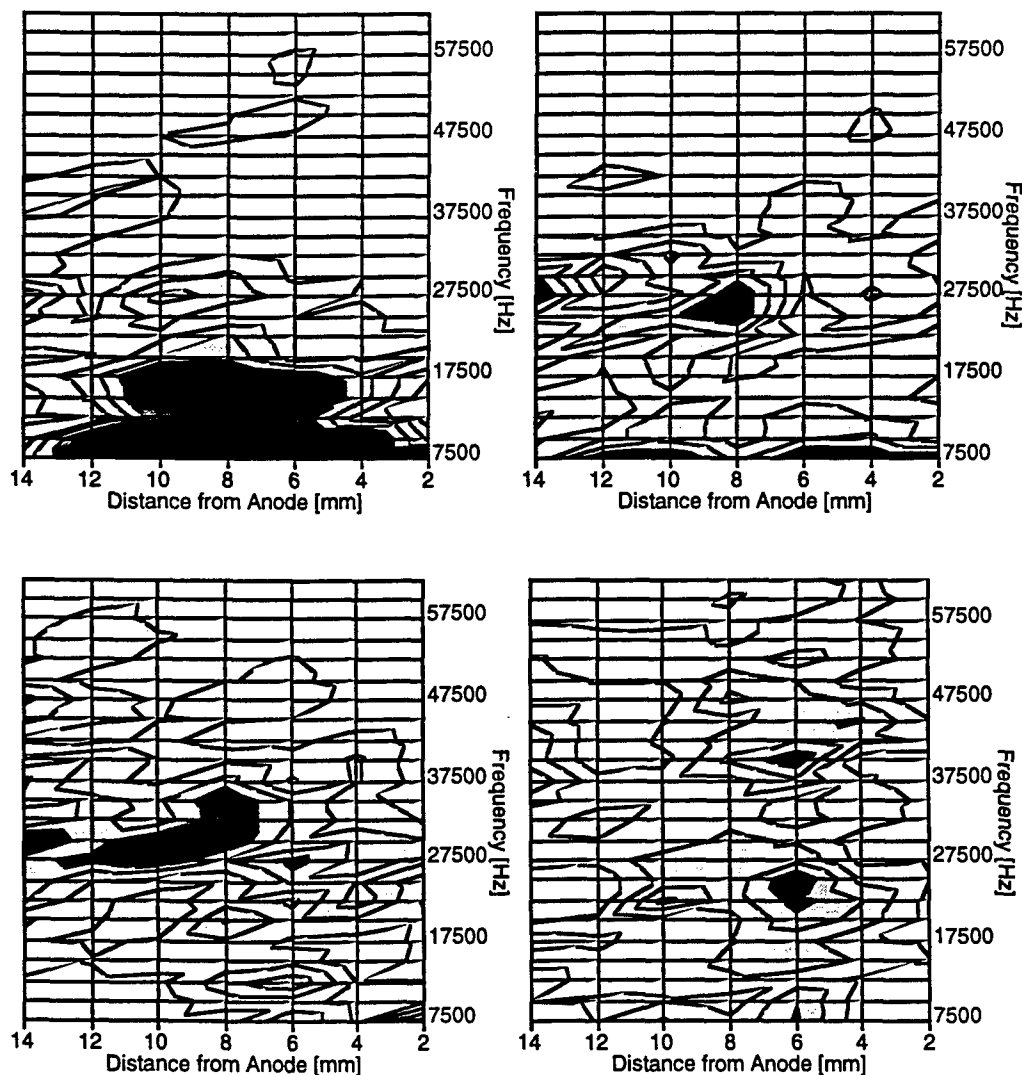

Figure 4. Contour diagrams of the power spectrum of the oscillations detected with the low-impedance probes at various locations within the thruster. The four diagrams refer to the for nominal operating set points: top left-SP1, top right - SP2, bottom left-SP3, bottom right-SP5.

Combining this result with that of the contour diagrams in Figure 4, we can summarize the following: (i) when operating on the current saturation region of the I-V curve, there appears to be a *weak* but very *coherent* traveling azimuthal wave near the exit plane of the thruster. The calculated wave speeds vary between 7-20 km/sec, increasing steadily as the peak in the magnetic field is approached from the exit plane inwards. We also see broader spectral activity (extending to 10 kHz). The strongest instabilities seem to be near the region corresponding to the maximum magnetic field, possibly so-called "loop" instabilities, which appear to be much less coherent than the waves closer to the exit plane in our thruster; (ii) operating closer to the "knee" region, we see the distinct presence of a strong traveling azimuthal wave near the exit plane. The wave speeds are slightly lower than the higher voltage conditions of set point SP1. There is very little high frequency disturbance (>35kHz), and any activity in the region where $dB_r/dz > 0$ appears to be uncorrelated; (iii) operating on the ionization portion of the I-V curve close to the knee, the traveling azimuthal wave is even more pronounced. It seems to extend further into the channel, and the frequencies associated with this wave seem to shift to higher values; (iv) At the low voltage end of the ionization region of the I-V curve, the traveling azimuthal wave is still distinct but present only in the region very near the anode. There is evidence here for some bifurcation of the wave, possibly into the m = 2 azimuthal mode.

The measured DC averaged variation in the floating and plasma potential (obtained with the heated emissive probe) with axial position within the discharge and in the near-plume region is shown in Figure 6. The conditions for these measurements correspond to operating set point SP1. Recall that the cathode plane is located at a distance of 2 cm beyond the channel exit or 34 mm from the anode. From these data, we see that there is at most a 10V drop in potential along the channel, and much of the potential drop takes place between the exit and cathode plane. This result is consistent with the ion velocities measured by laser-induced fluorescence (LIF) for similar operating conditions [12]. From the LIF data, the ions are found to have very low energies (typically 2-5 eV) at the exit plane, accelerating to approximately 50eV below the applied potential at the cathode plane. The surprising

result is that a relatively high plasma potential persists well beyond the cathode plane.

The difference between the plasma and floating potential is also depicted in Figure 6. Qualitatively, it is representative of the variation in the electron temperature of the plasma. A direct analysis of the potential that a floating surface will take relative to that of the distant plasma is difficult in this case in that an estimate of the ion flux to the floating probe is required. The ion flux will very with location within the discharge.
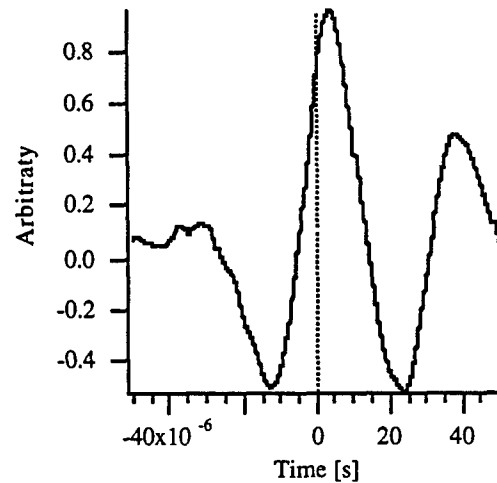

Figure 5. Cross-correlation spectrum of the two oscilloscope signal traces shown in Figure 2 corresponding to the exit plane of the thruster operating at set point SP1.

If the ion flux to the probe is limited by the Bohm velocity (a reasonable assumption inside the channel), then $\phi_p-\phi_f$ ~2.5kTe. If we assume that the effective electron and ion collection areas to the probe are equal. This estimate suggests that the electron temperature rises from about 8V near the anode, reaching a maximum of 25V at the exit plane. These temperatures are higher than those reported previously [9], and the difference can be attributed to the simple treatment of the ion current collected by the floating probe.

SP1

time delay (μsec)	4.1	4.5	2.7	1.8	1.3		
wave speed (km/s)	7.7	7.1	11.8	17.6	24.4		
coherence (poor/fair/good)	good	good	fair	fair	good	poor	poor
distance from anode (mm)	14	12	10	8	6	4	2

SP2

time delay (μsec)	8.6	7.5					
wave speed (km/s)	3.7	4.2					
coherence (poor/fair/good)	good	fair	poor	poor	poor	poor	poor
distance from anode (mm)	14	12	10	8	6	4	2

SP3

time delay (μsec)	5.7			5.7	4.5		
wave speed (km/s)	5.6			5.6	7.1		
coherence (poor/fair/good)	good	poor	poor	fair	good	poor	poor
distance from anode (mm)	14	12	10	8	6	4	2

SP4

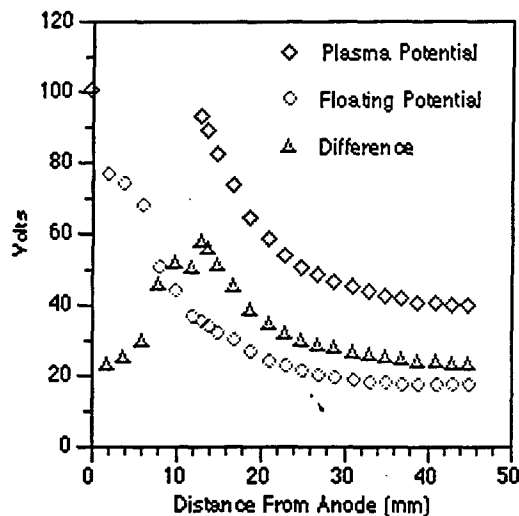| time delay (μsec)	9.8						
wave speed (km/s)	3.2						
coherence (poor/fair/good)	fair	poor	poor	poor	poor	poor	poor
distance from anode (mm)	14	12	10	8	6	4	2

Table 1

Figure 6. Plasma and floating potential variation and difference along the axial direction for the thruster operating at set point SP1 (100V). The plasma potential data extends from the plume to the exit plane.

A more direct measure of the electron temperature for conditions of set point SP1 was provided by the swept Langmuir probe. Figure 7 shows the corresponding variation in the electron temperatures with axial distance from the anode. We see that the temperatures derived from the Langmuir probe are considerably lower than that derived from the differences between the floating and plasma potential, and are in general qualitative agreement with the temperature measurements of Bishaev et al., [17] as given in Ref. 9. For the case shown in Figure 6, the Langmuir probe data indicates that the temperature rises from about 8eV at the cathode plane to 10eV near the exit plane.

Table 2 contains previously taken thrust measurements made on the Hall accelerator corresponding to several operating set points. From the measured thrusts and mass flows, mean propellant exit velocity, specific impulse, and thrust efficiency were computed [13]. It should be noted that these quantities are calculated using total mass flow and total system power. Total system power includes power dissipated in supporting the cathode discharge and producing the magnetic field. Adjustment is not made to account for cathode and magnetic circuit inefficiencies. However for all but one case, a minimum of 90% of the mass flow and 80% of the power dissipated was in the main discharge of the Hall thruster.

Comparing Figure 4 to the available thrust data for set point conditions SP1, SP3, and SP5 several trends are apparent. First, the Hall discharge is not operating in a particularly efficient regime. Difficulties with the thruster [13] and the necessity of inserting probes into the discharge required that the thruster be operated at lower than optimal voltages. These low voltages invariably
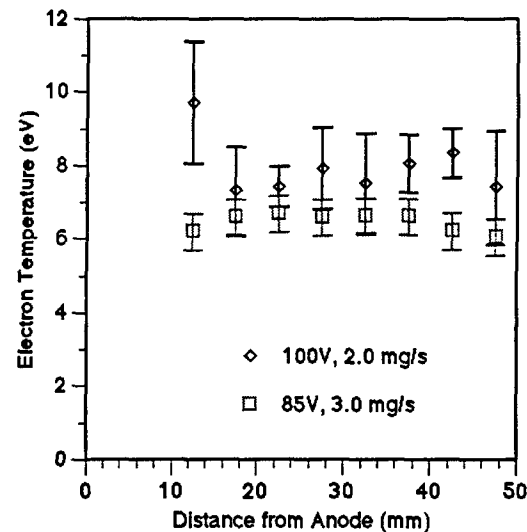

Figure 7. Swept Langmuir probe temperature data.

result in low thrust efficiencies. Second, SP1 and SP3 are significantly more efficient test points than SP5 by nearly a factor of three. Of these conditions, only SP5 exhibits significant higher frequency features. Although SP2 thrust data is not available, it too contains significant high frequency structure in Figure 4. This suggests a relationship between the apparent bifurcation of SP5 and its low efficiency.

Discussion

The results of our study are consistent with those of previous researchers [5-8]. We see clear evidence of the existence of traveling azimuthal waves that are excited predominantly near the exit plane of the Hall thruster in the vicinity where there is a negative gradient in the magnetic field. The strength of these relatively low frequency (~27 kHz) waves depends on the operating conditions, in particular, where in the region of the I-V curve the discharge is sustained, as seen previously [6]. These traveling azimuthal waves do not appear to be excited near the anode. Transient activity in this region where there is a positive gradient in the magnetic field seems to be more turbulent.

Where there was clear evidence for the coherence of these waves, an indirect estimate of the electric field can be obtained from the derivative of the time-varying potential and the measured of the wave speed. At the exit plane of the thruster operating at set point SP1, we estimate the maximum azimuthal electric field to be $E_\phi \sim$ 1 V/cm. This can be compared to the axial field at the exit plane, $E_z = 45$ V/cm, estimated from the axial variation in the plasma potential, as shown in Figure 6. A measure of the plasma density fluctuations would allow us to combine these results to determine the effective Bohm coefficient which characterizes the cross-field electron transport [5]. Using the measured wave speeds, which have much uncertainty in them, to evaluate the azimuthal field is tenuous. A closely-space dual probe is a better approach

Mass Flow (mg/s)	Anode Flow (mg/s)	Discharge Voltage (V)	Current (A)	Thrust (mN)	(+/-) (mN)	Mean V (m/s)	Specific Impulse (s)	Eff.	Specific Power (MJ/kg)
3.03	2.93	63	2.91	8.04	1.7	2653	270	0.04	78
3.03	2.93	85	4.35	17.7	0.5	5832	594	0.12	142
2.05	1.95	100	2.22	11.0	0.2	5341	544	0.11	135

Table 2

[5]. The probes in the dual-probe studies presented here were separated by too far a distance to use their differences to estimate the electric field.

The azimuthal wave speeds measured near the exit plane (~ 10 km/s) during operating set point SP1 can be compared to the $\mathbf{E} \times \mathbf{B}$ drift velocity, which for this case is 4.5×10^4 m/s. From Table 1, we see that the ratio v_p / v_d is approximately 0.2 - 0.4, in good agreement with that observed by others [9]. It is interesting to note that the data in Table 1 shows the measured wave speed to increase along the direction where the ratio of E_z/B decreases. This result has not been discussed in the prior literature. In essence, there is no unique value of the ratio v_p / v_d and it depends on the location within the thruster. This suggests that these waves are not directly excited by the azimuthal electron drift, but, rather, are more closely connected to the drift velocity associated with spatial gradients in the plasma properties.

The wavelengths of these traveling azimuthal waves can be estimated from their frequency and phase separation as measured by the probes separated by 45°. The traces in Figure 4 show that these azimuthal disturbances have wavelengths comparable to the channel circumference, confirming that indeed these disturbances correspond to the m = 1 (fundamental) azimuthal mode.

The difference between the measured floating and plasma potential, which is representative of the electron temperature, is a maximum close to where the magnetic field is a maximum in the channel. The previous LIF data (and the spatial variation in the plasma potential) show that the ionization zone and the acceleration zone are distinctly separated in this device. Also, it is apparent that the ions leave the exit of the channel with very low velocities, and gain their energy over a distance of about 2 cm outside the thruster, between the exit plane and cathode plane.

Future studies will be aimed at developing a more refined understanding of the structure of these low frequency azimuthal modes, and in extending the investigations to the transit-time and high frequency azimuthal oscillations as we develop a discharge that can operate closer to the "optimum" range of magnetic fields. In particular, non-intrusive, spatially and time-resolved laser measurements will be developed to replace the probe methods that we have employed in this study.

References

1. E.C. Lary, "Ion Acceleration in a Space-Charge Neutral Plasma," UAC Research Laboratory Report UAR-A125, June, 1962.

2. G.R. Seikel and E. Reshotko, "Hall Current Ion Acceleration," Bull. Am. Phys. Soc. 7, 414, 1962.

3. E.C. Lary, R.G. Meyerand Jr., and F. Salz, Ion Acceleration in a Gyro-dominated Neutral Plasma: Theory and Experiment," Bull. Am. Phys. Soc. 7, 441, 1962.

4. E.A. Pinsley, C.O. Brown, and C.M. Banas, "Hall Current Accelerator Using Surface Contact Ionization," J. Spacecraft 1, 525, 1964.

5. G.S. Janes and R.S. Lowder, "Anomalous Electron Diffusion and Ion Acceleration in a Low-Density Plasma," Phys. Fluids 6, 1115, 1966.

6. Morizov, A.I., Y.V. Esipchuk, A.M. Kapulkin, V.A. Nevroskii, and V.A. Smirnov, "Effect of the Magnetic Field on a Closed-Electronic-Drift Accelerator," Sov. Phys. - Tech. Phys. 17, 482, 1972.

7. Y.B. Esipchuk, A.I. Morozov, G.N. Tilinin, and A.V. Trofimov, "Plasma Oscillations in Closed-Drift Accelerators with an Extended Acceleration Zone," Sov. Phys. - Tech. Phys. 18, 928, 1974.

8. Y.B. Esipchuk and G.N. Tilinin, "Drift Instability in a Hall Current Plasma Accelerator," Sov. Phys. - Tech. Phys. 21, 417, 1976.

9. Choueiri, E.Y., "Characterization of Oscillations in Closed Drift Thrusters," AIAA-94-3013, 30th Joint Propulsion Conference, June 27-29, 1994, Indianapolis, IN.

10. V.I. Baranov, Y.S. Nazarenko, V.A. Petrosov, A.I. Vasin, and Y.M. Yashnov, "Theory of Oscillations and Conductivity for Hall Thrusters," AIAA 96-3192, 32nd Joint Propulsion Conference, July 1-3, 1996, Lake Buena Vista, FL.

11. Cedolin, R.J., W.A. Hargus, Jr., R.K. Hanson, and M.A. Cappelli, "Laser Induced Fluorescence Diagnostics for Xenon Hall Thrusters," AIAA-96-2986, 32nd Joint Propulsion Conference, July 1-3, 1996, Lake Buena Vista, FL.

12. Cedolin, R.J., W.A. Hargus, Jr., R.K. Hanson, and M.A. Cappelli, "Laser Induced Study of a Xenon Hall Thruster," AIAA 97-3053, 33rd Joint Propulsion Conference July 6-9, 1997, Seattle, WA.

13. Hargus, Jr., W.A., R.J. Cedolin, N.B. Meezan and M.A. Cappelli, "A Performance Study of a Low Power Hall Thruster," AIAA 97-3081, 33rd Joint Propulsion Conference July 6-9, 1997, Seattle, WA.

14. T. Randolph, V. Kim, H. Kaufman, K. Korzubusky, V. Zhurin, and M. Day, "Facility Effects on Stationary Plasma Thruster Testing," IEPC-93-93, 23rd International Electric Propulsion Conference Sept., 1993, Seattle, WA.

15. W.A. Hargus, Jr., N.B. Meezan, and M.A. Cappelli, "Transient Behavior of a Low Power Hall Thruster," AIAA-97-3050, 33rd Joint Propulsion Conference July 6-9, 1997, Seattle, WA.

16. M. Mitchner and C.H. Kruger, _Partially Ionized Gases_, J. Wiley and Sons, New York, 1973.

17. A.M. Bishaev, V.M. Gavryushin, A.I. Burgova, V. Kim, and V.K. Kharchvnikov, "The Experimental Investigations of Physical Processes and Characteristics of Stationary Plasma Thrusters with Closed Drift Electrons," RGC-EP 92-06, 1st Russian-German Conference on Electric Propulsion Engines and their Technical Applications, Giessen, Germany, 1992.